The Dissertation committee for Hunjoo Peter Lee Certifies that this is the approved version of the following dissertation:

FRACTURE PROPAGATION IN NATURALLY FRACTURED RESERVOIRS

Committee:

Jon E. Olson, Supervisor

Mukul M. Sharma

Maša Prodanović

Julia F.W. Gale

Jon T. Holder

Richard A. Schultz

FRACTURE PROPAGATION IN

NATURALLY FRACTURED RESERVOIRS

by

Hunjoo Peter Lee, B.S.; M.S.E.

Dissertation

Presented to the Faculty of the Graduate School of

The University of Texas at Austin

in Partial Fulfillment

of the Requirements

for the Degree of

Doctor of Philosophy

The University of Texas at Austin

December 2015

Dedication

To my Lord and Savior, Jesus Christ

"I can do everything through him who gives me strength."

Philippians 4:13

Acknowledgements

I give special thanks to ExxonMobil for its funding, and Pennsylvania General Energy (PGE) for its acquisition of the Marcellus core that was utilized in this study, and permission from both companies to publish the results. In particular, I thank Rodrick Myers for his discussions on this study and for his help and time going through the release process.

I would like to express my deepest gratitude to my supervisor, Dr. Jon E. Olson, for his guidance, understanding, and patience during my graduate studies at the University of Texas at Austin. He encouraged me to not only grow as an experimentalist and an engineer but also as an instructor and an independent thinker. It would have been impossible to complete this work without his helpful supervision.

I also want to extend my appreciations to the Department of Petroleum and Geosystems Engineering, especially those members of my doctoral committee, Dr. Mukul Sharma and Dr. Maša Prodanović, for their input, valuable discussions and advices. I express my thanks to Dr. Julia Gale for her guidance in extending my knowledge in a geologic point of view, and Dr. Richard Schultz for his advices in writing, presentations, and publications. I would like to especially thank Dr. Jon Holder who provided humor and entertainment in what could have otherwise been a somewhat stressful laboratory environment. Furthermore, I am grateful for the administrative support from Dori Coy which was essential for completing my study. Her smile and supportive attitude always made me happy during my graduate student life. I am also thankful for valuable advices in research from Dr. Chun Huh, for assistance in

understanding fracture mechanics from Dr. Chad Landis, for the graduate program advising from Frankie Hart, and for the technical support from Gary Miscoe and Daryl Nygaard.

I am very grateful for the friendship of all members in our research group, especially Farrokh, Li, Kan, Weiwei, Kaimin, Mohsen, Ben, Farrukh, Mehran, Emad, Valerie, Andreas, Nana, whom I worked closely and discussed research questions. I also want to thank all my friends, Dohoon, Saebom, Heesong, Sunghyun, Jongsoo, Kyunghaeng, Hyuntae, Ahra, Amos, Changmin, Hoonyoung, Ijung, Kwanghoon, Hyungjoo, Kwangjin, Dongkeun, Baehyun, Youngwoong, Yongdo, Hojung, Sanghyon, Bongjoon, Boumhee, for their all-around help during my graduate study.

I thank my parents, Sungkee Lee and Kyunghee Kim, for their faith in me and for their unending love and support in every way during my long educational career. I also thank my brother, Hunjin Lee, for his challenge and encouragement. Also, thank you to my parents-in-law, Sungil Lim and Kyungsoon Kwon, for their prayers and support.

Finally, and most importantly, I owe the greatest thanks to my beautiful wife, Esther Lim. Her support, encouragement, motivation, quiet patience and unwavering love were in the critical phase of my study what made this dissertation possible. I will always cherish the times we spent together at the University of Texas at Austin for our career and the happiest moment we shared with Yoonha and Joonha in Austin.

FRACTURE PROPAGATION IN NATURALLY FRACTURED RESERVOIRS

by

Hunjoo Peter Lee, Ph.D.

The University of Texas at Austin, 2015

Supervisor: Jon E. Olson

Investigations of hydrocarbons in tight formations require understanding of hydraulic fracturing in order to optimize the production and recovery of oil and natural gas. The classic description of hydraulic fracture is a single bi-wing planar feature, however, field observations show that hydraulic fracture growth in naturally fractured formations like shale is complex. Lack of knowledge concerning the remote stress impact and the interaction with planes of weakness on the fracture propagation trajectory leads to inaccurate predictions of the fracture geometry and the surface area required for the production estimation.

Most studies in engineering mechanics extended the standard mixed-mode fracture propagation models, based on the near-tip approximations, to include the impact of the tensile crack-parallel stress on the fracture propagation path. However, for fractures in the subsurface, the remote stress is compression, and internal fluid pressure or frictional

stress become important in the near-tip stress field and the propagation trajectory. The Modified Maximum Tangential Principal Stress criterion (MMTPS-criterion) was introduced to address and evaluate the remote and internal crack stresses in the propagation path. The predictions of the fracture propagation angles by the MMTPS-criterion agreed with published experimental results of fractures propagating under both tensile and compressive external loads. In addition, the predictions matched well with uniaxial compression tests on hydrostone samples with the critical radial distance, defined by the process zone size, for open fractures that satisfy the Small Scale Yielding conditions. For short open fractures, a larger critical radial distance was required to correspond with the experimental results. The MMTPS-criterion was also capable of predicting lower propagation angles for closed cracks with higher friction coefficients.

Preexisting discontinuities in shale, including natural fractures and bedding, act as planes of weakness that divert fracture propagation. To investigate the influence of weak planes on hydraulic fracture propagation, I performed Semi-Circular Bend (SCB) tests on Marcellus shale core samples containing calcite-filled natural fractures (veins). The approach angle of the induced fracture to the veins and the thickness of the veins had a strong influence on propagation. As the approach angle became more oblique to the induced fracture plane, and as the vein got thicker, the induced fracture was more likely to divert into the vein. Microstructural analysis of tested samples showed that the induced fracture propagated in the middle of the vein rather than the interface between vein and the rock matrix. Cleavage planes and fluid inclusion trails in the vein cements exerted some control on the fracture path. By combining the experimental results with theoretical

fracture-mechanics arguments, the fracture toughness of the calcite veins was estimated to range from $0.99\ \mathrm{MPa}\sqrt{\mathrm{m}}$ to $1.14\ \mathrm{MPa}\sqrt{\mathrm{m}}$, depending on the value used for the Young's modulus of the calcite vein material. Measured fracture toughness of unfractured Marcellus shale was $0.64\ \mathrm{MPa}\sqrt{\mathrm{m}}$.

A Discrete Element Method (DEM) based numerical modeling software, Particle Flow Code in three-dimensions (PFC3D), was utilized to reproduce and analyze the experimental results of Marcellus shale samples. The trend of numerical results correlated with the interaction feature of the experimental results for various approach angle and thickness (i.e., aperture) of the vein. Further sensitivity analysis on vein properties indicated that veins with lower strength and higher stiffness contribute to more fracture diversion than veins with higher strength and lower stiffness. Additionally, parallel bond breakages in the model show that microcracks were generated inside the vein before the induced fracture encountered the vein especially for the veins with higher stiffnesses when compared to the rock matrix. Most of the bond failure mode inside the vein and the induced fracture was tensile rather than shear mode.

TABLE OF CONTENTS

LIST OF TABLES ..... **XII**

LIST OF FIGURES ..... **XIII**

CHAPTER 1 : INTRODUCTION **1**

1.1 Hydraulic Fracturing 6

1.2 Rock Fracture Mechanics 10

1.3 Preexisting Discontinuities in Shale 12

1.4 Interaction of hydraulic fracture with preexisting discontinuities 16

1.5 Research Objectives 20

1.6 Dissertation Outline 21

CHAPTER 2 : MIXED-MODE FRACTURE PROPAGATION UNDER REMOTE STRESSES **23**

2.1 Energy-based Fracture Propagation Criterion 24

2.2 Strain-based Fracture Propagation Criterion 27

2.3 Stress-based Fracture Propagation Criterion 28

2.4 Modified Maximum Tangential Principal Stress Criterion 30

2.5 Critical Propagation Distance 43

2.6 Angled Fracture Problem 52

2.7 Experimental Set-Up 64

2.8 Open Fractures under Compression in Hydrostone 71

2.9 Closed Fractures under Compression 76

2.10 Discussion 83

2.11 Conclusions 86

CHAPTER 3 : THE INTERACTION OF PROPAGATING OPENING MODE FRACTURES WITH PREEXISTING DISCONTINUITIES IN SHALE **88**

3.1 Sample Properties 91

3.2 Semi-Circular Bend Test 94

3.3 Sample Preparation 95
3.4 Energy Release Rate Criterion 98
3.5 Samples without Veins 101
3.6 Influence of Approach Angle on Fracture Path 103
3.7 Theoretical Analysis of Fracture Interaction Results 105
3.8 Influence of Vein Thickness on Fracture Path 107
3.9 Microstructural Analysis 109
3.10 Discussion 112
3.11 Conclusions 114

CHAPTER 4 : FRACTURE INTERACTION ANALYSIS BY DISCRETE ELEMENT METHOD 116
4.1 Particle Flow Code 118
4.2 Sample Assembly Generation 120
4.3 Microscopic Parameter Determination 123
4.4 SCB Test Preparation 134
4.5 SCB Specimen with Vein 137
4.6 Influence of Approach Angle on Fracture Path 139
4.7 Influence of Vein Stiffness on Fracture Path 144
4.8 Influence of Vein Strength on Fracture Path 151
4.9 Influence of Vein Thickness on Fracture Path 152
4.10 Influence of Vein Location 155
4.11 Discussion 157
4.12 Conclusions 160

CHAPTER 5 : CONCLUSIONS AND RECOMMENDATIONS 163
5.1 Conclusions 163
5.2 Recommendations 167

REFERENCES 172

LIST OF TABLES

Table 1.1. Technically recoverable tight/shale oil and shale gas in United States and 41 other countries (EIA, 2014)
(http://www.eia.gov/todayinenergy/detail.cfm?id=14431) 3

Table 2.1. Hydrostone mechanical properties 67

Table 2.2. Hydrostone gypsum cement to water weight ratio (Bahorich et al., 2012) 68

Table 3.1. List of samples 97

Table 3.2. Fracture toughness results for samples without calcite-filled veins 102

Table 3.3. G_c^{vein} estimates based on crack propagation results 106

Table 4.1. Microproperties for the rock matrix in PFC3D 127

Table 4.2. The elastic properties and strengths of Marcellus shale in experiment and PFC3D 130

Table 4.3. Results of UCS/σ_T for flaw-contained materials in PFC3D 132

Table 4.4. Number of particles and parallel bonds for various SCB sample sizes 159

LIST OF FIGURES

Figure 1.1. Triangular composition diagram for Barnett, Eagle Ford Formation (EF), and clay-rich mudrock (Md), Monterey formation, and Marcellus Formation (after Gale et al., 2014). 2

Figure 1.2. Tight/shale oil and shale gas formations around the world (EIA, 2014). ..... (http://www.eia.gov/todayinenergy/detail.cfm?id=14431)..... 3

Figure 1.3. Shale plays in United States (EIA, 2011). ..... (http://www.eia.gov/analysis/studies/usshalegas/)..... 4

Figure 1.4. The trend of shale gas production by plays in United States (EIA, 2015). ..... (http://www.eia.gov/energy_in_brief/article/shale_in_the_united_states.cfm). 5

Figure 1.5. The trend of tight/shale oil production by plays in United States (EIA, 2015). (http://www.eia.gov/energy_in_brief/article/shale_in_the_united_states.cfm). 5

Figure 1.6. Estimated natural gas and crude oil in four countries as of 2014 (EIA, 2015). . (http://www.eia.gov/todayinenergy/detail.cfm?id=19991)..... 6

Figure 1.7. Trend of hydraulically fractured wells (blue) and hydraulic fracturing treatments (red) from 1947 to 2010 focused on states with more than 50 hydraulically fracture wells and 1,000 hydraulic fracturing treatments (Gallegos and Varela, 2015). 8

Figure 1.8. Schematic veiws of the three fracture modes based on the relative movement of fracture walls (Whittaker et al., 1992). 11

Figure 1.9. Histogram of sealed fracture aperture size ($>30\ \mu m$) from six formations (Gale et al., 2014). 15

Figure 1.10. Types of interaction between the hydraulic fracture (HF) and the natural fracture (NF): (a) HF arrested at NF, (b) HF crossing NF, (c) NF dilation after crossing, (d) HF diverting into NF (NF dilation) , (e) HF kinking back into the rock matrix before it reaches the tip of the NF, and (f) HF kinking at the tip of the NF after diversion (after Gu et al., 2011). 17

Figure 2.1. Sketch of the three near-tip stress components (σ_{rr}, $\sigma_{\theta\theta}$, $\sigma_{r\theta}$). All stress components are positive as drawn..... 29

Figure 2.2. A Comparison of fracture paths with two patch lengths (3.08 and 20.53 mm). Numerically predicted paths were generated by the MTS-criterion using JOINTS. Scales are in centimeters (Thomas and Pollard, 1993). 32

Figure 2.3. The predictions of the fracture propagation angles (θ) with respect to the fracture inclination angles (β) for angled fractures under uniaxial tension by the MTS-criterion. Experiment results are from Williams and Ewing (1972) and Pook (1971). The experimental scatters of Willams and Ewing (1972) are obtained from Sih and Kipp (1974). 33

Figure 2.4. Fracture paths predicted with four criterion for two crack types: (a) a slot crack under tensile loading (Maiti and Smith, 1983), and (b) an elliptical crack under compressive loading (Maiti and Smith, 1984). The experimenal result in (a) are from Kipp and Sih (1975). 36

Figure 2.5. Tri-polar coordinate system: (a) for a fracture with a length of 2a in the X_2-direction and (b) for points very close to the fracture tip (after Pollard and Segall, 1987). 39

Figure 2.6. Sketch of stress components for a fracture in the X_2-direction: (a) internal crack stresses and (b) remote stresses (after Pollard and Segall, 1987). All stress components are positive as drawn. 39

Figure 2.7. Fracture process zones of mode I fractures ($K_{\mathrm{I}} = 1\ \mathrm{MPa}\sqrt{\mathrm{m}}$, $K_{\mathrm{II}} = 0$) under various loading types: (a) remote stresses of $\sigma_{11}^{\,r}$, $\sigma_{22}^{\,r} = 0.5$ MPa with zero internal crack stresses ($\sigma_{11}^{\,c}$, $\sigma_{12}^{\,c} = 0$) to reproduce the prediction of Schmidt (1980), (b) the internal pressure of $\sigma_{11}^{\,c} = -0.5$ MPa with zero remote stresses ($\sigma_{11}^{\,r}$, $\sigma_{22}^{\,r} = 0$), (c) the internal pressure of $\sigma_{11}^{\,c} = -1$ MPa with $\sigma_{11}^{\,r}$, $\sigma_{22}^{\,r} = -0.5$ MPa. 46

Figure 2.8. Fracture process zones of pressurized fractures ($\sigma_{11}^{\,c} = -1$ MPa ; $K_{\mathrm{I}} = 1\ \mathrm{MPa}\sqrt{\mathrm{m}}$, $K_{\mathrm{II}} = 0$) under various remote differential stresses: (a) $\sigma_{22}^{\,r} / \sigma_{11}^{\,r} = 1$ (the example of Figure 2.7c) and (b) $\sigma_{22}^{\,r} / \sigma_{11}^{\,r} = 3$. For both cases, $\sigma_{11}^{\,r}$ is kept constant at –0.5 MPa. 48

Figure 2.9. Fracture process zones of pressurized fractures ($\sigma_{11}^{\,c} = -5.5$ MPa ; $K_{\mathrm{I}} = 1\ \mathrm{MPa}\sqrt{\mathrm{m}}$, $K_{\mathrm{II}} = 0$) under various remote differential stresses: (a), (b) $\sigma_{22}^{\,r} / \sigma_{11}^{\,r} = 3$, and (c), (d) $\sigma_{22}^{\,r} / \sigma_{11}^{\,r} = 4$. The fracture process zone of (a) and (c) are defined by the tensile strength (solid lines), and (b) and (d) are defined by the shear strength (dashed lines). For all cases, $\sigma_{11}^{\,r}$ is kept constant at –0.5 MPa. 50

Figure 2.10. Schematic views of the angled fracture problem under biaxial tensile loading: (a) a fracture located in the plane parallel to the X_2-direction in the global x-y coordinate, (b) the resolved stresses on the crack, (c) the internal crack stresses of the crack. All stress components are positive as drawn. 54

Figure 2.11. The predictions of the fracture propagation angles (θ) by the MMTPS-criterion (dashed lines), with various r/a values ranging from 0.0001 to 0.2, with the prediction of the conventional MTS-criterion (solid line) and experimental results. 56

Figure 2.12. The predictions of the fracture propagation angles (θ) by the MMTPS-criterion (red lines) and the MTPS-criterion (blue lines), for r/a values of 0.001, 0.01, and 0.1, with experimental results..... 57

Figure 2.13. The predictions of the fracture propagation angles (θ) with respect to the fracture inclination angles (β) for angled open fractures under uniaxial compressive loading by the MTS-criterion (with zero K_I and negative K_I) and the MMTPS-criterion (with negative K_I; red dashed-lines). Predictions are compared with experimental results of Tirosh and Catz (1981). Two data sets of the Tirosh and Catz (1981) reflect results of different fracture tip curvature radius to fracture half-length ratio (ρ/a) which is discussed in Figure 2.15. 60

Figure 2.14. The predictions of the fracture propagation angles (θ) with respect to the fracture inclination angles (β) by the MMTPS-criterion with (blue-dashed lines) and without (red-dashed lines) the modified mode I stress intensity factor (K_I) from Equation (2.33). The fracture tip curvature radius to the fracture half-length ratio (ρ/a) for the modification is 0.04. 62

Figure 2.15. The predictions of the fracture propagation angles (θ) with respect to the fracture inclination angles (β) by the MMTPS-criterion with the modified K_I and PMMA experimental results from Tirosh and Catz (1981). The fracture tip curvature radius to the fracture half-length ratios (ρ/a) are (a) 0.031 and (b) 0.055, respectively. 63

Figure 2.16. Porosity dependence on fracture propagation and the failure of a rock. (a), (c) shows the primary wing fracture propagation before the maximum stress and (b), (d) illustrates secondary fractures and shear failure after the maximum stress (Petit and Barquins, 1988)..... 65

Figure 2.17. The sequence of fracture growth for an angled fracture in a limestone sample under uniaxial compression loading (Ingraffea and Heuze, 1980). 66

Figure 2.18. The procedure of preparing hydrostone specimens with open fractures for the uniaxial compression test: (a) the molds with tick marks and shims prepared before hydrostone pouring, (b) the liquefied hydrostone poured into the molds with shims inserted in various inclination angles, and (c) hydrostone samples ready for the uniaxial compression test. 69

Figure 2.19. A hydrostone sample after unloading with primary wing fractures traced with the red marker. The tangent of the initial increments and the fracture inclination plane were marked with a pencil for the measurement of the propagation angle. (a) is the front view of the sample and (b) is the rear view of the same sample. 71

Figure 2.20. Experimental results of hydrostone samples with three fracture lengths (0.5 inch–black, 0.75 inch–blue, and 1.0 inch–red markers) and their best fit curves. 72

Figure 2.21. Experimental results of hydrostone samples with three fracture lengths (0.5 inch–black, 0.75 inch–blue, and 1.0 inch–red markers) and the predictions of the MMTPS-criterion with three r_c / a ratios (0.084–black, 0.056–blue, and 0.042–red-dashed lines, respectively). The ρ / a values were different for each case since the fracture half-length varied. 74

Figure 2.22. The predictions by the MMTPS-criterion and experimental results of hydrostone samples with three fracture lengths: (a) 25.4-mm (1.0-inch) fractures, (b) 19-mm (0.75-inch) fractures, (c) and (d) 12.7-mm (0.5-inch) fractures. The predictions of (a), (b), (c) are based on r_c of 0.53 mm (0.021 inch) and (d) is based on r_c of 1.07 mm (0.042 inch)..... 75

Figure 2.23. The predictions of the fracture propagation angles (θ) with respect to the fracture inclination angles (β) by the MMTPS-criterion for frictionless closed fractures under uniaxial compression with various r_c / a values ranging from 0.0001 to 0.2..... 79

Figure 2.24. The requirement of fracture inclination angles (β) for the fracture propagation of closed cracks with various friction coefficients (μ) under biaxial compression ($\sigma_{xx}^{\,r}, \sigma_{yy}^{\,r} < 0$) (after Li et al., 2012). 80

Figure 2.25. The predictions of fracture propagation angles for closed fractures with various friction coefficients (0, 0.3, 0.5) by the MMTPS-criterion and the experimental results of Bobet (2000) and Park and Bobet (2010). The r_c / a values utilized for the predictions are (a) 0.2, (b) 0.1, and (c) 0.02, respectively. (d) is the prediction from Li et al. (2012) with r_c / a of 0.02. 82

Figure 2.26. Schematic view of the fracture process zone and the *K*-annulus in the vicinity of the fracture tip. 84

Figure 3.1. Map view of fracture treatment showing the complexity of fracture networks in Barnett (Fisher et al., 2004). 89

Figure 3.2. Orientation of bedding relative to crack-propagation direction for arrester (left) and divider (right) configurations (after Chong et al., 1987). 92

Figure 3.3. Thin section photomicrographs of intact vein, (a) plane light photomicrograph showing inclusion trails parallel to fracture walls indicating crack-seal texture, and (b) with crossed polars showing individual crystals extending from wall to wall (arrows). 93

Figure 3.4. Schematic view of the SCB test specimen with discontinuity at angle θ_o (after Chong and Kuruppu, 1984). 95

Figure 3.5. Procedure of preparing samples for the SCB test: (a) original Marcellus shale containing calcite-filled vein core collected, (b) the octagonal shape template with 63.5-mm (2.5-inch) sides, (c) the specimen sliced into a half-octagonal shape, (d) the case for which the edges were ground from the half-octagonal shape, and (e) the specimen with a vein at $\theta_o = 90°$ loaded by three steel rollers. 96

Figure 3.6. Energy release rate, *G*, as a function of angle, θ : loading case ($G(0°)/G_c^{rock} = 1$) with lines representing the critical energy release rate for vein inclusions, represented as the ratio G_c^{vein}/G_c^{rock}, ranging from 0.25 to 1.00. $G_c^{vein}/G_c^{rock} = 1$ represents homogeneous material. Exemplary dotted line for case of $G_c^{vein}/G_c^{rock} = 0.5$ shows that the induced fracture diverts into the preexisting veins in the orientation of $-65° \le \theta \le 65°$. 99

Figure 3.7. Load versus displacement curves: (a) bedding parallel to sample base, $\alpha_{bed} = 0°$, and (b) inclined, $\alpha_{bed} = 30°$. 101

Figure 3.8. Results of SCB test from samples of same vein thickness (0.25 mm) with different θ_0 angles: angle θ_0 of (a) 90°, (b) 81°, (c) 58°, and (d) 43°. Induced fracture in (a) crossed the vein but it diverted for (b), (c), and (d). 105

Figure 3.9. SCB tests of orthogonal (angle θ_o of 90°) case with different vein thicknesses: (a) thickness of 1.9 mm, (b) 1.3 mm, (c) 0.9 mm, and (d) 0.25 mm. Induced fracture of (a) and (b) did not cross the vein but it crossed for (c) and (d). 108

Figure 3.10. SCB tests of cluster of veins: case of cluster at angle θ_o of (a) 90° and (b) 81°. 109

Figure 3.11. Thin section photomicrographs of tested samples with vein thickness of 0.25 mm in Figure 3.8: (a) angle θ_o of 90°, (b) 81°, (c) 58°, and (d) 43°. Induced fractures in (a) crossed but it diverted for (b), (c), and (d). Induced fracture (IF) is noted on the figure and the IF propagated from the top to bottom for all cases. 110

Figure 3.12. Thin section photomicrographs SCB tests of orthogonal (angle θ_o of 90°) case with different thicknesses: (a) thickness of 1.9 mm, (b) 1.3 mm, (c) 0.9 mm, and (d) 0.25 mm. Induced fractures in (a) and (b) did not cross but they crossed for (c) and (d). Induced fracture (IF) is noted on the figure and the IF fracture propagated from the bottom to top for all cases. 112

Figure 4.1. Schematic view of two spherical particles in contact and a parallel bond depicted as a cylinder of cementatious material between the particles (Itasca, 2008). 119

Figure 4.2. The cycle of calculation between particles and contacts in PFC3D (Itasca, 2008). 120

Figure 4.3. The procedure of sample assembly generation by PFC2D model: (a) randomly distributed particles before arrangement, (b) contact-force distribution after installing isotropic stress, (c) elimination of floating particles, and (d) installation of the parallel bond network (Potyondy and Cundall, 2004). 122

Figure 4.4. The relationship between the stiffness ratio ($k_n/k_s = \overline{k_n}/\overline{k_s}$) and Poisson's ratio. 126

Figure 4.5. Axial stess-versus-axial strain curves from the uniaxial compression tests of Marcellus shale. Blue line illustrates the PFC3D result and red line is the laboratory result. 128

Figure 4.6. The experimental set-up of SCB test and the numerically modeled SCB test with PFC3D..... 129

Figure 4.7. Load-versus-displacement curves from the SCB test of Marcellus shale. Blue line illustrates the PFC3D result and red line is one example from the laboratory results (sample 16d in Table 3.2). The PFC3D specimen for this example was set with diameter of 61 mm and a thickness of 20.3 mm to match the size of sample 16d. 129

Figure 4.8. PFC3D Results of flaw-contained materials (parallel bonds deletion of 0%, 10%, 20%, 30%, and 40%): (a) stress-strain curves from the uniaxial compression test and (b) load-strain curves from the Brazilian test. 133

Figure 4.9. Load-versus-displacement curves of the SCB test under various loading rates in PFC3D..... 135

Figure 4.10. The impact of parallel bond strengths ($\bar{\sigma}$ and $\bar{\tau}$) on the fracture toughness in PFC3D..... 136

Figure 4.11. Schematic views of SCB test set-up in PFC3D: (a) particles representing shale matrix (dark gray) with a vein (white) at 75° and (b) parallel bonds of the rock matrix (black) and the vein (white). 138

Figure 4.12. SCB test results with vein ($0.5\times K_{Ic}^{rock}$ and $1\times E^{*rock}$) of approach angles from 20° to 90°. Red and blue boxes indicate fracture diversion and fracture crossing, respectively. 140

Figure 4.13. Induced fracture propagation in PFC3D specimens with a vein ($0.5\times K_{Ic}^{rock}$ and $1\times E^{*rock}$) at an approach angle of 30°. Figures (a) to (h) correspond to the points marked in the (i) load–displacement curve measured from the loading roller. 143

Figure 4.14. SCB test results with veins ($1.0\times K_{Ic}^{rock}$ and $10\times E^{*rock}$) at approach angles from 20° to 90°. Red and blue boxes indicate diversion and crossing, respectively. 146

Figure 4.15. SCB test results with veins ($1.0\times K_{Ic}^{rock}$ and $10\times E^{*rock}$) of approach angles of 65° and 70° from three view angles: (a) and (b) are 0° or front view, (c) and (d) are 45°-inclined, (e) and (f) are 90° or top view. Red and blue boxes indicate fracture diversion and crossing, respectively. 147

Figure 4.16. Induced fracture propagation in PFC3D specimens with a vein ($1.0\times K_{Ic}^{rock}$ and $10\times E^{*rock}$) at an approach angle of 30°. Figures (a) to (h) correspond to the points marked in the (i) load–displacement curve measured from the loading roller. 149

Figure 4.17. SCB results of veins at 60° with three stiffnesses: stiffness of (a) $1\times E^{*rock}$, (b) $5\times E^{*rock}$, and (c) $10\times E^{*rock}$. (d), (e), (f) are the 45°-inclined view of (a), (b), (c), respectively. The fracture toughness of the vein is kept constant with 0.5 ratio to the rock fracture toughness ($0.5\times K_{Ic}^{rock}$) for all three cases..... 150

Figure 4.18. SCB results of veins at 60° with three parallel bond strengths: fracture toughness of (a) $0.5\times K_{Ic}^{rock}$, (b) $0.7\times K_{Ic}^{rock}$, (c) $1.0\times K_{Ic}^{rock}$. (d), (e), (f) are the 45°-inclined view of (a), (b), (c), respectively. For all samples, the vein stiffness is 5 times greater than the rock matrix ($5\times E^{*rock}$). 151

Figure 4.19. SCB results of veins at 90° with three thicknesses: (a) 1.9 mm, (b) 2.5 mm, (c) 3.2 mm. For all samples, the vein stiffness is 5 times greater than the rock matrix ($5\times E^{*rock}$) and the fracture toughness is 0.5 ratio ($0.5\times K_{Ic}^{rock}$) to the rock matrix. (d), (e), (f) are the 45°-inclined view of (a), (b), (c), respectively. 153

Figure 4.20. SCB results of veins at 90° with three thicknesses: (a) 1.9 mm, (b) 2.5 mm, (c) 3.2 mm. For all samples, the vein stiffness is same with the rock matrix ($1\times E^{*rock}$) and the fracture toughness is 0.3 ratio ($0.3\times K_{Ic}^{rock}$) to the rock matrix. (d), (e), (f) are the 45°-inclined view of (a), (b), (c), respectively.... 154

Figure 4.21. SCB test results with three different vein locations. : (a) $1a$, (b) $1.5a$, and (c) $2a$ above the notch tip. The vein approach angle, thickness, stiffness, parallel bond strength are kept constant with 60°, 1.9 mm, $1\times E^{*rock}$ and $0.3\times K_{Ic}^{rock}$, respectively. 156

Figure 4.22. SCB test results with three different vein locations. : (a) $1a$, (b) $1.5a$, and (c) $2a$ above the notch tip. The vein approach angle, thickness, stiffness, parallel bond strength are kept constant with 75°, 2.5 mm, $10\times E^{*rock}$, and $1.0\times K_{Ic}^{rock}$, respectively. 156

Figure 4.23. PFC3D results of the SCB test with (a) 58.4-mm (2.3-inch) and (b) 56-mm (2.2-inch) diamter samples with veins of same properties ($1\times E^{*rock}$ and $0.5\times K_{Ic}^{rock}$) at 45°. 158

Figure 4.24. PFC3D results of the SCB test with (a) 58.4-mm (2.3-inch) and (b) 56-mm (2.2-inch) diamter samples with veins of same properties ($10\times E^{*rock}$ and $1.0\times K_{Ic}^{rock}$) at 45° 158

Figure 4.25. PFC3D results of the SCB test with (a) 38.1-mm (1.5-inch), (b) 58.4-mm (2.3-inch), (c) 76.2-mm (3-inch) and (d) 101.6-mm (4-inch) diamter samples with veins of same properties ($1\times E^{*rock}$ and $0.5\times K_{Ic}^{rock}$) at 45°. 160

CHAPTER 1: INTRODUCTION

An unconventional reservoir is any reservoir that requires special recovery techniques from the conventional operating method in order to produce hydrocarbon. Shale, also known as mudrock or mudstone, is an unconventional reservoir rock predominantly made up of silt and clay-size minerals, including quartz and calcite cements. The host rock composition varies widely by shale formations as shown in Figure 1.1. Some shale properties play an important role in hydrocarbon generation and accumulation. Shale's low permeability inhibits oil and natural gas migration and allows shale to act as a cap rock. Also, shale itself is a source rock since it contains organic materials that break down into oil and natural gas trapping hydrocarbon in the small pores.

Abundant hydrocarbon deposits exist in low-permeability shale and tight sandstone reservoirs. The EIA (2014) reported that the estimated tight/shale oil and shale gas resources in the United States and 41 other countries (Figure 1.2), constitutes 10% of the world's technically recoverable crude oil and 32% of the natural gas (Table 1.1). Focusing on the technically recoverable resources, the United States is ranked second in tight/shale oil after Russia (75 billion barrels) and fourth in shale gas after China (1115 trillion cubic feet, Tcf), Argentina (802 Tcf), and Algeria (707 Tcf). Shale plays lie in more than 30 states in the United States, including the Barnett shale and the Marcellus shale (Figure 1.3). The dramatic increase of technically recoverable resources in these shale reservoirs is mainly due to the development of horizontal drilling (DOE, 1993; Fisher et al., 2004; Wiley et al., 2004; Waters et al., 2006) and hydraulic fracturing (Waters et al., 2009; King, 2012). These techniques provided access to the massive

amount of accumulated resources in these low permeability (in the magnitude of nano-darcies) reservoirs that were previously uneconomical to produce from using the conventional approach.

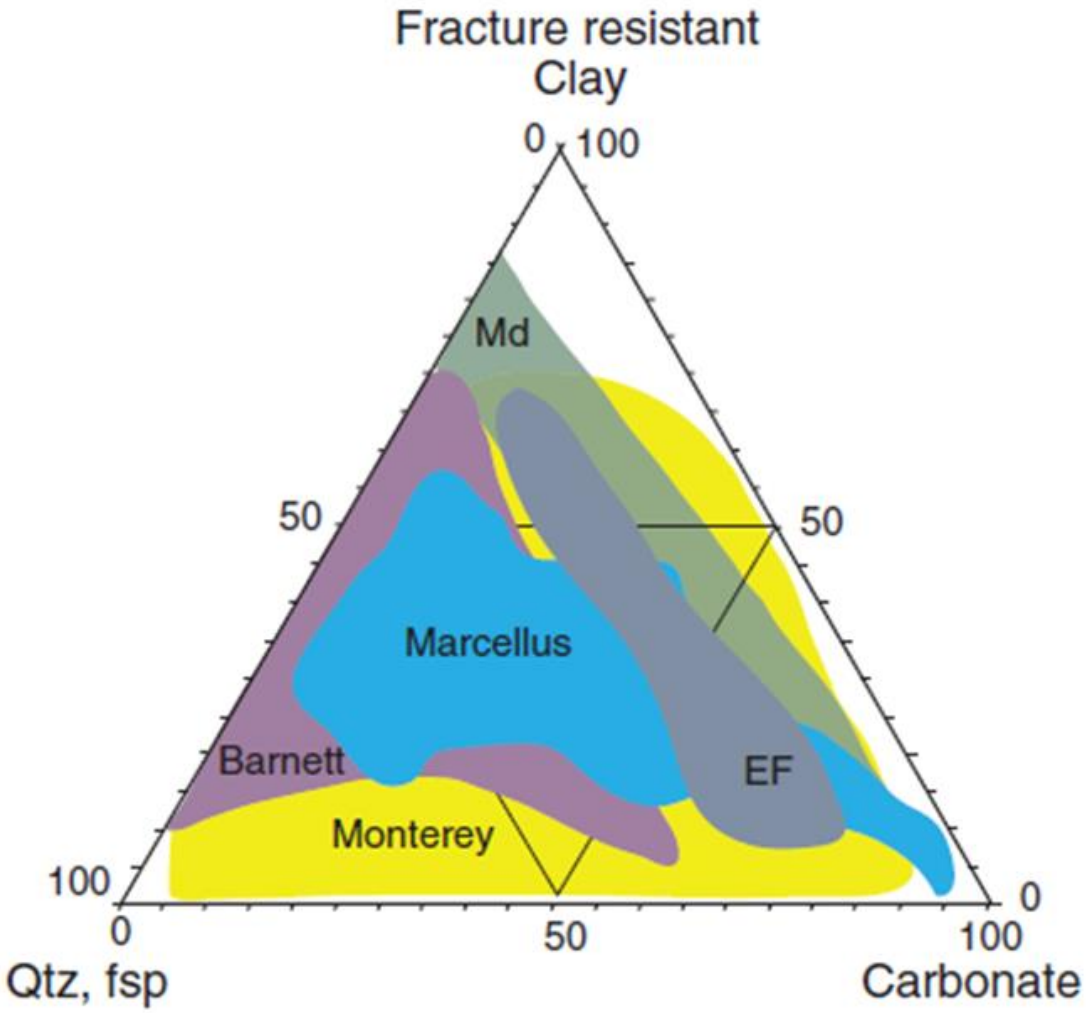

Figure 1.1. Triangular composition diagram for Barnett, Eagle Ford Formation (EF), and clay-rich mudrock (Md), Monterey formation, and Marcellus Formation (after Gale et al., 2014).

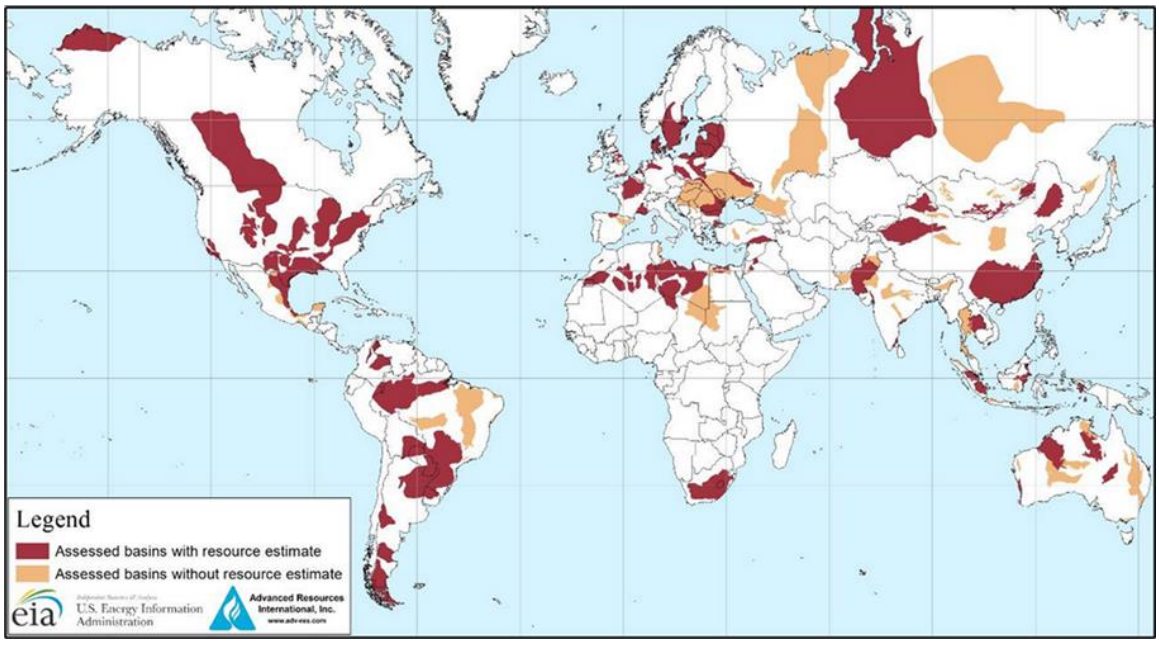

Figure 1.2. Tight/shale oil and shale gas formations around the world (EIA, 2014). (http://www.eia.gov/todayinenergy/detail.cfm?id=14431)

Table 1.1. Technically recoverable tight/shale oil and shale gas in United States and 41 other countries (EIA, 2014) (http://www.eia.gov/todayinenergy/detail.cfm?id=14431)

		Crude oil (billion barrels)	Wet natural gas (trillion cubic feet, Tcf)
United States	Tight/shale oil and shale gas Non-shale **Total**	58 (26%) 165 (74%) **223**	665 (27%) 1766 (73%) **2431**
Other countries	Tight/shale oil and shale gas Non-shale **Total**	287 (9%) 2,847 (91%) **3,134**	6,634 (32%) 13,817 (68%) **20,451**
Total world	Tight/shale oil and shale gas Non-shale **Total**	345 (10%) 3,012 (90%) **3,357**	7,299 (32%) 15,583 (68%) **22,882**

*%: Pertentage from the total amount of each category

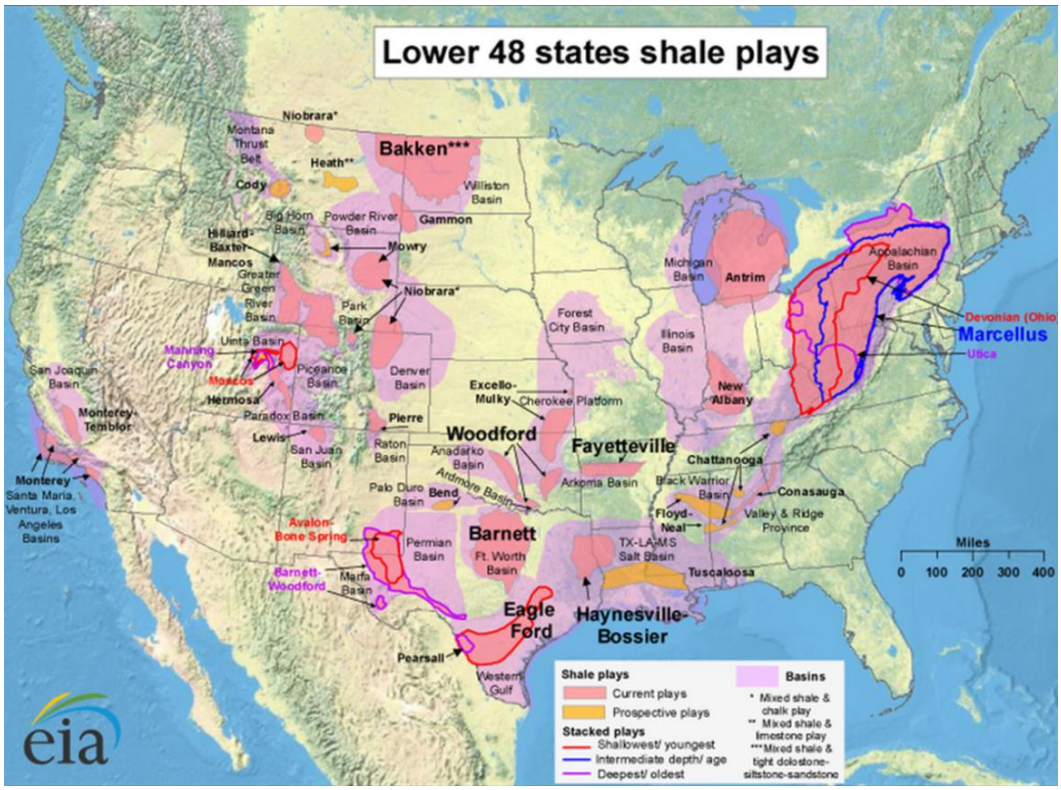

Figure 1.3. Shale plays in United States (EIA, 2011).
(http://www.eia.gov/analysis/studies/usshalegas/)

Shale gas production in the United States began to increase sharply around 2010 (Figure 1.4) when production from the Marcellus, the Haynesville, and the Eagle Ford was added to the production of the Barnett play, the first major commercial shale gas play. Tight/shale oil production increased explosively around 2011 (Figure 1.5), due to large-scale production in plays countrywide including the Eagle Ford and the Bakken. As of 2014, estimated tight/shale oil and shale gas production in the United States represented 45% and 53% of the United States total daily production of crude oil and natural gas, respectively (EIA, 2015; see Figure 1.6). Overall, the productivity of oil and natural gas is steadily increasing due to the increase in the number of wells drilled and the advancement of effective technology to enhance recovery in these tight plays.

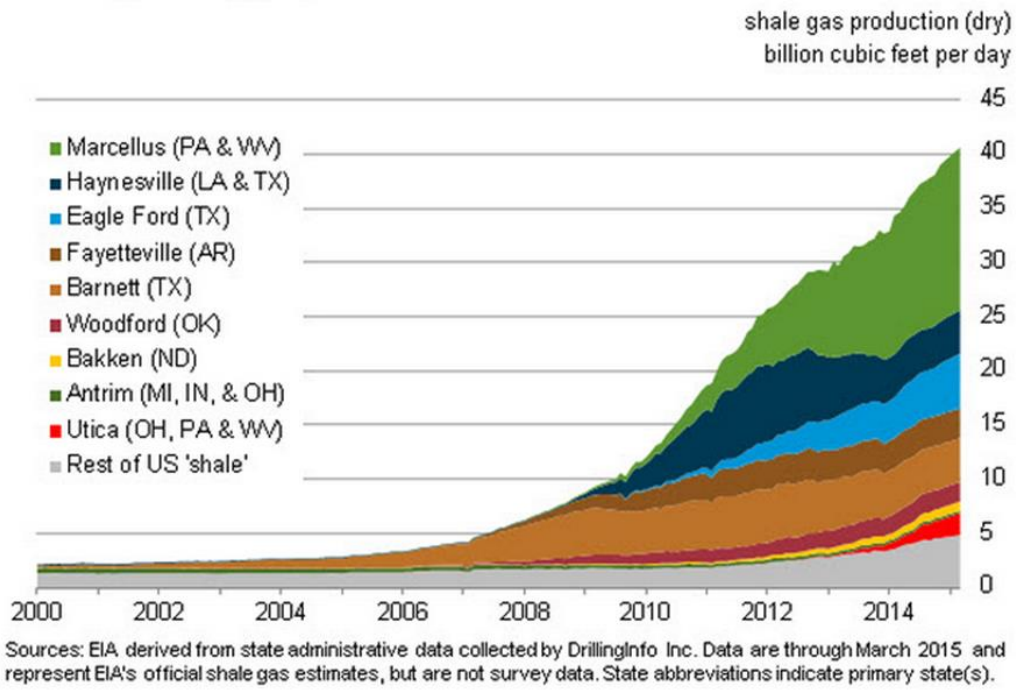

Figure 1.4. The trend of shale gas production by plays in United States (EIA, 2015). (http://www.eia.gov/energy_in_brief/article/shale_in_the_united_states.cfm)

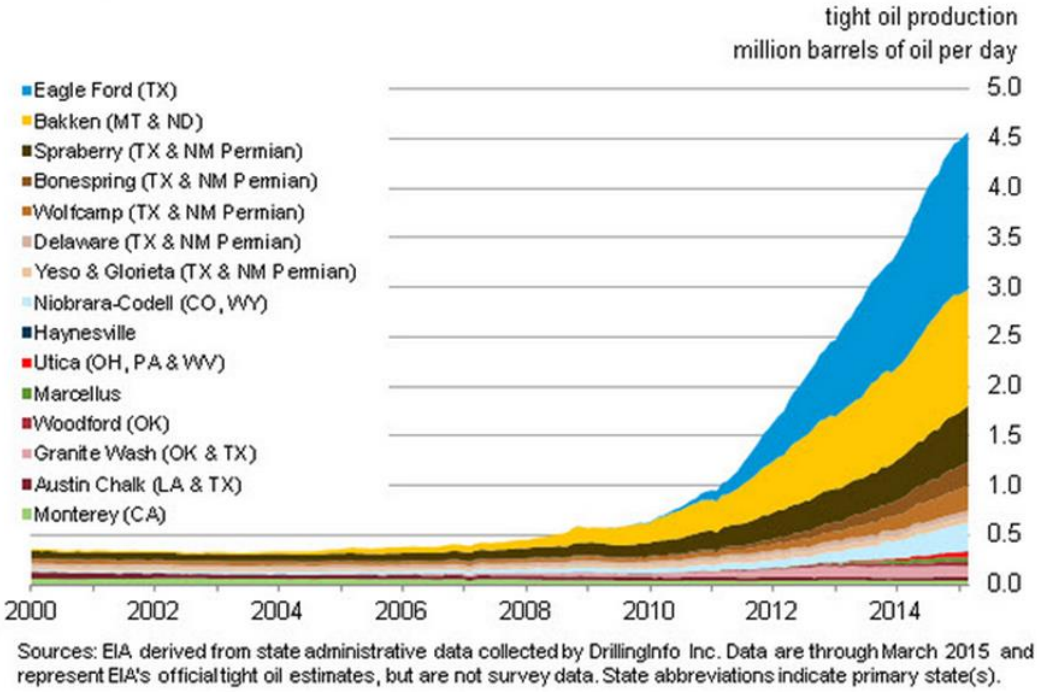

Figure 1.5. The trend of tight/shale oil production by plays in United States (EIA, 2015). (http://www.eia.gov/energy_in_brief/article/shale_in_the_united_states.cfm)

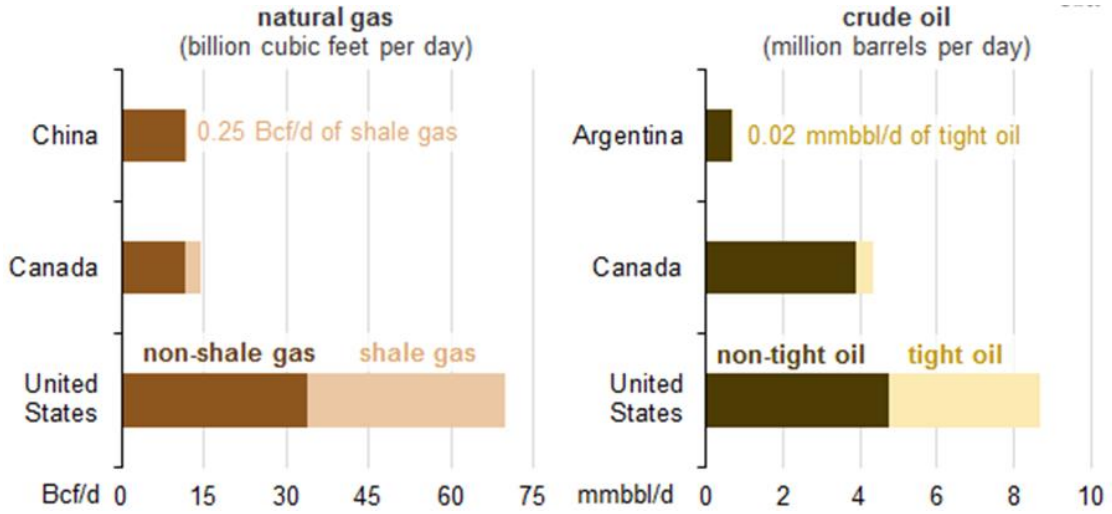

Figure 1.6. Estimated natural gas and crude oil in four countries as of 2014 (EIA, 2015). (http://www.eia.gov/todayinenergy/detail.cfm?id=19991)

1.1 HYDRAULIC FRACTURING

Hydraulic fracturing is a well-stimulation technique that enhances the production and recovery of oil, natural gas, and geothermal resources from low permeability reservoirs (Sasaki, 1998; Dahi-Taleghani, 2009; Beckwith, 2010; McClure, 2012). It increases the contact area between the well and the reservoir, which produces hydrocarbon or heat energy, and acts as a connection between the reservoir and the well (Martin and Economides, 2010). In some investigations, applications of hydraulic fracturing are extrapolated to the acquisition of water and waste disposals (Hainey et al., 1999, Dahi-Taleghani, 2009).

Historically, the first hydraulic fracture experiment began in 1947 by Stanolind at the Hugoton gas field in Kansas (Charlez, 1997; Cahoy et al., 2012; King, 2012). After two years, in 1949, the first industrial use of hydraulic fracturing was by Halliburton Oil

Well Cementing Company with two commercial hydraulic fracturing jobs in Oklahoma and Texas (Montgomery and Smith, 2010). Mitchell Energy, in 1997, was first to extract shale gas commercially with hydraulic fracturing, using slick water as the fracturing fluid (Waters et al., 2006; Cahoy et al., 2012). The success in the Barnett shale was noted and adapted to other organic-rich shale plays in the United States, which resulted in a tight/shale oil and shale gas boom in the early 21st century.

Since the 1950s, around 50% of oil wells and 70% of natural gas wells have been hydraulically fractured for stimulation (Valko and Economides, 1995; Renard et al., 2009). According to the DOE (2013), hydraulic fracture stimulation was used to stimulate at least two million oil and natural gas wells in the United States. Halliburton, the oilfield services company, reported that almost 90% of the new onshore wells being drilled in United States are hydraulically fractured. In fact, hydraulically fractured wells and hydraulic fracturing treatments increased rapidly between 2000 and 2010 (Figure 1.7). Among all the states in United States, Texas showed the largest increase in both hydraulically fractured wells and hydraulic fracturing treatments during this period of time.

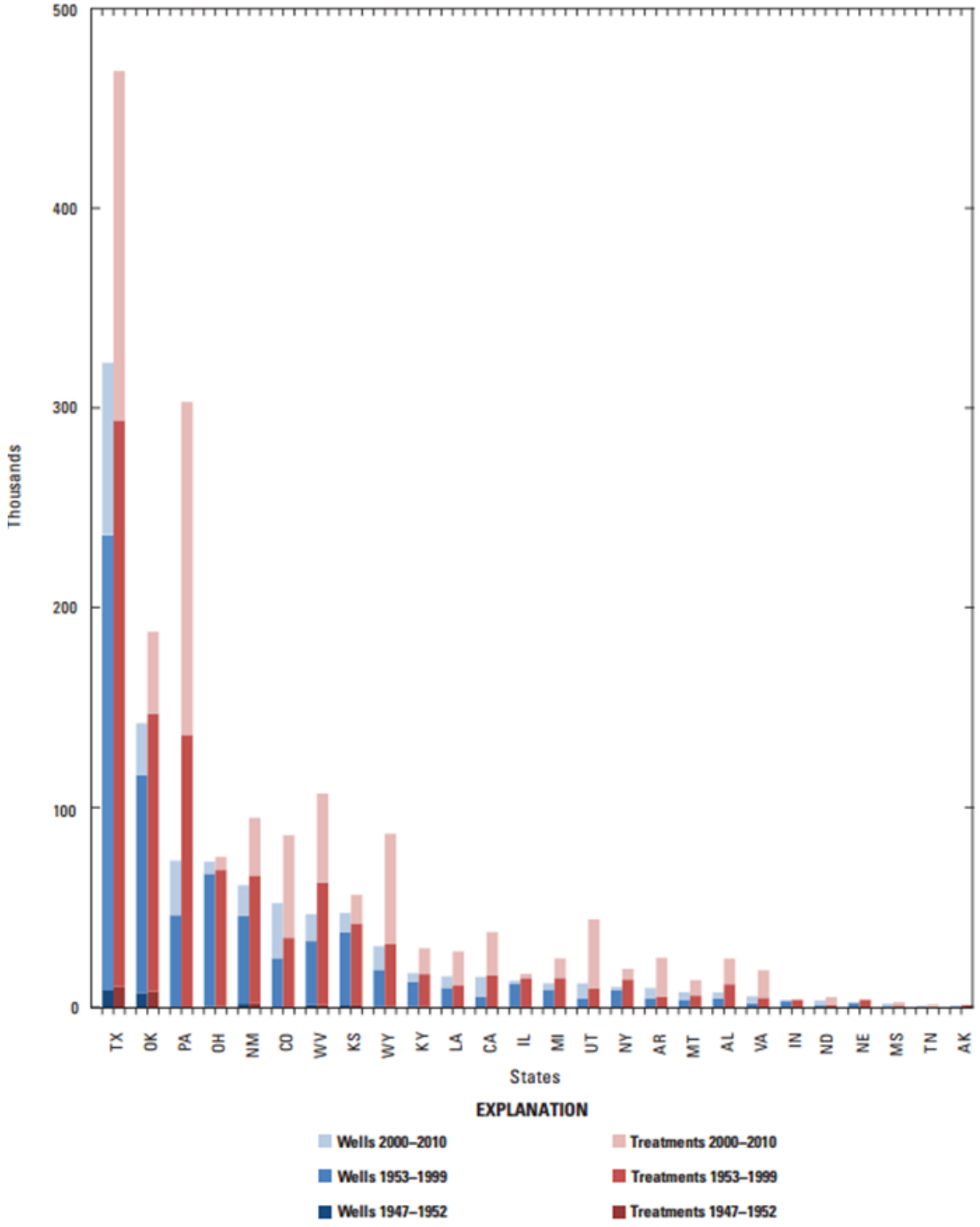

Figure 1.7. Trend of hydraulically fractured wells (blue) and hydraulic fracturing treatments (red) from 1947 to 2010 focused on states with more than 50 hydraulically fracture wells and 1,000 hydraulic fracturing treatments (Gallegos and Varela, 2015).

Generally, to create hydraulic fractures in a formation, large amounts of a fracturing fluid (a mixture of water, sand, and chemicals) are injected into the wellbore to build up pressure and exceed the breakdown pressure, the pressure which the fracture initiates in the formation. After the fracture initiates, the fracture grows orthogonally to the plane of the least principal stress, in a bi-wing planar manner (Ode, 1957; Griggs and Handin, 1960), and with a velocity depending on the injection rate. However, studies of microseismic imaging (Fisher et al., 2002; Maxwell et al., 2002; Fisher et al., 2005) and core observations (Warpinski et al., 1993) show that hydraulic fractures can be much more complex than the classical description.

The induced fracture geometry is governed by the reservoir rock mechanical properties, in-situ stress state, the fracture fluid properties, injection rate, well orientation, and the natural fracture system. Above all, the complexity of the fracture geometry in shale is mainly due to the preexisting discontinuities in the reservoir, including natural fractures and bedding planes (Gale et al., 2007; Fisher and Warpinski, 2012). In some reservoirs, production increases with complex fracture geometry (Cipolla et al., 2008). On the other hand, Warpinski (1991) observed that the fracture complexity requires higher treatment pressure and reduces the effective fracture length which provides negative effect to the recovery. Therefore, an advanced understanding of the physics of hydraulic fracture and preexisting discontinuity interaction will lead to better fracture design which, in turn, will improve the oil and natural gas recovery.

1.2 ROCK FRACTURE MECHANICS

Linear Elastic Fracture Mechanics (LEFM) is a basic theory of fracture that was developed to interpret fracture growth and its relationship to the failure of isotropic and linear elastic materials. It is based on elasticity theory to calculate the near-tip stress field which is a function of the loading, the geometry of the material, the physical properties of the material, and the location of the point from the fracture tip (Lawn and Wilshaw, 1975). LEFM is applicable to the treatment of materials with small process zones, the zone of inelastic deformation around the fracture tip. This refers to Small-Scale Yielding (SSY) where the process zone size is smaller compared to all of the other relevant length scales in the problem structure, such as fracture half-length, thickness, and width of the structure. Brittle and semi-brittle rocks generally satisfy SSY conditions.

The framework of modern fracture mechanics is based on the theory of Griffith (1920) that was introduced to measure the potential energy of a system with respect to crack length. The theory assumes that the propagation of inherent cracks inside the material governs the total material failure. However, it was difficult to quantify the energy through experiments. The theory became popular when Irwin (1957) expressed the near-tip stress concentration at the fracture tip in terms of stress intensity factors (K_{I}, K_{II}, K_{III}) dependent upon the loading mode (Figure 1.8). The in-situ remote (far-field) stresses and internal stresses of the fracture govern the relative motions of the fracture wall and stress concentration at the fracture tip (Jaeger and Cook, 1979).

By the relative motion of the fracture walls, fracture tip displacement modes for a single flat sharp crack can be divided into three types (Whittaker et al., 1992): mode I, mode II, and mode III (Figure 1.8). Each displacement mode has a unique stress field in the vicinity of a fracture tip which controls the fracture propagation direction. Mode I is the tensile opening mode of fracture extension. The tensile stress normal to the fracture separates the walls symmetrically with respect to the fracture plane. Mode II is the in-plane sliding mode where fracture walls slide relative to each other. The fracture tip is under in-plane shear stress and the displacements of the wall are skew-symmetric to the fracture plane. Mode III is the tearing (out-of-plane) mode. The fracture is under out-of-plane shear stress and the walls slide in the plane, parallel to the fracture tip. Mixed-mode fracture is any combination of these three modes. For example, mixed mode I-II is the combination of mode I and mode II loadings on the fracture that causes kinking or curving paths (Olson and Pollard, 1989).

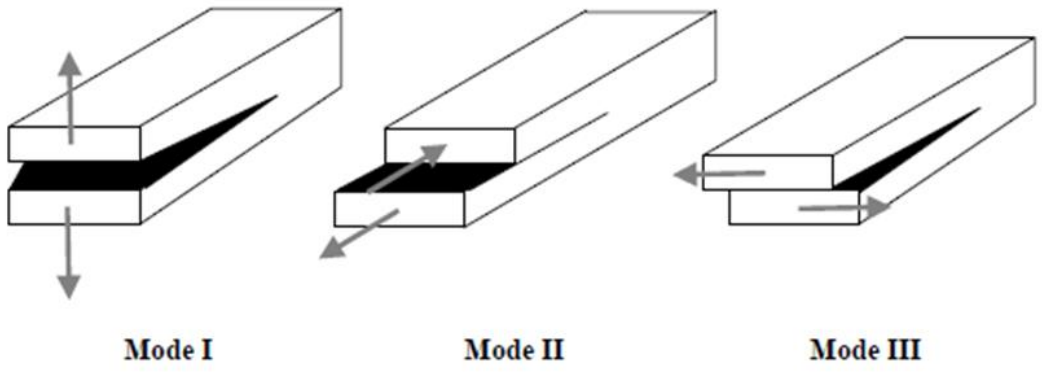

Figure 1.8. Schematic veiws of the three fracture modes based on the relative movement of fracture walls (Whittaker et al., 1992).

Fracture mechanics was first developed to understand the failure of materials such as glass and metal engineering structures. Due to its relatively simple fracture criteria, fracture mechanics was adapted to describe rock fracture, including earthquake mechanics (Rice and Rudnicki, 1979; Rudnicki, 1980), plate tectonics (Li and Rice, 1983), uplift and erosion of crustal rocks (Bruner, 1984), and in-situ stress determination and hydraulic fracturing (Abou-Sayed et al., 1978; Schmidt, 1980).

Phenomenological failure criteria, such as the Mohr-coulomb or Hoek-Brown strength criterion, are popular for their good approximations of macroscopic rock failure. However, they may not be suitable for describing rock failure mechanism in detail (Bieniawski, 1967; Shen et al., 2014) since the failure of brittle and semi-brittle rocks is predominantly controlled by the process of fracture initiation and propagation. LEFM has an advantage in interpreting rock failure mechanism because it depends on the fact that all engineering materials contain small cracks. These small cracks are the source of fracture initiation and propagation and lead to total rock failure.

1.3 PREEXISTING DISCONTINUITIES IN SHALE

Natural fractures are ubiquitous structures in the earth's crust generated by natural processes (Ramsay, 1980; Engelder, 1987). In shale reservoirs, many discontinuities exist such as bedding planes, joints, veins, faults and other natural fractures (Barton and Zoback, 2002; Gale et al., 2007; King, 2010; Gale et al., 2014). Core observations support the existence of abundant natural fractures in shale. Gale et al. (2014) calculated the ratio of fracture surface area to shale core volume, a parameter for fracture density,

from 18 shale formations which ranged from 0.33 /m to 4.01 /m with a mean of 1.66 /m . Marcellus shale, for example, had a total of 92 fractures within 331 *m* of core length, and its surface area to volume ratio was 1.66 /m , which is close to the mean value.

Preexisting discontinuities, from microcracks to continental-scale faults, can be divided into two modes based on the relative wall displacements: shearing mode and opening mode. Faults are associated with shearing mode, whereas joints, veins and dikes are opening mode fractures (Pollard and Aydin, 1988; Gale et al., 2014). Joints are the most common opening mode brittle fracture in the earth's crust (Caputo, 2010). Joints develop in the subsurface due to a reduction in overburden stress during the process of uplift (Price, 1966) or through the counteraction of large internal fluid pressures with the far-field compression generating extension fractures (Secor, 1965). This latter mechanism is similar to the creation of hydrofractures in the petroleum industry (Engelder, 1987).

Based on geologic characterization from subsurface oil and gas reservoirs, natural fractures can range from being uncemented frictional interfaces to fully or partially cemented cohesive interfaces (Ramsay, 1980; Laubach, 2003; Gale et al., 2014). The mechanical properties of the natural fracture are crucial in the analyzation of the interaction between hydraulic fractures and natural fractures. Uncemented frictional interfaces can only resist shear stresses. Some of these planes of weakness are highly permeable and they can act as fluid conduits in the reservoir (Pollard and Aydin, 1988). When the internal fluid pressure, reaches a significant fraction of the normal stress acting on the frictional interface, the resolved shear stress exceeds the friction and shear failure is likely to occur (Jaeger and Cook, 1979; Olson et al., 2009).

Bonded interfaces, such as cemented fractures (veins), not only have resistance against shear stress but also have cohesion that can transmit tensile stress (Caputo, 2010). These filled natural fractures can have different mechanical properties than those of the host rock (Virgo et al., 2013), such as stiffness, tensile and shear strengths, dependent on the properties of the cement filling the natural fracture. The mechanical discontinuity created by the cemented natural fracture generates stress heterogeneity in the reservoir which disturbs the hydraulic fracture path. This distinguishes veins from other frictional interfaces for interaction analysis with the hydraulic fracture.

Veins have finite apertures, or thicknesses, which can follow a power law distribution over a wide range (Marrett, 1996; Marrett et al., 1999; Gale, 2002; Laubach, 2003). Figure 1.9 shows the distribution of vein apertures in various shale formations. These veins have different degrees of cement fill depending on the relative rate between fracture opening and mineral precipitation (Laubach, 2003). This can determine the porosity of the vein and also its resistance to both shear and tensile stresses. Larger fractures tend to have large continuous porosity whereas microfractures, with apertures less than 0.1 mm, tend to be sealed or have small discontinuous porosity. When the vein is fully cemented, the mechanical properties of microstructures in veins become important for interaction analysis.

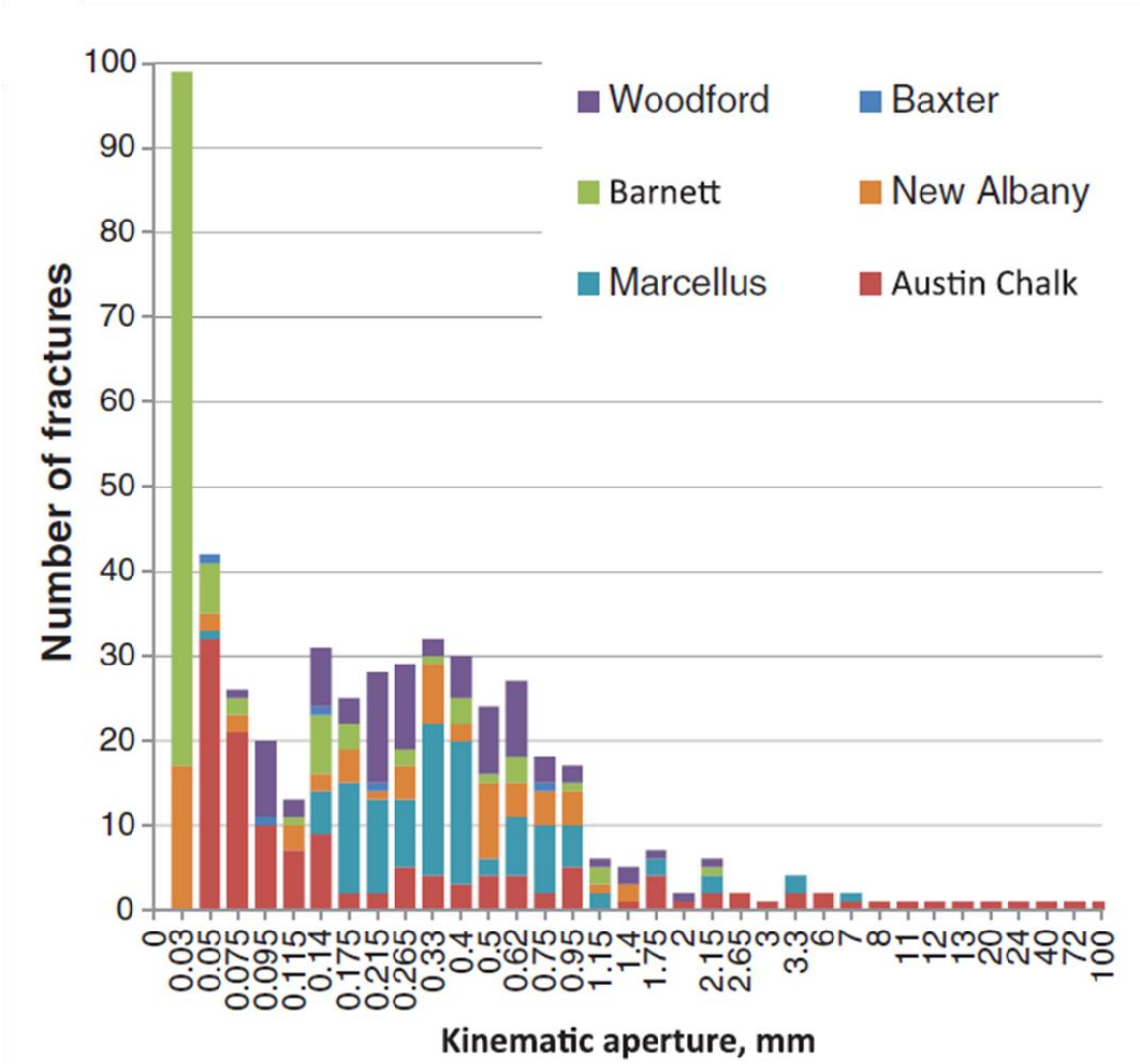

Figure 1.9. Histogram of sealed fracture aperture size (>30 μm) from six formations (Gale et al., 2014).

In general, a hydraulic fracture is likely to divert into the weaker plane between the two: the vein–rock interface or the weak planes inside the vein. The cemented natural fractures in the Barnett typically break along the vein–shale interface suggesting a weak crystal bond between the calcite cement and the host rock (Gale et al., 2007). In contrast, some cemented natural fractures, such as quartz cement in fractures of tight gas

sandstones, have bonding on the interface (Laubach, 2003) which might not be the weakest plane in the discontinuity. In fact, planes of weakness inside veins, such as mineral boundaries, cleavage planes, fluid or solid inclusion trails due to crack-seal events, can be utilized when hydraulic fractures divert into veins. Crack-seal structure (Ramsay, 1980) is one of the mechanically weak planes inside the vein generated by multiple refracturing and sealing events. It is ubiquitous in cemented fractures and is present in veins as thin as 35 μm (Laubach, 2003).

1.4 INTERACTION OF HYDRAULIC FRACTURE WITH PREEXISTING DISCONTINUITIES

Preexisting discontinuities in the reservoirs act as planes of weakness which generate complex hydraulic fracture networks (Gale et al., 2007; Cipolla et al., 2008; Wu, 2014; Wu and Olson, 2014) of various types (Figure 1.10). Previous studies have examined the interaction between hydraulic fracture and preexisting discontinuities, theoretically, numerically and experimentally with various methods in order to accurately predict fracture geometry (Anderson, 1981; Blanton, 1986; Warpiniski and Teufel, 1987; Blair et al., 1989 Renshaw and Pollard, 1995; Beugelsdijk et al., 2000; de Pater and Beugelsdijk, 2005; Potluri et al., 2005; Suarez-Rivera et al., 2006; Zhou et al., 2008; Jeffery et al., 2009; Dahi-Taleghani and Olson, 2009; Gu and Weng, 2010; Gu et al., 2011; Bahorich et al., 2012; Olson et al., 2012; Chuprakov et al., 2013; Suarez-Rivera et al., 2013; Wang et al., 2013; Chuprakov et al., 2014).

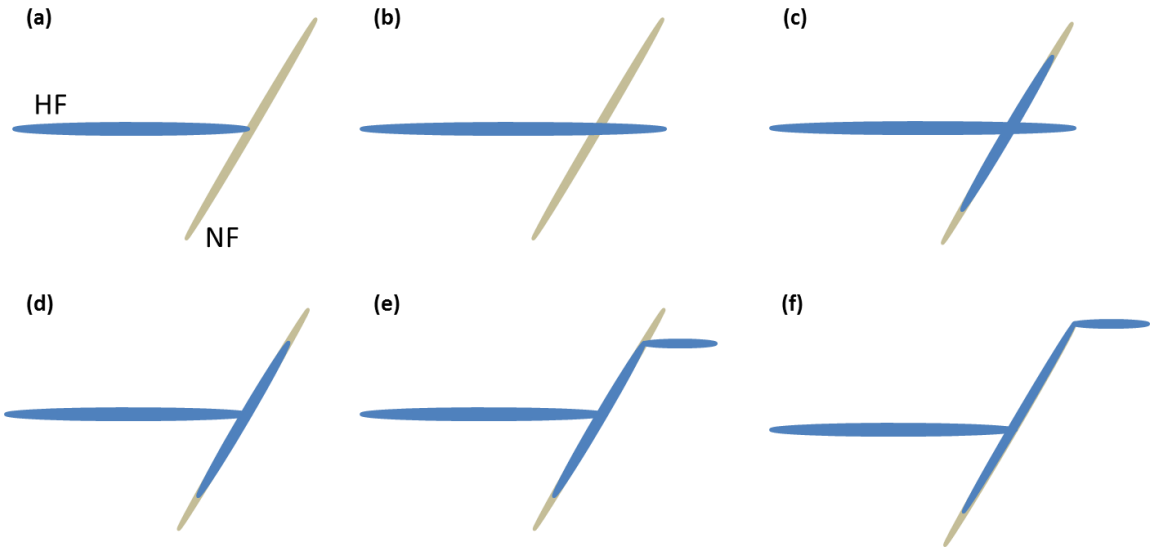

Figure 1.10. Types of interaction between the hydraulic fracture (HF) and the natural fracture (NF): (a) HF arrested at NF, (b) HF crossing NF, (c) NF dilation after crossing, (d) HF diverting into NF (NF dilation) , (e) HF kinking back into the rock matrix before it reaches the tip of the NF, and (f) HF kinking at the tip of the NF after diversion (after Gu et al., 2011).

Most of these efforts have focused on the interaction of hydraulic fracture with frictional interfaces. Blanton (1986) provided the basis of fracture propagation at the interface by hydraulically fracturing blocks of Devonian shale and hydrostone that include frictional interfaces. His analytical criterion predicts hydraulic fracture crossing or opening the natural fracture based on the differential stress and the angle of interaction. The induced fracture crosses the interface when pressure inside the fracture exceeds the stress acting parallel to the natural fracture plus the tensile stress of the rock. On the other hand, opening of the natural fracture occurs when the pressure inside the interface is greater than the normal stress acting on the weak plane.

Warpinski and Teufel (1987) performed scaled hydraulic fracture experiments on Coconino sandstone with pre-cut joints in various orientations and differential stresses.

They considered whether or not the approaching hydraulic fracture could cause the frictional interface to slip, to arrest the hydraulic fracture, and/or to dilate. Based on the linear friction law, shear slippage occurs when the resolved shear stress on the weak plane is greater than the sum of the interface inherent shear strength and the friction. Additionally, dilation occurs when the pore pressure in a pre-cut interface near the hydraulic fracture overcomes the normal stress acting against the interface plane. Potluri et al. (2005) applied the work of Warpinski and Teufel (1987) analytically to investigate the location of the kinking after the dilation of the natural fracture.

Renshaw and Pollard (1995) analyzed fracture interaction using the LEFM stress field in the vicinity of the fracture tip for orthogonal interfaces. They examined the compressive stress normal to the interface which prevents slipping and the tensile stress parallel to the interface which opens the opposite side to determine fracture path. The criterion suggests two types of fracture propagation: continuous propagation and discontinuous propagation. Continuous propagation is when the fracture crosses the interface as if the interface does not exist. Discontinuous propagation, however, is when the induced fracture stops at the interface and reinitiates a new fracture on the other side of the interface leaving an offset.

Since natural fractures can be partially or fully cemented, fracture interaction models need to include more than just frictional properties. Recently, experimental and theoretical investigations on the interaction of hydraulic fracture with bonded interfaces have been carried out. Gu and Weng (2010) studied further applications of the Renshaw and Pollard criterion for non-orthogonal cohesive interfaces. The effect of cohesion

increased the tendency of crossing rather than slipping. Suarez-Rivera et al. (2006) examined the influence of bonded interfaces by pressurizing a wellbore in a confined glass slice containing epoxy bonded interfaces. The induced fractures were initially arrested by the interface regardless of the confining stress state and required an additional pressure increment for the fractures to propagate further after having reached the bonded interface. Confining stress was necessary for the induced fracture to cross the interface.

Zhou et al. (2008) stimulated hydraulic fractures in poured cement blocks, a mixture of Chinese cement no. 325 and fine sand, with embedded paper sheets of varying frictional properties. Three types of paper sheets had various shear strengths and thicknesses, and the results showed that increased shear strength increased the likelihood of hydraulic fracture arrest. Bahorich et al. (2012) performed low stress hydraulic fracturing in hydrostone blocks containing glass, gypsum plaster, and Berea sandstone slices to represent sealed natural fractures. Hydraulic fractures were not only arrested or diverted at the natural fracture but also bypassed over and below the discontinuities since the embedded inclusions were shorter than the hydraulic fracture's height. They characterized the different modes of fracture (mode I-II kinking and mode I-III twisting) that occurred when the hydraulic fracture diverted into the natural fracture and found that failure of the simulated sealed natural fractures predominantly occurred on the interface between natural fracture cement and host rock. Wang et al. (2013) assessed the approach angle, strength, and thickness of the inclusion with a Semi-Circular Bend (SCB) test indicating that the greater approach angle and strength of the inclusion generates more crossing behavior which agrees with the block test results. They concluded that the

fracture crossing versus diversion result did not depend on the thickness of the inclusion, but the step over length was longer for the thicker inclusions when compared to the thinner ones.

Dahi-Taleghani and Olson (2009) introduced an energy release rate criterion to predict the interaction of opening mode fractures with cemented natural fractures analytically. They defined the critical energy release rate, the smaller value between the interface cohesion and the cement strength in order to determine fracture crossing or diversion. In this energy criterion, fracture toughness, also known as the mode I critical stress intensity factor, and the stiffness of the vein is necessary to evaluate the propagation direction. This criterion will be discussed in detail in Chapter 3.

1.5 RESEARCH OBJECTIVES

The purpose of this work is to improve the understanding of the mechanics and mechanisms of hydraulic fracture propagation in naturally fractured reservoirs.

Key research objectives are:

- Evaluate the impact of remote and internal crack stresses on the fracture propagation trajectory.
- Investigate a new simple method to quantify the critical strength of the natural fracture.
- Examine the effect of bedding planes on the fracture toughness anisotropy.

- Understand the fracture interaction process when a propagating fracture approaches and encounters the preexisting discontinuity.
- Determine the failure mode of the vein when the fracture interaction occurs.
- Analyze the influence of vein properties on the fracture interaction.

1.6 DISSERTATION OUTLINE

This dissertation consists of five chapters.

Chapter 1 reviews the general background of hydraulic fracturing, rock fracture mechanics, preexisting discontinuities in shale, and the interaction analysis between the hydraulic fracture and natural fractures.

Chapter 2 discusses various mixed-mode fracture propagation criteria and a modification of the fracture propagation criterion that includes the remote and internal crack stresses effect on the propagation direction. The angled fracture problem is discussed both analytically and experimentally to evaluate the validity of the modified criterion. I plan to submit this chapter to the *Engineering Fracture Mechanics* for publication.

Chapter 3 is based on the paper published in the *Journal of Geophysical Research: Solid Earth* in January 2015 with Jon E. Olson, Jon Holder, Julia F. W. Gale, and Rodrick D. Myers as co-authors. It evaluates the interaction of a propagating opening mode fracture with veins in Marcellus shale samples using the Semi-Circular Bend (SCB) test.

The vein strength is quantified by the energy release rate criterion of Dahi-Taleghani and Olson (2009).

Chapter 4 employs the Discrete Element Method (DEM) to reproduce the experimental results from Chapter 3 and to perform sensitivity analyses on the influence of approach angle, strength, stiffness, and thickness of veins on fracture interaction. The DEM results provide an advanced understanding of the mechanics of fracture interaction. I plant to present this chapter at the 50th US Rock Mechanics/Geomechanics Symposium.

Lastly, Chapter 5 is the overall conclusion of the dissertation. Recommendations and future work are discussed as well.

CHAPTER 2: MIXED-MODE FRACTURE PROPAGATION UNDER REMOTE STRESSES

The classic description of hydraulic fractures assumes planar opening mode (mode I) propagation of a fracture perpendicular to the least compressive remote stress orientation (Ode, 1957; Griggs and Handin, 1960). For example, a vertical hydraulic fracture is expected to propagate in the direction of the maximum horizontal stress, perpendicular to the minimum horizontal stress, in a single bi-wing planar geometry. However, observations of naturally formed fractures (including joints, veins, and dikes) indicate that fractures do not always propagate straight but can curve in reponse to variety of loading and geometric fractors (Lawn and Wilshaw, 1975; Engelder, 1987; Olson and Pollard, 1989; Martel, 1997).

Fracture path curvature in brittle materials occurs mainly due to the disturbance of a local stress field in the vicinity of a fracture tip. However, if the misaligned fracture is dominantly controlled by the far-field stresses, the resolved shear stress on the fracture tip from the remote stresses promotes curving in the fracture and restores its propagation direction to the plane perpendicular to the minimum compressive stress (Engelder, 1987; Olson and Pollard, 1989; Olson, 1991). Other studies have focused on the relationship of remote stress trajectories and joint orientation (Engelder and Geiser, 1980), suggesting that the orientation of natural fractures is governed by the far-field stresses.

A variety of theoretical and experimental contributions to the development of mixed-mode fracture propagation theory facilitate the understanding and prediction of the

fracture propagation path. Well-developed fracture propagation criteria can be divided into three major categories: energy-based, strain-based, and stress-based. This chapter introduces various mixed-mode I–II fracture propagation criteria and discusses the advantages and limitations of each criterion.

To account for the remote stress contribution on the near-tip stress trajectory, the chapter introduces a modified mixed-mode fracture propagation criterion based on the stress-based approach. To support the applicability of the modified criterion, the study performs uniaxial compression tests of hydrostone specimens with inclined cracks are performed. Discussions in this chapter focus on the mechanical behavior of fractures in homogeneous and isotropic linear elastic material. Fracture propagation in heterogeneous materials including interaction analysis with preexisting discontinuities will be discussed in Chapter 3.

2.1 ENERGY-BASED FRACTURE PROPAGATION CRITERION

An energy-based fracture propagation criterion is derived from the theory of Griffith (1920) for an opening mode crack initiating in its own plane. Griffith proposed an energetic approach in which the crack, under two-dimensional remote stresses, propagates when the energy stored in the system overcomes the surface energy of the crack for a perfectly brittle material. The energy release rate, G, is defined as

$$G = 2\gamma \tag{2.1}$$

where γ is the surface energy per unit area of the surface. Crack propagation occurs when

$$G = G_c \tag{2.2}$$

where G_c is the critical energy release rate, a material constant. The energy release rate can be considered as the driving force for the fracture to propagate. In order to apply Griffith's theory, the material must be linear elastic, isotropic, homogeneous, and perfectly brittle with small cracks.

Irwin (1957) modified Griffith's theory and introduced the concept of the Stress Intensity Factor (SIF). The SIF's for the three fracture modes are determined from the solution of the infinitesimal elasticity problem (Irwin, 1958), which can be written as

$$\begin{aligned} K_{\mathrm{I}} &= \sqrt{\pi a}\Delta\sigma_{\mathrm{I}} = \sqrt{\pi a}\sigma_{11}{}^{r} \\ K_{\mathrm{II}} &= \sqrt{\pi a}\Delta\sigma_{\mathrm{II}} = \sqrt{\pi a}\sigma_{12}{}^{r} \\ K_{\mathrm{III}} &= \sqrt{\pi a}\Delta\sigma_{\mathrm{III}} = \sqrt{\pi a}\sigma_{13}{}^{r} \end{aligned} \tag{2.3}$$

where a is the fracture half-length, and $\Delta\sigma_{\mathrm{I}}$, $\Delta\sigma_{\mathrm{II}}$, $\Delta\sigma_{\mathrm{III}}$ are modes I, II, and III driving stresses, respectively. The three driving stresses can be expressed with $\sigma_{11}{}^{r}$, the remote tensile stress in X_1-direction, $\sigma_{12}{}^{r}$ and $\sigma_{13}{}^{r}$, the remote shear stresses acting on the fracture in X_2 and X_3 directions, when the fracture is aligned with the X_2-X_3 plane.

In Linear Elastic Fracture Mechanics (LEFM), the energy release rate and stress intensity factors have a direct fundamental relationship (Erdogan and Sih, 1963; Ichikawa and Tanaka, 1982). Through Irwin's relation, the energy release rate can be expressed as

$$G = \frac{K_{\mathrm{I}}^{\,2} + K_{\mathrm{II}}^{\,2}}{E^{*}} \tag{2.4}$$

where $E^{*} = E\big/\left(1-\nu^{2}\right)$ is the plane modulus, E is Young's modulus and ν is Poisson's ratio.

Palaniswamy and Knauss (1972) introduced the maximum energy release rate criterion (G-criterion) based on the Kolosov-Muskhelishvili stress functions which are utilized to numerically solve a branched fracture problem. The fracture propagates in the direction of the maximum value of the energy release rate around the fracture tip when it reaches the critical value of a material (G_c). The G-criterion is an analysis of fracture propagation in isotropic, homogenous and linearly elastic material, and as presented by Palaniswamy and Knauss, it does not include the stresses acting on the fracture walls.

The G-criterion has been utilized in non-coplanar crack extension studies (Hussain et al., 1974; Nuismer, 1975; Wang, 1977) to solve the branched fracture problem analytically. Investigations have focused on deriving proper SIFs in specific orientations to account for the kinked fracture. The approach of Nuismer (1975) led to the use of the G-criterion in kinking fractures. For fracture propagation in a given orientation, θ_o, the parameters K_{I}, K_{II} and G are replaced with, $\overline{K_{\mathrm{I}}}$, $\overline{K_{\mathrm{II}}}$ and $\overline{G}$ as

$$\overline{K_{\mathrm{I}}} = \frac{1}{2}\cos\frac{\theta_o}{2}\left[K_{\mathrm{I}}\left(1+\cos\theta_o\right) - 3K_{\mathrm{II}}\sin\theta_o\right]$$
$$\overline{K_{\mathrm{II}}} = \frac{1}{2}\cos\frac{\theta_o}{2}\left[K_{\mathrm{I}}\sin\theta_o + K_{\mathrm{II}}\left(3\cos\theta_o - 1\right)\right] \tag{2.5}$$
$$\overline{G} = \frac{\overline{K_{\mathrm{I}}}^2 + \overline{K_{\mathrm{II}}}^2}{E^*}$$

where θ_o is an angle from the fracture plane counter clockwise. $\overline{K_{\mathrm{I}}}$ and $\overline{K_{\mathrm{II}}}$ are derived from the singular terms of the near-tip stress components from Equation (2.10) introduced below in Section 2.3.

2.2 STRAIN-BASED FRACTURE PROPAGATION CRITERION

Sih (1973) introduced the minimum strain energy density criterion (S-crterion) to predict a load at failure. The strain energy density function, *S*, is the strength of the near-tip elastic energy which can be expressed as

$$S = a_{11}K_{\mathrm{I}}^2 + 2a_{12}K_{\mathrm{I}}K_{\mathrm{II}} + a_{22}K_{\mathrm{II}}^2 \tag{2.6}$$

where the coefficients $a_{ij}\,(i, j = 1, 2)$ are functions of the counter-clockwise angle (θ) from the in-plane projection of the fracture plane, which are defined as

$$a_{11} = \frac{1}{16G\pi}\left[\left(1+\cos\theta\right)\left(\kappa-\cos\theta\right)\right]$$
$$a_{12} = \frac{1}{16G\pi}\sin\theta\left[2\cos\theta-\left(\kappa-1\right)\right] \tag{2.7}$$
$$a_{22} = \frac{1}{16G\pi}\left[\left(\kappa+1\right)\left(1-\cos\theta\right)+\left(1+\cos\theta\right)\left(3\cos\theta-1\right)\right]$$

where *G* is the shear modulus, and κ is $(3-\nu)/(1+\nu)$ for plane stress and $(3-4\nu)$ for

plane strain conditions. The author reasoned that the fracture propagation occurs when S reached a critical value,

$$S = S_c . \tag{2.8}$$

Propagation occurs in the direction of the minimum value of S, which can be found from

$$\begin{matrix} \dfrac{\partial S}{\partial \theta} = 0 \\ \dfrac{\partial^2 S}{\partial \theta^2} < 0 \end{matrix} . \tag{2.9}$$

The S-criterion has an advantage over other methods in that it includes the value of Poisson's ratio, ν, and predicts different propagation directions dependent on material elastic properties. However, in some cases, the S-criterion does not provide a unique solution and has several minimum values, and there are other situations where no minimum exists (Chang, 1982).

2.3 STRESS-BASED FRACTURE PROPAGATION CRITERION

Erdogan and Sih (1963) introduced the maximum tangential stress criterion (MTS-criterion), also known as the maximum circumferential stress criterion. It is based on the first singular term of the two-dimensional stress functions in the vicinity of a fracture tip. In cylindrical coordinates under plane strain conditions, the three near-tip stress components (Figure 2.1) can be expressed as

$$
\begin{aligned}
\sigma_{rr} &= \frac{1}{\sqrt{2\pi r}}\left[K_{\mathrm{I}} \left\{ \cos\frac{\theta}{2}\left(1+\sin^2\frac{\theta}{2}\right)\right\} + K_{\mathrm{II}} \left\{ \sin\frac{\theta}{2}\left(1-3\sin^2\frac{\theta}{2}\right)\right\}\right] \\
&\quad + T\cos^2\theta + O\left(r^{1/2}\right) + \ldots \\
\sigma_{\theta\theta} &= \frac{1}{\sqrt{2\pi r}}\left[K_{\mathrm{I}} \left\{ \cos^3\frac{\theta}{2}\right\} - K_{\mathrm{II}} \left\{ 3\sin\frac{\theta}{2}\cos^2\frac{\theta}{2}\right\}\right] \\
&\quad + T\sin^2\theta + O\left(r^{1/2}\right) + \ldots \\
\sigma_{r\theta} &= \frac{1}{\sqrt{2\pi r}}\left[K_{\mathrm{I}} \left\{ \sin\frac{\theta}{2}\cos^2\frac{\theta}{2}\right\} + K_{\mathrm{II}} \left\{ \cos\frac{\theta}{2}\left(1-3\sin^2\frac{\theta}{2}\right)\right\}\right] \\
&\quad - T\sin\theta\cos\theta + O\left(r^{1/2}\right) + \ldots
\end{aligned}
\tag{2.10}
$$

where T is the constant stress parallel to the crack (Rice, 1974), r is the radial distance from the fracture tip (Williams, 1957; Irwin, 1958). Since the hypothesis for the MTS-criterion is that the fracture propagates from the fracture tip with an infinitesimal fracture increment length ($r \to 0$), the criterion neglects the non-singular terms (T-stress and higher order terms ($O\left(r^{1/2}\right)+\ldots$)).

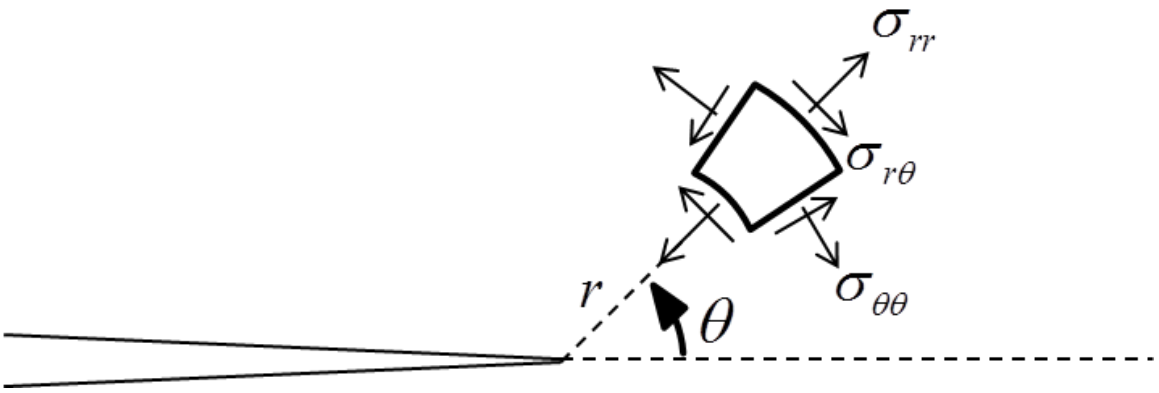

Figure 2.1. Sketch of the three near-tip stress components (σ_{rr}, $\sigma_{\theta\theta}$, $\sigma_{r\theta}$). All stress components are positive as drawn.

The fracture tip extends radially along the path of maximum tangential stress, $\sigma_{\theta\theta}$, when the near-tip stress overcomes the critical value of the material, σ_T. The fracture will propagate in a direction where the following conditions are satisfied,

$$\begin{aligned} &\sigma_{\theta\theta} \geq \sigma_T \\ &\frac{\partial \sigma_{\theta\theta}}{\partial \theta} = 0 = \cos\frac{\theta}{2}\left[K_{\mathrm{I}}\left(\sin\theta\right) + K_{\mathrm{II}}\left(3\cos\theta - 1\right)\right]. \end{aligned} \tag{2.11}$$

This provides the same result as prescribing $\sigma_{r\theta}$ to be zero.

2.4 MODIFIED MAXIMUM TANGENTIAL PRINCIPAL STRESS CRITERION

The analysis of classical linear fracture mechanics is applicable to mode I fractures (Ingraffea and Heuze, 1980) as well as mode II fractures. In fact, for fractures under pure mode II loading, the G-criterion, S-criterion, and MTS-criterion are capable of predicting a fracture propagation angle around 70.5° which agrees with the experiments on plexiglass plates under concentrated shear loading (Erdogan and Sih, 1963). However, the predictions of these conventional fracture propagation criteria deviate from each other for mixed-mode I and II cracks (Smith et al., 2001) and numerical applications for cracks under crack-parallel compressive stress generate errors when using finite crack propagation increment lengths (Thomas and Pollard, 1993).

Thomas and Pollard (1993) examined the fracture propagation path of two mechanically interacting fractures under three different stress states: all-around tension (AAT), uniaxial tension (UNI), and crack-parallel compression (CPC). These are

characterized by crack-parallel differential stresses ($\Delta\sigma^r$), or *T*-stress, of zero ($\Delta\sigma^r = \sigma_{22}{}^r - \sigma_{11}{}^r = 0$), equal to the driving stress ($\Delta\sigma^r = \sigma_{11}{}^r = \Delta\sigma_{\mathrm{I}}$), and twice the driving stress ($\Delta\sigma^r = 2\sigma_{11}{}^r = 2\Delta\sigma_{\mathrm{I}}$), respectively. Thomas and Pollard utilized the MTS-based numerical model of Olson and Pollard (1989), also known as JOINTS, to validate the experimental results of PMMA plates under external biaxial loading. The JOINTS program (Olson and Pollard, 1989; Olson, 1991; Olson and Pollard, 1991) is a boundary element fracture propagation model which has multiple crack propagation path models including the MTS-based model. It is capable of generating two-dimensional fractures under in-plane mixed-mode I and II loading.

Thomas and Pollard (1993) observed that if longer crack propagation lengths were utilized in the numerical method, the predicted path oscillated to self-correct its trajectory (Figure 2.2). The MTS-criterion only focuses on the local stress perturbation without considering the remote stress effect and incorrectly predicts the incipient fracture propagation angle. The resolved shear stresses from the far-field compression generate fracture oscillations to correct its path to the principal stress trajectory (Cotterell, 1966). In addition, a larger far-field differential stress more dominantly corrects any errors in the predicted path by the MTS-criterion.

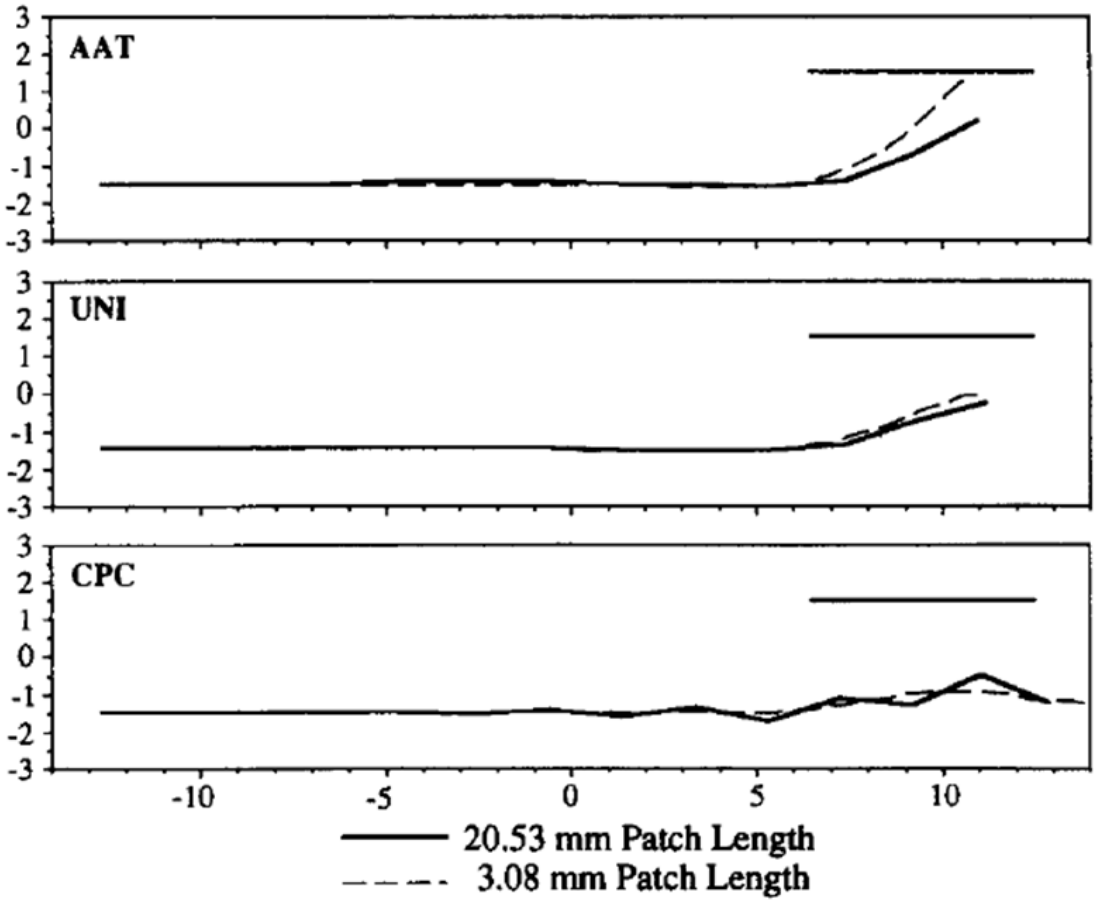

Figure 2.2. A Comparison of fracture paths with two patch lengths (3.08 and 20.53 mm). Numerically predicted paths were generated by the MTS-criterion using JOINTS. Scales are in centimeters (Thomas and Pollard, 1993).

The error in numerically predicted fracture paths is mainly due to the mixed-mode fracture propagation criterion omitting the non-singular terms, including the remote stresses. Cotterell (1966) concluded that the non-singular terms have significant impact on the fracture propagation direction under simple tension, and this was corroborated with experiments of angle-cracked samples under tension loading (Willams and Ewing, 1972; Theocaris and Andrianopoulos, 1982; Kong et al., 1995).

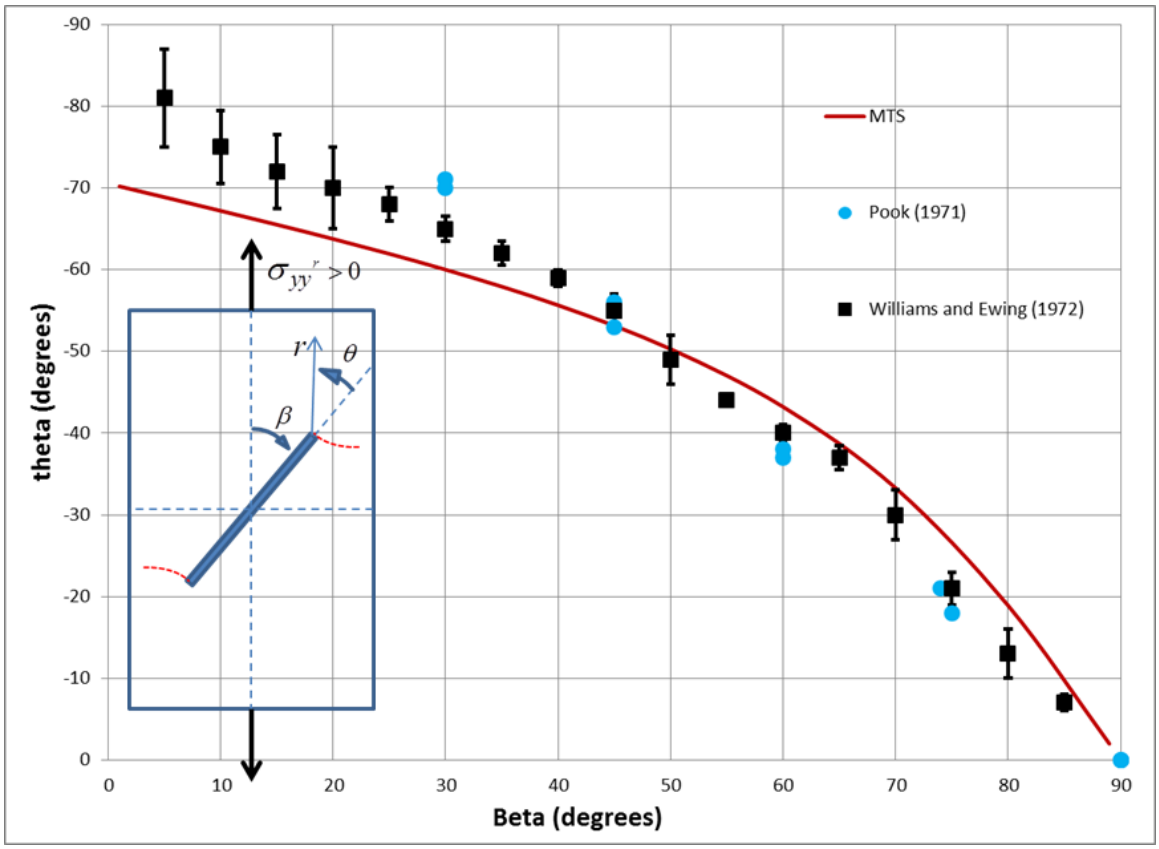

Figure 2.3. The predictions of the fracture propagation angles (θ) with respect to the fracture inclination angles (β) for angled fractures under uniaxial tension by the MTS-criterion. Experiment results are from Williams and Ewing (1972) and Pook (1971). The experimental scatters of Willams and Ewing (1972) are obtained from Sih and Kipp (1974).

For an angled crack under uniaxial tension, Williams and Ewing (1972) showed the discrepancy between the experimental results and the predictions of the classical MTS-criterion (Figure 2.3) and suggested predicting crack propagation direction with the two-term approximation, a criterion based on the first and second terms in the series expansion of $\sigma_{\theta\theta}$ (Equation (2.10)). Finnie and Saith (1973) found that the two-term approximation of Williams and Ewing (1972) ignored the normal stress acting on the fracture which led to an error in correlating for fracture inclination angles greater than

$45°$. The crack inclination angle is the angle between the initial crack and the loading direction. Sih and Kipp (1974), in their discussion on the paper of Williams and Ewing (1972), showed that the experimental results fit better with the computed exact solutions of a degenerate elliptical cavity for all crack angles from $0°$ to $90°$.

Maiti and Smith (1983) argued that when including the non-singular terms in the MTS-criterion, which Smith et al. (2001) called the generalized MTS-criterion (I will call this the GMTS-criterion), the predicted fracture propagation plane is not the principal direction. The direction predicted by $\partial\sigma_{\theta\theta}/\partial\theta = 0$ (GMTS-criterion) is close but different from what is calculated by $\sigma_{r\theta} = 0$. This is due to the fact that the angle θ is not the rotational angle at the locus of a point because of the finite radial distance from the fracture tip. Consequently, they introduced the maximum tangential principal stress criterion (MTPS-criterion) to predict the propagation direction in the principal direction ($\sigma_{r\theta} = 0$).

Maiti and Smith (1983, 1984) compared the accuracy of crack path predictions for four methods: the MTS-criterion with non-singular terms (GMTS), maximum tangential principal stress (MTPS), maximum tangential strain (MTSN), and strain energy density (S-criterion). The fracture propagation path predicted by the MTPS-criterion is nearly same to the paths of the GMTS-criterion and MTSN-criterion for fractures under tensile loading. Some distinction, however, has been found amongst results with a change in crack inclination angle for the S-criterion (Figure 2.4a). For elliptical cracks under compression (Figure 2.4b), the discrepancy of predicted propagation paths by four

different criteria are significant. As the crack inclination angle increases, fracture paths appear to diverge from one another. The paths predicted by three criteria (GMTS, MTPS, MTSN) except the S-criterion eventually line up parallel to the compressive loading direction. The predictions of GMTS, MTPS, and MTSN are about the same, thus, this study will focus on the modification of the MTPS-criterion because it assumes a mode I-type propagation that ensures the local symmetry (Cotterell and Rice, 1980).

Previous studies related to mixed-mode fractures have mostly concentrated on engineering mechanics applications where fractures are generally under tensile loading. The standard models, based on near-tip approximations, tend to be more accurate under tensile loading. However, hydraulic and natural fractures in the subsurface are different in that there is an internal fluid pressure in the crack with all-around remote compressive stress. These loading conditions result in generally stable propagation as compared to the typically unstable propagation of fractures under tensile loading (Hoek and Bieniawski, 1965). In addition, for some natural fractures, the frictional stress on the fracture walls becomes important in understanding the mechanics of the mixed-mode fracture propagation.

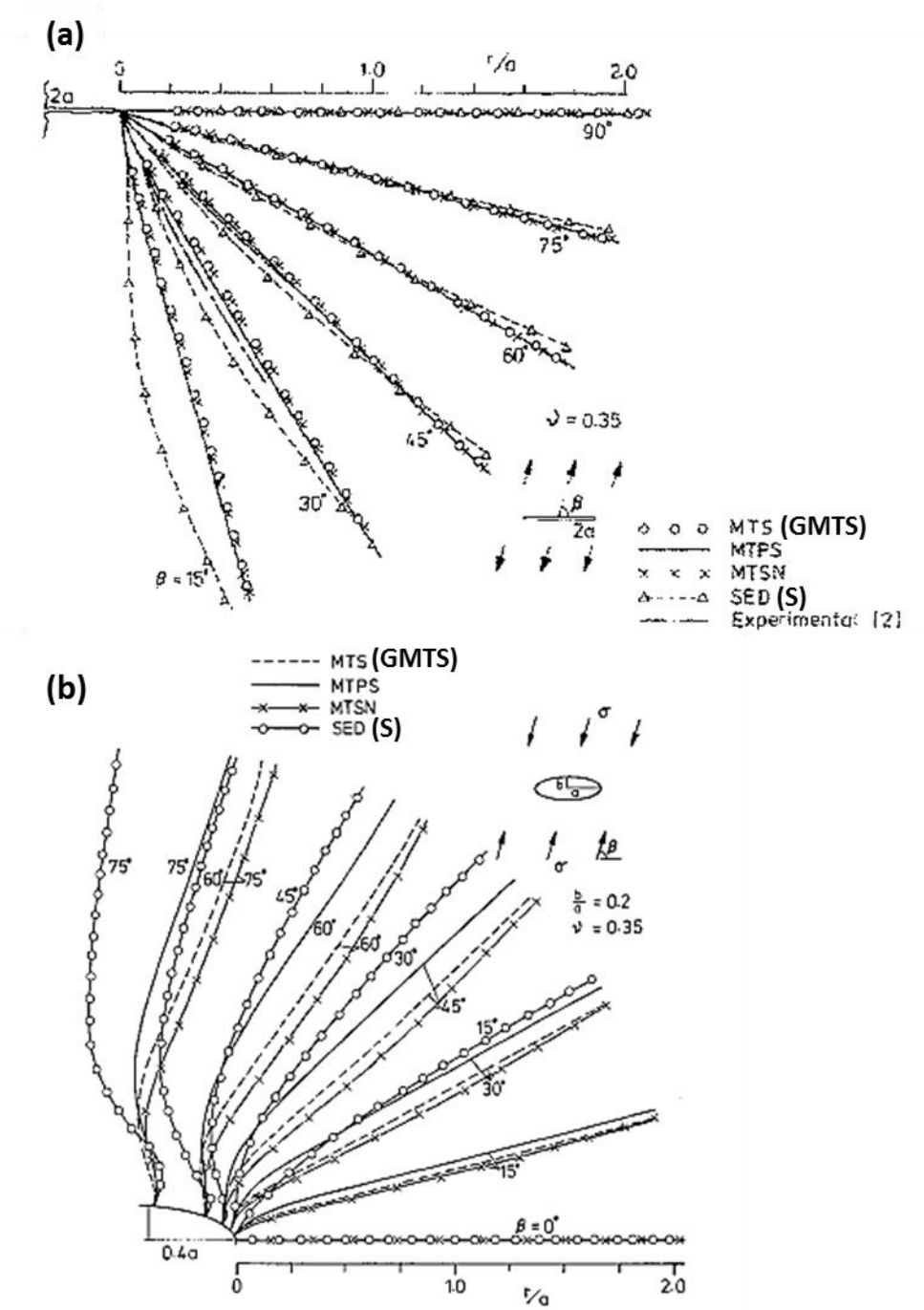

Figure 2.4. Fracture paths predicted with four criterion for two crack types: (a) a slot crack under tensile loading (Maiti and Smith, 1983), and (b) an elliptical crack under compressive loading (Maiti and Smith, 1984). The experimenal result in (a) are from Kipp and Sih (1975).

Under these conditions, the near-tip stress field approximation (dominated by the singular terms in LEFM) and the developed models that include the non-singular terms have inadequacies in addressing the contribution of the remote and internal crack stresses on the hydraulic and natural fracture paths. To explicitly investigate the role of these stress components on the near-tip stress field and the fracture propagation trajectory, this study utilized a full stress field based on the plane strain equations for a uniformly loaded crack in an elastic, infinite media as described in Pollard and Segall (1987). The plane strain equations apply to linear elastic material that is homogeneous, isothermal, and isotropic. By modifying their coordinate system to tri-polar coordinates with the crack perpendicular to the X_1-axis (Figure 2.5a) and keeping the sign convention as tension being positive, the driving stresses (Figure 2.6) are defined as

$$\begin{aligned} \Delta\sigma_{\mathrm{I}} &= {\sigma_{11}}^{r} - {\sigma_{11}}^{c} \\ \Delta\sigma_{\mathrm{II}} &= {\sigma_{12}}^{r} - {\sigma_{12}}^{c} \\ \Delta\sigma_{\mathrm{III}} &= {\sigma_{13}}^{r} - {\sigma_{13}}^{c} \end{aligned} . \tag{2.12}$$

The SIFs can be modified from Equation (2.3) to include internal crack stresses as

$$\begin{aligned} K_{\mathrm{I}} &= \sqrt{\pi a}\Delta\sigma_{\mathrm{I}} = \sqrt{\pi a}\left({\sigma_{11}}^{r} - {\sigma_{11}}^{c}\right) \\ K_{\mathrm{II}} &= \sqrt{\pi a}\Delta\sigma_{\mathrm{II}} = \sqrt{\pi a}\left({\sigma_{12}}^{r} - {\sigma_{12}}^{c}\right) \\ K_{\mathrm{III}} &= \sqrt{\pi a}\Delta\sigma_{\mathrm{III}} = \sqrt{\pi a}\left({\sigma_{13}}^{r} - {\sigma_{13}}^{c}\right) \end{aligned} . \tag{2.13}$$

The six stress components around the fracture tip are

$$
\begin{aligned}
\sigma_{22} &= \sigma_{22}{}^{r} + \Delta\sigma_{\mathrm{I}}\left[\frac{r}{R}\cos(\theta-\Gamma)-1-a^2\frac{r}{R^3}\sin\theta\sin 3\Gamma\right] \\
&\quad + \Delta\sigma_{\mathrm{II}}\left[2\frac{r}{R}\sin(\theta-\Gamma)-a^2\frac{r}{R^3}\sin\theta\cos 3\Gamma\right] \\
\sigma_{11} &= \sigma_{11}{}^{r} + \Delta\sigma_{\mathrm{I}}\left[\frac{r}{R}\cos(\theta-\Gamma)-1+a^2\frac{r}{R^3}\sin\theta\sin 3\Gamma\right] \\
&\quad + \Delta\sigma_{\mathrm{II}}\left[a^2\frac{r}{R^3}\sin\theta\sin 3\Gamma\right] \\
\sigma_{12} &= \sigma_{12}{}^{r} + \Delta\sigma_{\mathrm{II}}\left[\frac{r}{R}\cos(\theta-\Gamma)-1-a^2\frac{r}{R^3}\sin\theta\sin 3\Gamma\right] \\
&\quad + \Delta\sigma_{\mathrm{I}}\left[a^2\frac{r}{R^3}\sin\theta\sin 3\Gamma\right] \\
\sigma_{33} &= \nu\left[\sigma_{11}+\sigma_{22}\right] \\
\sigma_{13} &= \sigma_{13}{}^{r} + \Delta\sigma_{\mathrm{III}}\left[\frac{r}{R}\cos(\theta-\Gamma)-1\right] \\
\sigma_{23} &= \sigma_{23}{}^{r} + \Delta\sigma_{\mathrm{III}}\left[\frac{r}{R}\sin(\theta-\Gamma)\right]
\end{aligned}
\qquad (2.14)
$$

by using the definitions

$$
\begin{aligned}
R &= \sqrt{r_1 r_2} \\
\Gamma &= \frac{\theta_1+\theta_2}{2}\cdot
\end{aligned}
\qquad (2.15)
$$

To simplify the components of the near-tip stress field, the following approximations are made for the locus of points very close to the fracture tip (see Figure 2.5b).

$$
\theta=\theta_2=0,\ r=a,\ r_1=r_1,\ r_2=2a,\ R=\sqrt{r_1 2a},\ \Gamma=\frac{\theta_1}{2},\ r\sin\theta=r_1\sin\theta_1 \qquad (2.16)
$$

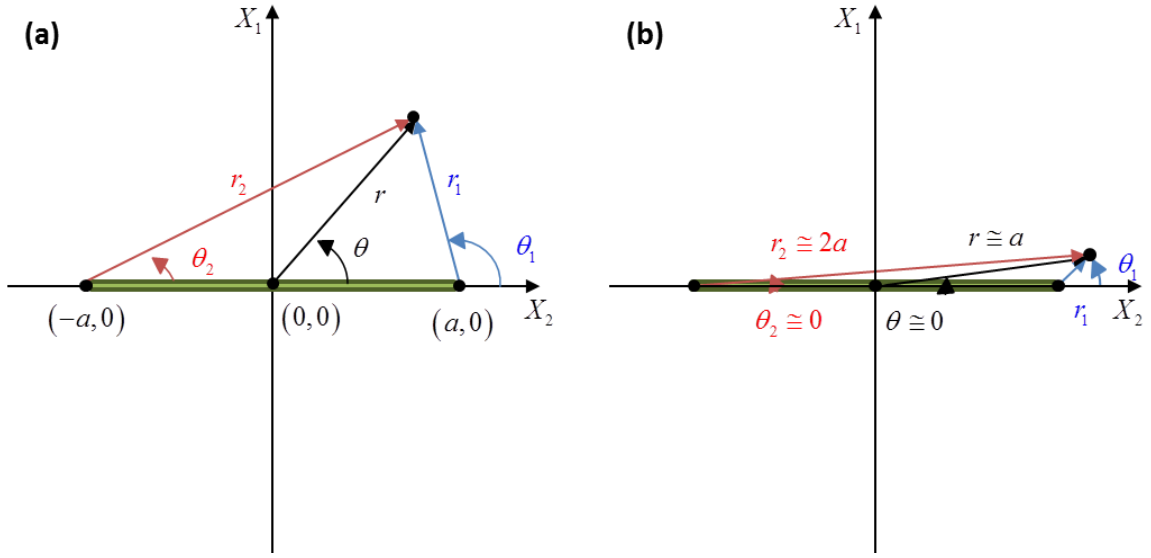

Figure 2.5. Tri-polar coordinate system: (a) for a fracture with a length of 2a in the X_2-direction and (b) for points very close to the fracture tip (after Pollard and Segall, 1987).

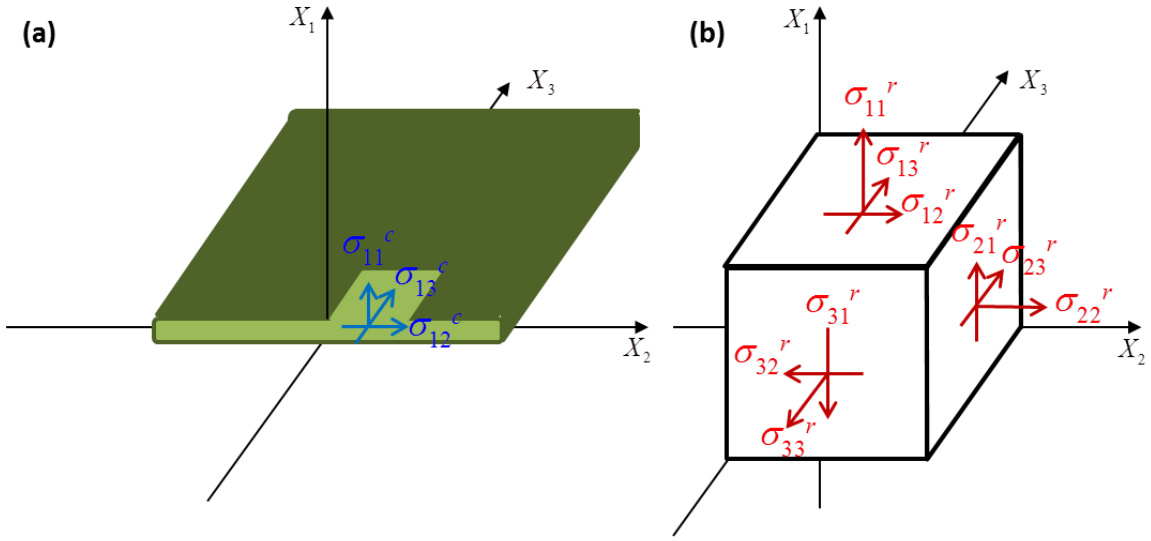

Figure 2.6. Sketch of stress components for a fracture in the X_2-direction: (a) internal crack stresses and (b) remote stresses (after Pollard and Segall, 1987). All stress components are positive as drawn.

Re-writing the stress components as a function of SIFs and changing θ_1 and r_1 to θ and r results in

$$\begin{aligned}
\sigma_{22} &= \frac{1}{\sqrt{2\pi r}}\left[K_{\mathrm{I}} \left\{ \cos\frac{\theta}{2}\left(1-\sin\frac{\theta}{2}\sin\frac{3\theta}{2}\right)\right\} - K_{\mathrm{II}} \left\{ \sin\frac{\theta}{2}\left(2+\cos\frac{\theta}{2}\cos\frac{3\theta}{2}\right)\right\}\right] \\
&\quad + \sigma_{11}{}^{c} + \left(\sigma_{22}{}^{r} - \sigma_{11}{}^{r}\right) \\
\sigma_{11} &= \frac{1}{\sqrt{2\pi r}}\left[K_{\mathrm{I}} \left\{ \cos\frac{\theta}{2}\left(1+\sin\frac{\theta}{2}\sin\frac{3\theta}{2}\right)\right\} + K_{\mathrm{II}} \left\{ \sin\frac{\theta}{2}\cos\frac{\theta}{2}\cos\frac{3\theta}{2}\right\}\right] \\
&\quad + \sigma_{11}{}^{c} \\
\sigma_{12} &= \frac{1}{\sqrt{2\pi r}}\left[K_{\mathrm{I}} \left\{ \sin\frac{\theta}{2}\cos\frac{\theta}{2}\cos\frac{3\theta}{2}\right\} + K_{\mathrm{II}} \left\{ \cos\frac{\theta}{2}\left(1-\sin\frac{\theta}{2}\sin\frac{3\theta}{2}\right)\right\}\right] \\
&\quad + \sigma_{12}{}^{c} \\
\sigma_{33} &= \nu\left[\sigma_{11}+\sigma_{22}\right] \\
\sigma_{13} &= \frac{1}{\sqrt{2\pi r}}\left[K_{\mathrm{III}} \cos\frac{\theta}{2}\right] + \sigma_{13}{}^{c} \\
\sigma_{23} &= \frac{1}{\sqrt{2\pi r}}\left[-K_{\mathrm{III}} \sin\frac{\theta}{2}\right] + \sigma_{23}{}^{r}
\end{aligned} \quad . \tag{2.17}$$

Neglecting the plane strain stress components in the *Z*-direction, the transformation to cylindrical coordinates can be accomplished using the following equations (Sadd, 2009),

$$\begin{aligned}
\sigma_{rr} &= \sigma_{22}\cos^2\theta + \sigma_{11}\sin^2\theta + \sigma_{12}\sin 2\theta \\
\sigma_{\theta\theta} &= \sigma_{22}\sin^2\theta + \sigma_{11}\cos^2\theta - \sigma_{12}\sin 2\theta \,. \\
\sigma_{r\theta} &= \left(\sigma_{11}-\sigma_{22}\right)\sin\theta\cos\theta + \sigma_{12}\cos 2\theta
\end{aligned} \tag{2.18}$$

Applying the transformation of Equation (2.18) to Equation (2.17), the three components of the near-tip stress field in cylindrical coordinates can be written as

$$
\begin{aligned}
\sigma_{rr} &= \frac{1}{\sqrt{2\pi r}}\left[K_{\mathrm{I}} \left\{ \cos\frac{\theta}{2}\left(1+\sin^2\frac{\theta}{2}\right)\right\} + K_{\mathrm{II}} \left\{ \sin\frac{\theta}{2}\left(1-3\sin^2\frac{\theta}{2}\right)\right\}\right] \\
&\quad + {\sigma_{11}}^{c} + {\sigma_{12}}^{c}\sin 2\theta + \left({\sigma_{22}}^{r} - {\sigma_{11}}^{r}\right)\cos^2\theta \\
\sigma_{\theta\theta} &= \frac{1}{\sqrt{2\pi r}}\left[K_{\mathrm{I}} \left\{ \cos^3\frac{\theta}{2}\right\} - K_{\mathrm{II}} \left\{ 3\sin\frac{\theta}{2}\cos^2\frac{\theta}{2}\right\}\right] \\
&\quad + {\sigma_{11}}^{c} - {\sigma_{12}}^{c}\sin 2\theta + \left({\sigma_{22}}^{r} - {\sigma_{11}}^{r}\right)\sin^2\theta \\
\sigma_{r\theta} &= \frac{1}{\sqrt{2\pi r}}\left[K_{\mathrm{I}} \left\{ \sin\frac{\theta}{2}\cos^2\frac{\theta}{2}\right\} + K_{\mathrm{II}} \left\{ \cos\frac{\theta}{2}\left(1-3\sin^2\frac{\theta}{2}\right)\right\}\right] \\
&\quad + {\sigma_{12}}^{c}\cos 2\theta - \left({\sigma_{22}}^{r} - {\sigma_{11}}^{r}\right)\sin\theta\cos\theta
\end{aligned}
\qquad . \qquad (2.19)
$$

All three components include the remote differential stress (${\sigma_{22}}^{r} - {\sigma_{11}}^{r}$) and internal crack stresses (normal, ${\sigma_{11}}^{c}$, and shear, ${\sigma_{12}}^{c}$).

For typical hydraulic fracturing applications, ${\sigma_{11}}^{c}$ is the internal fluid pressure against the fracture wall, ${\sigma_{22}}^{r}$ is the maximum horizontal stress and ${\sigma_{11}}^{r}$ is the minimum horizontal stress. The frictional stress, ${\sigma_{12}}^{c}$, would not be considered for an open fracture. However, for closed fractures, ${\sigma_{12}}^{c}$ represents the frictional stress acting between the fracture walls facing each other due to the crack-perpendicular compressive stress.

The near-tip stress components are analogous to what others have derived from eigenseries expansion (Eftis and Subramonian, 1978; Chao and Zhang, 1997; Smith et al., 2001) except that Equation (2.19) contains the internal crack stresses and ignores the higher order terms ($O\left(r^{1/2}\right)+...$). Chao and Zhang (1997) suggested that higher order terms may have influence on the stress field, but the effect, in the experiments, is smaller

than the impact of the constant terms. In addition, Larsson and Carlsson (1973) noted that the higher order terms are zero near the fracture tip.

Using the stress components in Equation (2.19), the fracture propagation path can be determined as

$$\sigma_{\theta\theta P} \geq \sigma_T$$
$$\sigma_{r\theta} = 0 = \frac{1}{\sqrt{2\pi r}} \cos\frac{\theta}{2}\left[K_{\mathrm{I}} \sin\theta + K_{\mathrm{II}}\left(3\cos\theta - 1\right)\right] \qquad (2.20)$$
$$-\left[\left(\sigma_{22}{}^{r} - \sigma_{11}{}^{r}\right)\sin 2\theta - 2\sigma_{12}{}^{c}\cos 2\theta\right]$$

where $\sigma_{\theta\theta P}$ is the tangential stress in the direction of $\sigma_{r\theta} = 0$. This mixed-mode fracture propagation criterion is designated as the modified maximum tangential principal stress criterion (MMTPS-criterion). The MMTPS-criterion is unique since no other criterion, such as the MTPS-criterion (Maiti and Smith, 1983) and the GMTS-criterion (Smith et al., 2001), includes the remote and internal crack stresses together.

The internal pressure ($\sigma_{11}{}^{c}$) does not contribute to the direction of the fracture path but it does impact the magnitude of $\sigma_{\theta\theta}$. For closed fractures under compression, $\sigma_{12}{}^{c}$ plays a role in predicting the fracture propagation trajectory when the mode II driving stress is sufficient for a fracture to propagate.

The direction predicted by the MMTPS-criterion differs from the path predicted by $\partial\sigma_{\theta\theta}/\partial\theta = 0$, the derivative utilized in the GMTS-criterion, which can be expressed as

$$\sigma_{\theta\theta} \geq \sigma_T$$

$$\frac{\partial \sigma_{\theta\theta}}{\partial \theta} = 0 = \frac{1}{\sqrt{2\pi r}} \cos\frac{\theta}{2}\left[K_{\mathrm{I}} \sin\theta + K_{\mathrm{II}}\left(3\cos\theta - 1\right)\right] - \frac{4}{3}\left[\left(\sigma_{22}{}^{r} - \sigma_{11}{}^{r}\right)\sin 2\theta - 2\sigma_{12}{}^{c}\cos 2\theta\right] \quad . \qquad (2.21)$$

The singular term is analogous to Equation (2.20) but the non-singular term—the remote differential stress and the internal friction—have more impact in the case of $\partial\sigma_{\theta\theta}/\partial\theta = 0$ by a factor of $4/3$.

2.5 CRITICAL PROPAGATION DISTANCE

Including the non-singular terms in the MMTPS-criterion requires a value of radial distance from the fracture tip, *r*, to investigate the near-tip stress field and to predict the fracture propagation angle. It is evident that as *r* approaches zero, the non-singular terms become unimportant and the stress equations (Equation (2.19)) revert to the traditional near-tip stress field and the prediction of fracture propagation direction is analogous to the conventional MTS-criterion. However, many experimental and theoretical studies (Williams and Ewing, 1972; Ueda et al., 1977; Maiti and Smith, 1983; Maiti and Smith, 1984; Papadopoulos and Poniridis, 1989; Yeh and Kim, 1994) report that non-zero *r* improves the prediction of the fracture propagation trajectory.

One question may arise if a characteristic *r* exists for a material which is related to the fracture increment length. For quasi-brittle materials, such as rocks and gypsum cements, studies described the critical *r* as the size of the fracture process zone around the

crack tip where material yields or non-linear processes occur (Bobet, 2000; Aliha et al., 2010; Aliha and Ayatollahi, 2011). The near-tip inelastic behavior in rocks, induced by the high tensile stress concentration, is generally described as microcracks around the fracture tip in laboratory specimens (Hoagland et al., 1973) or adjacent joints of dikes in outcrops (Delaney et al., 1986).

To estimate the size of the rock fracture process zone, Schmidt (1980) suggested a maximum principal stress model to replace the Von Mises yield condition in the plastic zone model. The principal stresses in the plane strain condition can be expressed with near-tip stress components as

$$\sigma_1 = \frac{\sigma_{22} + \sigma_{11}}{2} + \sqrt{\left(\frac{\sigma_{22} - \sigma_{11}}{2}\right)^2 + {\sigma_{12}}^2}$$
$$\sigma_3 = \frac{\sigma_{22} + \sigma_{11}}{2} - \sqrt{\left(\frac{\sigma_{22} - \sigma_{11}}{2}\right)^2 + {\sigma_{12}}^2} \qquad (2.22)$$

where σ_1 is the maximum and σ_3 is the minimum principal stress. The maximum principal stress model predicts the boundary of the fracture process zone simply by

$$\sigma_1 = \sigma_T \,. \qquad (2.23)$$

Based on the singular terms of the near-tip stress equations for a mode I fracture, Schmidt (1980) described the fracture process zone as

$$r_p(\theta) = \frac{1}{2\pi}\left(\frac{K_{\mathrm{I}}}{\sigma_T}\right)^2\left[\cos\frac{\theta}{2}\left(1+\sin\frac{\theta}{2}\right)\right]^2 \quad \text{for } 0° \le \theta \le 180°$$
$$r_p(\theta) = \frac{1}{2\pi}\left(\frac{K_{\mathrm{I}}}{\sigma_T}\right)^2\left[\cos\frac{\theta}{2}\left(1-\sin\frac{\theta}{2}\right)\right]^2 \quad \text{for } -180° \le \theta \le 0° \tag{2.24}$$

where r_p is the radial length from the fracture tip to the boundary of the process zone. In addition, he noted that by simply adding the hydrostatic stress terms into the principal stresses in Equation (2.22), the size of the fracture process zone decreased with the compressive confining stress.

To evaluate the impact of the internal pressure and the remote differential stress on the process zone size, the maximum principal stress model can be modified. Substituting the singular near-tip stress equations with the stress components from Equation (2.17), allows inclusion of the remote and internal crack stresses. For a pressurized crack under isotropic stress state, the model simplifies to something similar to Equation (2.24) as

$$r_{pT}(\theta) = \frac{1}{2\pi}\left(\frac{K_{\mathrm{I}}}{\sigma_T - \sigma_{11}{}^c}\right)^2\left[\cos\frac{\theta}{2}\left(1+\sin\frac{\theta}{2}\right)\right]^2 \quad \text{for } 0° \le \theta \le 180°$$
$$r_{pT}(\theta) = \frac{1}{2\pi}\left(\frac{K_{\mathrm{I}}}{\sigma_T - \sigma_{11}{}^c}\right)^2\left[\cos\frac{\theta}{2}\left(1-\sin\frac{\theta}{2}\right)\right]^2 \quad \text{for } -180° \le \theta \le 0° \tag{2.25}$$

where r_{pT} stands for the radial length of the fracture process zone defined by the tensile strength.

For the sake of a simple but comparable example, fractures of a given half-length ($1.27\ (=4/\pi)$ m) with mode I loading ($K_{\mathrm{II}} = 0$) under various loading conditions were selected. To generate the same $K_{\mathrm{I}} = 1\ \mathrm{MPa}\sqrt{\mathrm{m}}$ alternately with remote tension and

internal fluid pressure, same driving stress of 0.5 MPa was applied. The tensile strength (σ_T) of the material is 1 MPa.

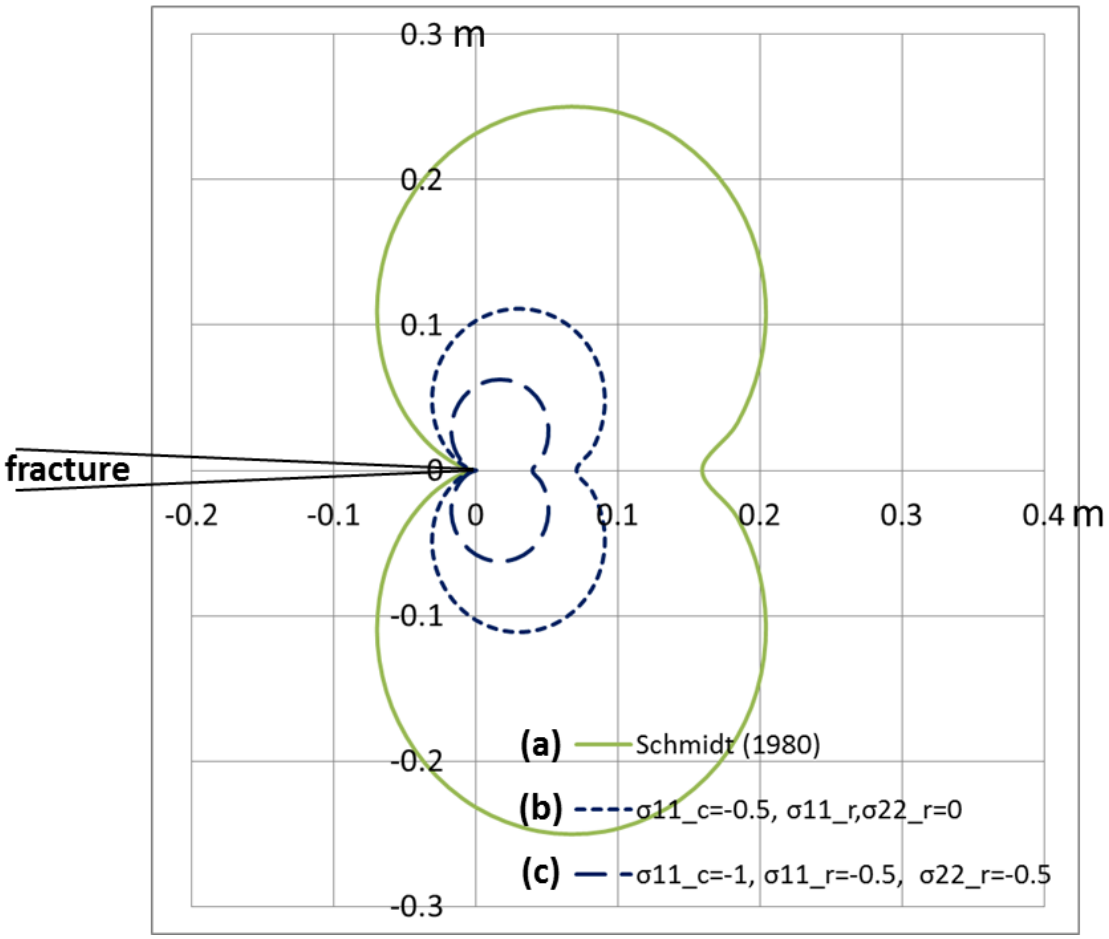

Figure 2.7. Fracture process zones of mode I fractures ($K_{\mathrm{I}} = 1\ \mathrm{MPa}\sqrt{\mathrm{m}}$, $K_{\mathrm{II}} = 0$) under various loading types: (a) remote stresses of ${\sigma_{11}}^r$, ${\sigma_{22}}^r = 0.5$ MPa with zero internal crack stresses (${\sigma_{11}}^c$, ${\sigma_{12}}^c = 0$) to reproduce the prediction of Schmidt (1980), (b) the internal pressure of ${\sigma_{11}}^c = -0.5$ MPa with zero remote stresses (${\sigma_{11}}^r$, ${\sigma_{22}}^r = 0$), (c) the internal pressure of ${\sigma_{11}}^c = -1$ MPa with ${\sigma_{11}}^r$, ${\sigma_{22}}^r = -0.5$ MPa.

Although K_I was identical and the shape of the process zone did not change, the r_{pT} generated by internal pressure (–0.5 MPa; Figure 2.7b) was only 44% of that created

under remote tensile stress (0.5 MPa; Figure 2.7a). For a fracture under all-around compression (–0.5 MPa; Figure 2.7c), which requires -1 MPa of internal fluid pressure to generate same driving stress, the process zone size became even smaller (25% of Figure 2.7a) compared to the previous case. The results indicate that the remote compressive stress, that is the subsurface conditions, significantly reduces the process zone size.

If the remote differential stress is included, the estimation model becomes complicated and cannot be expressed in a simple equation, but the effect of the anisotropic insitu stress state on the process zone size can be estimated numerically. Assuming that the hydraulic fracture is perpendicular to the least compressive stress, Figure 2.8 shows that the crack-parallel compressive stress slightly compressed the fracture process zone, generating a narrower region. Regardless of the different remote differential stresses, all three process zone boundaries converged at θ of 0° and ±60°. At $\theta = 0°$, which is the expected fracture propagation direction for mode I fractures, the maximum and minimum principal stress were the tangential ($\sigma_{\theta\theta}$) and the radial stress (σ_{rr}), respectively. Nonetheless, the overall size of the process zone did not change significantly indicating that the fracture process zone, as defined by tensile strength, does not depend on the remote differential stress.

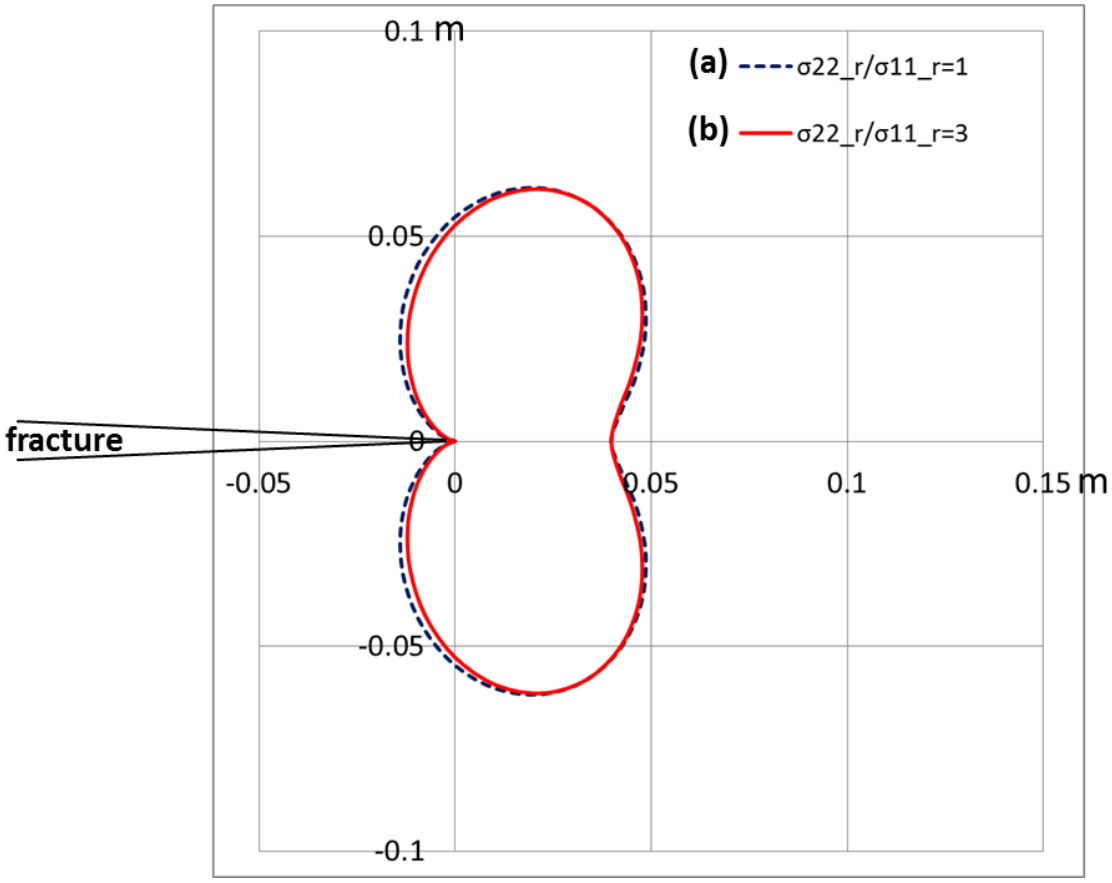

Figure 2.8. Fracture process zones of pressurized fractures ($\sigma_{11}^{\,c} = -1$ MPa ; $K_{\mathrm{I}} = 1\ \mathrm{MPa}\sqrt{\mathrm{m}}$, $K_{\mathrm{II}} = 0$) under various remote differential stresses: (a) $\sigma_{22}^{\,r} / \sigma_{11}^{\,r} = 1$ (the example of Figure 2.7c) and (b) $\sigma_{22}^{\,r} / \sigma_{11}^{\,r} = 3$. For both cases, $\sigma_{11}^{\,r}$ is kept constant at –0.5 MPa.

If the process zone is defined using shear failure as the criterion, however, the remote compressive differential stress becomes important. The boundary of the fracture process zone defined by the shear strength (r_{pS}) can be examined with a simple Mohr-Coulomb criterion, which can be expressed in terms of the principal stresses (Equation (2.22)) as

$$\sigma_1 = n\sigma_3 + UCS\,. \tag{2.26}$$

where *UCS* is the Unconfined Compressive Strength, *n* is the slope of the failure envelope that can be calculated from

$$n = \left(\sqrt{1+\mu_i^{\,2}} + \mu_i\right)^2 \tag{2.27}$$

where μ_i is the coefficient of internal friction. To examine the remote differential compressive stress on the fracture process zone (r_{pS}), the parameters are selected as *UCS* of 10 MPa (ten times the tensile strength) and μ_i of 0.8. The remote differential stress are varied from –10 MPa to –20 MPa to induce shear failure while $\sigma_{11}^{\,r}$ is kept constant at –5 MPa. To generate the same driving stress of 0.5 MPa to the previous examples, the internal fluid pressure was –5.5 MPa.

As in Figure 2.8, the process zones (r_{pT}), as defined by the tensile strength, were nearly identical and overlapped each other regardless of the increase in the remote differential stress (Figure 2.9a and Figure 2.9c). However, under the same conditions, the shear strength defined process zones (r_{pS}) were dominantly controlled by the remote differential compressive stress (Figure 2.9b and Figure 2.9d). As the crack-parallel compression ($\sigma_{22}^{\,r}$) increased from –15 MPa to –20 MPa, the r_{pS} of the process zone almost doubled its length in the angular direction of $\pm 60°$.

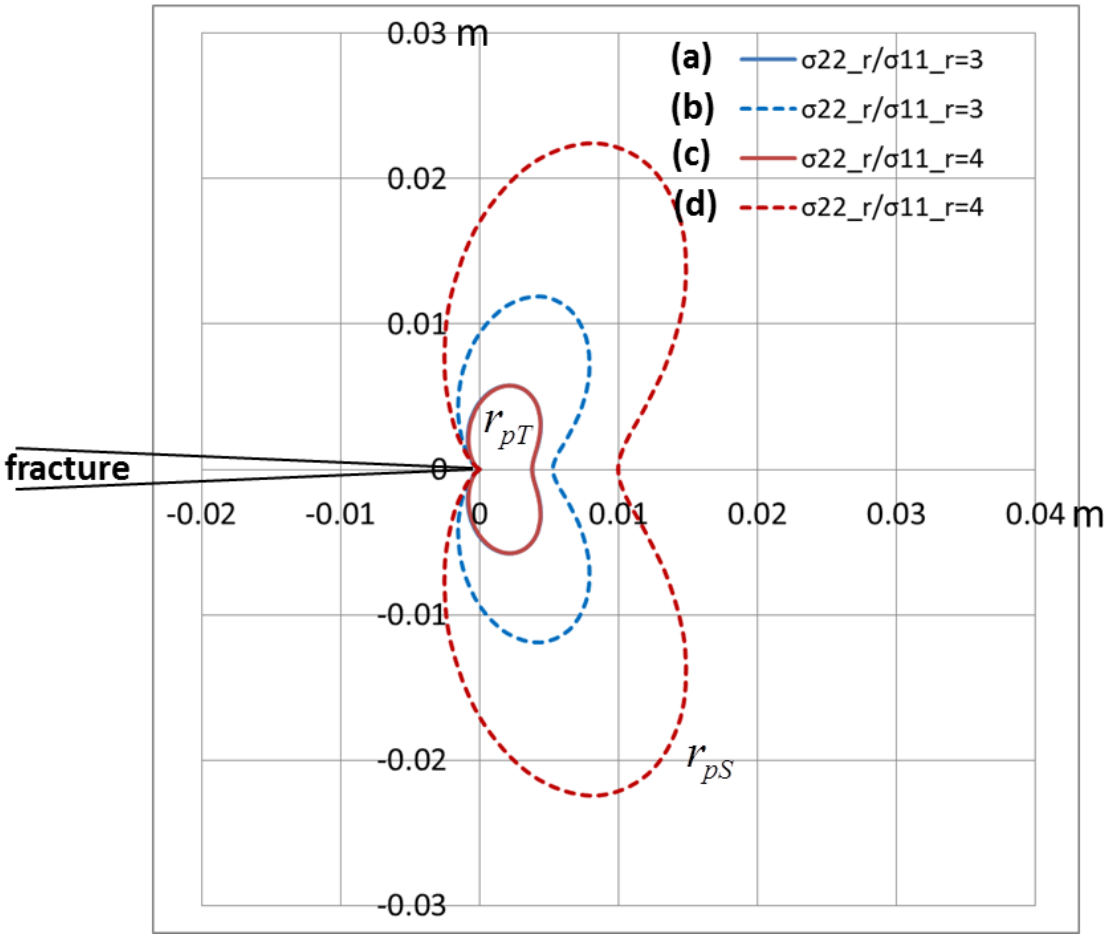

Figure 2.9. Fracture process zones of pressurized fractures ($\sigma_{11}^{\,c} = -5.5$ MPa ; $K_{\mathrm{I}} = 1\,\mathrm{MPa}\sqrt{\mathrm{m}}$, $K_{\mathrm{II}} = 0$) under various remote differential stresses: (a), (b) $\sigma_{22}^{\,r}/\sigma_{11}^{\,r} = 3$, and (c), (d) $\sigma_{22}^{\,r}/\sigma_{11}^{\,r} = 4$. The fracture process zone of (a) and (c) are defined by the tensile strength (solid lines), and (b) and (d) are defined by the shear strength (dashed lines). For all cases, $\sigma_{11}^{\,r}$ is kept constant at –0.5 MPa.

Many studies relate the process zone size to the crack initiation distance, r_c, which can be treated as a material-dependent characteristic length in the fracture propagation criterion (Williams and Ewing, 1972; Streit and Finnie, 1980; Chen et al., 1999; Pettit, 2000; Pettit et al., 2001; Ingraffea and Wawrzynek, 2003; Aliha et al., 2010; Aliha and Ayatollahi, 2011). In addition, Hoek and Bieniawski (1965) observed a sudden finite

crack increment, approximately 0.2 times the initial crack length, in glass specimens as the fracture propagated under uniaxial compression test, which supports the physical existence of the r_c.

For angled fractures under tension in PMMA, Williams and Ewing (1972) determined the critical r_c of PMMA to be 0.05 mm (0.002 inch) by matching the analytical solutions of the two-term approximation with the experimental results. They noted that the fracture length did not have a significant impact on the fracture propagation angle and utilized the value of 12.7 mm (0.5 inch) from four different fracture half-lengths (7.6, 12.7, 17.8, and 25.4 mm) for *a* in predictions. By using the photoelastic methods, Streit and Finnie (1980) estimated r_c for 7075-T651 aluminum to be 0.13 and 0.25 mm (0.005 or 0.01 inch) for side-grooved and un-grooved specimens, respectively. Most of the investigations on r_c have been performed on elastic-plastic materials, such as aluminum (Streit and Finnie, 1980; Kosai et al., 1992; Chen et al., 1999), by observing the onset of crack turning for mode I dynamic fractures under crack-parallel tensile stress.

For fractures in rocks, studies calculated r_c by simplifying the maximum principal stress model of Schmidt (1980) with the measured fracture toughness (K_{Ic}) and tensile strength of the rock (Aliha et al., 2010; Aliha and Ayatollahi, 2011). The simplified model describes the critical initiation distance as

$$r_c = \frac{1}{2\pi}\left(\frac{K_{Ic}}{\sigma_T}\right)^2. \tag{2.28}$$

For mode I fractures, r_c is analgous to r_p at $\theta = 0°$ from Equation (2.24) which is the minimum r_p ahead of the crack tip ($-90° \le \theta \le 90°$). This agrees with the discussion of Ingraffea and Wawrzynek (2003) that r_c should not be longer than the inelastic zone since it is related to some type of failure process. Based on this simplified model, Aliha et al. (2010) proposed an r_c of 2.3 mm (0.09 inch) for limestone and Aliha and Ayatollahi (2011) calculated an r_c of 3.05 mm (0.12 inch) for marble rock to correlate the fracture propagation trajectory in the Semi-Circular Bend (SCB) test with the mixed-mode experimental results.

Although Williams and Ewing (1972) noted that r_c does not depend on the fracture length for fractures under tensile loading, other studies on r_c (Streit and Finnie, 1980; Theocaris and Papadopoulos, 1982) developed empirical equations which depend on the fracture length, stress intensity factors, and the second term including the remote stress of the near-tip stress series. Thus, the angled fracture problem under compression is discussed in this study to evaluate the impact of crack length on r_c and to examine the applicability of the MMTPS-criterion.

2.6 ANGLED FRACTURE PROBLEM

Numerous studies have endeavored to verify adequate analytical criterion that agrees with experimental results from various fracture propagation experimental set-ups. One of the simplest methods to evaluate the mixed-mode fracture initiation angle and

load is the angled fracture test under uniaxial or biaxial loading (Erdogan an Sih, 1963; Cotterell, 1972; Williams and Ewing, 1972; Tirosh and Catz, 1981; Theocaris and Andrianopoulos, 1982; Vallejo, 1987; Wu and Li, 1989; Kong et al., 1995; Bobet and Einstein, 1998; Bobet, 2000; Wong and Einstein, 2006; Park and Bobet, 2010).

The case of a biaxially loaded fracture of length $2a$ inclined at an angle β clockwise to the direction of the exterior loading, ${\sigma_{yy}}^r$, is chosen to demonstrate mixed-mode fracture propagation (Figure 2.10a). By utilizing the two-dimensional coordinate transformation (Sadd, 2009), the resolved stress components on the fracture in the local X_1 - X_2 coordinate can be expressed with the directly applied boundary conditions of ${\sigma_{xx}}^r$ and ${\sigma_{yy}}^r$ from the global x - y coordinate as

$$\begin{aligned}
\sigma_{np} &= {\sigma_{xx}}^r \sin^2\beta + {\sigma_{yy}}^r \cos^2\beta = \left({\sigma_{xx}}^r - {\sigma_{yy}}^r\right)\sin^2\beta + {\sigma_{yy}}^r \\
\sigma_{nn} &= {\sigma_{xx}}^r \cos^2\beta + {\sigma_{yy}}^r \sin^2\beta = \left({\sigma_{xx}}^r - {\sigma_{yy}}^r\right)\cos^2\beta + {\sigma_{yy}}^r \\
\sigma_{nt} &= -\left({\sigma_{xx}}^r - {\sigma_{yy}}^r\right)\sin\beta\cos\beta
\end{aligned} \tag{2.29}$$

where σ_{np} is the crack-parallel normal stress, σ_{nn} is the crack-perpendicular normal stress, and σ_{nt} is the resolved shear stress on the crack (Figure 2.10b). Based on Equation (2.12) and (2.29), the SIFs for an angled fracture under biaxial tensile loading (Sih et al, 1962, Eftis and Subramonian, 1978) are

$$\begin{aligned}
K_{\mathrm{I}} &= \sqrt{\pi a}\Delta\sigma_{\mathrm{I}} = \sqrt{\pi a}\left(\sigma_{nn} - {\sigma_{11}}^c\right) = \sqrt{\pi a}\left[\left({\sigma_{xx}}^r - {\sigma_{yy}}^r\right)\cos^2\beta + {\sigma_{yy}}^r\right] \\
K_{\mathrm{II}} &= \sqrt{\pi a}\Delta\sigma_{\mathrm{II}} = \sqrt{\pi a}\left(\sigma_{nt} - {\sigma_{12}}^c\right) = \sqrt{\pi a}\left[-\left({\sigma_{xx}}^r - {\sigma_{yy}}^r\right)\sin\beta\cos\beta\right]
\end{aligned}. \tag{2.30}$$

The internal crack stresses (${\sigma_{11}}^c$ and ${\sigma_{12}}^c$) are zero for cracks under tensile loading.

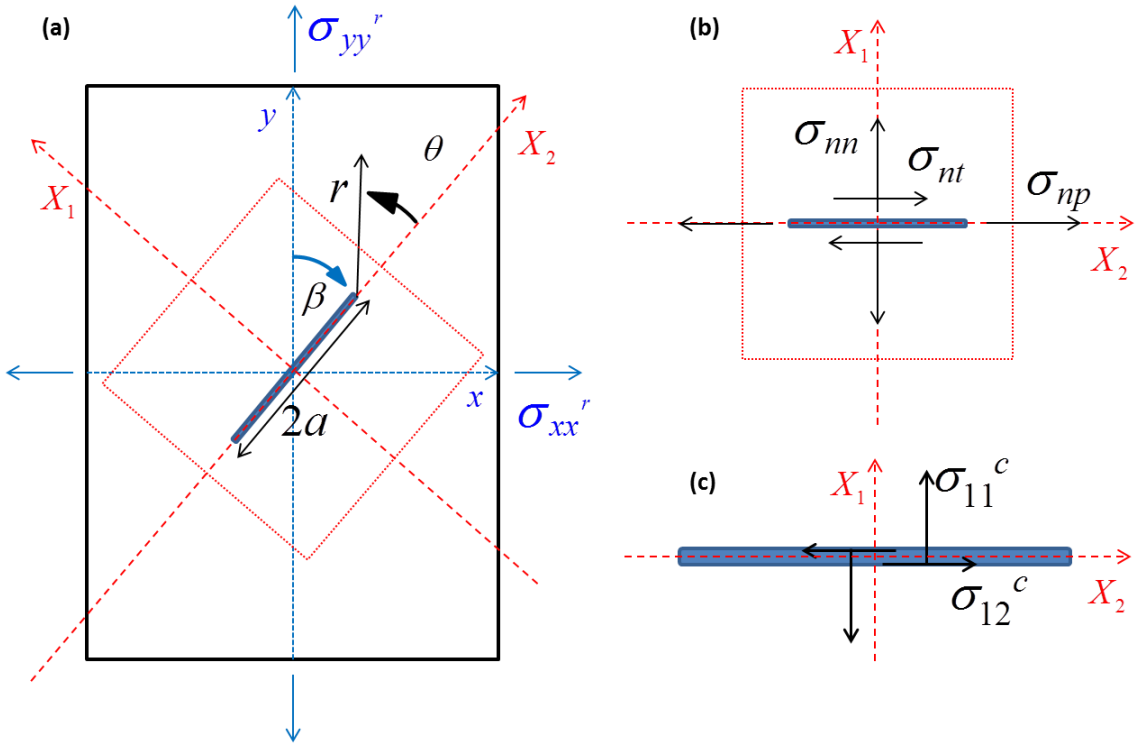

Figure 2.10. Schematic views of the angled fracture problem under biaxial tensile loading: (a) a fracture located in the plane parallel to the X_2-direction in the global x-y coordinate, (b) the resolved stresses on the crack, (c) the internal crack stresses of the crack. All stress components are positive as drawn.

Researchers have conducted experiments on the angled crack problem under tensile loading (Erdogan and Sih, 1963; Pook, 1971; Willams and Ewing, 1972; Ueda et al., 1977; Kong et al., 1995). Their results have been analyzed with various theoretical approaches (Finnie and Saith, 1973; Sih and Kipp, 1974; Theocaris and Andrianopoulos, 1982; Wu and Li, 1989; Khan and Khaisheh, 2000) to reduce the mismatch between the experimental results and the conventional mixed-mode fracture propagation criteria. The MMTPS-criterion can be evaluated by comparing its predictions of fracture propagation angles with the experimental results of Willams and Ewing (1972) and Pook (1971)

(Figure 2.11). With Equations (2.20) and (2.30), the prediction of the fracture propagation direction by the MMTPS-criterion can expressed as

$$\begin{aligned}
&\sigma_{\theta\theta P} \geq \sigma_T \\
&\sigma_{r\theta} = 0 = \cos\frac{\theta}{2}\left\{\begin{array}{l}\left[\left(\sigma_{xx}{}^{r} - \sigma_{yy}{}^{r}\right)\cos^2\beta + \sigma_{yy}{}^{r}\right]\sin\theta \\ \quad -\left[\left(\sigma_{xx}{}^{r} - \sigma_{yy}{}^{r}\right)\sin\beta\cos\beta\right]\left(3\cos\theta - 1\right)\end{array}\right\}. \\
&\qquad -\sqrt{\frac{2r_c}{a}}\left\{\left[-\left(\sigma_{xx}{}^{r} - \sigma_{yy}{}^{r}\right)\cos 2\beta\right]\sin 2\theta\right\}
\end{aligned} \tag{2.31}$$

The fracture propagation angle depends on the external loading, the fracture inclincation angle, and the ratio of r_c / a . By matching the analytical predictions with the experimental results, r_c can be determined since all other paramters are known from the experiment set-up.

The predictions of the MMTPS-criterion agree with the experiment results for all inclination angles from $0°$ to $90°$, when r_c / a are 0.01 for the results of Willams and Ewing (1972) and 0.1 for Pook (1971). As r_c / a approaches zero, the MMTPS-criterion converges to the conventional MTS-criterion for inclination angles above $10°$ overestimating propagation angles for crack angles above $45°$ and underestimating them for angles below $45°$.

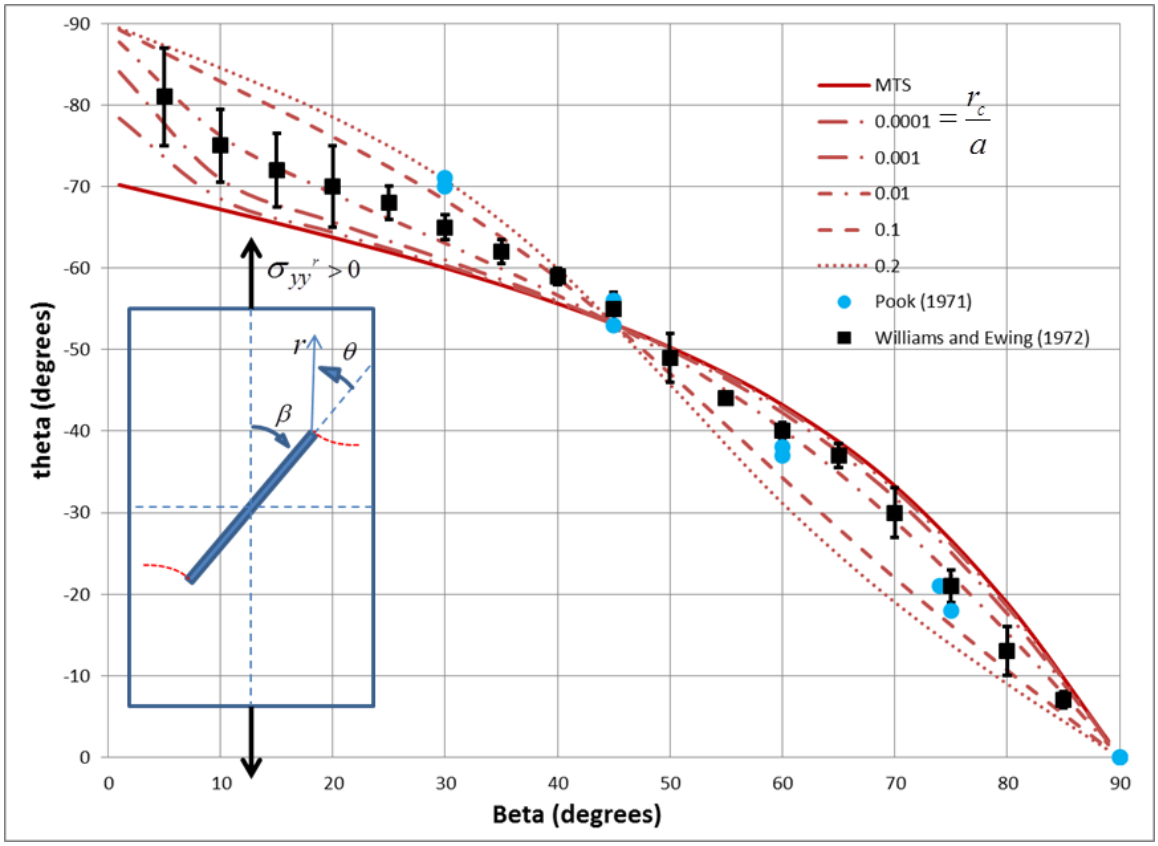

Figure 2.11. The predictions of the fracture propagation angles (θ) by the MMTPS-criterion (dashed lines), with various r/a values ranging from 0.0001 to 0.2, with the prediction of the conventional MTS-criterion (solid line) and experimental results.

The prediction curves from the MMTPS-criterion and the MTPS-criterion converge as r_c/a become smaller (below 0.1), and both of the predictions, when r_c/a are 0.1, agree well with the experiment results of Williams and Ewing (1972) (Figure 2.12). However, the distinction between the predictions of the MMTPS-criterion and the MTPS-criterion can be observed when r_c/a is 0.1, and the experimental results of Pook (1971) matches better with the MMTPS-criterion compared to the MTPS-criterion. In fact, all curves from the MTPS-criterion converge around β of 38° and θ of 57°, whereas the

predictions of the MMTPS-criterion converge at β of 45° and θ of 53°. Overall, the MMTPS-criterion works well for predicting fracture propagation angles of fractures under tensile loading.

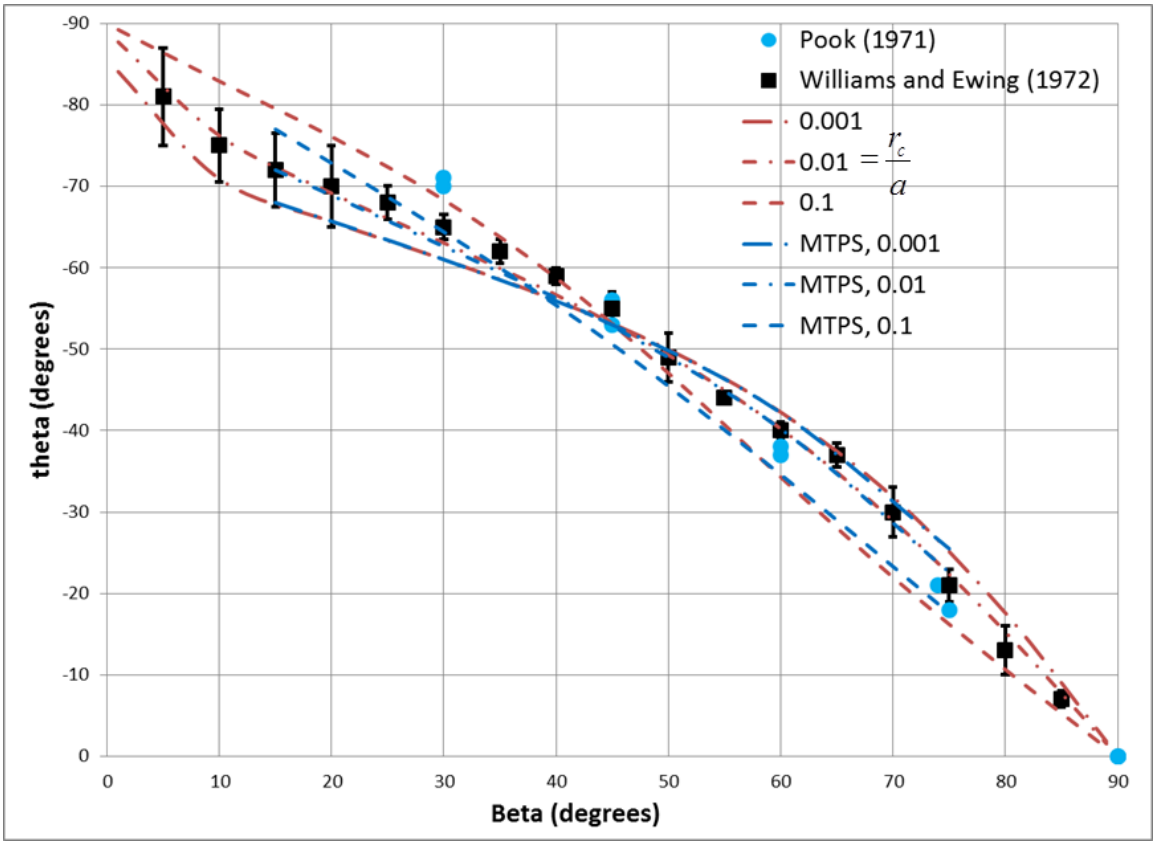

Figure 2.12. The predictions of the fracture propagation angles (θ) by the MMTPS-criterion (red lines) and the MTPS-criterion (blue lines), for r/a values of 0.001, 0.01, and 0.1, with experimental results.

Under subsurface conditions, fractures experience compressive normal stress which complicates propagation when compared to fractures under tension (Ingraffea and Heuze, 1980). The crack-perpendicular compressive stress forces fracture walls to close for initially open cracks and it generates friction beween fracture walls for closed cracks. Experimental and theoretical studies on the angled fracture under compression have

mostly focused on open cracks (Brace and Bombolakis, 1963; Cotterell, 1972; Tirosh and Catz, 1981; Vallejo, 1987; Wu and Li, 1989; Reyes, 1991; Shen et al., 1995; Wong and Einstein, 2006). The overall trend of the experimental results from previous studies for open fractures indicate that the fracture propagation angle increases as the inclination angle increases, implying that the fracture does not propagate as pure mode II behavior of the MTS-criterion. To explain this response, researchers have introduced various theoretical approaches, such as maximum tangential stress around an elliptical crack (Hoek and Bieniawski, 1965; Lajtai, 1970; Tirosh and Catz, 1981), rather than utilizing the criterion developed for angled fractures under tension with SIFs. In general, the assumption of K_{I} being negative was not a common approach to solving the problem of open cracks under compression. Without this assumption the MTS-criterion does not agree with the trend of experimental results (Figure 2.13).

Bobet (1997) visualized fracture closure under compression with a light source passing through the fracture and asserted that fracture closure coincided with fracture propagation. As the exterior compressive load increased, the aperture of the fracture reduced, though the fracture stayed open before the propagation. If the fracture is initially open and stays open before the propagation, the internal crack stresses are zero and the SIFs from Equation (2.30) are valid. Since ${\sigma_{xx}}^r$ and ${\sigma_{YY}}^r$ are negative (compressive stress), K_{I} is always negative based on Equation (2.30), which can be written as

$$K_{\mathrm{I}} = \sqrt{\pi a}\left[{\sigma_{xx}}^r \cos^2\beta + {\sigma_{yy}}^r \sin^2\beta \right] < 0 . \tag{2.32}$$

Although the external loadings are compressive and K_I is negative, there still exists tensile stress concentration in the vicinity of a fracture tip due to K_{II} which drives the fracture to propagate at sharp angles from the initial crack plane rather than the coplanar fracture growth (Brace and Bombolakis, 1963; Hoek and Bieniawski, 1965; Nemat-Nasser and Horii, 1982). Studies have utilized negative K_I in the MTS-criterion (Tirosh and Catz, 1981; Theocaris and Sakellariou, 1990; Maji et al., 1991; Khan and Khraisheh, 2000) which aligns more closely to the trend of the experimental outcome but is not an exact agreement (Figure 2.13).

The MMTPS-criterion improves the correlation with the experimental results and matches well for prediction curves of r_c / a from 0.1 to 0.2 (Figure 2.13). Although the predictions require some modification in K_I since generating sharp fractures in a material is quite difficult and artificially created open fractures tend to have a blunt tip. The bluntness of the fracture tip diminishes the stress singularity and changes the near-tip stress trajectory, which differs from the sharp practical fracture tip. There is still some controversy as to how to deal with the impact of the fracture shape on the theoretical approach. Some researchers have selected the elliptical fracture approach (Cotterell, 1972; Wu and Chang, 1978; Chang and Wu, 1980; Tirosh and Catz, 1981) while others have selected the mixed-mode fracture propagation criterion with modifications in the SIFs (Tirosh and Catz, 1981) for slot cracks. In this study, the slot crack geometry is selected for experiments of angled open fractures under compressive loading since it is applicable in evaluating the MMTPS-criterion with modified K_I . Furthermore, Brace and

Bombolkis (1963) asserted that the sharpness of the slot crack tip does not significantly alter the direction of crack extension in the vicinity of a slot tip.

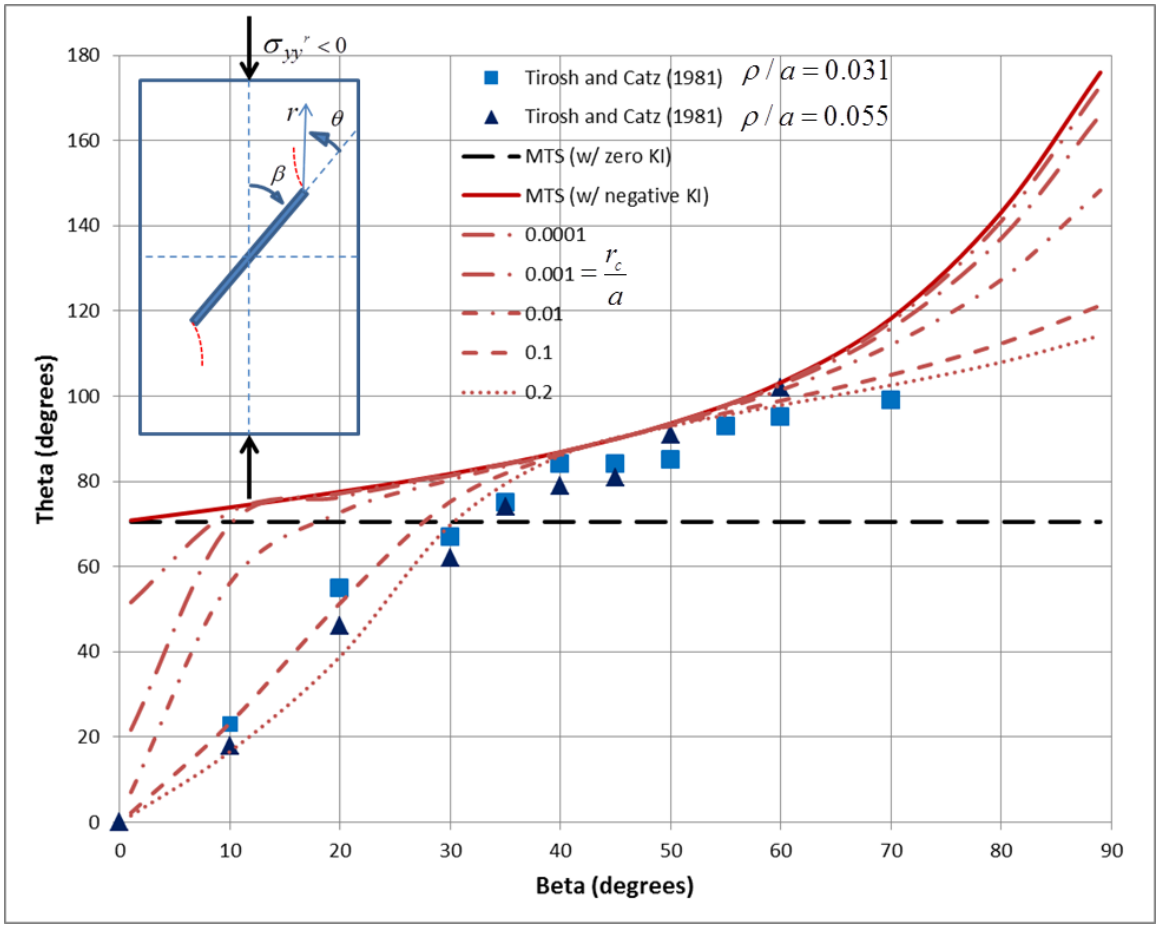

Figure 2.13. The predictions of the fracture propagation angles (θ) with respect to the fracture inclination angles (β) for angled open fractures under uniaxial compressive loading by the MTS-criterion (with zero K_I and negative K_I) and the MMTPS-criterion (with negative K_I; red dashed-lines). Predictions are compared with experimental results of Tirosh and Catz (1981). Two data sets of the Tirosh and Catz (1981) reflect results of different fracture tip curvature radius to fracture half-length ratio (ρ / a) which is discussed in Figure 2.15.

To consider the influence of the crack-parallel compressive stress on the SIF, Tirosh and Catz (1981) introduced the modified K_I for a slot crack with tip radius of curvature (ρ) as

$$\begin{aligned} K_I &= \sqrt{\pi a}\left(\sigma_{nn} - \frac{1}{2}\sqrt{\frac{\rho}{a}}\sigma_{np}\right) \\ &= \sqrt{\pi a}\left\{\left(\sigma_{xx}{}^{r} - \sigma_{yy}{}^{r}\right)\cos^2\beta + \sigma_{yy}{}^{r} - \frac{1}{2}\sqrt{\frac{\rho}{a}}\left[\sigma_{xx}{}^{r} - \left(\sigma_{xx}{}^{r} - \sigma_{yy}{}^{r}\right)\cos^2\beta\right]\right\}. \\ &= \sqrt{\pi a}\left[\left\{\left(\sigma_{xx}{}^{r} - \sigma_{yy}{}^{r}\right)\cos^2\beta\right\}\left(1 + \frac{1}{2}\sqrt{\frac{\rho}{a}}\right) + \sigma_{yy}{}^{r} - \frac{1}{2}\sqrt{\frac{\rho}{a}}\sigma_{xx}{}^{r}\right] \end{aligned} \quad (2.33)$$

This is similar to K_I in Equation (2.30) but has an additional term including the effect of the crack-parallel compressive stress which generates the opening mode and reduces the magnitude of negative K_I. The impact of the crack-parallel compressive stress is emphasized for slots with greater ρ.

Based on this modification, the predictions of the fracture propagation angle by the MMTPS-criterion show that the bluntness of the fracture tip have greater impact when the inclination angles (β) are below 45° (Figure 2.14). The fracture propagation angle (θ) is lower for fractures with greater fracture tip curvature radius (ρ). However, as β increases, the sharpness degree of the fracture tip becomes unimportant, and the prediction converges to the analytical solution of the sharp crack. This is because the crack-parallel compressive stress, which resolves tensile stress at the slot tip, is diminished as the slot becomes more perpendicular to the plane of uniaxial compressive loading.

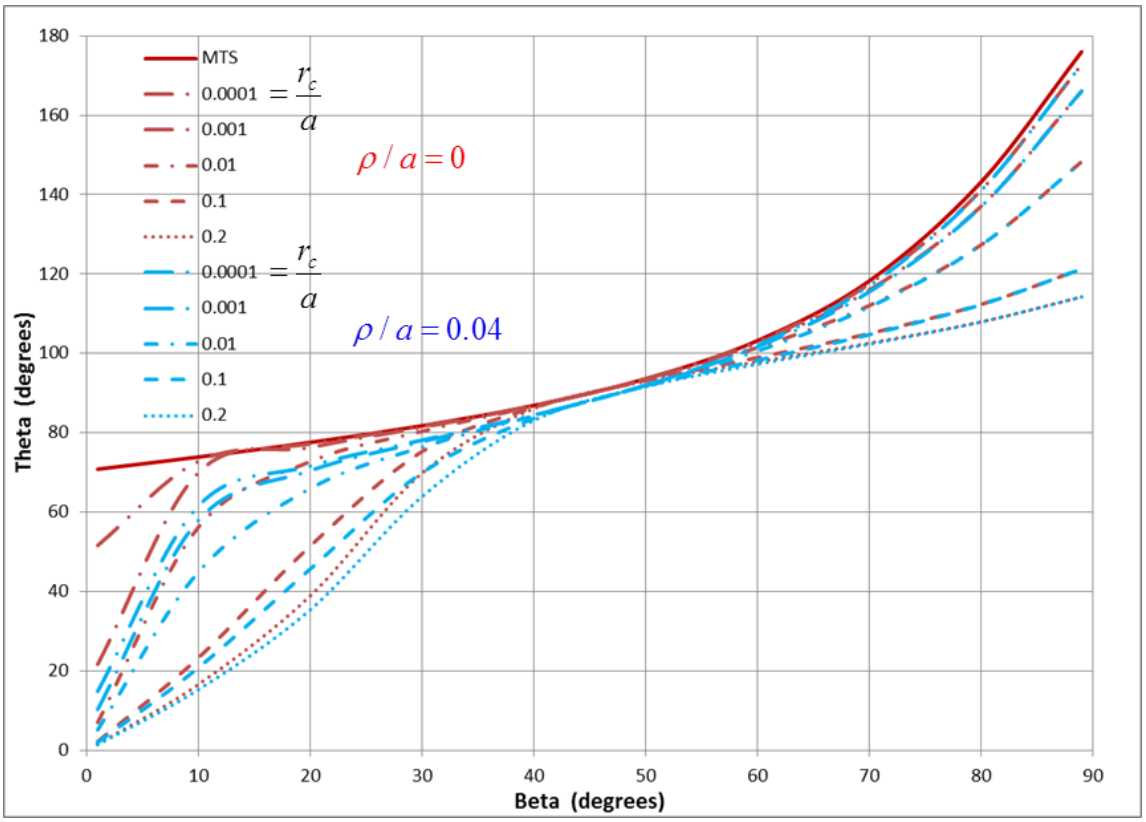

Figure 2.14. The predictions of the fracture propagation angles (θ) with respect to the fracture inclination angles (β) by the MMTPS-criterion with (blue-dashed lines) and without (red-dashed lines) the modified mode I stress intensity factor (K_I) from Equation (2.33). The fracture tip curvature radius to the fracture half-length ratio (ρ/a) for the modification is 0.04.

Figure 2.15 shows the prediction of the MMTPS-criterion with modified K_I and the experimental results of Tirosh and Catz (1981) with two different ρ/a values. The experimental results for $\rho/a = 0.031$ (Figure 2.15a) follow the prediction trend between r_c/a value of 0.01 and 0.1, and the $\rho/a = 0.055$ case (Figure 2.15b) is close to the prediction with r_c/a of 0.1.

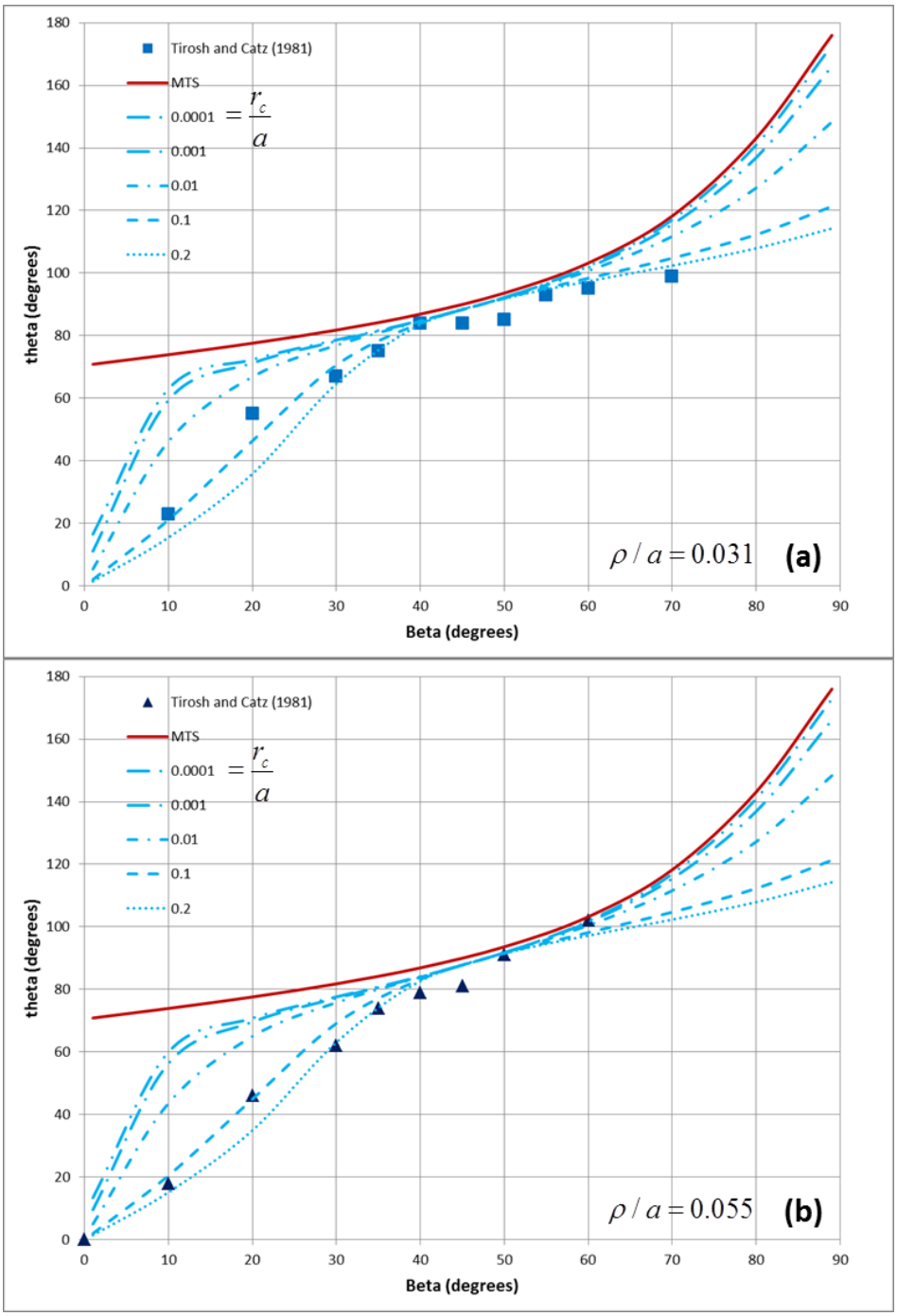

Figure 2.15. The predictions of the fracture propagation angles (θ) with respect to the fracture inclination angles (β) by the MMTPS-criterion with the modified K_I and PMMA experimental results from Tirosh and Catz (1981). The fracture tip curvature radius to the fracture half-length ratios (ρ / a) are (a) 0.031 and (b) 0.055, respectively.

2.7 EXPERIMENTAL SET-UP

Petit and Barquins (1988) discussed the difference in the fracturing processes under compression in sandstone and in PMMA. In sandstone, the primary crack—referred to in some studies as wing fractures (Reyes and Einstein, 1991; Reyes, 1991; Bobet, 2000)—develops better in low-porosity rocks than in high-porosity rocks. The primary fracture path is roughly curvilinear and closes after unloading. High-porosity rocks, in addition, have a greater fracture propagation angle under the same conditions than low-porosity rocks (Figure 2.16). On the other hand, for PMMA, the primary wing fracture is always present and well developed. The fracture path reflects curvilinear geometry, and remains partially open after unloading. In addition, Ingraffea and Heuze (1980) performed uniaxial compression tests on limestone and granodiorite samples with angled fractures, pointing out that, after primary wing cracks develop, the secondary cracks propagate in a stable manner (see Figure 2.17). These secondary shear cracks are not observed in experiments of PMMA under compression but develop in rocks.

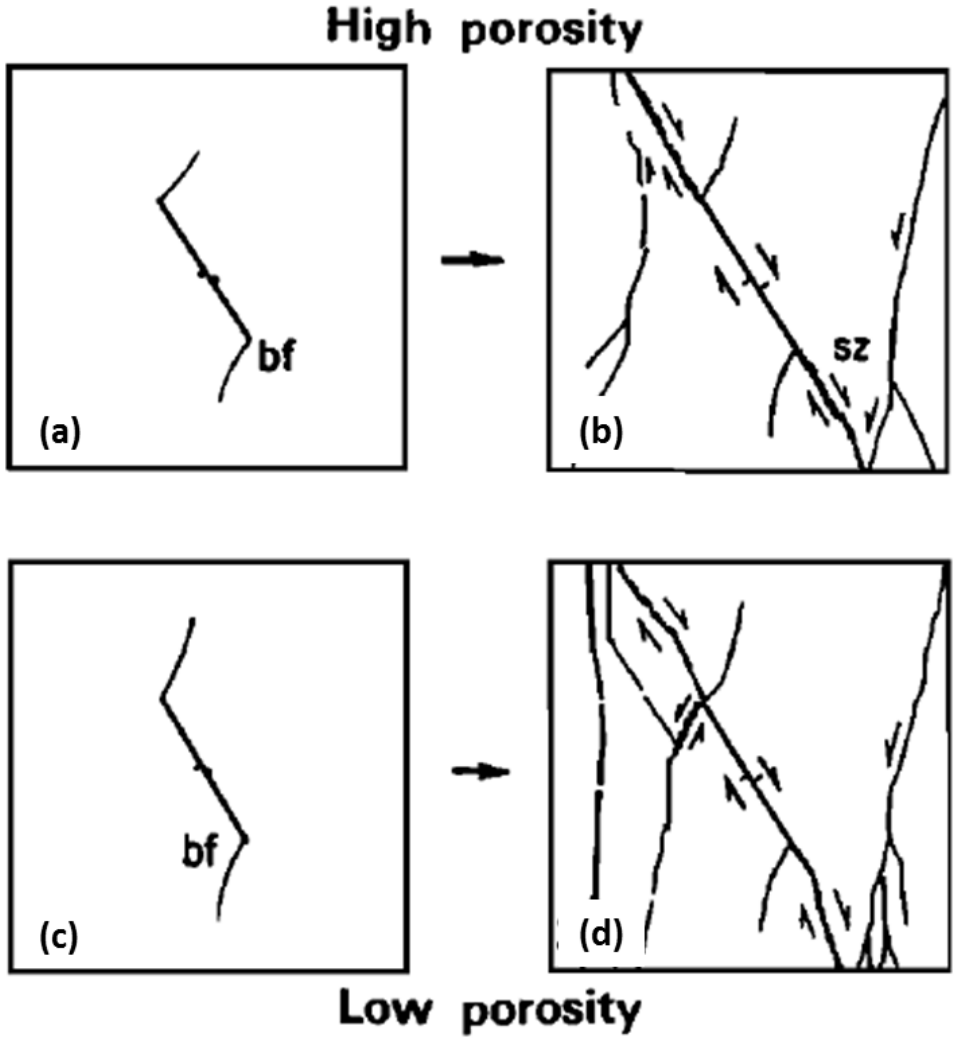

Figure 2.16. Porosity dependence on fracture propagation and the failure of a rock. (a), (c) shows the primary wing fracture propagation before the maximum stress and (b), (d) illustrates secondary fractures and shear failure after the maximum stress (Petit and Barquins, 1988).

Some studies have examined the angled fracture problem on rocks (Ingraffea and Heuze, 1980; Petit and Barquins, 1988; Huang et al., 1990), gypsum-based materials (Lajtai, 1970; Lajtai and Lajtai, 1974; Bobet, 2000; Wong and Einstein, 2006; Park and Bobet, 2010), and other cement molds (Vallejo, 1987; Wu and Li, 1989). However, previous experimental studies on rock-like materials under compressive loading have

concentrated solely on the effect of the fracture inclination angle on the fracture propagation angle without varying the fracture length limiting them to an evaluation of the influence of fracture length on r_c . Consequently, to estimate the material characteristic r_c of a rock-like material, uniaxial compression tests on hydrostone samples with angled fractures of three different lengths were performed.

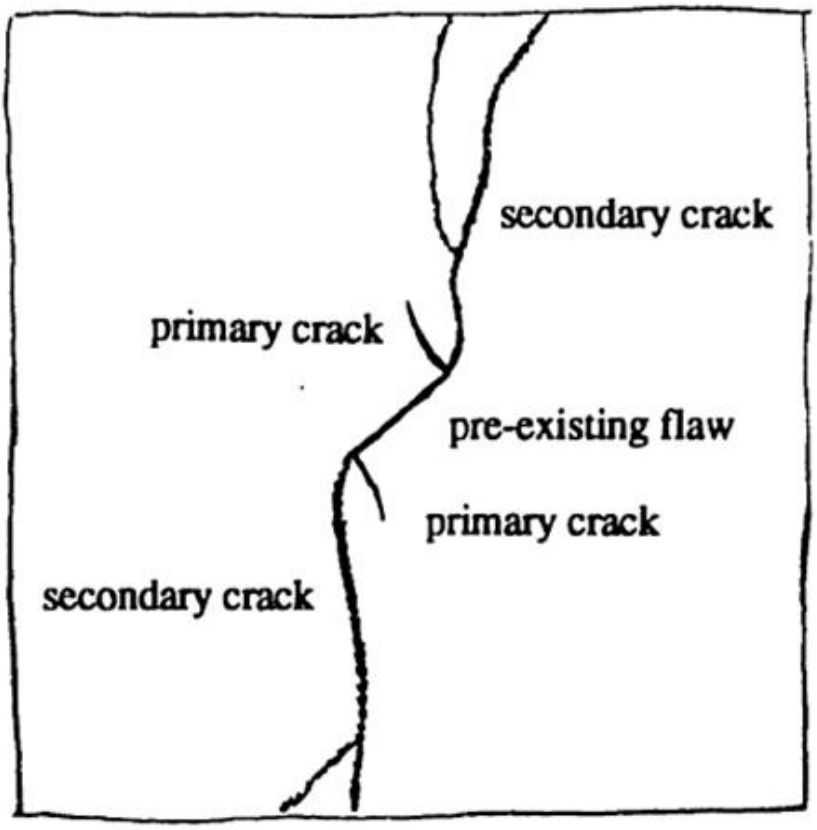

Figure 2.17. The sequence of fracture growth for an angled fracture in a limestone sample under uniaxial compression loading (Ingraffea and Heuze, 1980).

The selection of hydrostone (a type of gypsum cement) as a rock simulant for this study is recommended by the similarity in the fracturing process to rocks and possessing the mechanical properties of rocks. Since it is brittle and relatively weak, hydrostone is

useful. Moreover, it is easy to manufacture and amenable to generating open fractures. These attractive features led studies to utilize hydrostone or cement in rock-strength measurements (Bahorich, 2012; Wang et al., 2013) and scaled block hydraulic fracturing experiments (Zhou et al., 2008; Bahorich et al., 2012; Olson et al., 2012).

Hydrostone is a mixture of gypsum and Portland cement produced by United States Gypsum Company (IG-123-F1-50BAG/6-99). Its mechanical properties are listed in Table 2.1.

Table 2.1. Hydrostone mechanical properties

Material	Dry Compressive Strength (from product data) (MPa)	Tensile Strength (from Bahorich, 2012) (MPa)
Hydrostone	70 (10,000 psi)	4.8 (700 psi)

The procedure for casting hydrostone specimens was as follows (Figure 2.18):

1. Ten 76-mm (3-inch) tall aluminum molds that are 38 mm (1.5 inches) wide and deep were prepared to mold rectangular parallel-piped samples from low-viscous slurry hydrostone. Tick marks were made on the sides of the molds to enable approximate alignment of the steel shims being inserted at various inclination angles. Brass shims of 0.76 mm (0.03 inch) thickness and 50.8 mm (2 inches) long and of various widths (12.7, 19, 25.4 mm) were prepared to create open fractures in the hydrostone specimens while they were curing. The thickness of the shim represented the aperture of the open fracture and the various widths were to examine the fracture length effect. The shims were long

enough (50.8 mm) to extend from the front to the rear face of the sample. The shims were covered with silicon spray lubricant in order to remove them from the hydrostone after setting.

2. Hydrostone powder was mixed mechanically with water (Table 2.2) for approximately two minutes to generate a liquefied hydrostone slurry. After the mixing, the slurry was poured into the prepared molds. By shaking the molds during and after the pouring, air bubbles were removed to generate a homogeneous sample.

Table 2.2. Hydrostone gypsum cement to water weight ratio (Bahorich et al., 2012)

Material	Dry Cement Weight (%)	Water Weight (%)
Hydrostone	75.7	24.3

3. Brass shims were inserted into the liquefied hydrostone to create open fractures (slot crack) in various inclination angles. Insertions were carried out within five minutes of pouring of the hydrostone, before curing and hardening. After the hydrostone had set, shims were pulled out of the hydrostone, approximately 15 minutes after having been inserted. If left longer, the shims were difficult to remove.
4. Hydrostone samples were left in the molds for three days. The molds were dismantled for hydrostone samples to dry out completely at room temperature for additional four days. When the hydrostone samples were completely dried,

the specimens were ground on their fronts and backs to generate a flat surface that would enable a better observation of the fracture growth.

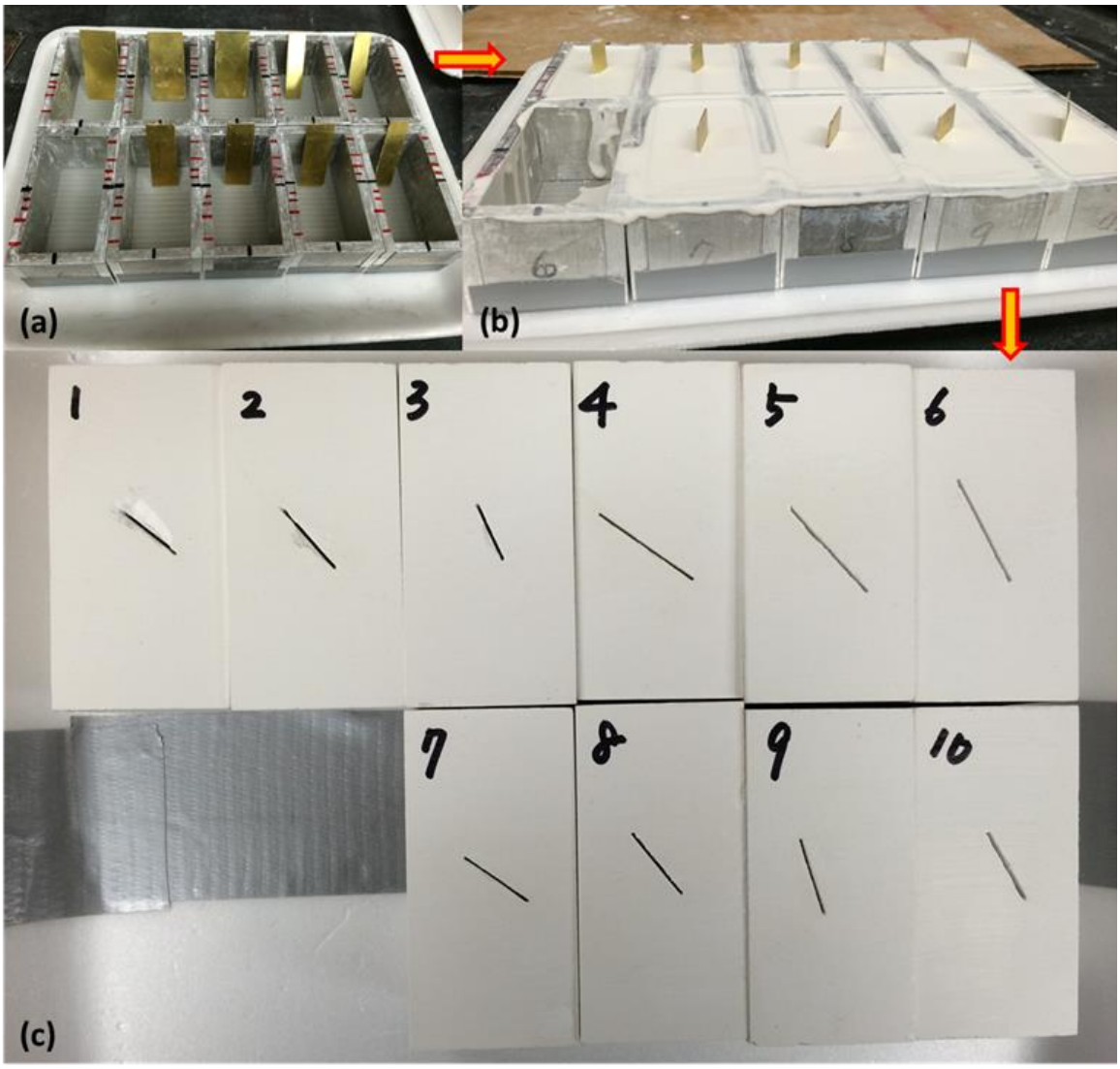

Figure 2.18. The procedure of preparing hydrostone specimens with open fractures for the uniaxial compression test: (a) the molds with tick marks and shims prepared before hydrostone pouring, (b) the liquefied hydrostone poured into the molds with shims inserted in various inclination angles, and (c) hydrostone samples ready for the uniaxial compression test.

Samples were measured for size, fracture inclination angle, thickness and lengths of shims with a digital protractor, caliper, and ruler. The hydrostone samples were loaded with a 10,000-lb Humboldt loading machine at a convergence rate of 4.23×10^{-6} m/s (0.01 in/min) until the fracture propagated from the open slot tip. A Linear Voltage Displacement Transducer (LVDT) measured the displacement of the sample in the axial loading direction while loading.

All samples reflected at least one primary wing fracture propagation, at either the top or the bottom of the slot, before the total failure of the sample. The initial open slot stayed open during the loading and unloading which made the interpretation of the negative K_1 valid for the application of the MMTPS-criterion. Whenever the primary wing fracture was observed, the loading machine was stopped and the fracture path was marked with the red marker. This was done prior to the sample being unloaded since it was difficult to visualize the induced fracture after fracture closure. The hydrostone absorbed red ink when the fracture was open, which, after the loading, left a darker mark on the propagated wing fracture path (see Figure 2.19).

The angle between the initial open slot and the tangent of the first increment of the primary wing fracture from the initial slot tip was measured accurately with a digital protractor. Frature propagation angles from both the front and rear sides of the sample were measured. Only the primary wing fractures propagating from the tip of the initial slot was analyzed in the results. Samples with fractures propagating at a distance from the fracture tip were discarded.

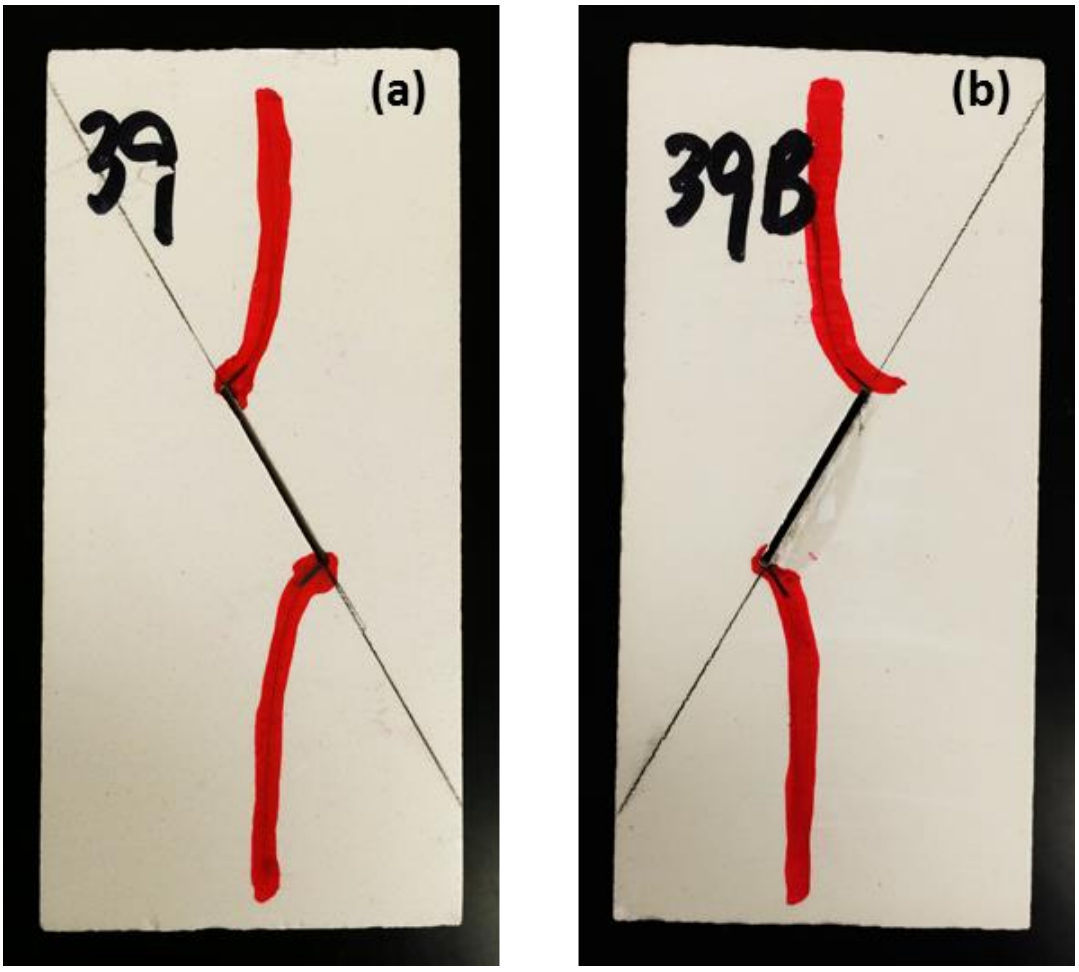

Figure 2.19. A hydrostone sample after unloading with primary wing fractures traced with the red marker. The tangent of the initial increments and the fracture inclination plane were marked with a pencil for the measurement of the propagation angle. (a) is the front view of the sample and (b) is the rear view of the same sample.

2.8 OPEN FRACTURES UNDER COMPRESSION IN HYDROSTONE

This study examined a total of 31 samples with open slot fractures of various fracture lengths (9 samples of 12.7-mm (0.5-inch), 11 samples of 19-mm (0.75-inch), and 11 samples of 25.4-mm (1.0-inch) open fracture length). The results are illustrated in Figure 2.21 with the analytical predictions of the fracture propagation angle from the

MMTPS-criterion. Based on Equation (2.28) and the values of $K_{Ic} = 0.28\ \text{MPa}\sqrt{\text{m}}$ and $\sigma_T = 4.83\ \text{MPa}$ for hydrostone (Bahorich et al., 2012), r_c was calculated to be 0.53 mm (0.021 inch). The slot tip curvature radius of the open-slot fracture was assumed to be 3.8 mm (0.15 inch), half of the aperture, for K_I calculation.

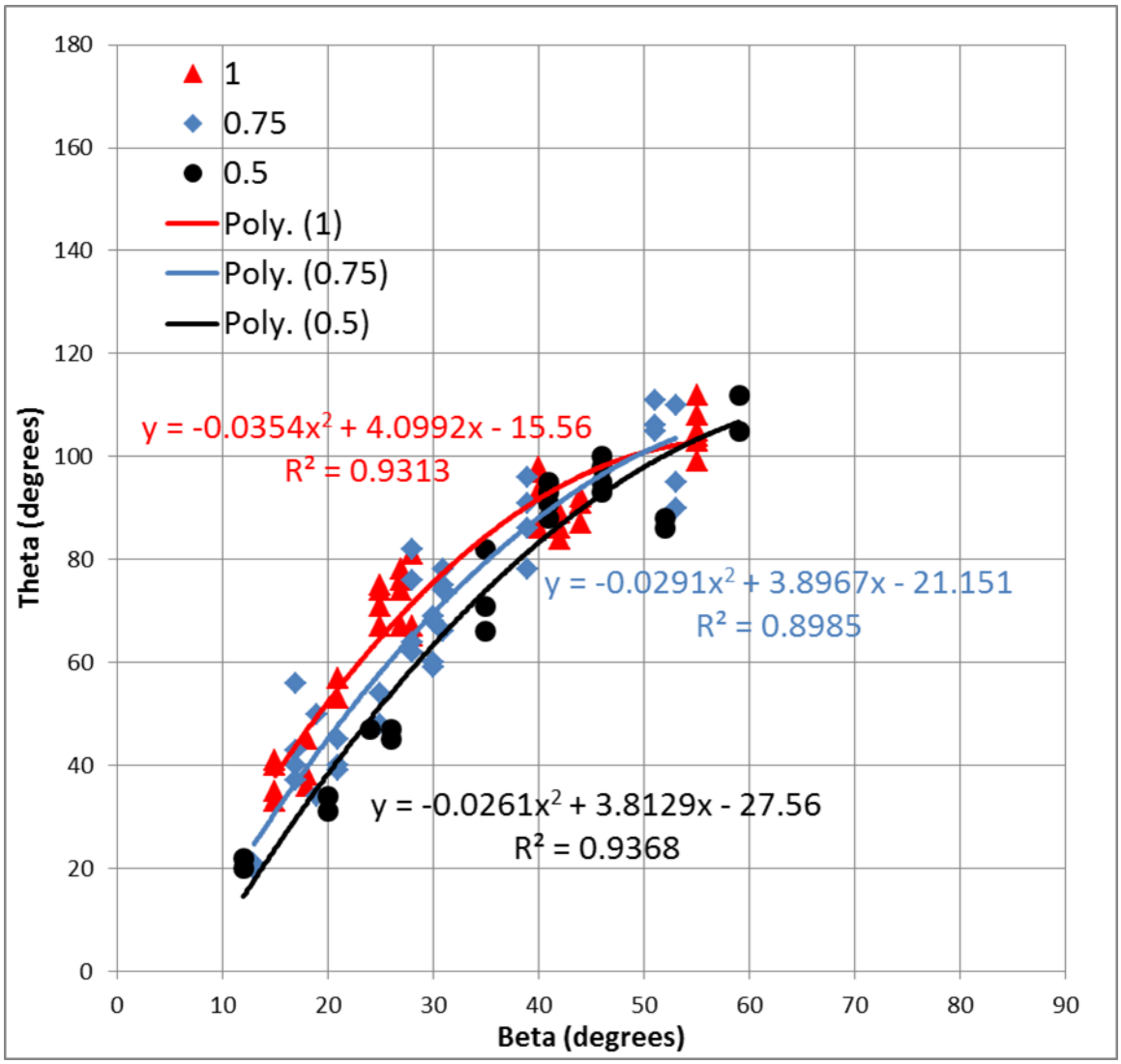

Figure 2.20. Experimental results of hydrostone samples with three fracture lengths (0.5 inch–black, 0.75 inch–blue, and 1.0 inch–red markers) and their best fit curves.

Regardless of the experimental scatter, the results show a set of fracture propagation angles that are lower than the prediction of the MTS-criterion for low β angles ($\beta < 45°$) (Figure 2.21). The angle θ increases with β, which agrees with the experimental results from Tirosh and Catz (1981) (Figure 2.13). For high β angles ($\beta > 45°$), some experimental results are greater than the prediction of the MTS-criterion. None of the cracks of β above $60°$ propagated from the tip and are not marked in Figure 2.13. An interesting outcome of this experiment is that the longest fractures of 25.4-mm (1.0-inch) have higher θ angles when compared to the shortest (12.7-mm (0.5-inch)) fractures for $\beta < 45°$. The θ angles of 19-mm (0.75-inch) fractures have the largest scatter (R^2 below 0.9) compared to the other two cases which does not provide reliable results, however, the other two cases (R^2 greater than 0.93) indicate a positive correlation between the fracture length and the theta (Figure 2.20).

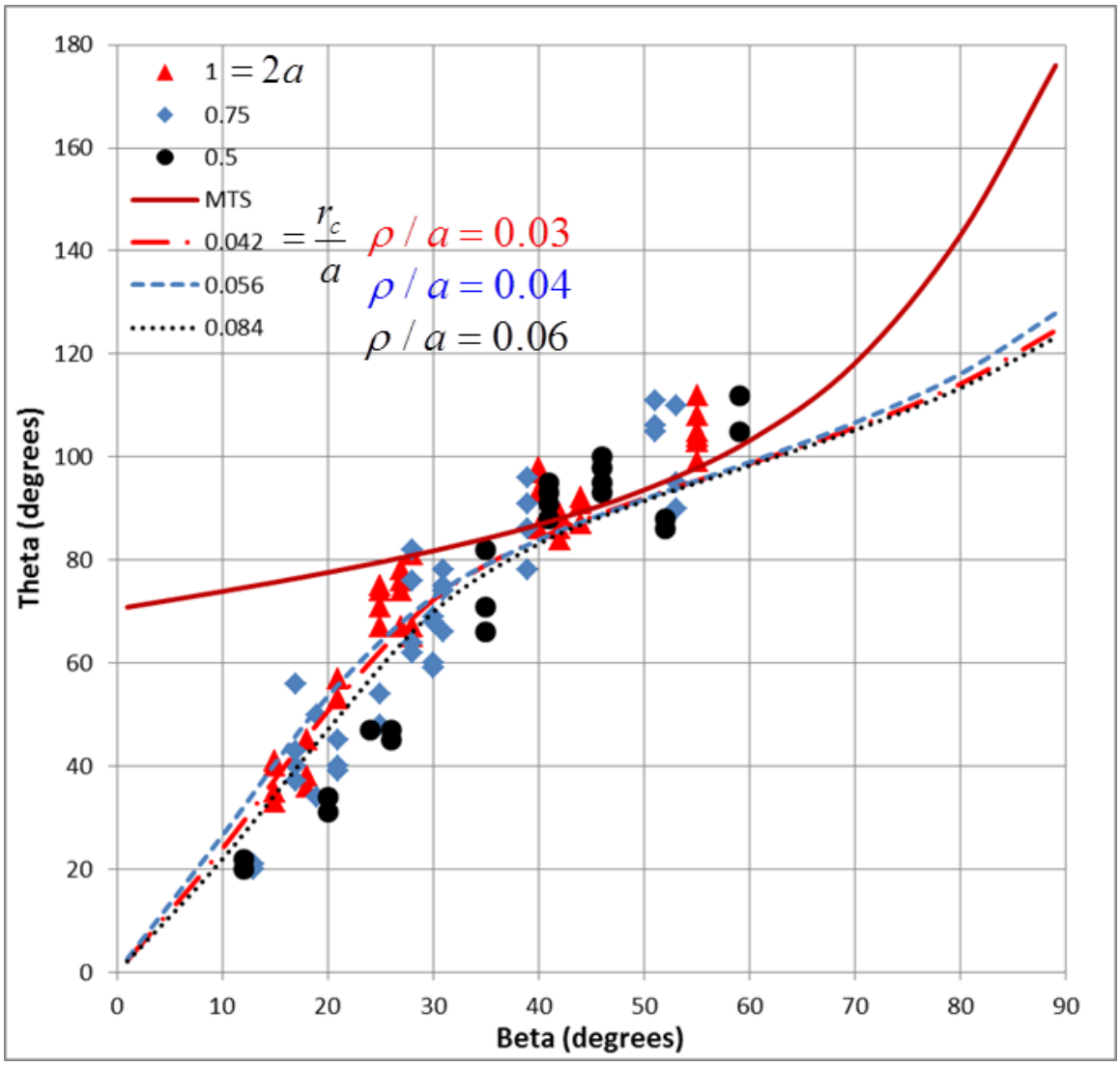

Figure 2.21. Experimental results of hydrostone samples with three fracture lengths (0.5 inch–black, 0.75 inch–blue, and 1.0 inch–red markers) and the predictions of the MMTPS-criterion with three r_c / a ratios (0.084–black, 0.056–blue, and 0.042–red-dashed lines, respectively). The ρ / a values were different for each case since the fracture half-length varied.

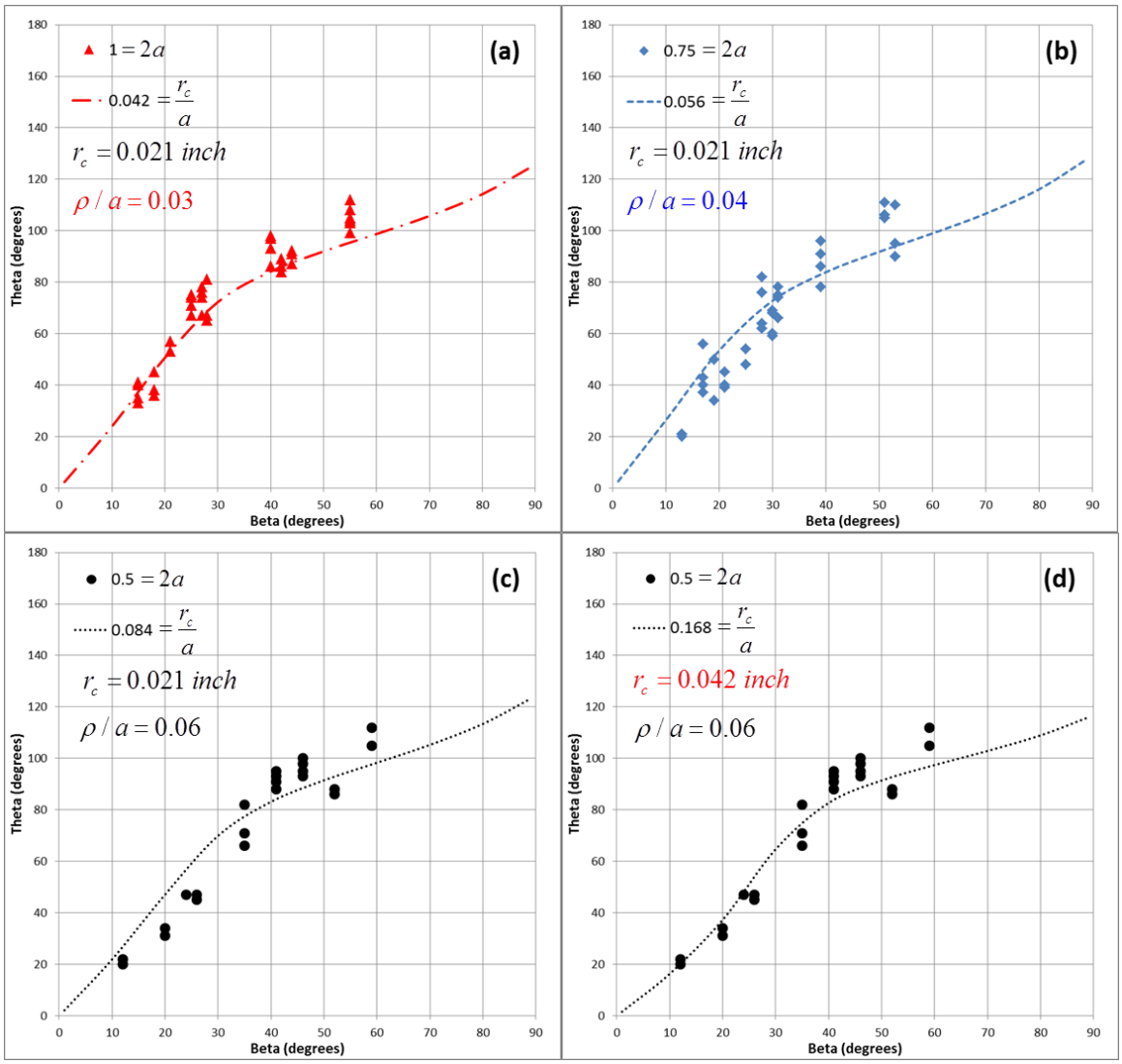

Figure 2.22. The predictions by the MMTPS-criterion and experimental results of hydrostone samples with three fracture lengths: (a) 25.4-mm (1.0-inch) fractures, (b) 19-mm (0.75-inch) fractures, (c) and (d) 12.7-mm (0.5-inch) fractures. The predictions of (a), (b), (c) are based on r_c of 0.53 mm (0.021 inch) and (d) is based on r_c of 1.07 mm (0.042 inch).

Assuming that all three fractures of different lengths have the same r_c and ρ, the predictions of the MMTPS-criterion are shown in Figure 2.21. The three predictions, though different, are close to each other, and lie within the experimental scatter. The

prediction agrees well with the experimental results of 25.4-mm (1.0-inch) open fractures (Figure 2.22a). Although the experimental scatter is large for 19-mm (0.75-inch) fractures, the prediction passes through the scatter and seems to match with the experiment results (Figure 2.22b). However, the prediction of 12.7-mm (0.5-inch) fractures overestimates the fracture propagation angle for fractures of $\beta < 45°$ (Figure 2.22c). If r_c is assumed to be 1.07 mm (0.042 inch)—twice the calculated r_c of 0.53 mm (0.021 inch)—the prediction of the MMTPS-criterion agrees better with the experiment results of the 12.7-mm (0.5-inch) fractures (Figure 2.22d).

2.9 CLOSED FRACTURES UNDER COMPRESSION

Some natural fractures, such as faults, are closed and act as frictional interfaces in the subsurface. The fracture processes of the closed crack are similar to the open crack under compression generating tensile wing fractures and secondary shear fractures from the tip of the crack (Park and Bobet, 2010). However, the frictional interfaces are not allowed to close and the negative K_I, which helped improve path predictions for open fractures in the MMTPS method, can no longer be employed. In addition, the internal crack stresses are non-zero, and the friction coefficient of the interface becomes important in predicting the kink angles of the tensile wing fractures.

Most of the other modified MTS-criterion for mixed-mode fractures generally neglected the crack-perpendicular normal stress, σ_{nn}, and only included the crack-parallel normal stress, σ_{np}, on fracture path prediction (Eftis et al., 1977; Wong, 1987;

Khan and Khaisheh, 2000; Smith et al., 2000). Li et al. (2009), on the other hand, emphasized the importance of the crack-perpendicular compressive stress which generated friction between the fracture walls for closed fractures under compression. They included the terms of crack-perpendicular stress and frictional stress in the GMTS-criterion in order to analyze the fracture propagation angle. However, their sign convention of the frictional stress ($\sigma_{12}{}^{c}$) in the stress components is the opposite of that used in this study, generating different results. This element is discussed carefully in this section.

For fractures that are initially closed and remain closed during loading, it is applicable to set K_{I} value to zero since the crack-perpendicular compressive stress (σ_{nn}) is transferred through the crack (Bobet, 2000) and the internal crack stress ($\sigma_{11}{}^{c}$) is equal to σ_{nn}. However, the resolved shear stress on the crack is constrained by the shear strength of the crack (Bobet, 2000), and the expression of K_{II} changes to account for the friction ($\sigma_{12}{}^{c}$) between the crack walls. This friction acts against the resolved shear stress (σ_{nt}) when the mode II driving stress is sufficient. Because of the fact that $\sigma_{12}{}^{c}$ is always against σ_{nt} and σ_{nn} is always negative for closed cracks under compression, $\sigma_{12}{}^{c}$ can be described with Coulomb's law of friction as

$$\begin{aligned} &\text{when } |\sigma_{nt}| > \mu \cdot |(\sigma_{nn})| \text{ and } \sigma_{nt} > 0 \\ &\sigma_{12}{}^{c} = \mu \cdot (-\sigma_{nn}) > 0 \end{aligned} \tag{2.34}$$

or

$$\begin{aligned} &\text{when } |\sigma_{nt}| > \mu \cdot |(\sigma_{nn})| \text{ and } \sigma_{nt} < 0 \\ &\sigma_{12}{}^{c} = \mu \cdot (\sigma_{nn}) < 0 \end{aligned} \tag{2.35}$$

where μ is the friction coefficient. In this study's setting (Figure 2.10), σ_{nt} is always negative for closed cracks at an angle β between 0° and 90°. Therefore, the SIFs for cracks under compression can be expressed as

$$\begin{aligned} K_{\mathrm{I}} &= \sqrt{\pi a}\left(\sigma_{nn} - \sigma_{11}{}^{c}\right) = 0 \\ K_{\mathrm{II}} &= \sqrt{\pi a}\left(\sigma_{nt} - \sigma_{12}{}^{c}\right) = \sqrt{\pi a}\left[\sigma_{nt} - \mu \cdot (\sigma_{nn})\right] \end{aligned}. \tag{2.36}$$

Note that the frictional stress always reduces the magnitude of K_{II}.

If the closed crack is frictionless, the problem is simple. The stress intensity factors for closed fractures from Equation (2.36) become

$$\begin{aligned} K_{\mathrm{I}} &= 0 \\ K_{\mathrm{II}} &= \sqrt{\pi a}\,(\sigma_{nt}) = \sqrt{\pi a}\left[-\left(\sigma_{xx}{}^{r} - \sigma_{yy}{}^{r}\right)\sin\beta\cos\beta\right] \end{aligned}. \tag{2.37}$$

Applying the mode I and mode II stress intensity factors from Equation (2.37) to the MMTPS-criterion, Equation (2.21) becomes

$$\begin{aligned} &\sigma_{r\theta} = 0 = \cos\frac{\theta}{2}(3\cos\theta - 1)\sin 2\beta - 2\sqrt{\frac{2r_c}{a}}\sin 2\theta\cos 2\beta \\ &\frac{\cos\frac{\theta}{2}(3\cos\theta - 1)}{\sin 2\theta} = 2\sqrt{\frac{2r_c}{a}}\tan^{-1} 2\beta \end{aligned}. \tag{2.38}$$

This shows that the fracture propagation angle is independent of the magnitude of the exterior loading, but it is governed by the ratio of the critical initiation distance to the

fracture half-length and the crack inclination angle. Figure 2.23 illustrates the variation of kinking angles rather than only $70.5°$ for all inclination angles dependent on β and r_c/a.

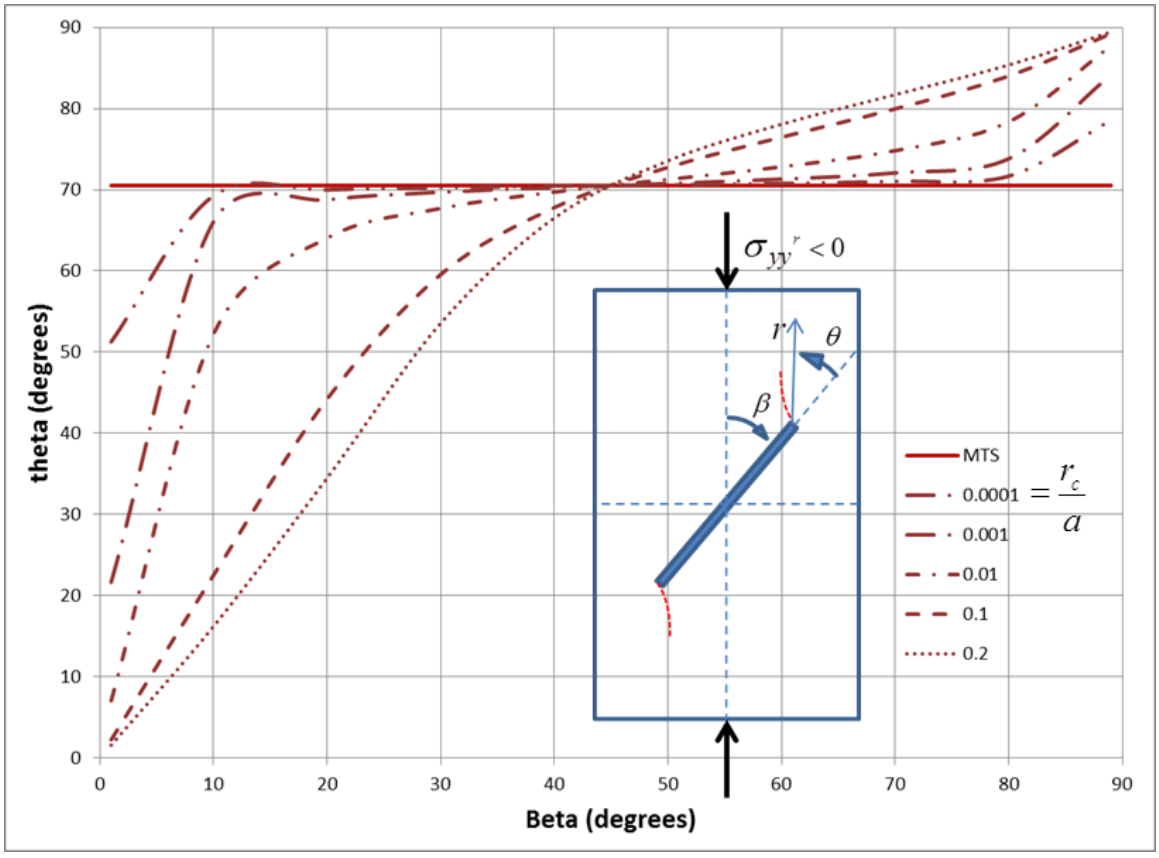

Figure 2.23. The predictions of the fracture propagation angles (θ) with respect to the fracture inclination angles (β) by the MMTPS-criterion for frictionless closed fractures under uniaxial compression with various r_c/a values ranging from 0.0001 to 0.2.

In general, however, closed cracks have friction and the frictional stress term needs to be considered in the near-tip stress field and the stress intensity factor. Li et al., (2012) reported that if the resolved shear stress does not exceed the frictional stress, K_{II} is zero, which means there is no driving stress for a crack to propagate. Consequently, the following condition shoud be satisfied for non-zero K_{II} (Figure 2.24),

$$\begin{aligned} &|\sigma_{nt}| > \mu \cdot |\sigma_{nn}| \\ &\left|-\left(\sigma_{xx}{}^{r} - \sigma_{yy}{}^{r}\right)\sin\beta\cos\beta\right| > \mu \cdot \left|\left(\sigma_{xx}{}^{r} - \sigma_{yy}{}^{r}\right)\cos^2\beta + \sigma_{yy}{}^{r}\right| \end{aligned} \quad (2.39)$$

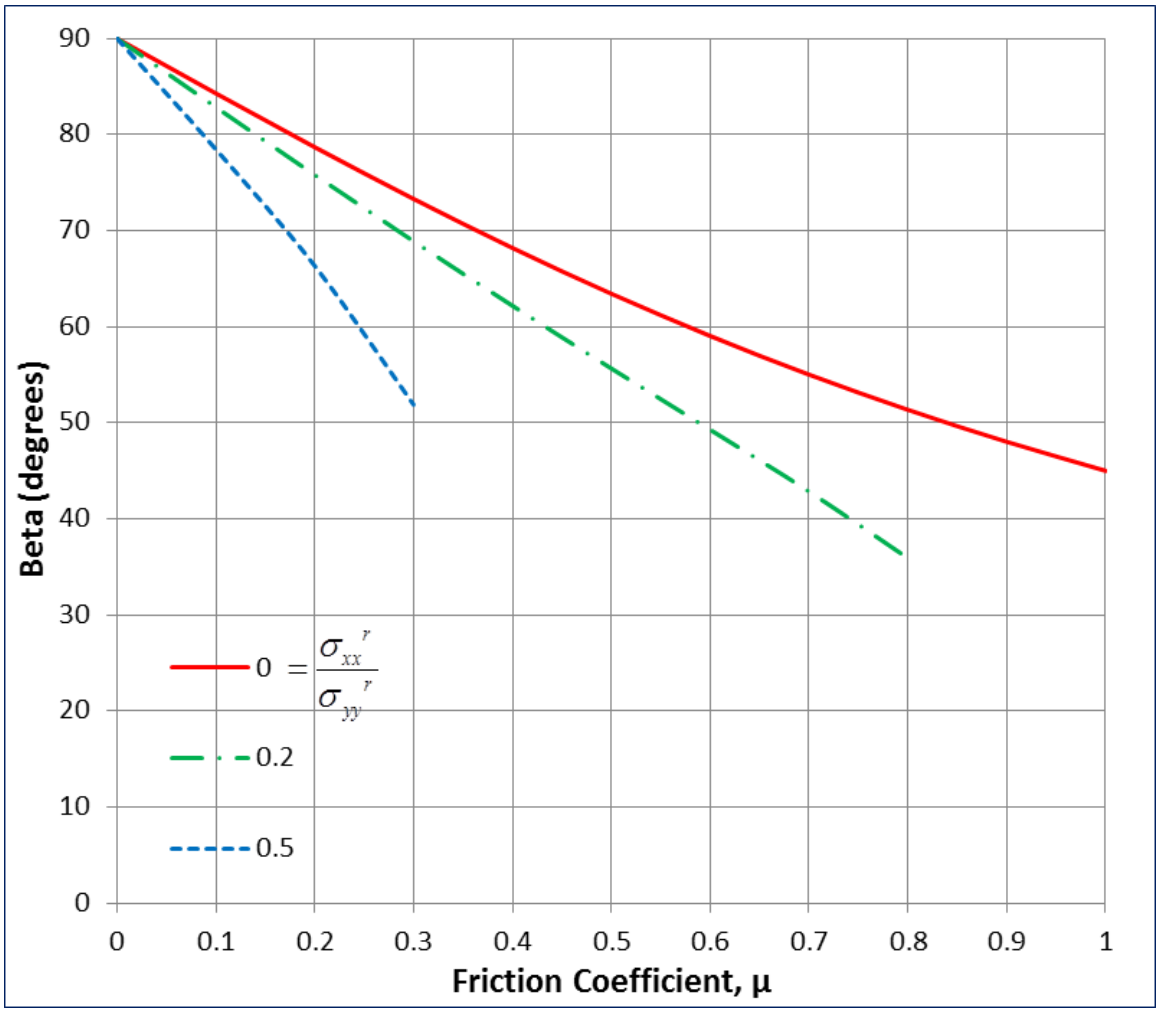

Figure 2.24. The requirement of fracture inclination angles (β) for the fracture propagation of closed cracks with various friction coefficients (μ) under biaxial compression ($\sigma_{xx}{}^{r}, \sigma_{yy}{}^{r} < 0$) (after Li et al., 2012).

If the condition in Equation (2.39) is satisfied, based on Equation (2.19), the near-tip stress field can be re-written as

$$\sigma_{rr} = \frac{1}{\sqrt{2\pi r}}\left[K_{\mathrm{II}} \left\{ \sin\frac{\theta}{2}\left(1-3\sin^2\frac{\theta}{2}\right)\right\}\right] + \left(\sigma_{np}-\sigma_{nn}\right)\cos^2\theta + \sigma_{nn} + \mu\sigma_{nn}\sin 2\theta$$

$$\sigma_{\theta\theta} = \frac{1}{\sqrt{2\pi r}}\left[-K_{\mathrm{II}} \left\{ 3\sin\frac{\theta}{2}\cos^2\frac{\theta}{2}\right\}\right] + \left(\sigma_{np}-\sigma_{nn}\right)\sin^2\theta + \sigma_{nn} - \mu\sigma_{nn}\sin 2\theta \qquad .(2.40)$$

$$\sigma_{r\theta} = \frac{1}{\sqrt{2\pi r}}\left[K_{\mathrm{II}} \left\{ \cos\frac{\theta}{2}\left(1-3\sin^2\frac{\theta}{2}\right)\right\}\right] - \left(\sigma_{np}-\sigma_{nn}\right)\sin\theta\cos\theta + \mu\sigma_{nn}\cos 2\theta$$

The near-tip stress components are similar to the stress field of Li et al. (2012) except that for $\sigma_{12}{}^{c}$ they substituted $\mu\cdot(-\sigma_{nn})$ instead of $\mu\cdot(\sigma_{nn})$ which results in wrong predictions.

Figure 2.25c and Figure 2.25d show the difference between the MMTPS-criterion and the approach of Li et al. (2012) for r_c / a of 0.02 along with experiment results from Bobet (2000) and Park and Bobet (2010) for closed cracks under compression. The predictions of Li et al. (2012) for fractures below β of 27°, where all curves converge, are almost identical regardless of the variation of μ. However, for inclination angles above 27°, the predictions show that θ is greater for cracks with higher μ (Figure 2.25d). This is the opposite of the predictions of the MMTPS-criterion (Figure 2.25c) where θ decreases with μ. In addition, the experimental results from Chaker and Barquins (1996), which were utilized for validation in the study of Li et al. (2012), should not be considered to validate the prediction of closed crack propagation direction since they were from open cracks with steel inclusions. The different stiffness of the steel inclusion to the matrix can generate non-zero K_{I} which is not applicable to represent closed cracks of zero K_{I}.

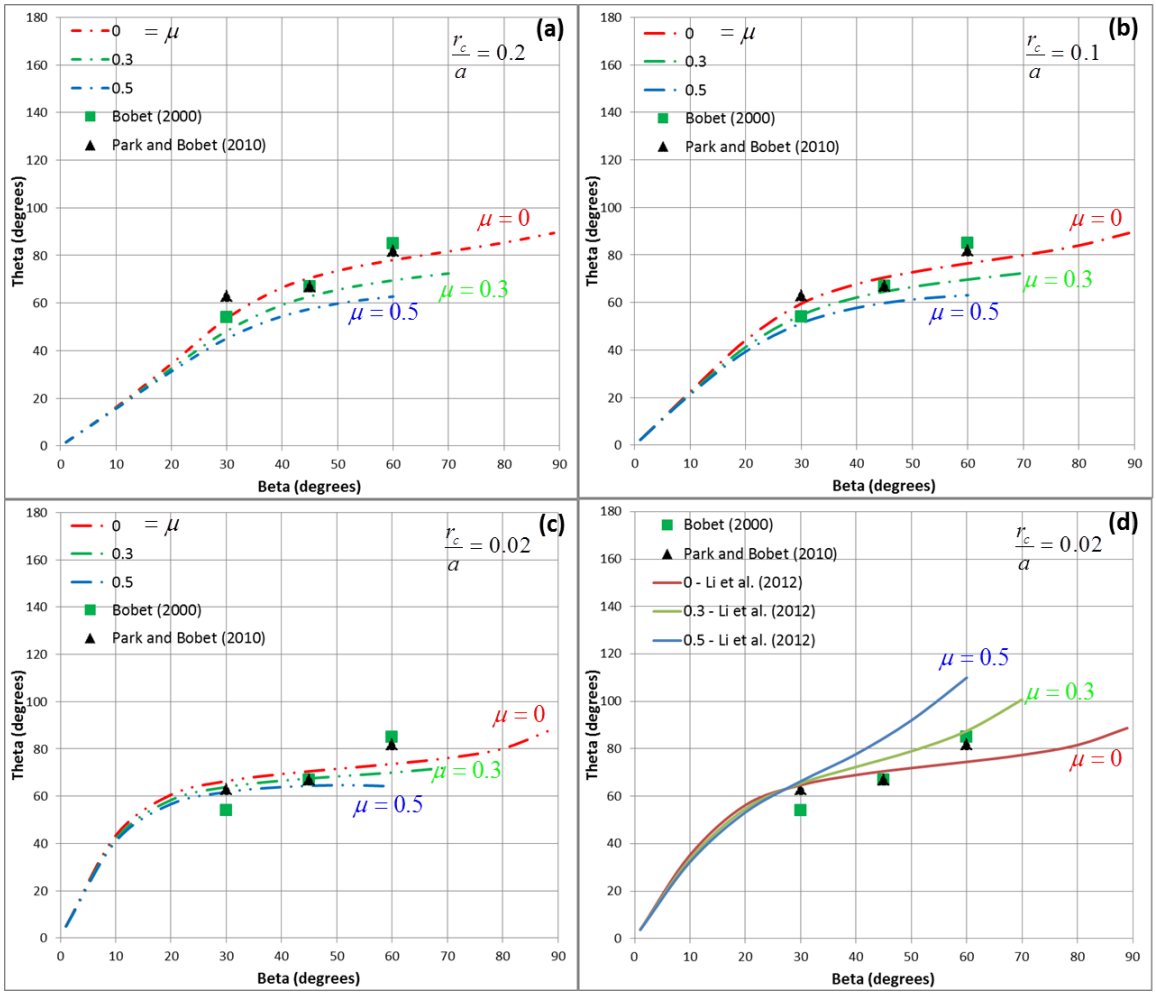

Figure 2.25. The predictions of fracture propagation angles for closed fractures with various friction coefficients (0, 0.3, 0.5) by the MMTPS-criterion and the experimental results of Bobet (2000) and Park and Bobet (2010). The r_c / a values utilized for the predictions are (a) 0.2, (b) 0.1, and (c) 0.02, respectively. (d) is the prediction from Li et al. (2012) with r_c / a of 0.02.

Figure 2.25a and Figure 2.25b show the predictions of the fracture propagation angles by the MMTPS-criterion with experiment results from Bobet (2000) and Park and Bobet (2010) for r_c / a of 0.2 and 0.1, respectively. Although the experimental results are limited, the predictions of three different friction coefficients follow the trend of the

experiment's results. The friction coefficient, in general, lowers the fracture propagation angle which agrees with the theoretical study of Nemat and Horii (1982), and the impact of μ is more significant for cracks with greater inclination angles. As r_c / a value decreases, the overall trend of the prediction converges to $70.5°$, which is the solution of the conventional MTS-criterion, for β inclination angles between 10° and 80° (Figure 2.25c). The best fit with the experiment's results is the prediction with $r_c / a = 0.1$ when μ is between 0 and 0.3 (Figure 2.25b). Bobet (2000) did not report the fracture toughness and therefore the material r_c / a is unknown, but the estimate of the friction coefficient is reasonable since it is close to the reported value of 0.283 – 0.3.

2.10 DISCUSSION

The near-tip stress field and the application of the MMTPS-criterion in this study are based on LEFM which is limited to Small-Scale Yielding (SSY) problems. LEFM is applicable when a *K*-dominant zone, a region between r_p and r_K (Figure 2.26), exists ($r_p < r_K$) in the vicinity of the fracture tip. In general, the boundary of the *K*-dominant zone (r_K) is at least an order of magnitude smaller than any characteristic dimension including the length of the crack.

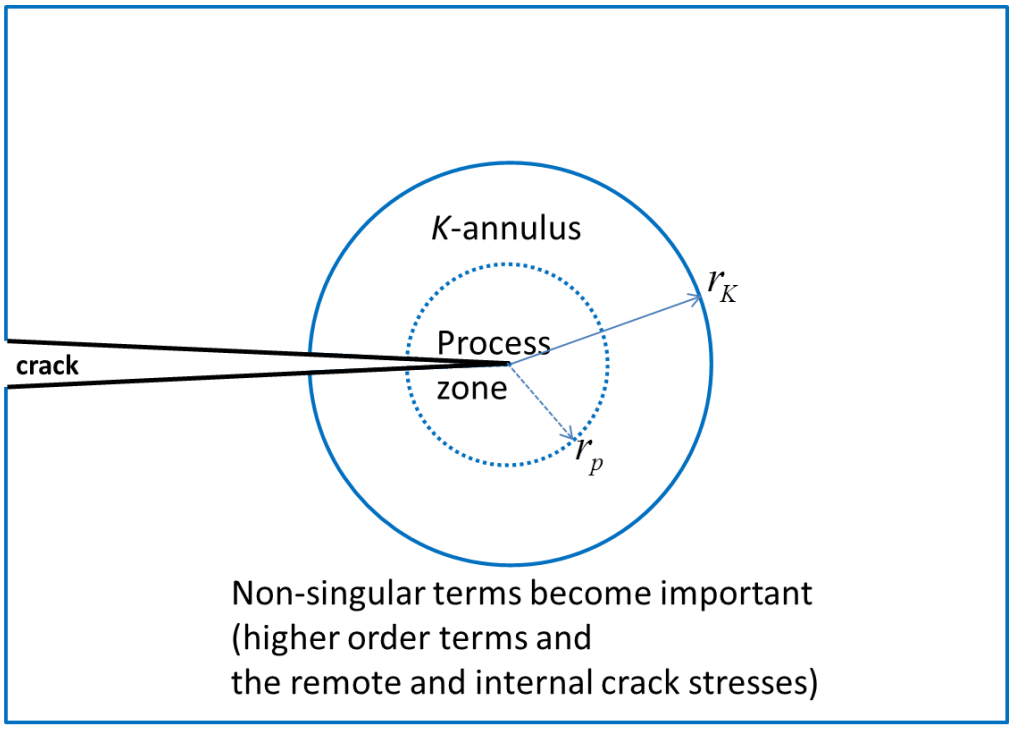

Figure 2.26. Schematic view of the fracture process zone and the *K*-annulus in the vicinity of the fracture tip.

The analytical results of the process zone size indicate that the high confining stress minimizes r_p, which is the condition for hydraulic fracture applications. Schmidt (1980) discussed that a decrease in the size of the process zone under confining stress corresponds to an increase in the apparent fracture toughness of limestone (Schmidt and Huddle, 1977). This is comparable to the increase in process zone size with the decrease in crack length, for cracks that do not satisfy SSY conditions, since the apparent fracture toughness increased with crack lengths in Indiana Limestone (Ingraffea and Schmidt, 1978). For SSY conditions, the requirement of fracture half-length can be expressed as (Ouchterlony, 1990)

$$a \geq 2.5\left(\frac{K_{Ic}}{\sigma_T}\right)^2 \tag{2.41}$$

and with Equation (2.28),

$$\frac{r_c}{a} \leq \frac{1/2\pi}{2.5} = 0.064\,. \tag{2.42}$$

When this condition is satisfied, the fracture toughness and the process zone size are independent of the fracture length. If not, the size of the process zone increases as the crack becomes shorter than the minimum a.

Recalling the mechanical properties ($K_{Ic} = 0.28$ MPa$\sqrt{\text{m}}$, $\sigma_T = 4.83$ MPa) of hydrostone from Bahorich et al. (2012) in Section 2.8, the minimum *a* is calculated to be 8.4 mm (0.33 inch). This means that the fracture length should be greater than 16.8 mm (0.66 inch) for Equation (2.28) to be applicable in calculating r_c of the hydrostone. This agrees with the analysis of fracture propagation angles by the MMTPS-criterion for open cracks in hydrostone specimens. The predictions based on the calculated r_c (0.53 mm) matched only with experimental results of the 25.4-mm (1.0-inch) and the 19-mm (0.75-inch) open cracks but not with the 12.7-mm (0.5-inch) cracks, a result not meeting the requirement of the SSY conditions. However, when a larger r_c, 1.07 mm (0.042 inch), is assumed for the 12.7-mm (0.5-inch) cracks, the prediction agreed well with the fracture propagation angles, suggesting that the process zone is larger for the short crack.

The estimated r_c / a are 0.042 and 0.056 for 25.4-mm (1.0-inch) and 19-mm (0.75-inch) open cracks and 0.17 for 12.7-mm (0.5-inch) open fractures in hydrostone samples

under compressive loading. Although the r_c/a of the 12.7-mm (0.5-inch) crack was much greater than 0.064 from Equation (2.42), not satisfying SSY conditions, the prediction based on the linear elastic stress field fits well with the experimental results, showing the applicability of MMTPS-criterion for fractures with large process zones.

2.11 CONCLUSIONS

Developing a mixed-mode fracture propagation path model that works under both tensile and compressive conditions has proved challenging. Fractures under tensile loading are predictable with established mixed-mode fracture propagation criteria, but fractures under compressive loading have relatively poor agreement with the predictions. To improve the correlation with the experimental results, this chapter introduced the MMTPS-criterion, a criterion modified from the MTPS-criterion, which includes the remote and internal crack stresses additional to the singular terms of the asymptotic near-tip stress field.

The MMTPS-criterion predicts relatively accurate results for the fracture propagation angles in various orientations under both tensile and compressive loadings. For cracks under compression, different features between the open and closed cracks were interpreted with modified stress intensity factors for the application of the MMTPS-criterion. For open cracks, the mode I stress intensity factor can be negative if the slot stays open prior to fracture propagation from the slot tip. With the negative K_I, experimental results of hydrostone specimens agreed well with the interpretation of the

MMTPS-criterion for 25.4-mm (1.0-inch) and 19-mm (0.75-inch) open cracks under compression with the critical r_c of 0.53 mm (0.021 inch). The critical propagation distance was calculated from the maximum principal stress model (Schmidt, 1980) based on the fracture toughness and the tensile strength of the hydrostone. However, to match the predictions of the fracture propagation angles with the experimental results of 12.7-mm (0.5-inch) cracks, the MMTPS-criterion required an r_c of 1.07 mm (0.042 inch). Although it is a larger process zone than the longer cracks and does not satisfy the SSY conditions, the predictions of the MMTPS-criterion correlated well with the experimental results.

On the other hand, for closed cracks without friction, K_I is zero, and the fracture kinking angle is governed by the fracture half-length, the fracture inclination angle, and the critical initiation distance. If friction exists, under the same condition, the MMTPS-criterion based on Coulomb's law of friction predicts that the higher friction coefficient lowers the fracture propagation angle. Although the experimental results on frictional interfaces are quite limited, the analytical predictions of the MMTPS-criterion agreed well with them. Thus, the insight of the friction effect on propagation path can be applied in structural geology to interprete the field splay fractures with kinking angles of substantially lower than $70.5°$ to the main fault in geological observations (Cruikshank et al., 1991; Martel et al., 1988; Segall and Pollard, 1983; Willemse and Pollard, 1998).

CHAPTER 3: THE INTERACTION OF PROPAGATING OPENING MODE FRACTURES WITH PREEXISTING DISCONTINUITIES IN SHALE [1]

Microseismic monitoring performed in formations like the Barnett shale (Fisher et al., 2002; Maxwell et al., 2002) depict broad areas of disturbance during hydraulic fracture treatments that are hundreds of feet wide and a thousand or more feet long (Figure 3.1). This diagnostic data implies that hydraulic fracture growth in shale and naturally fractured formations is a complex propagation of multi-fracture networks rather than the extension of a single planar fracture. Core observations from tight gas sandstones have also demonstrated that multiple fracture planes can be created from a single fracture treatment. In the Piceance Basin, as many as 30 sub-parallel, gel-filled fractures were discovered in a transversely oriented core related to a single hydraulic fracture treatment from a vertical wellbore (Warpinski et al., 1993). These observations lead to the hypothesis that natural fractures act as planes of weakness which divert hydraulically induced fractures. The interaction between hydraulic and natural fractures is thought to be the key to creating the surface area required for economic production in extremely low permeability formations such as shale (Maxwell et al., 2002).

[1]The material in this chapter has been published in Journal of Geophysical Research: Solid Earth: Lee, H. P., Olson, J. E., Holder, J., Gale, J. F. W., Myers, R. D., The interaction of propagating opening mode fractures with preexisting discontinuities in shale, Journal of Geophysical Research: Solid Earth, 120, 169–181, doi:10.1002/2014JB011358. This paper was overall supervised by Jon E. Olson. Jon Holder supported the laboratory experiments, Julia F.W. Gale performed the microstructural analysis, and Rodrick D. Myers provided helpful discussions in this study.

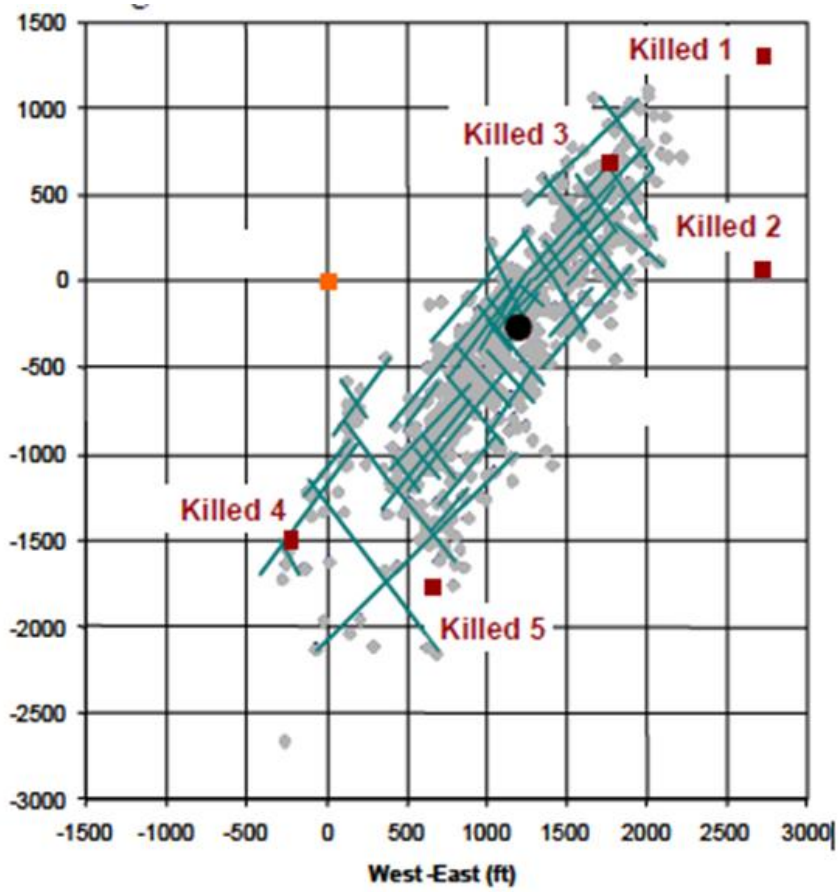

Figure 3.1. Map view of fracture treatment showing the complexity of fracture networks in Barnett (Fisher et al., 2004).

Experimental and theoretical investigations on the interaction of hydraulically induced fractures and frictional interfaces showed that the approach angle, fracture friction coefficient, and horizontal differential stress parallel to the hydraulic fracture direction controlled whether a hydraulic fracture would be arrested, divert into or cross a preexisting fracture (Blanton, 1982; Warpinski and Teufel, 1987; Renshaw and Pollard, 1995; Gu and Weng, 2010; Gu et al., 2011). The tendency for a hydraulic fracture to cross a preexisting fracture is higher for more orthogonal approach angles, higher friction coefficients, and higher differential stress. Preexisting fractures considered in this

previous work were either barren joints in natural rock or unbonded interfaces created in rock or model material (typically hydrostone) with saw cuts.

Although barren joints and faults are common in surface outcrops, Gale et al. (2007) described fully or partially cemented fractures in Barnett shale core and speculated that these cemented fractures were responsible for hydraulic fracture complexity. Consequently, some recent papers have addressed bonded rather than frictional preexisting fractures and their impact on hydraulic fracture propagation (Zhou et al., 2008; Bahorich et al., 2012; Wang et al., 2013). These types of experiments on bonded interfaces demonstrate that even healed fractures can influence hydraulic fracture growth, but the properties of the cement filling the fracture are important in controlling propagation behavior.

I have performed systematic fracture propagation experiments on Marcellus shale cores containing cemented natural fractures, which I will refer to as veins for the rest of this study, in order to characterize the fracture interaction properties of actual subsurface fractures, as opposed to laboratory-made proxies. I have chosen the Semi-Circular Bend (SCB) fracture mechanics test because of its ease of execution, repeatability, and modest sample size requirement (since we must prepare samples from a limited number of 101.6-mm (4-inch) diameter cores). The Marcellus shale samples tested contained calcite-filled veins of various thicknesses, and we drove tensile cracks via SCB loading into these veins with the goal of learning more about the interaction between hydraulic fractures and preexisting discontinuities in shale reservoirs. The objective was to find the key parameters controlling the fracture interaction results: arrest, crossing, or diversion.

3.1 SAMPLE PROPERTIES

A total of six naturally fractured Marcellus shale samples, each 101.6 mm (4 inch) in diameter, were collected for this study. All of the samples were from the same well and were approximately 101.6 mm (4 inch) in height. The sample host rock is a dark, fine-grained shale with dispersed detrital grains of carbonate, organic pellets, some fossil fragments up to 3 mm long, and pyrite grains typically <0.1 mm across, but in one specimen reaching up to 0.5 mm across. The texture and composition of the samples appears consistent throughout the sample set based on the petrographic thin sections. No X-ray diffraction (XRD) data was available for the samples tested. The mineral composion of the Marcellus shale has a wide range in a clay-quartz-calcite ternary plot (Figure 1.1), but given the predominance of calcite in the observed veins in the test samples, it is likely their composition lies in the lower right region of the diagram. In hand specimen, subtle laminae are seen parallel to bedding. Bedding and laminae are not seen in the thin sections because the sections were made parallel to the bedding.

Uniaxial compression tests (i.e., Unconfined Compressive Strength tests) were performed to measure the physical properties of the Marcellus shale. Homogeneous samples were cut from the core avoiding any veins. The loading of the Uniaxial compression test was oriented parallel to the bedding to match the divider loading orientation to be used for the SCB test specimens described later (Figure 3.2). The mean Young's Modulus (E_{rock}) was 8.9 GPa (standard deviation, $SD = 0.17$ GPa , for 3

samples) and Unconfined Compressive Strength (UCS_{rock}) was 53.4 MPa ($SD = 8.6$ GPa, for 2 samples).

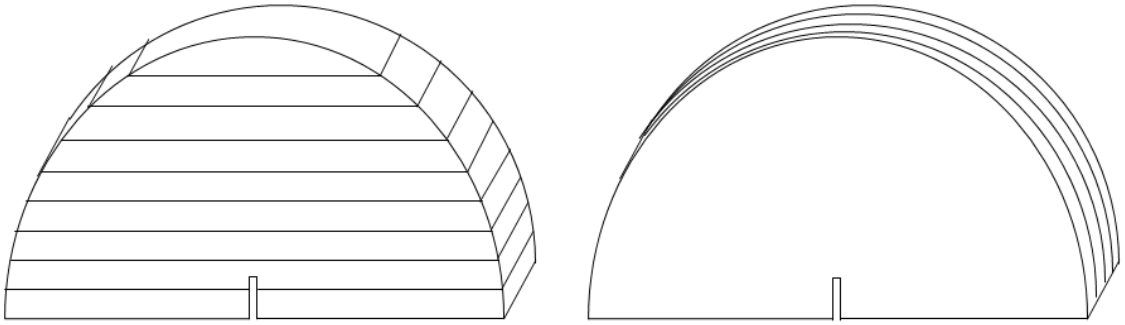

Figure 3.2. Orientation of bedding relative to crack-propagation direction for arrester (left) and divider (right) configurations (after Chong et al., 1987).

Four of the six core samples contain one main vein down the middle and two core samples have two veins next to each other. The veins in the core were oriented roughly orthogonal to bedding and varied in thickness (i.e., aperture) from 0.25 to 1.9 mm. One core sample includes a cluster of veins. The cluster is formed of several veins of various thicknesses with shale in between, giving several interfaces between the rock matrix and calcite cement. The total thickness of the cluster ranges from 1.3 to 2.0 mm, which is in the range of thick single vein cases in this paper.

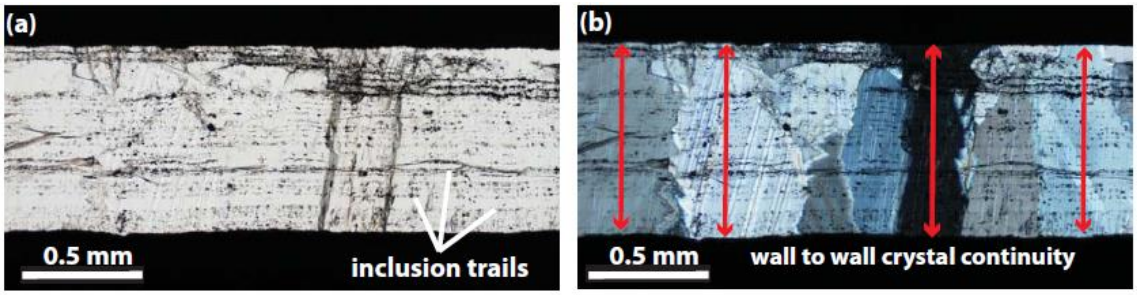

Figure 3.3. Thin section photomicrographs of intact vein, (a) plane light photomicrograph showing inclusion trails parallel to fracture walls indicating crack-seal texture, and (b) with crossed polars showing individual crystals extending from wall to wall (arrows).

Textures in the vein calcite vary (Figure 3.3). In some veins individual calcite crystals extend from one side of the vein to the other and inclusion trails parallel to the vein walls are developed throughout, whereas in others the inclusion trails are confined to the vein margins, with the central portion having a more blocky texture and fewer inclusion trails. Some of the inclusions are solid, including small slivers of shale host rock, while others are fluid inclusions. Isolated inclusions and planes or trails of multiple inclusions, termed fluid inclusion assemblages (FIAs), are both present. Some FIAs are parallel to the vein walls and cut across crystal boundaries, and we interpret these as secondary inclusions developed during a crack-seal process (Ramsay, 1980), where the calcite has broken and resealed numerous times throughout the opening history of the vein. Entrainment of host rock particles suggests breaks along the vein–shale interface, but the presence of fluid inclusions alone suggests breaking within the calcite rather than at the calcite–shale interface.

3.2 SEMI-CIRCULAR BEND TEST

Chong and Kuruppu (1984) suggested a method called the Semi-Circular Bend (SCB) test as a standard method of rock fracture toughness measurement (Figure 3.4). Thiercelin and Roegiers (1986) pointed out that the 3-point bending load results in a compressive stress field ahead of the crack tip, reducing process zone size and increasing the applicability of Linear Elastic Fracture Mechanics (LEFM) analysis. Given the reduced process zone size and the lack of dependence of results on sample thickness (Lim et al., 1994), the SCB test is attractive for testing in situations where rock samples are small and difficult to collect, as is the case for subsurface shale.

Fracture toughness (K_{Ic}) from the SCB test can be calculated by the following equations (Basham, 1989; Lim et al., 1993),

$$K_{Ic} = \frac{P_{max}\sqrt{\pi a}}{2rt} Y_I \tag{3.1}$$

$$Y_I = 5.6 - 22.2\frac{a}{r} + 166.9\left(\frac{a}{r}\right)^2 - 576.2\left(\frac{a}{r}\right)^3 + 928.8\left(\frac{a}{r}\right)^4 - 505.9\left(\frac{a}{r}\right)^5 \tag{3.2}$$

where P_{max} is the peak load, a is the notch length, r is the specimen radius, t is the specimen thickness, and Y_I is a dimensionless coefficient. Equation (3.2) is valid for $0.03 \le a/r \le 0.8$ and $s/r = 0.8$, where s is the length from the notch to the support roller. The SCB test in this study was set to match s/r equal to 0.8 and the a/r ratios for the samples are between 0.2 and 0.3.

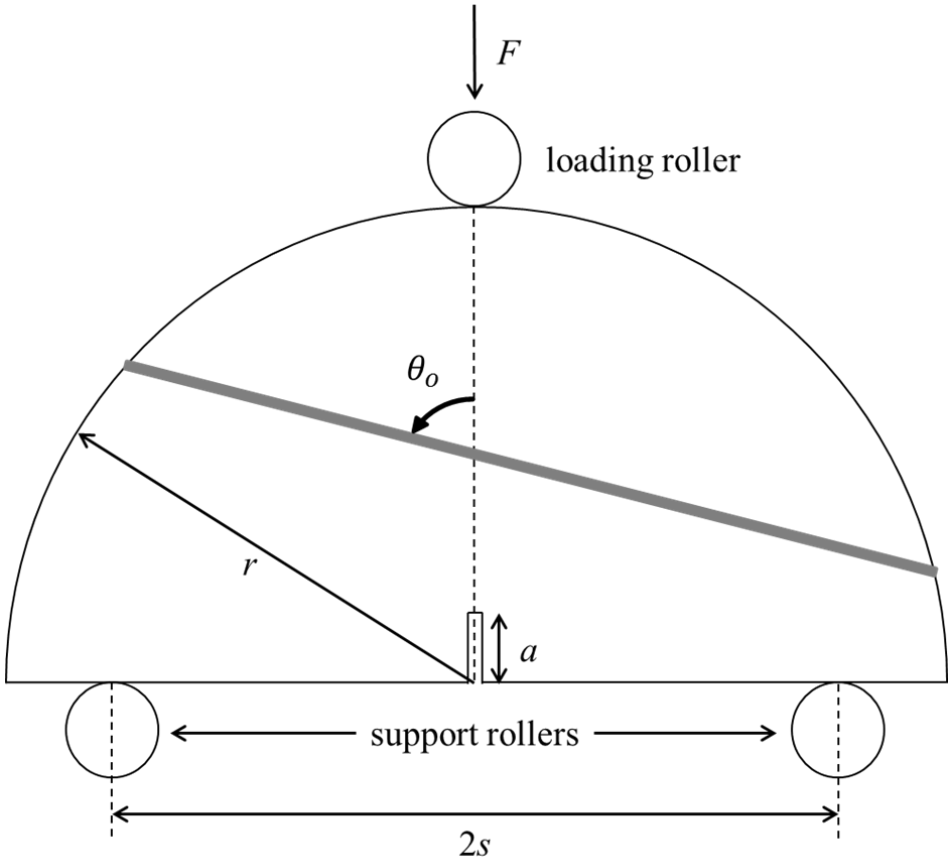

Figure 3.4. Schematic view of the SCB test specimen with discontinuity at angle θ_o (after Chong and Kuruppu, 1984).

3.3 SAMPLE PREPARATION

Core samples were sliced and core-plugged or cut into a total of 53 SCB specimens (19 core-plugged samples and 34 saw-cut samples), and the results of 21 specimens are presented in this section (Table 3.1). To avoid the vibration and subsequent damage inherent in drilling plugs out of the base samples (as is customarily done when making SCB specimens), the original cores were saw-cut with an oil-based rock saw into octagonal-shaped disks 12.7 to 25.4 mm (0.5 to 1 inch) thick (Figure 3.5). Specimens

prepared by multiple saw-cuts had over a 90 percent survival rate whereas core-plugging resulted in only 20 percent success. The octagonal-shaped disks were cut in two samples (see Figure 3.5c) to approximate the prescribed semi-circular shape of standard SCB specimens. For some samples corners were rounded using a grinder, but that modification did not seem to affect the test results significantly.

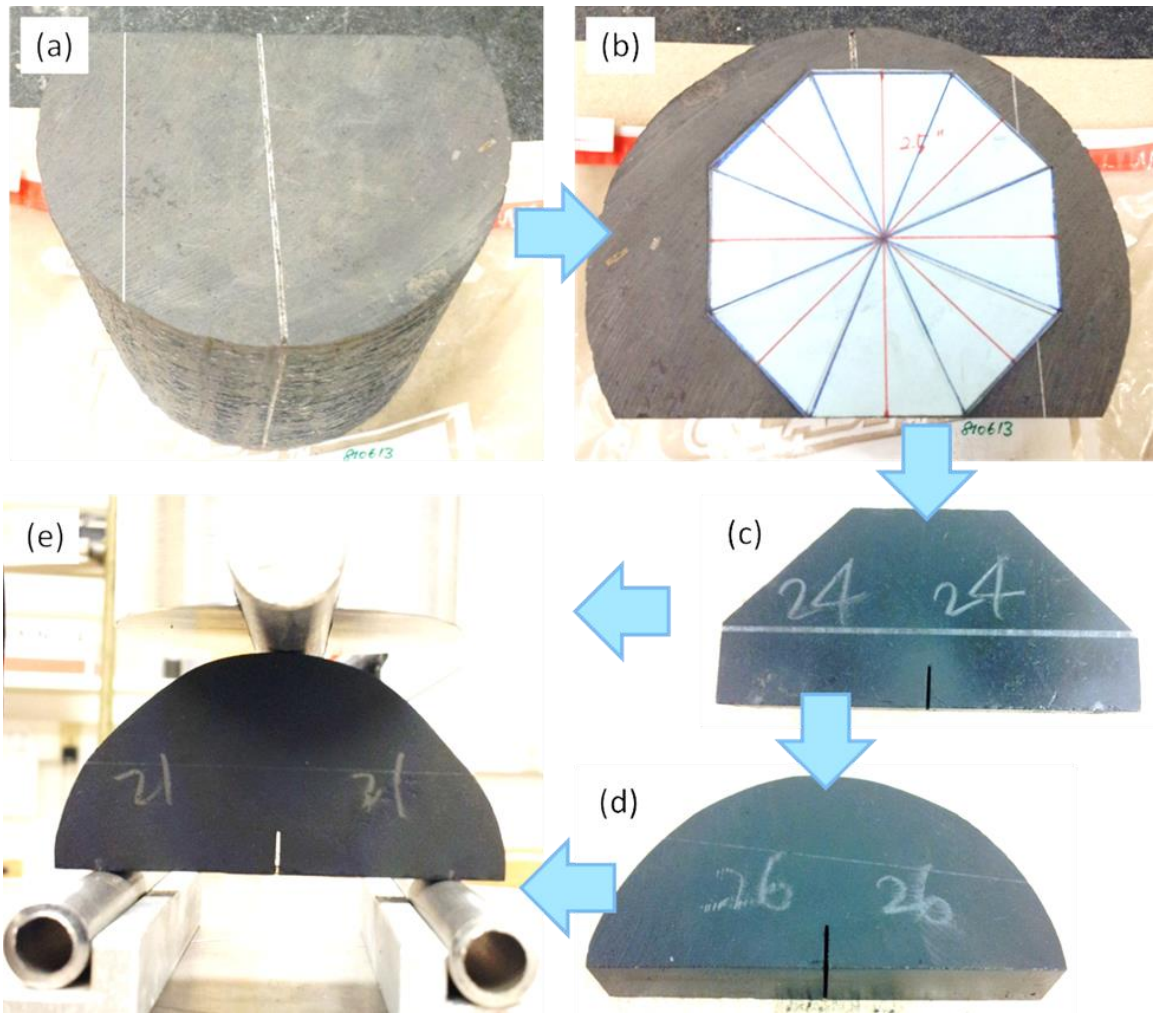

Figure 3.5. Procedure of preparing samples for the SCB test: (a) original Marcellus shale containing calcite-filled vein core collected, (b) the octagonal shape template with 63.5-mm (2.5-inch) sides, (c) the specimen sliced into a half-octagonal shape, (d) the case for which the edges were ground from the half-octagonal shape, and (e) the specimen with a vein at $\theta_o = 90°$ loaded by three steel rollers.

Table 3.1. List of samples

Sample Number	Table Number	Figure Number	Vein Angle (θ_o) (°)
1d	Table 3.2		N/A
2d	Table 3.2		N/A
3d	Table 3.2		N/A
4d	Table 3.2		N/A
5d	Table 3.2		N/A
6d	Table 3.2		N/A
7d	Table 3.2		N/A
8d	Table 3.2		N/A
9d	Table 3.2		N/A
10d	Table 3.2		N/A
11d	Table 3.2		N/A
12d	Table 3.2		N/A
13d	Table 3.2		N/A
14d	Table 3.2		N/A
15d	Table 3.2		N/A
16d	Table 3.2		N/A
17d	Table 3.2		N/A
18d	Table 3.2		N/A
19d	Table 3.2		N/A
1a0	Table 3.2		N/A
2a0	Table 3.2		N/A
5a0	Table 3.2	Figure 3.7a	N/A
6a0	Table 3.2		N/A
7a0	Table 3.2		N/A
3a30	Table 3.2	Figure 3.7b	N/A
4a30	Table 3.2		N/A
1		Figure 3.9a, Figure 3.12a	90
5		Figure 3.9b, Figure 3.12b	90
8		Figure 3.9d, Figure 3.12d	90
21		Figure 3.8a, Figure 3.11a	90
22		Figure 3.8c, Figure 3.11c	58
23		Figure 3.8d, Figure 3.11d	43
24		Figure 3.9c, Figure 3.12c	90
26		Figure 3.8b, Figure 3.11b	81
32		Figure 3.10a	90
33		Figure 3.10b	81

*N/A: Not Applicable

The specimens were mostly cut such that bedding was parallel to the plane of the octagon, termed the divider configuration (Chong et al., 1987), although seven samples were made in the arrester configuration (Figure 3.2). The samples were cut to place the veins a short distance (about one and a half notch length) above the notch and at various approach angles relative to the notch, ranging from 25° to 90°. The notch to specimen diameter ratio was 0.1. The samples were loaded using a 50,000 N (10,000 lb) Humboldt Multi-speed Load Frame. The steel support rollers at the bottom of the sample were located at $s/r = 0.8$ (Figure 3.5), with diameters of 9.5 mm (0.375 inch) for the support rollers and 12.7 mm (0.5 inch) for the loading roller. The sample was loaded at a convergence rate of 0.076 mm (0.003 inch) per minute until sample failure.

After the SCB test, the broken samples were prepared for petrographic microstructural analysis. Test samples were impregnated with blue-dyed epoxy resin in order to stabilize them prior to cutting the thin-section chips; samples that were broken during testing were reconstructed as closely as possible. Impregnation was not complete for all samples but was sufficient to hold the sample together during chip preparation. A second, clear epoxy was used during the thin-section making.

3.4 ENERGY RELEASE RATE CRITERION

A crack propagation criterion based on the maximum energy release rate (G-criterion) was proposed for hydraulic fractures interacting with natural veins by Dahi-Taleghani and Olson (2009). Fractures propagate when the energy release rate reaches a

critical value, G_c. For a homogeneous body, the fracture growth is expected in the direction of maximum G (Lawn and Wilshaw, 1975). The energy release rate for a crack propagating in an arbitrary direction from an existing crack tip is given by (Nuismer, 1975), Equation (2.5) in Section 2.1. For pure mode I loading for the propagating crack ($K_{\mathrm{I}} > 0$, $K_{\mathrm{II}} = 0$), G is maximized at $\theta = 0°$, and in-plane propagation (no crack-path diversion) would be expected for a homogeneous body.

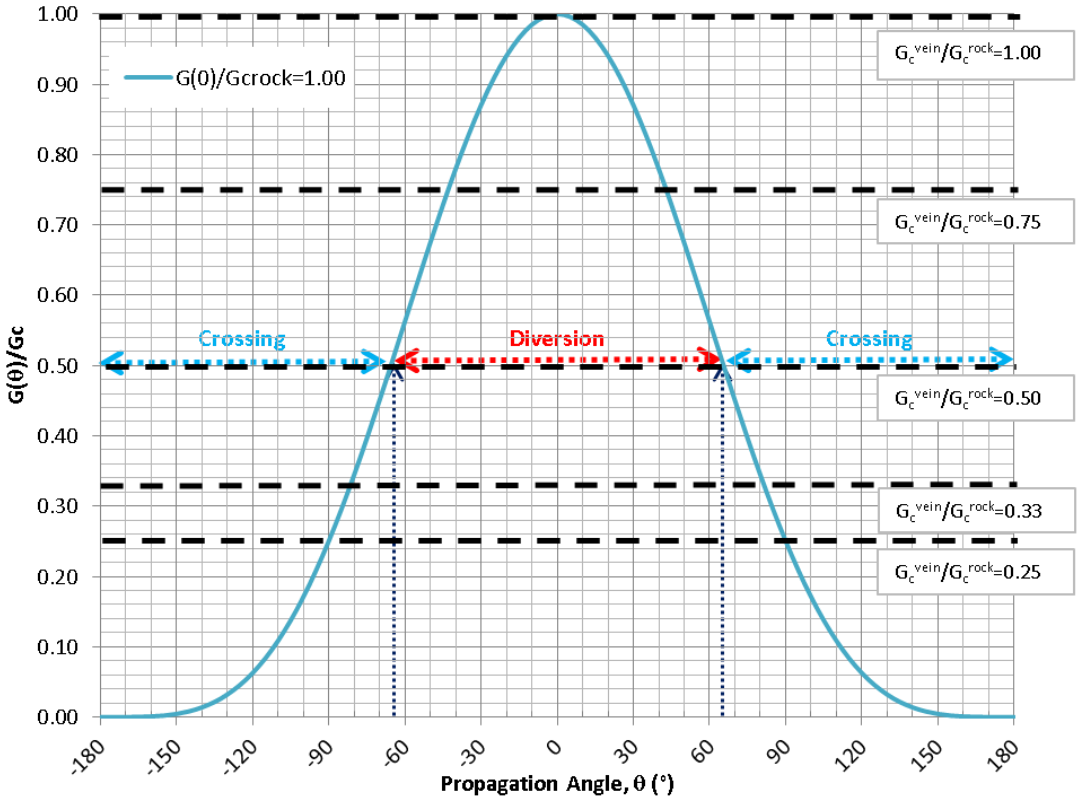

Figure 3.6. Energy release rate, G, as a function of angle, θ: loading case ($G(0°)/G_c^{rock} = 1$) with lines representing the critical energy release rate for vein inclusions, represented as the ratio G_c^{vein}/G_c^{rock}, ranging from 0.25 to 1.00. $G_c^{vein}/G_c^{rock} = 1$ represents homogeneous material. Exemplary dotted line for case of $G_c^{vein}/G_c^{rock} = 0.5$ shows that the induced fracture diverts into the preexisting veins in the orientation of $-65° \le \theta \le 65°$.

Two values of the critical energy release rate (G_c) characterize a material containing sealed fractures, one representing the strength of the rock matrix, G_c^{rock}, and one for the vein, G_c^{vein}. If more than one path has a $G > G_c$, then the path with the greatest G/G_c should be favored (Dahi-Taleghani and Olson, 2009). The variation of $G(\theta)/G_c^{rock}$ with θ is illustrated in Figure 3.6 for the loading level of $G(0°)/G_c^{rock} = 1$, which is the minimum loading magnitude for a crack to propagate within the rock matrix. Where a given $G(\theta)/G_c^{rock}$ curve exceeds a critical G_c^{vein}/G_c^{rock} ratio, the veins oriented within that range of θ would be expected to fail, diverting the propagation of the main crack. Straight propagation across a vein is expected if $G(\theta)/G_c^{rock}$ reaches the value of 1 before the vein failure condition is reached.

As an example, consider a case where the critical energy ratio between vein and rock is $G_c^{vein}/G_c^{rock} = 0.5$. The curve exceeds the $G_c^{vein}/G_c^{rock} = 0.5$ for the orientations of $-65° \le \theta \le 65°$, i.e., G/G_c^{vein} is greater than 1, and a vein –if present– fails, diverting fracture propagation. If no veins exist within the limits of $-65° \le \theta \le 65°$, then straight propagation within the rock is favored. If we consider a case where the critical energy ratio between the vein and rock is greater than the previous case, such as $G_c^{vein}/G_c^{rock} = 0.75$, diversion of fracture propagation along preexisting veins is favored over a narrower range of θ, ±43° from the main crack path (Figure 3.6). Orthogonal diversion of the initial crack requires an energy ratio of $G_c^{vein}/G_c^{rock} = 0.25$.

3.5 SAMPLES WITHOUT VEINS

A total of 26 specimens were prepared without veins to measure the fracture toughness of the shale (Table 3.2). The average toughness for the arrester configuration (where the bedding is parallel to the base of the specimen, $\alpha_{bed} = 0°$) had the highest mean at $K_{Ic} = 0.73\ \text{MPa}\sqrt{\text{m}}$ (standard deviation, $SD = 0.21\ \text{MPa}\sqrt{\text{m}}$, for 5 samples). The next toughest configuration was the divider, with a mean $K_{Ic} = 0.64\ MPa\sqrt{m}$ ($SD = 0.17\ \text{MPa}\sqrt{\text{m}}$, 19 samples). The lowest toughness was for the arrester configuration with the bedding inclined 30° from the base of the sample, $\alpha_{bed} = 30°$, with a mean $K_{Ic} = 0.18\ \text{MPa}\sqrt{\text{m}}$ ($SD = 0.04\ \text{MPa}\sqrt{\text{m}}$, 2 samples).

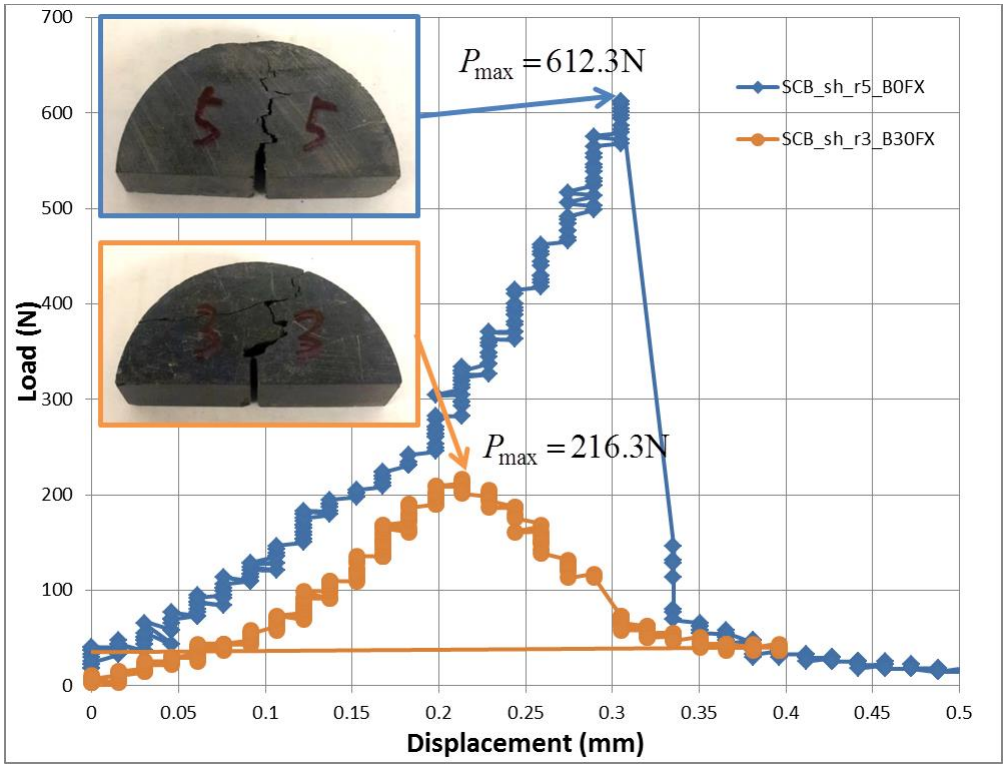

Figure 3.7. Load versus displacement curves: (a) bedding parallel to sample base, $\alpha_{bed} = 0°$, and (b) inclined, $\alpha_{bed} = 30°$.

Table 3.2. Fracture toughness results for samples without calcite-filled veins

Sample Number	Orientation	Diameter (mm)	Fracture Toughness (K_{Ic}) ($MPa\sqrt{m}$)
1d	Divider	38.1	0.7170
2d	Divider	38.1	0.2414
3d	Divider	25.4	0.4965
4d	Divider	25.4	0.4442
5d	Divider	36.8	0.8158
6d	Divider	37.1	0.67
7d	Divider	37.1	0.5545
8d	Divider	37.1	0.6133
9d	Divider	37.1	0.9229
10d	Divider	36.8	0.6532
11d	Divider	37.1	0.9939
12d	Divider	37.1	0.802
13d	Divider	56.1	0.4969
14d	Divider	57.2	0.6192
15d	Divider	61.5	0.6646
16d	Divider	58.9	0.7102
17d	Divider	61.5	0.6527
18d	Divider	61.0	0.4733
19d	Divider	62.5	0.5894
1a0	Arrester, $\alpha_{bed} = 0°$	25.4	1.1042
2a0	Arrester, $\alpha_{bed} = 0°$	25.4	0.7832
5a0	Arrester, $\alpha_{bed} = 0°$	36.8	0.6848
6a0	Arrester, $\alpha_{bed} = 0°$	36.8	0.4716
7a0	Arrester, $\alpha_{bed} = 0°$	37.3	0.6183
3a30	Arrester, $\alpha_{bed} = 30°$	37.1	0.2181
4a30	Arrester, $\alpha_{bed} = 30°$	37.1	0.1389

The relationship between bedding and crack propagation affected not only the peak load, from which toughness is computed, but also the nature of the post-peak load versus displacement curve. In the divider configurations, the load drops precipitously to 0 from the peak value after crack initiation and the sample cleaves in two pieces, reflecting a complete loss of strength due to fracture. For the arrester ($\alpha_{bed} = 0°$) case, there is also a big drop in load upon crack initiation, but some residual strength persists, presumably a result of the jagged, non-planar nature of the fracture and of the frictional resistance along the bedding planes (Figure 3.7a). For $\alpha_{bed} = 30°$ (Figure 3.7b), this residual strength is even more pronounced with very gradual load decline after the peak rather than an abrupt drop, implying even more frictional sliding in the post-peak behavior, as the fracture again follows a tortuous path divided between propagation along and across bedding planes. Given that the area under a stress–strain curve represents strain energy, the slow unloading in the $\alpha_{bed} = 30°$ case represents additional energy dissipation as the fracture propagates all the way through the sample. The lower peak load for $\alpha_{bed} = 30°$ indicates a lower toughness, but that probably is not a complete explanation for the behavior as post-initiation resistance to propagation is greater because of bedding-parallel friction.

3.6 Influence of Approach Angle on Fracture Path

The samples with veins were organized by approach angle and vein thickness. The specimens including the thinnest veins (~0.25 mm) were tested at four different approach

angles ($\theta_o = 90°, 81°, 58°$, and $43°$). All four specimens were sliced from the same core sample and intersected the same contiguous vein, such that all specimens shared roughly the same strength, stiffness, and microstructural properties.

At an approach angle of 90° (Figure 3.8a), the induced fracture started straight from the notch and crossed the vein, although there was a slight deflection from a planar path near the vein itself. For approach angles of $\theta_o = 58°$ (Figure 3.8c) and $\theta_o = 43°$ (Figure 3.8d), the propagating fracture curved toward a more orthogonal approach to the vein. When the fracture reached the vein, it diverted along the vein in the direction away from the notch (toward the top of the sample). Propagation followed this one fracture wing until the sample was completely broken, leaving the other wing of the vein intact. For the approach angle of $\theta_o = 81°$ (Figure 3.8b), the propagation was more complicated. Fracture initiation did not come from the tip of the notch but the side, and the fracture jogged in direction a couple of times before reaching the included vein. Once the fracture reached the vein, it diverted along it, but only for a short segment, after which it kinked back into the shale to continue propagation through the rest of the sample. This step over (jog) behavior was repeated in other near orthogonal approach angle cases described below.

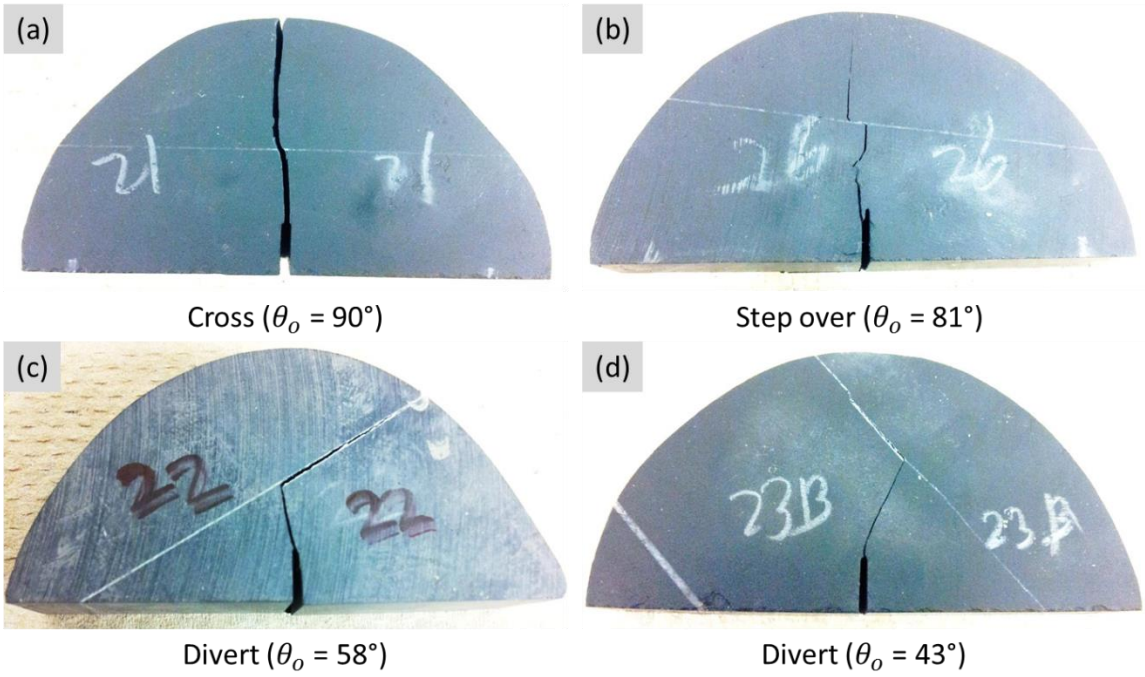

Figure 3.8. Results of SCB test from samples of same vein thickness (0.25 mm) with different θ_0 angles: angle θ_0 of (a) 90°, (b) 81°, (c) 58°, and (d) 43°. Induced fracture in (a) crossed the vein but it diverted for (b), (c), and (d).

3.7 THEORETICAL ANALYSIS OF FRACTURE INTERACTION RESULTS

For the non-orthogonal approach-angle cases, the propagating fracture diverted at least temporarily along the vein. In all but one case, the diversion was uni-directional, with the crack propagating along the part of the vein that makes an acute angle with the load direction, *F*. This propagation path is consistent with a propagation criterion based on the maximum energy release rate by Dahi-Taleghani and Olson (2009).

The SCB experiments delimit conditions where the introduced crack either crosses or diverts at the vein (Figure 3.8). These results can be used to constrain the strength of the vein relative to the host shale (Table 3.3). Given that crossing occurred at 90° (Figure

3.8a) and diversion at 81° (Figure 3.8b), a fairly narrow range for the critical energy release ratio is required, $0.25G_c^{rock} \le G_c^{vein} \le 0.33G_c^{rock}$ (Table 3.3). The critical energy release rate depends on toughness and elastic properties as (Lawn and Wilshaw, 1975)

$$G_c = \frac{K_{Ic}^{\ 2}}{E^*}. \tag{3.3}$$

Table 3.3. G_c^{vein} estimates based on crack propagation results

Vein Angle (θ_o)	Result	G_c^{vein} implication
90°	crossing	$> 0.25G_c^{rock}$
81°	diversion	$< 0.33G_c^{rock}$
58°	diversion	$< 0.59G_c^{rock}$
43°	diversion	$< 0.75G_c^{rock}$

We measured E_{rock} for the homogeneous shale samples to be 8.9 GPa (from Section 3.1). For the calcite cement, we estimate $E_{vein} = 84.3$ GPa based on single calcite crystal measurements (Carmichael, 1989). The test results (Table 3.2) for the divider configuration for the shale gave an average toughness of $K_{Ic} = 0.64$ MPa$\sqrt{\text{m}}$ (from Section 3.5). Consequently, the fracture toughness for the vein can be determined using the equation

$$K_{Ic}^{\ vein} = K_{Ic}^{\ rock} \sqrt{\frac{G_c^{\ vein} \cdot E_{vein}^{\ *}}{G_c^{\ rock} \cdot E_{rock}^{\ *}}}. \tag{3.4}$$

Substituting all the values mentioned above and assuming that the Poisson's ratios for shale (ν_{rock}) and calcite cement (ν_{vein}) are similar enough such that

$E_{vein}^{*} / E_{rock}^{*} = E_{vein} / E_{rock}$, fracture toughness for the vein falls in the range of $0.99 \text{ MPa}\sqrt{\text{m}} \le K_{\text{Ic}}^{vein} \le 1.14 \text{ MPa}\sqrt{\text{m}}$, almost twice the fracture toughness of the shale matrix. Given the E_{vein} we used for the vein was measured on a calcite crystal without any flaws, and our samples include substantial heterogeneity within the crystals composing the veins, it is probable that the actual vein stiffness is lower. If we consider a lower vein stiffness case where E^{*} is the same for both the fracture cement and the shale, the estimate of vein toughness reduces to $0.32 \text{ MPa}\sqrt{\text{m}} \le K_{\text{Ic}}^{vein} \le 0.37 \text{ MPa}\sqrt{\text{m}}$, lower than the fracture toughness of the matrix.

3.8 INFLUENCE OF VEIN THICKNESS ON FRACTURE PATH

A further property we investigated was vein thickness. Four different thicknesses (1.9, 1.3, 0.9, and 0.25 mm) of calcite-filled veins were available in our core collection, and we tested orthogonal approach angles for each ($\theta_o = 90°$). The samples were from different depths and so, unlike the previous series of tests, the shale and fracture cement properties could not be considered as uniform from test to test. We found that fracture crossing was more likely for thin veins and diversion was more likely for thicker ones (Figure 3.9), implying that increasing the thickness of the vein reduced its overall strength (where the critical strength for crossing vs diversion for the $\theta = 90°$ case is $G_c^{vein} = 1/4 \cdot G_c^{rock}$). In all cases of diversion, the failure was only within the calcite, not along the interface between the calcite and the shale host-rock.

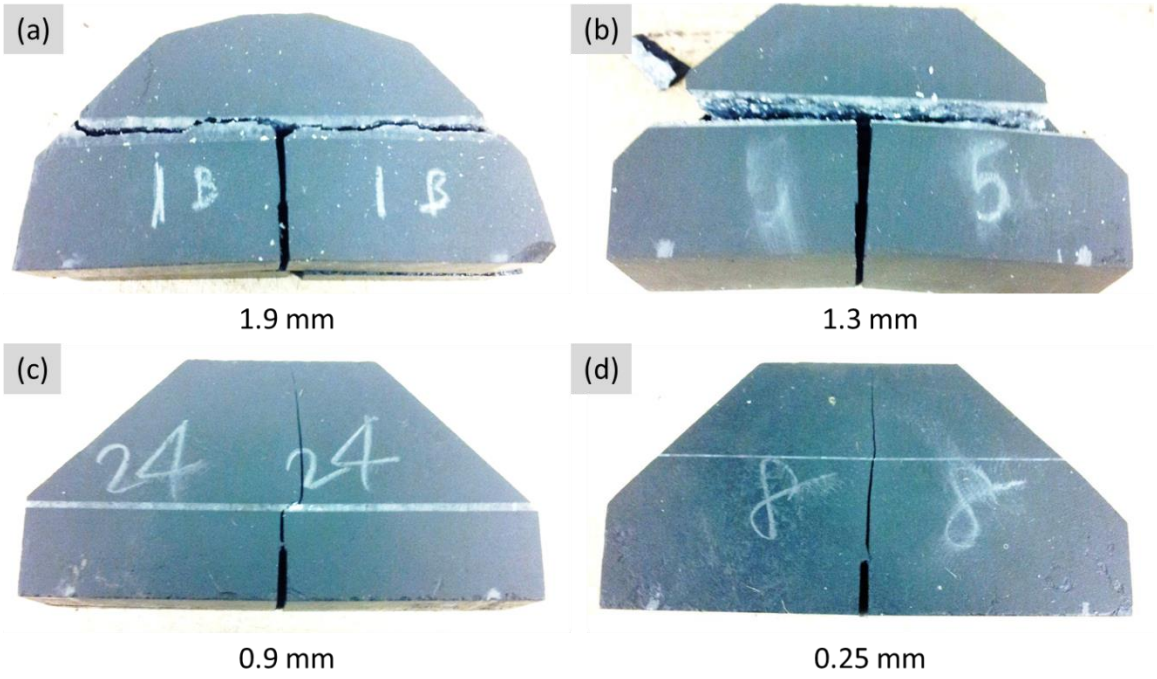

Figure 3.9. SCB tests of orthogonal (angle θ_o of 90°) case with different vein thicknesses: (a) thickness of 1.9 mm, (b) 1.3 mm, (c) 0.9 mm, and (d) 0.25 mm. Induced fracture of (a) and (b) did not cross the vein but it crossed for (c) and (d).

All the experiment results discussed above are single vein cases. Two specimens of approach angle (angle θ_o of 90° and 81°) were tested to evaluate the difference between the impact of single vein and vein cluster on induced fracture propagation (Figure 3.10). The breakage path through the cluster was more like the thin-vein cases (Figure 3.8) as the fracture crossed to the other side for both approach angles, even though the cumulative thickness of the cluster was more like the thick-vein cases (Figure 3.9a and Figure 3.9b).

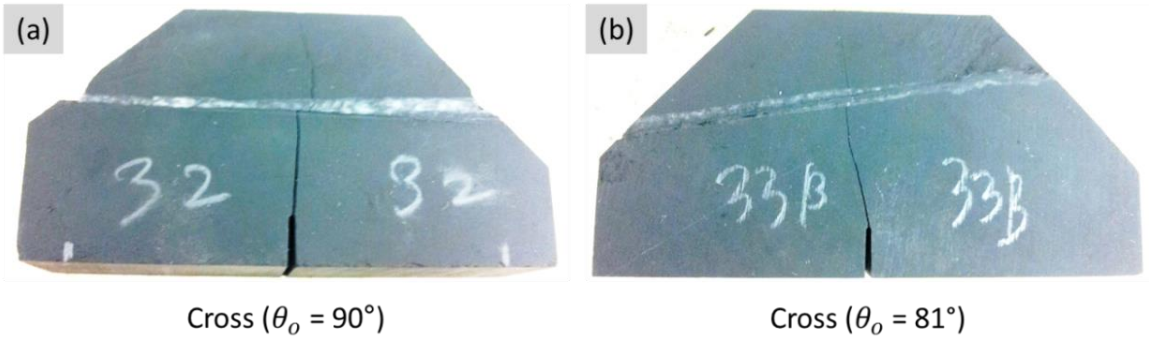

Figure 3.10. SCB tests of cluster of veins: case of cluster at angle θ_o of (a) 90° and (b) 81°.

3.9 MICROSTRUCTURAL ANALYSIS

Thin sections of the SCB test specimens viewed with transmitted light microscopy reveal details of the induced fracture–vein interactions. For the specimen including a thin, single vein with approach angle of 90° (Figure 3.8a), the induced fracture crossed without diverting along the apparent oblique cleavage planes or fluid inclusion trails (Figure 3.11a). However, the induced fracture in the 81° approach angle sample (Figure 3.11b) diverted along the narrow calcite-filled vein, causing a substantial amount of vein–wall parallel damage, which seems to be aided by cleavage planes in the calcite. The main induced fracture path leaves the vein and kinks back into the shale after about 1 mm, but the damage extends beyond the kink point within the calcite. The approach angle cases of $\theta = 58°$ and 43° both show fracture diversion (Figure 3.11c, Figure 3.11d). In the macroscopic photo of the 58° sample (Figure 3.8c), it is clear that both sides of the diverted fracture are calcite lined. Only one half of the sample was recovered in the thin section, but there is a thin coating of calcite cement on the vein wall, indicating the

diverted fracture path continued within the vein cement as it moved away from the intersection point (Figure 3.11c). Again, the diverted fracture path was within the calcite cement rather than along the shale–calcite interface (Figure 3.11d).

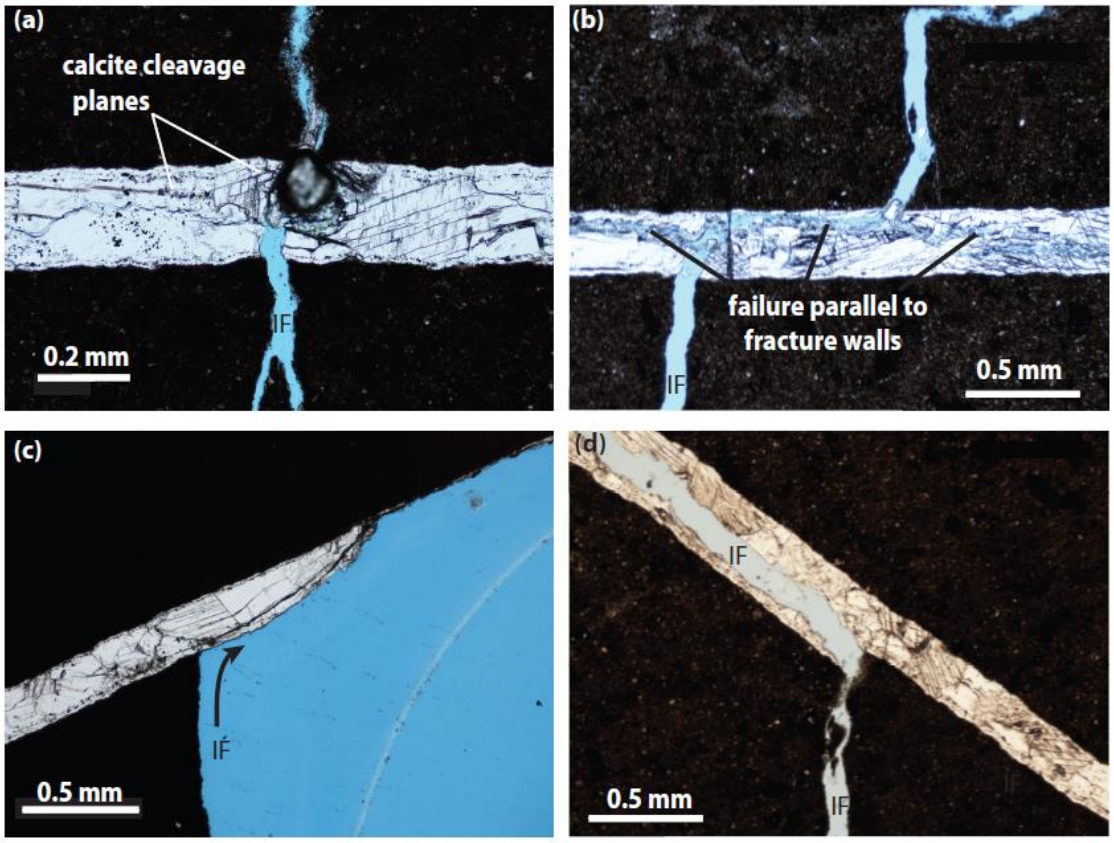

Figure 3.11. Thin section photomicrographs of tested samples with vein thickness of 0.25 mm in Figure 3.8: (a) angle θ_o of 90°, (b) 81°, (c) 58°, and (d) 43°. Induced fractures in (a) crossed but it diverted for (b), (c), and (d). Induced fracture (IF) is noted on the figure and the IF propagated from the top to bottom for all cases.

All four specimens with various thicknesses of veins (Figure 3.9) had different microstructures (Figure 3.12). In the thickest sample (Figure 3.9a, Figure 3.12a – 1.9mm), the induced fracture appears to have utilized the median line in the cement, marked by a plane of solid inclusions. Fluid-inclusion planes located to either side of the median line

apparently provided zones of weakness as well. The next thickest sample (Figure 3.9b, Figure 3.12b – 1.3 mm) also broke within the calcite of the vein, roughly parallel to the vein walls, but the breakage was much more jagged, partially utilizing cleavage planes but not uniformly following them or any other obvious internal plane of weakness.

In the two thinner vein specimens, there was no vein-parallel diversion of the induced fracture. For the vein with a thickness of 0.9 mm (Figure 3.9c, Figure 3.12c), the induced fracture crossed the vein without any appreciable deflection, even though oblique cleavage planes were present within the calcite crystals. For the thinnest vein (Figure 3.9d, Figure 3.12d – 0.25 mm), the induced fracture crossed the vein along a direct path, but that path diverts along the cleavage plane orientation within the vein, about a 30° kink compared to the fracture orientation coming from the shale.

Originally, our hypothesis was that a well-cemented, non-porous discontinuity would transmit sufficient shear stress to allow an opening mode fracture to cross. If reactivation were to occur, it was assumed on the basis of previous observations on cores (e.g. Gale et al., 2007) that the bond between calcite and shale would be the weakest feature, not the internal flaws within the calcite. However, the experimental results in this paper are consistent with the reactivation behavior of some veins in the test samples (Figure 3.3), where fluid inclusion trails indicate multiple refracturing events within the calcite after the initial break occurred in the shale.

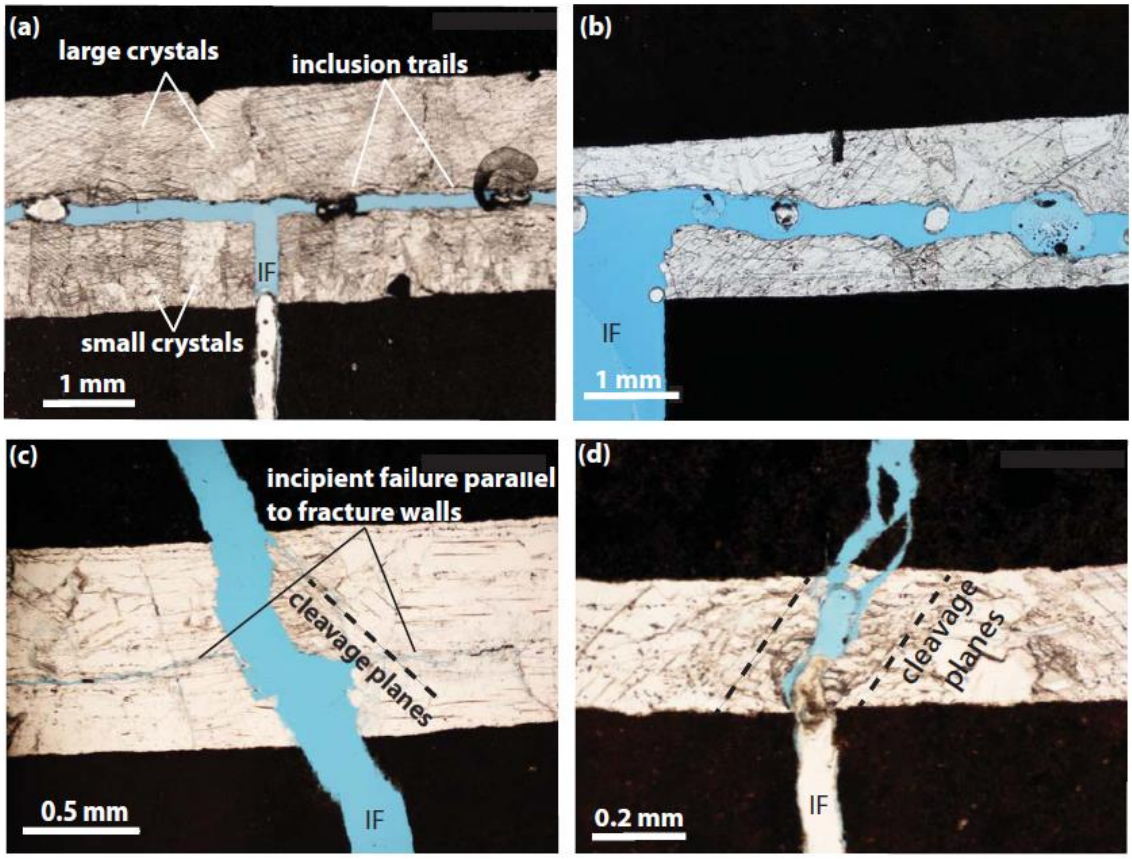

Figure 3.12. Thin section photomicrographs SCB tests of orthogonal (angle θ_o of 90°) case with different thicknesses: (a) thickness of 1.9 mm, (b) 1.3 mm, (c) 0.9 mm, and (d) 0.25 mm. Induced fractures in (a) and (b) did not cross but they crossed for (c) and (d). Induced fracture (IF) is noted on the figure and the IF fracture propagated from the bottom to top for all cases.

3.10 DISCUSSION

Hydraulic fracturing in naturally fractured rocks is an important aspect of shale gas and shale/tight oil development operations. The resulting hydraulic fracture network geometry for Barnett shale wells is thought to be largely dictated by the interaction of hydraulic fractures with natural fractures (Gale et al., 2007). The source of the driving

mechanism for propagation constitutes one major difference between the SCB tests performed in this study and the conditions of a subsurface hydraulic fracture treatment. In the SCB tests, tension at the notch is induced by bending, and the crack propagates unstably once initiated, whereas a hydraulic fracture is driven stably by fluid pressure in the fracture, and the crack tip velocity is limited by the rate at which fluid is pumped into the well. The difference between stable and unstable crack growth in this context could be important. However, similar fracture diversion results have been generated in scaled hydraulic fracture experiments on gypsum blocks, where the fracture was clearly propagating slowly, suggesting at least that the SCB results are applicable to fluid driven fracture behavior (Bahorich, 2012; Bahorich et al., 2012).

Another difference between subsurface fracturing and SCB testing is the nature of the ambient stress state. In the subsurface, the all-around stress is compressive, typically with an anisotropy in the horizontal plane on the order of 1 to 10 MPa parallel to the hydraulic fracture propagation direction. This anisotropy can suppress the opening of fractures that are orthogonal or oblique to the hydraulic fracture. The SCB test is essentially unconfined, but does have a vertical, notch-parallel compression induced by the top loading roller. The horizontal stress in the sample is nominally tensile, giving the same sense of anisotropy observed in the subsurface (the normal stress is more compressive along the primary fracture propagation direction, orthogonal to the veins), but in the SCB test that anisotropy is of much smaller magnitude, on the order of 0.1 MPa. However, this lesser anisotropy may not be too much of a cause for concern, as fracture propagation path is largely dictated by the ratio of the driving stress to the remote stress

anisotropy (Olson and Pollard, 1989). In the subsurface where stress anisotropies are higher, the driving stress of the fracture is also much higher, also on the order of 1 to 10 MPa.

3.11 CONCLUSIONS

This chapter utilized the SCB test to evaluate the impact of calcite-filled veins in Marcellus shale on opening mode crack propagation paths. The SCB test was chosen for this work because of its simple set up and sample size requirement. For the veins with the same thickness and mechanical properties, the more non-orthogonal the angle of approach the more likely the induced fracture was to divert into the vein, consistent with other more elaborate hydraulic fracture experiments on blocks with frictional and bonded interfaces (Blanton, 1982; Zhou et al., 2008; Gu et al., 2011). Even a very thin (~0.25 mm) vein had an impact on a fracture propagating with an oblique angle of approach. Increased vein thickness also made fracture diversion more likely as demonstrated in orthogonal approach angle experiments. Post-test sample observations showed that in cases of fracture diversion into veins, failure occurred within the vein filling calcite, often along preexisting weaknesses such as cleavage or fluid-inclusion planes. Failure did not occur at the vein–rock interface. Based on our experimental results, our best estimate for the fracture toughness of calcite-filled veins in the Marcellus samples is $0.99\ \mathrm{MPa}\sqrt{\mathrm{m}}$ to $1.14\ \mathrm{MPa}\sqrt{\mathrm{m}}$. However, the toughness estimate depends strongly on the Young's modulus value of the calcite, which could not be measured directly on our samples. Consequently, a more useful way of assessing vein strength would be to limit the

discussion to the energy release rate, G, which combines the toughness and modulus effect into one parameter.

Bedding in the shale also provided planes of weakness that were exploited by the propagating fracture. The load–displacement curves for the experiments with significant bedding plane slip or separation exhibited lower peak loads but demonstrated more post-peak residual strength, implying a more cohesive crack tip behavior than the purely brittle response observed when bedding planes were not activated.

CHAPTER 4: FRACTURE INTERACTION ANALYSIS BY DISCRETE ELEMENT METHOD

To overcome the limitations of the experimental approach, numerical modeling can be used. A variety of numerical models have been proposed to generate practical deformation and failure behavior of rocks. One such model is the Discrete Element Method (DEM), also known as the Distinct Element Method. It consists of spherical particles and bonds to represent rock-type materials. The densely packed particles simulated by DEM can reproduce many analogous rock behaviors. These include the following: elasticity, fracturing, acoustic emission, hysteresis, dilation, rock anisotropy due to damage accumulation, and post-peak softening and strengthening effect with confining stresses (Potyondy and Cundall, 2004).

Potyondy et al. (1996) categorized two methods in modeling inelastic deformation and fracture of brittle materials including rocks. One is the indirect method where damage is represented by constitutive laws. The other is the direct method, where damage is expressed by discrete cracks. DEM is a direct method that models movements and interactions of particles (Cundall and Strack, 1979). Park et al. (2004) noted that the direct method has several advantages over the indirect methods. For example, DEM does not consider complex constitutive relationships but directly applies Newton's second law to trace the movements and interactions of particles. Particles interact with one another through contacts or bonds, and cracks are simply predicted by the applied strength that exceeds the tensile or shear strength of the bonds. Fracture patterns are determined by the

cluster of bond breakages. Thus, multi-stranded fractures can develop as one fracture interacts with planes of weakness. Since DEM is based on microscopic mechanisms and the mechanical behavior of a rock is not predefined as in continuum methods, it is ideal to understand and investigate the factors of rocks' complex macro-mechanical behavior (Schöpfer et al., 2009). Another important feature of DEM is that the fracture propagation process requires no special meshing. These capabilities can enable researchers to understand the interaction analysis of opening mode fractures with preexisting discontinuities.

After Cundall (1971) and Cundall and Strack (1979) introduced DEM to rock and soil mechanics, respectively, DEM has been utilized in many investigations to understand the physics of rock mechanics. Researchers have used DEM to solve applications of geomechanics (Potyondy et al., 1996, Potyondy and Cundall, 2004; Lee et al., 2006), tectonics (Finch et al., 2003; Hardy and Finch, 2006; Hardy and Finch, 2007), wave propagation (Young and Pettitt, 2000; Narayanasamy, 2002), and fracture propagation (Thallak et al., 1991; Gumbsch, 1995; Park et al., 2004; Park, 2006).

Virgo et al. (2013) investigated the interaction between preexisting veins and extension fractures using tension tests on notched samples with three-dimensional (3D) DEM models. They analyzed the impact of the approach angle and the strength of the vein on fracture diversion, bifurcation and nucleation in the vein. In addition, Virgo et al. (2014) showed that DEM can mimic the crack-seal mechanism in natural fractures. Using a two-dimensional (2D) DEM, Spence and Finch (2014) studied fracture network development in reservoirs with chert nodules. They found that the influence of

mechanical stratigraphy on fracture propagation created complex fracture geometry. DEM offered analogous outcomes of fracture geometry to the outcrops. Zhang et al. (2014) introduced a 2D hybrid DEM–FDM (Finite Difference Method) to simulate hydraulic fracture interactions with planes of weakness. They investigated how the interaction was impacted by the stress conditions, stiffness and strength ratio between the two materials, approach angle, friction coefficient of the interface, injection rate, and injection fluid viscosity. Their DEM application focused on the interaction between hydraulically pressurized fractures and the frictional interfaces.

In this chapter, the 3D DEM technique is introduced to investigate micromechanical fracture interaction behavior, and to reproduce and analyze the SCB experiments in Chapter 3. The influence of the approach angle, strength, stiffness, and thickness of the vein on fracture interaction is assessed and interpreted through the results of the numerical modeling.

4.1 PARTICLE FLOW CODE

The Particle Flow Code in three-dimensions (PFC3D) (Itasca, 2008) is also known as the Bonded-Particle Model (BPM) that directly mimics the behavior of rocks. It uses three main characters: particles, bonds, and walls. Particles are the main components that consist of mass and volume, and they could be used to represent grains or clusters of grains, as in this study, in granular materials. Adjacent particles are held together with bonds, which is analogous to the cement between the grains in brittle rocks. PFC3D uses two types of bond models called parallel bonds and contact bonds. Parallel bonds are

suitably representative of cement between the grains since they can resist moment or rotation. Contact bonds only resist normal forces. Figure 4.1 is a schematic diagram of spherical particles and a parallel bond in PFC3D. Particles and bonds together form a densely packed assembly, or a rock specimen, under boundary conditions applied by walls. Walls act as the boundary for sample generation and as the loading surface of a loading machine.

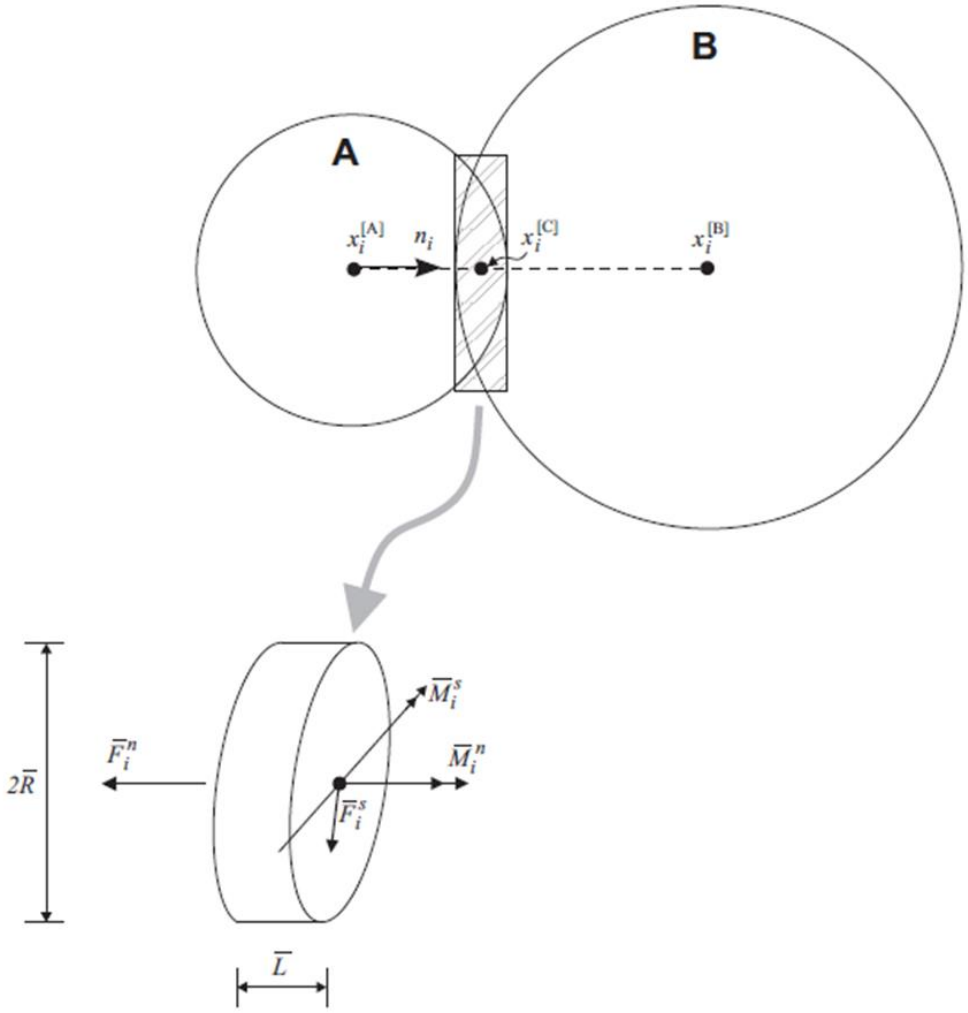

Figure 4.1. Schematic view of two spherical particles in contact and a parallel bond depicted as a cylinder of cementatious material between the particles (Itasca, 2008).

Contacts, cracks, and positions of particles are calculated every time step, providing the information of fracture interaction process (Figure 4.2). Its straightforward application of expressing heterogeneous materials by simply applying different particle and parallel bond properties for a specific zone makes PFC3D attractive for the fracture interaction analysis of opening mode fractures with veins.

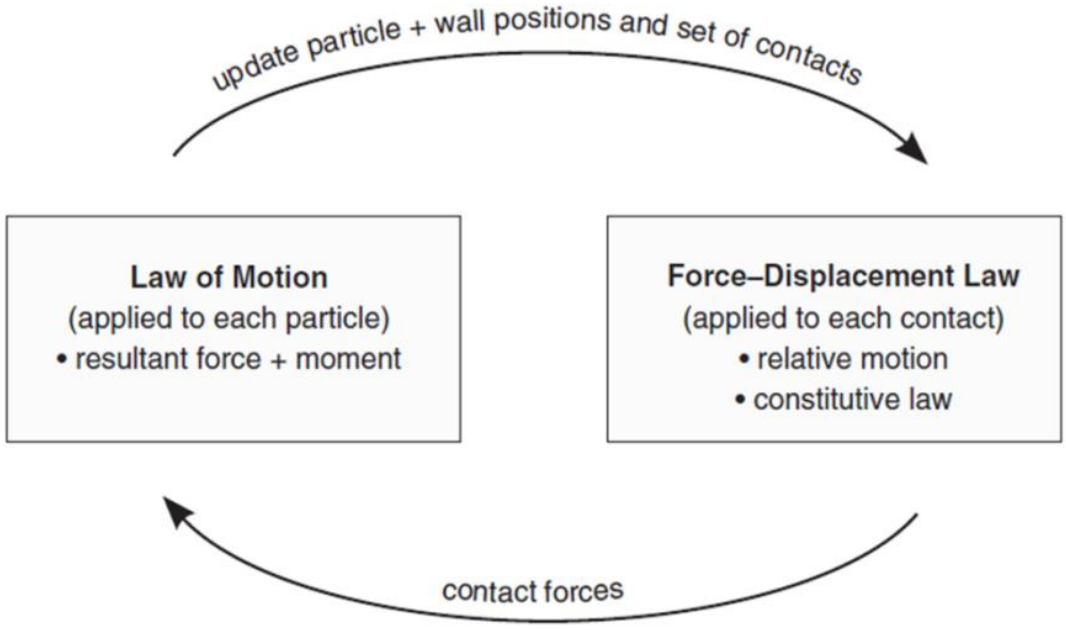

Figure 4.2. The cycle of calculation between particles and contacts in PFC3D (Itasca, 2008).

4.2 SAMPLE ASSEMBLY GENERATION

The procedure for generating a sample assembly in PFC3D was as follows. Figure 4.3 illustrates a sample assembly by PFC2D from Potyondy and Cundall (2004).

1. To contain the particles and to apply boundary conditions, six frictionless boundary walls were set in a rectangular parallel-piped shape based on the

final specimen size. To fill the vessel, seed particles were randomly distributed inside the boundary walls of a specified range. The diameter of the seed particles are initially set at half of the final particle diameter and followed the uniform distribution bounded by the minimum ($D_{\min}$) and maximum ($D_{\max}$) diameters.

2. The particles were expanded to the desired diameter. Particles were set to be frictionless so they could rotate and rearrange position to fill in the gaps for a stable dense-packed sample. Forces that were locked in during the expansion were removed by the movement of the boundary walls. The iteration of wall movement ended when the boundary stress reached the applied isotropic stress.
3. Floating particles (particles with fewer than three contacts) were eliminated by increasing their diameters to make contact with adjacent particles, resulting in a compact assembly. While expanding the floating particles, an iteration of wall movement was operated to remove the locked-in forces.

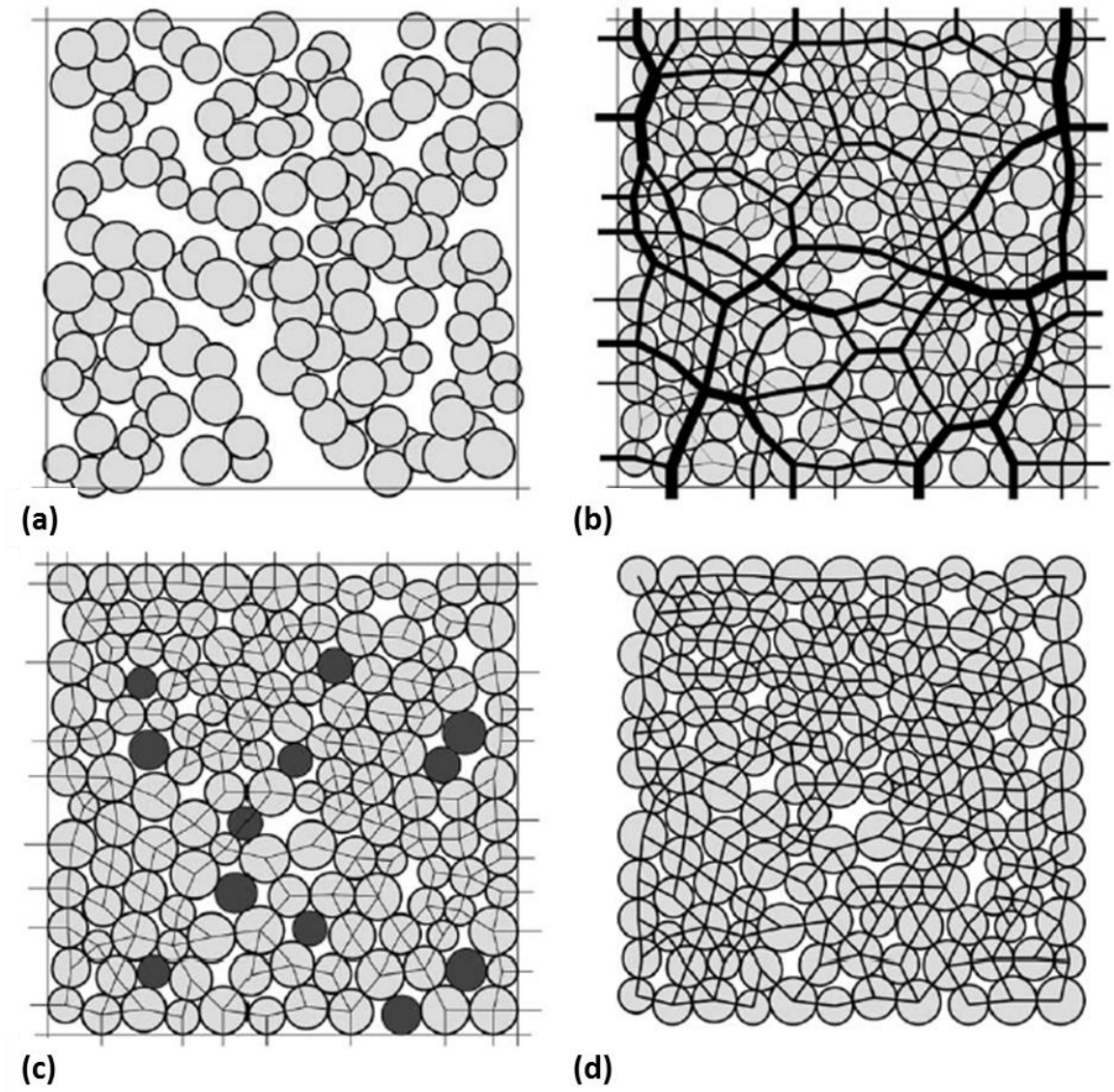

Figure 4.3. The procedure of sample assembly generation by PFC2D model: (a) randomly distributed particles before arrangement, (b) contact-force distribution after installing isotropic stress, (c) elimination of floating particles, and (d) installation of the parallel bond network (Potyondy and Cundall, 2004).

4. Parallel bonds were installed at particle–particle contacts to represent cement between the grains in a rock. The necessary microscopic mechanical properties were particle friction coefficient, parallel bond radius multiplier, particle and parallel bond stiffnesses, particle and parallel bond normal to

shear stiffness ratios, parallel bond normal and shear strengths. These properties were determined by comparison to triaxial compression test results and from values reported in literatures as described in Section 4.3. The parallel bond radius multiplier ($\bar{\lambda}$), which is an input parameter, is the ratio of the parallel bond radius to the smaller of the particle radius of the two particles in contact. To generate heterogeneity or preexisting discontinuity, different stiffness and parallel bond strength were assigned for specified zones.

5. The boundary walls were removed to allow the dense-packed assembly to relax and reach static equilibrium.
6. To create SCB samples, particles and parallel bonds outside the range of the semi-circular shape were deleted. Three cylindrical walls were newly assigned (one above and two below the specimen) to represent the loading roller and supporting rollers, respectively. Particles and parallel bonds representing the vein were grouped together and assigned with a different set of microscopic properties compared to the rock matrix.

4.3 MICROSCOPIC PARAMETER DETERMINATION

Park et al. (2004) utilized the sand grain size for the size of a particle in their numerically-modeled SCB specimen. However, the grain size of shales, generally less than 0.004 mm in diameter, is inappropriate for the particle size in PFC3D since a substantial amount of particles are required to model a sample (diameter of 58.4 mm and

thickness of 14 mm) similar to the experimental SCB specimen of Marcellus shale. In fact, the total number of particles in DEM governs the overall computational time and it is unreasonable to set a particle to express one grain. Therefore, the particles in this study represent clusters of grains or finite elements to form a rock-like material and to minimize the computational cost. The minimum particle diameter ($D_{\min}$) is 0.45 mm and $D_{\max}/D_{\min}$ is 1.65 for arbitrary isotropic packing (Potyondy and Cundall, 2004). The average diameter of particles is approximately 150 times greater than the grain size of shale, around the grain size of sand (Camacho, 2001; Zietlow and Labuz, 1998), but small enough, 0.1% and 4% of the specimen diameter and thickness, to describe the fracture propagation in the SCB specimen. Further analysis on particle size to sample size ratio is discussed in section 4.12.

To match the input microscopic properties of particles and bonds to the measured rock mechanical properties (e.g., E, ν, UCS, σ_T) in the laboratory, it is necessary to carry out a trial-and-error process with conventional experimental tests in PFC3D, such as the Brazilian test, the uniaxial and the triaxial compression test. Generally, Young's modulus and internal friction primarily constrain stiffness of the particles (k_n for normal, k_s for shear stiffness) and parallel bonds ($\overline{k_n}$ for normal, $\overline{k_s}$ for shear stiffness), while UCS and cohesion (S_o) constrain the parallel bond strengths ($\overline{\sigma}$ for normal, $\overline{\tau}$ for shear strength). Macroscopic mechanical properties (E_{rock} of 8.9 GPa and UCS_{rock} of 53.4 MPa) of collected shale samples from Section 3.1 are utilized to determine microscopic properties of the particles and parallel bonds.

Some guidelines to assist the matching process are given by Itasca (2008) and Potyondy and Cundall (2004). For PFC3D, particle stiffness can be expressed as

$$\begin{aligned} k_n &= 4RE_p \\ k_s &= \frac{k_n}{k_n/k_s} \end{aligned} \tag{4.1}$$

where E_p is the particle Young's modulus, and R is the radius of the particle. Normal and shear parallel bond stiffnesses can be calculated from

$$\begin{aligned} \overline{k_n} &= \frac{\overline{E}}{R^A + R^B} \\ \overline{k_s} &= \frac{\overline{k_n}}{\overline{k_n}/\overline{k_s}} \end{aligned} \tag{4.2}$$

where $\overline{E}$ is the parallel bond Young's modulus, R^A and R^B are the radii of particles in contact. Young's moduli for particle (E_p) and parallel bond ($\overline{E}$) are set equal to $E_{rock} = 8.9$ GPa for the initial input.

The porosity and Poisson's ratio of Marcellus shale were not measured in the setting of experiments but are required for microproperties in PFC3D. They were selected from the literature for an approximate value. Smrecak (2011) described that the porosity of Marcellus shale ranges between 0% to 18%. For this study the porosity is assumed to be 15% which matches with the parallel bond radius multiplier ($\overline{\lambda}$) of 0.9 in Park's (2006) study. The $\overline{\lambda}$ governs the volume of the cement that eventually controls the porosity of the assembly.

In PFC3D, Poisson's ratio is independent of particle size and only depends on the stiffness ratio of the particles (k_n/k_s) and the parallel bonds ($\overline{k_n}/\overline{k_s}$). When determining k_n/k_s and $\overline{k_n}/\overline{k_s}$ by matching the Poisson's ratio of the modeled assembly to the value of a real rock, both k_n/k_s and $\overline{k_n}/\overline{k_s}$ are set as equal to minimize the number of free parameters (Potyondy and Cundall, 2004).

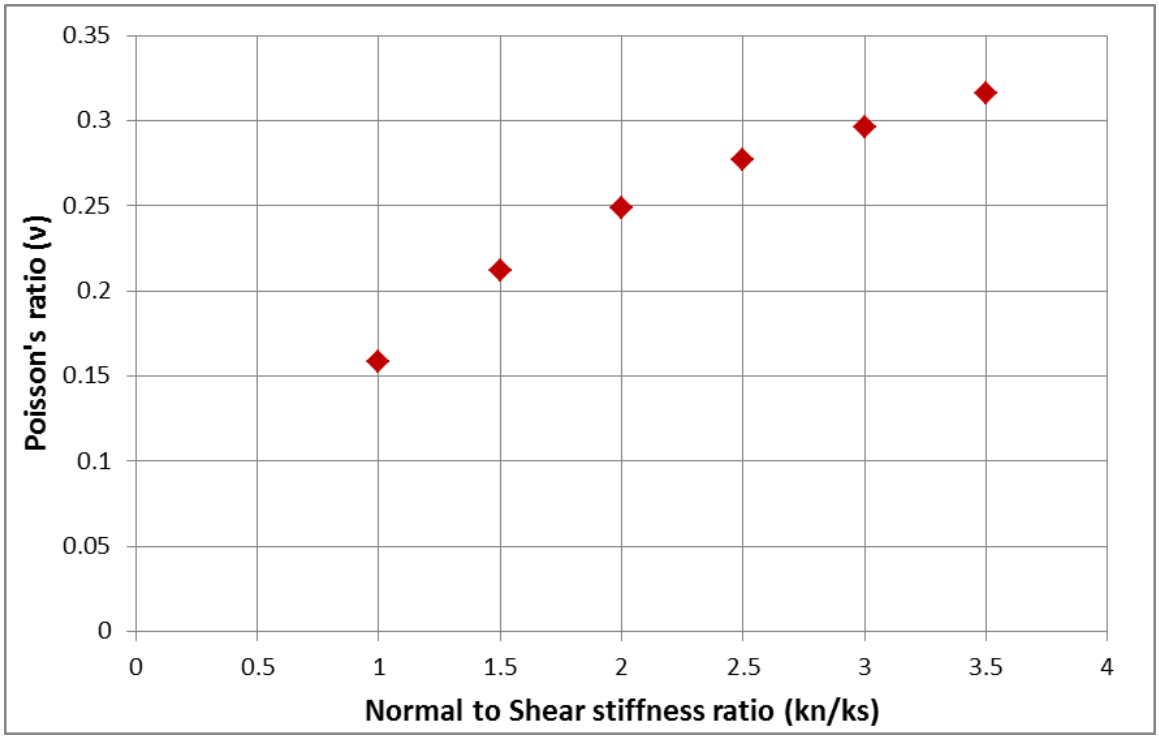

Figure 4.4. The relationship between the stiffness ratio ($k_n/k_s = \overline{k_n}/\overline{k_s}$) and Poisson's ratio.

Figure 4.4 shows the dependence of Poisson's ratio on k_n/k_s ($k_n/k_s = \overline{k_n}/\overline{k_s}$) in uniaxial compression tests. Poisson's ratio generally increases with stiffness ratio. Based on the Marcellus shale well data (Gargouri, 2012; Izadi et al., 2014), Poisson's ratio ranges between 0.25 and 0.3. Corresponding to 0.275, k_n/k_s is 2.5 (Figure 4.4).

After the calibration, microscopic input parameters for the rock matrix are determined as listed in Table 4.1. The friction coefficient (μ) was assumed to be 0.75, a value within the range of μ for rocks, 0.6 to 0.85 (Byerlee, 1978).

Table 4.1. Microproperties for the rock matrix in PFC3D

Particle properties	
Modulus, E_p (GPa)	11.0
Normal/Shear Stiffness Ratio, k_n/k_s	2.5
Minimum Particle Diameter, $D_{\min}$ (mm)	0.45
Maximum/Minimum Diameter Ratio, $D_{\max}/D_{\min}$	1.65
Friction Coefficient, μ	0.75
Density, ρ (kg/m^3)	2650
Parallel bond properties	
Modulus, $\overline{E}$ (GPa)	11.0
Normal/Shear Stiffness Ratio, $\overline{k_n}/\overline{k_s}$	2.5
Normal Strength, $\overline{\sigma}$ (MPa)	45.0 $\pm$ 4.5 (mean $\pm$ SD)
Shear Strength, $\overline{\tau}$ (MPa)	45.0 $\pm$ 4.5 (mean $\pm$ SD)
Radius Multiplier, $\overline{\lambda}$	0.9

Macroscopic mechanical properties of the modeled rock are determined from the uniaxial compression and SCB tests (Table 4.2). Illustrated in Figure 4.5 are the unconfined uniaxial compression test results of the numerically modeled assembly and the Marcellus shale. The stepping curves from the laboratory experiment (red curves in Figure 4.5 and Figure 4.7) are due to the low resolution of the displacement transducer. The linear portion of the stress-strain curve, i.e., the slope, represents the Young's modulus (8.93 GPa) and the peak load represents the *UCS* (46.4 MPa) of the modeled rock. Also, an SCB test was performed in PFC3D to measure the fracture toughness of

the rock. The trend of the PFC3D curve matched well with the experimental result but the peak load was approximately 400 N greater resulting in different fracture toughness (see Figure 4.7).

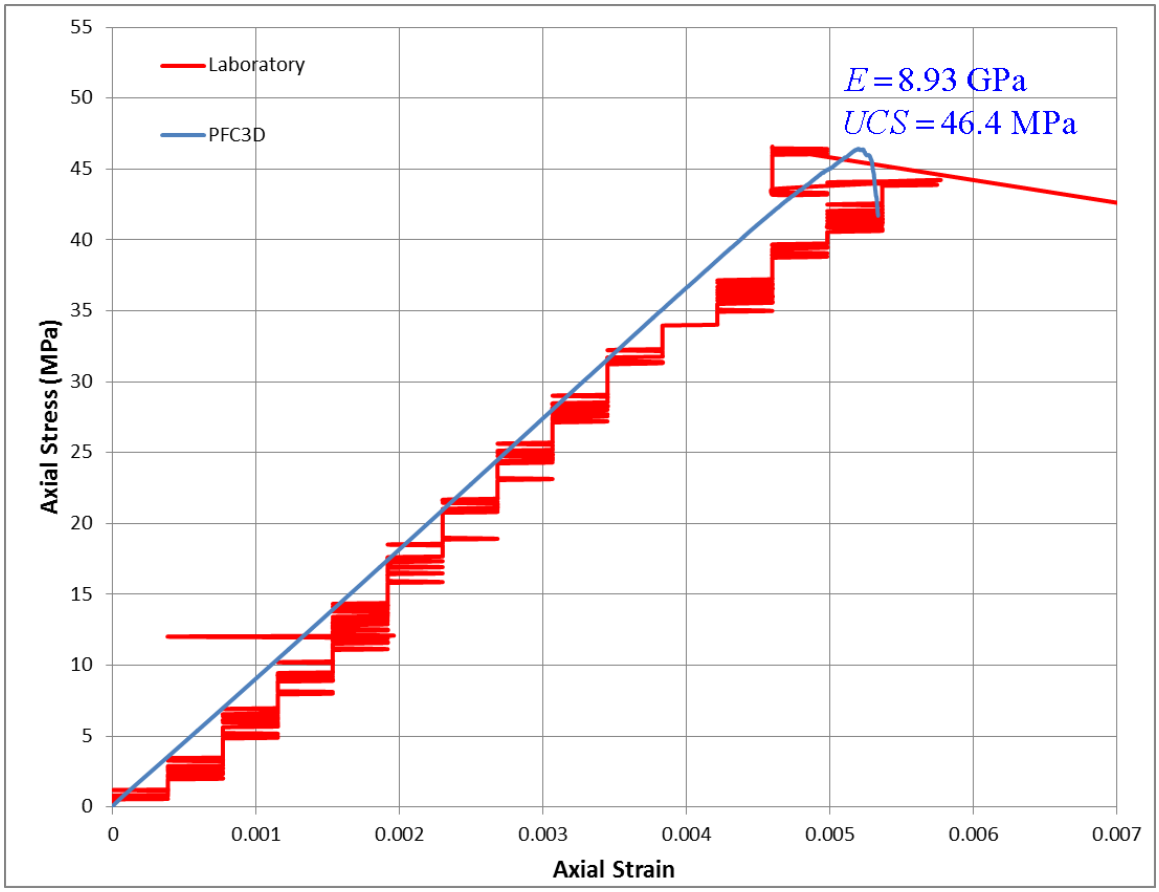

Figure 4.5. Axial stess-versus-axial strain curves from the uniaxial compression tests of Marcellus shale. Blue line illustrates the PFC3D result and red line is the laboratory result.

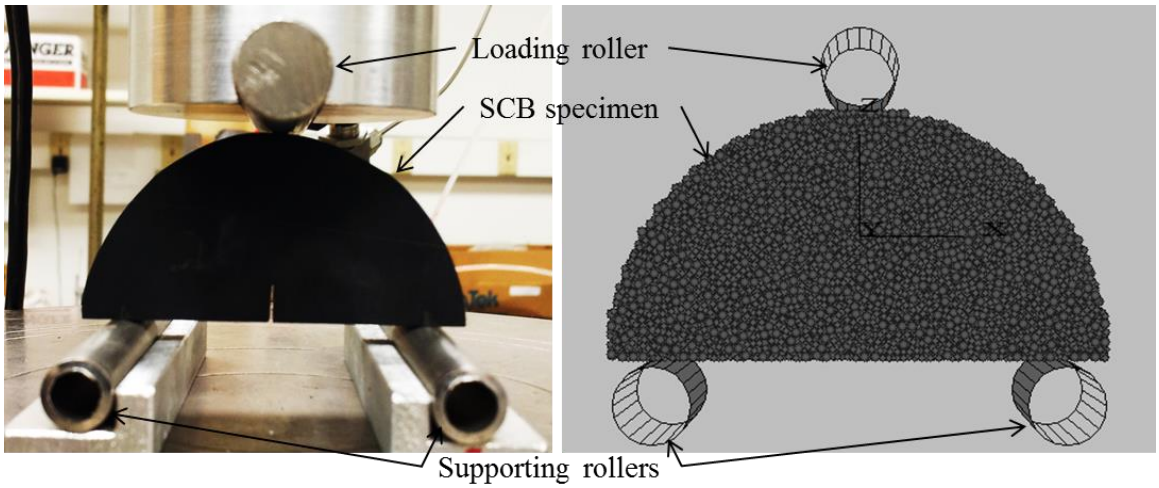

Figure 4.6. The experimental set-up of SCB test and the numerically modeled SCB test with PFC3D.

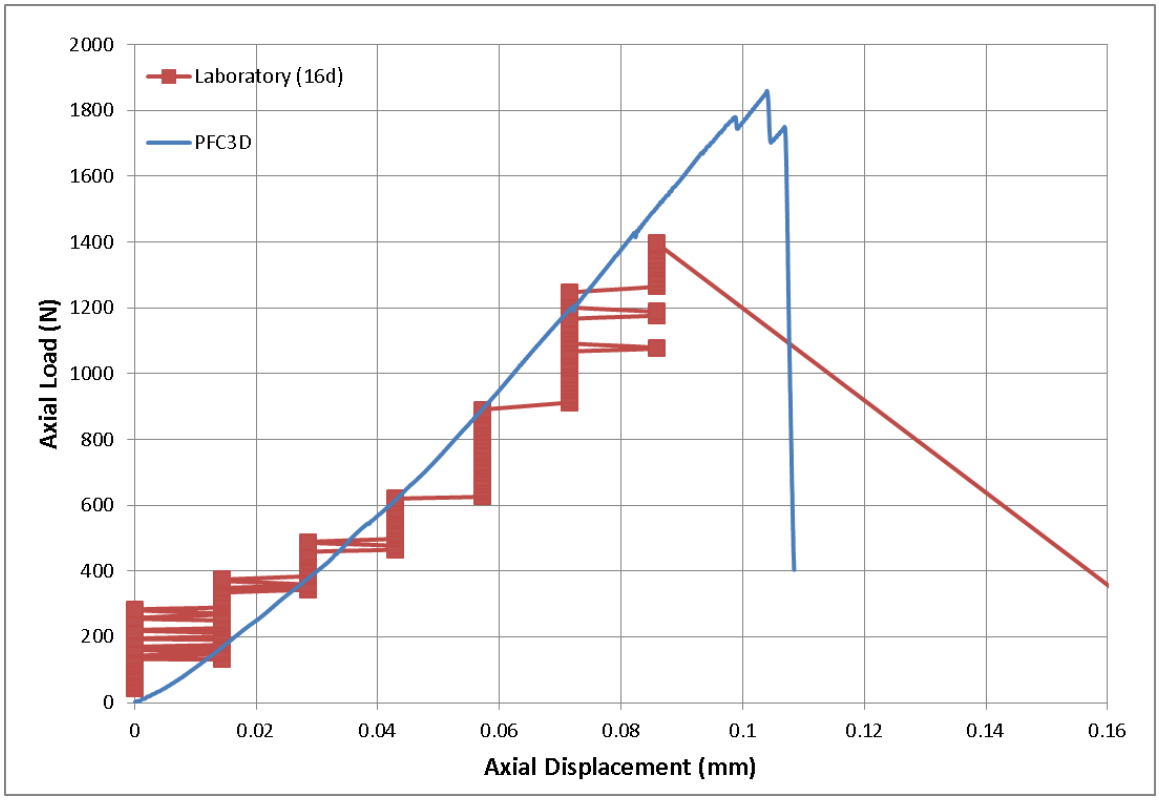

Figure 4.7. Load-versus-displacement curves from the SCB test of Marcellus shale. Blue line illustrates the PFC3D result and red line is one example from the laboratory results (sample 16d in Table 3.2). The PFC3D specimen for this example was set with diameter of 61 mm and a thickness of 20.3 mm to match the size of sample 16d.

The tensile strength (σ_T) of the sample assembly in PFC3D is measured from the Brazilian test which is an indirect tensile test. Following the standard method of ISRM (1978), the tensile strength of the numerically-modeled assembly was 16.4 MPa from

$$\sigma_T = \frac{2P}{\pi DL} \tag{4.3}$$

where P is the peak load, D is the diameter of the sample, and L is the length of the cylindrical sample (Claesson and Bohloli, 2002). Unfortunately, the tensile strength of the Marcellus shale was not measured for comparison because all Marcellus core samples were used in the SCB tests.

Table 4.2. The elastic properties and strengths of Marcellus shale in experiment and PFC3D

Property	Experiment	PFC3D
Young's modulus, E (GPa)	8.9 ($SD = 0.17$)	8.93
Unconfined Compressive Strength, UCS (MPa)	53.4 ($SD = 8.6$)	46.4
Fracture Toughness, K_{Ic} ($\mathrm{MPa}\sqrt{\mathrm{m}}$)	0.64 ($SD = 0.17$)	1.08
	Literature	PFC3D
Poisson's ratio, ν	0.25 – 0.3	0.277
Tensile Strength, σ_T (MPa)	–	16.4

The UCS/σ_T ratio was around 2.83 (Table 4.2). This is lower than laboratory test results of rocks from other studies that generally provide a UCS/σ_T ratio of between 10 and 50 (Vutukuri et al., 1974; Nazir et al., 2013). Several studies have noted that PFC3D usually predicts higher tensile strength compared to experiments and it is impossible to

match *UCS* and σ_T at the same time (Potyondy and Cundall, 2004; Park, 2006). Potyondy and Cundall (2004) argued that high σ_T value might result from the spherical grain shape and the fact that the particles cannot break in PFC3D. Park (2006) noted that the experimental rock tensile strength is strongly influenced by the testing method, sample size, heterogeneity, and flaw distribution in the rock sample. Moreover, Park et al. (2004) noted that *UCS* represents more of the material strength than σ_T because σ_T depends more on the sample size than does *UCS* . Therefore, microproperties are matched with the *UCS* value and analysis of the interaction will mostly focus not so much on an exact quantitative value but on the relative fracture toughness between the rock and the vein.

Rocks generally have flaws that control the failure strength. Schöpfer et al. (2009) showed that the increase in the percentage of non-bonded contacts, which can be interpreted as flaws in rocks, increases the UCS/σ_T in PFC3D. To simulate the natural properties of the rock and increase the UCS/σ_T ratio closer to the real rock in PFC3D, flaws were artificially generated in the numerical model. Flaws were represented as parallel bonds in the assembly being randomly deleted by percentage (10%, 20%, 30%, 40%, 50%) from the total parallel bond number. With the deletion of parallel bonds, the modeled assembly became more compliant which is analogous to the results of Schöpfer et al. (2009). In order to correspond with the material's Young's modulus, it was necessary to increase the stiffnesses of both particles and parallel bonds.

Table 4.3. Results of UCS/σ_T for flaw-contained materials in PFC3D

Flaw percentage (%)	UCS (MPa)	σ_T (MPa)	UCS/σ_T
0	46.4	16.4	2.83
10	40.4	15.1	2.82
20	35.4	13.6	2.61
30	29.7	11.8	2.51
40	23.6	10.9	2.15

Figure 4.8 displays the results from the uniaxial compression and Brazilian tests of the flaw-embedded materials. The PFC3D results in Table 4.3 show that the flaws inside the material do not improve the UCS/σ_T ratio. In fact, they even lower the UCS/σ_T which is the opposite of the results of Schöpfer et al. (2009). The discrepancy between the trends is possibly from different tensile strength tests, the Brazilian test for this study and the direct extension test for Schöpfer et al. (2009). The SCB test, utilized for the interaction analysis in this study, is accomplished by 3-point compressive loading that is similar to the compressive load in the Brazilian test rather than the tensile loading in the direct extension test. Thus, hereafter, all the samples in PFC3D were generated without any flaws based on the highest UCS/σ_T case in Table 4.3.

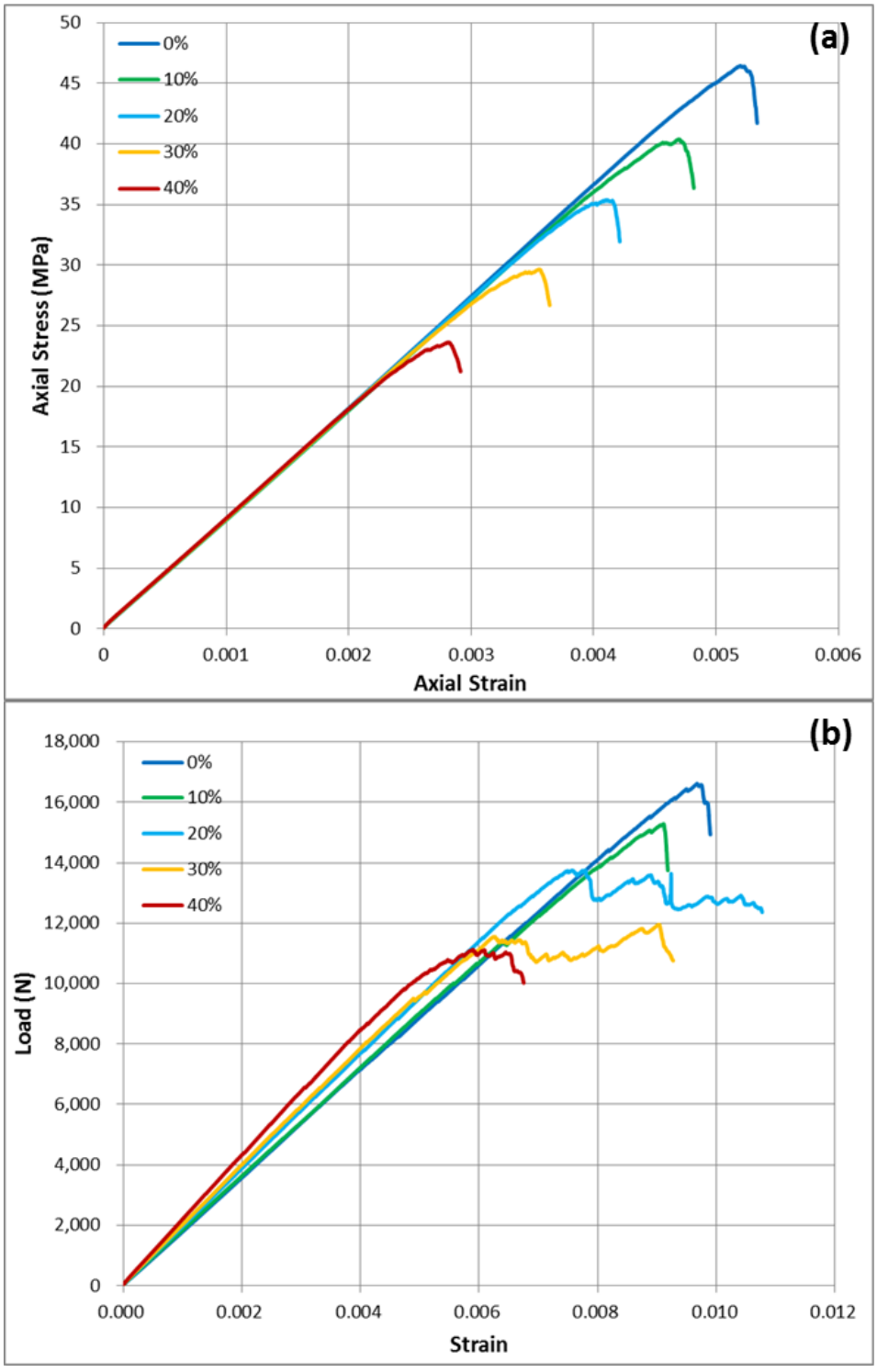

Figure 4.8. PFC3D Results of flaw-contained materials (parallel bonds deletion of 0%, 10%, 20%, 30%, and 40%): (a) stress-strain curves from the uniaxial compression test and (b) load-strain curves from the Brazilian test.

4.4 SCB TEST PREPARATION

In PFC3D, forces and displacements are calculated each time step and the time step depends on the stiffness of the particle, parallel bond, and loading rate. Since the stiffness is fixed for a certain rock specimen and the particle size is determined, the loading rate is the only input parameter that can be modified to control the overall computational time. If the loading rate is to match the laboratory set up (0.003 inch/min or 1.27×10^{-6} m/s), the total running time of PFC3D is approximately one week to load one SCB sample until failure. Also, PFC3D utilizes a high damping coefficient of 0.7 to efficiently dissipate the kinetic energy generated in the system making the model highly-damped to approximate the real rock response (Potyondy and Cundall, 2004; Itasca, 2008). This makes it impossible for PFC3D to load the model at the same rate as the standard rock experimental tests. If the problem is only focusing on the quasi-static behavior, PFC3D model can run at higher loading rate than the experiment to reproduce the deformation (Ding et al., 2014; Zhang and Wong, 2013). Other studies have utilized loading rates in the range of 0.005 m/s to 0.6 m/s in PFC2D and PFC3D (Hazzard et al., 2000; Potyondy and Cundall, 2004; Cho et al, 2007; Itasca, 2008; Park and Song, 2009; Ghazvinian et al., 2012; Zhang and Wong, 2013; Ding et al., 2014).

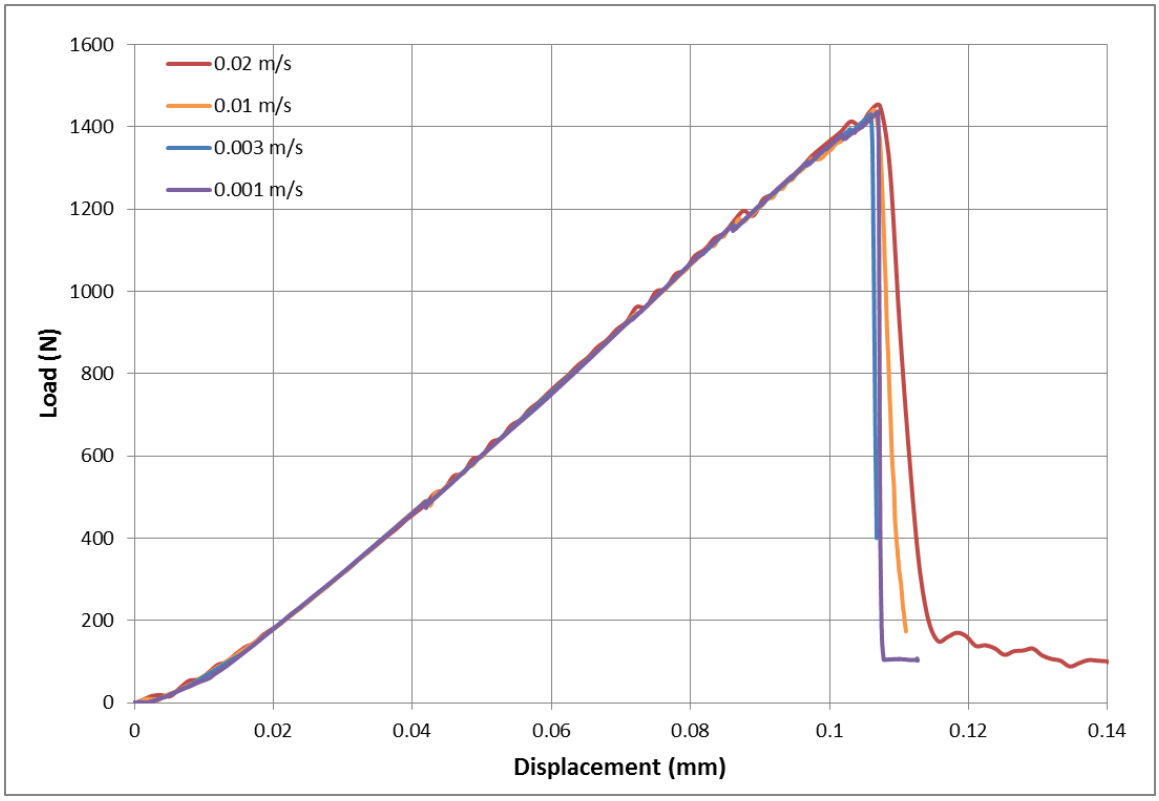

Figure 4.9. Load-versus-displacement curves of the SCB test under various loading rates in PFC3D.

Zhang and Wong (2013) concluded that the loading rate would have an impact on the cracking process in PFC2D model and that a lower loading rate range (0.005 m/s to 0.08 m/s) was a reasonable loading rate for flaw-contained specimen under compressive loading. In this study, to select an appropriate loading rate for the SCB test, four loading rates (0.02 m/s, 0.01 m/s, 0.003 m/s, 0.001 m/s) were examined and compared. The results show that the load-displacement curves converged to a similar rock deformation behavior for loading rates under 0.003 m/s (Figure 4.9). Thus, the loading rate of 0.003 m/s was selected for the SCB test in PFC3D.

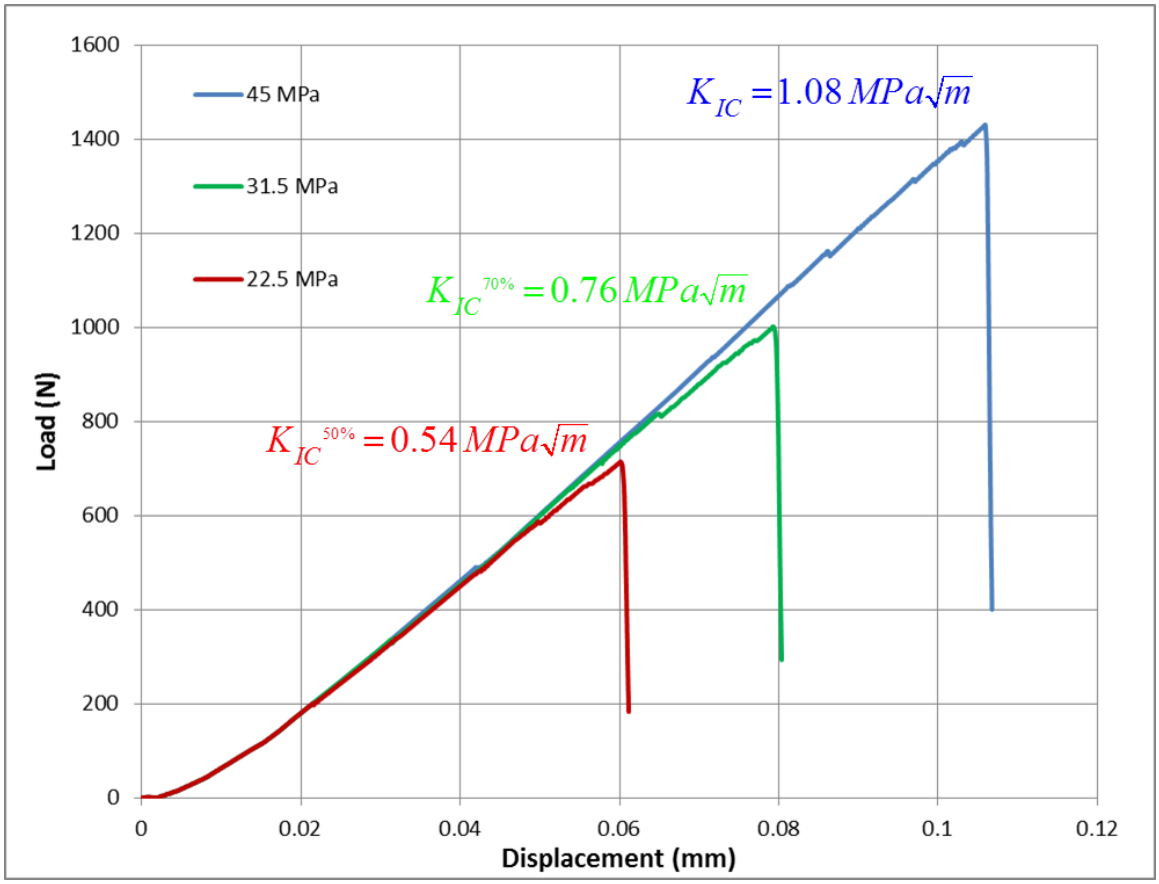

Figure 4.10. The impact of parallel bond strengths ($\bar{\sigma}$ and $\bar{\tau}$) on the fracture toughness in PFC3D.

The relationship between the parallel bond strength and the fracture toughness was evaluated with the SCB test by reducing both normal and shear strengths (70% and 50%) from the Marcellus shale case. Figure 4.10 shows the load-versus-displacement curve of the SCB test with three different parallel bond strengths (45 MPa – Marcellus shale, 31.5 MPa, and 22.5 MPa).

The 31.5 MPa case (70% of Marcellus shale) and the 22.5 MPa case (50% of Marcellus shale) reveal that the fracture toughnesses were exactly a 0.7 ratio ($0.76\ \text{MPa}\sqrt{\text{m}}$) and a 0.5 ratio ($0.54\ \text{MPa}\sqrt{\text{m}}$) to the fracture toughness of the

Marcellus shale in PFC3D ($1.08\ \mathrm{MPa}\sqrt{\mathrm{m}}$), respectively, indicating that the fracture toughness was directly proportional to the parallel bond strength. The slope of the load-displacement curve before the failure (peak load) does not change with the various parallel bond strength, and all three cases show brittle post-peak response.

4.5 SCB SPECIMEN WITH VEIN

The mechanical properties of the calcite vein are different from the shale matrix. They disturb the stress field in the specimen, introducing difficulties in the analytical prediction of fracture crossing or diversion. The main objective of the numerical analysis is to understand the mechanisms and important factors in the interaction between the induced fracture and the vein, factors impossible to evaluate through laboratory SCB tests. In the PFC3D model, calcite veins were implemented with various strengths, thicknesses, approach angles, and stiffness ratios to the rock matrix to perform sensitivity analysis on each constituent.

Following the steps described in Section 4.2, a SCB test specimen was made ready for loading as shown in Figure 4.11. The diameter of the modeled sample is 58.4 mm (2.3 inch), and the thickness is 14 mm (0.55 inch) for all cases and it is formed of a total 19,697 particles and 54,544 parallel bonds. Dark gray particles represent shale matrix and white particles compose the calcite-cemented vein (Figure 4.11a). The notch at the bottom of the sample is created by deleting the parallel bonds inside the range (Figure 4.11b). Three cylindrical walls represent the loading and supporting rollers to mimic the

experimental set-up that will provide a three-point bending force on the sample to generate opening mode fracture from the tip of the notch when loading.

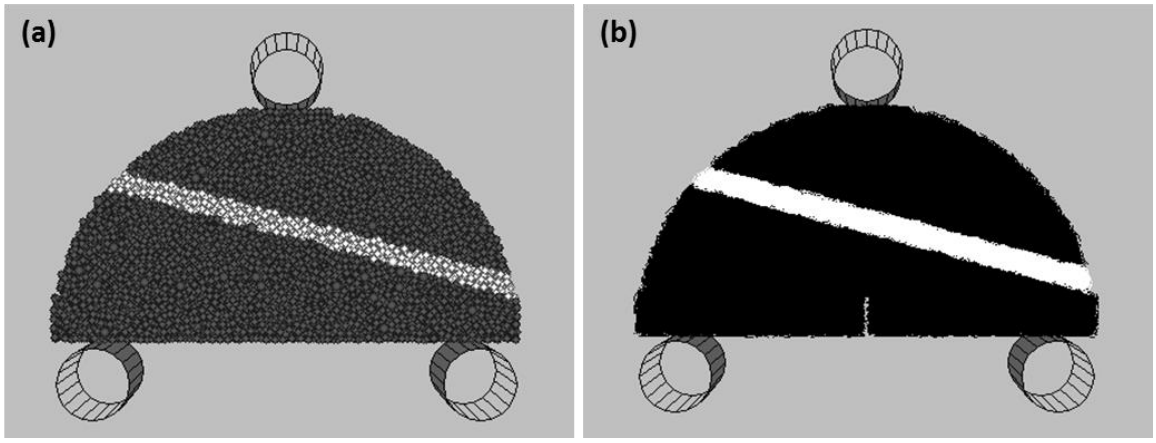

Figure 4.11. Schematic views of SCB test set-up in PFC3D: (a) particles representing shale matrix (dark gray) with a vein (white) at 75° and (b) parallel bonds of the rock matrix (black) and the vein (white).

The variables for the vein properties are restricted to the stiffnesses and strengths. The microscopic properties of the vein, the stiffness and strength of parallel bonds and the stiffness of particles, are modified by the ratio to the rock matrix while keeping the normal to shear ratios analogous to the setting of the rock matrix. To represent weaker and stiffer veins in the rock matrix, the parallel bond strengths ranged between 0.3 and 1.0 times the strength of the shale and the stiffnesses of the particles and parallel bonds ranged between 1 and 10 times the stiffnesses of the shale. Although the bond strength of the shale-calcite interface might differ from the rock matrix and vein, the interface was not specified with lower strengths than the rock matrix so as to drive the induced fracture to propagate down the middle of the vein and not down the interface. This way the interaction results in the laboratory experiments were mimicked.

4.6 INFLUENCE OF APPROACH ANGLE ON FRACTURE PATH

The approach angle is an important factor that governs the fracture interaction result (Blanton, 1982; Zhou et al., 2008; Gu and Weng, 2010; Wang et al., 2013; Lee et al., 2015). In naturally fractured Marcellus shale experiments, the number of core samples is limited to evaluating the impact of the approach angle in detail. PFC3D is capable of generating samples with veins of various approach angles with the same mechanical properties. In this study, the increment of the vein approach angle in the sample was $5°$ starting from a vein at $0°$.

The particle size in PFC3D constrains the minimum vein thickness. The vein aperture cannot be smaller than two times the maximum particle diameter ($2D_{\max} = 1.485$ mm) since parallel bonds are required within the vein for the induced fracture to divert into the vein. Otherwise the interaction results will be biased towards fracture crossing. So the thinnest case (0.25 mm) in the lab experiment was impossible to reproduce with the current set-up in PFC3D. For a reasonable vein thickness based on the particle size, the main vein thickness was set as 1.9 mm. This is the thickest vein case in Marcellus shale experiments.

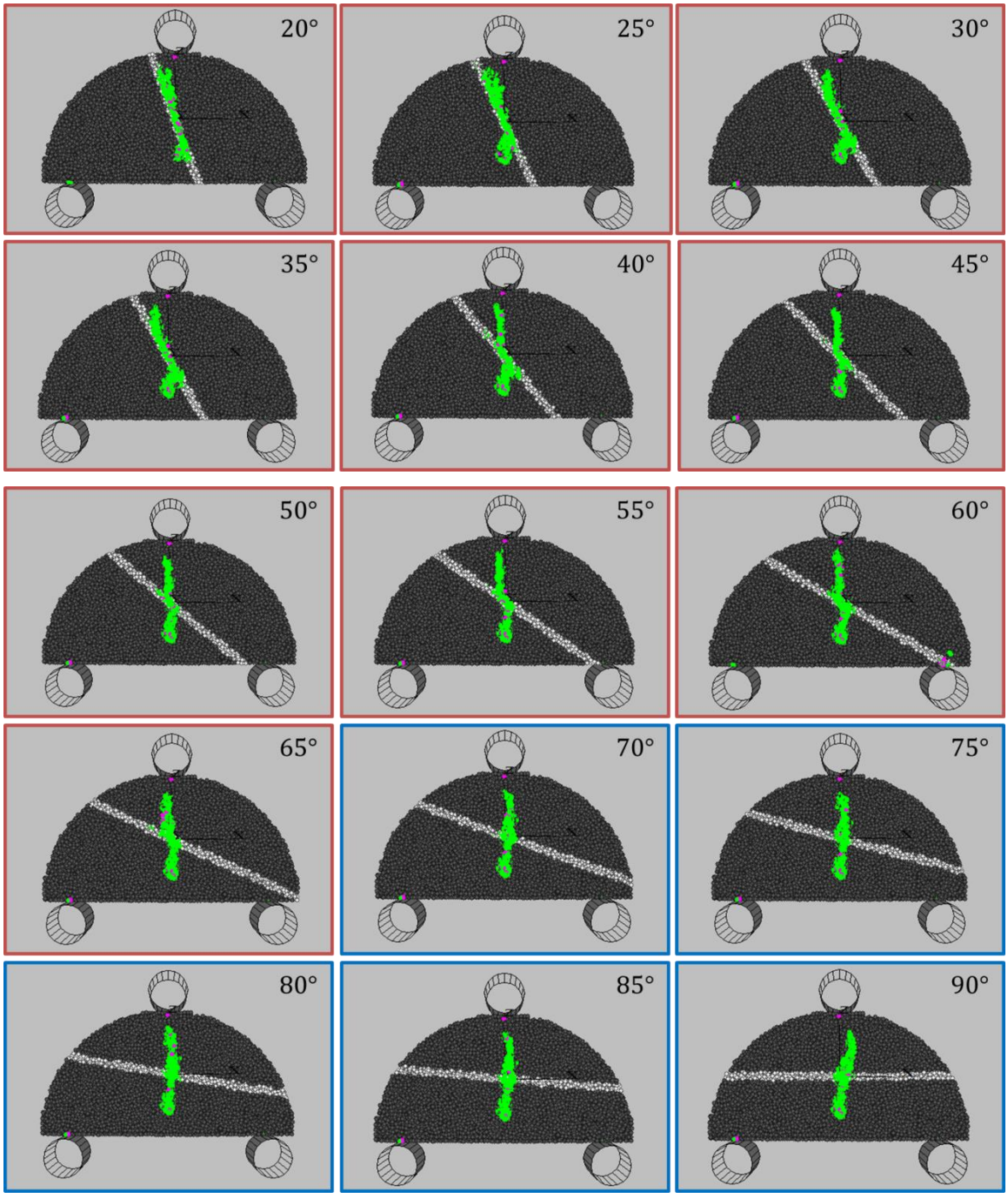

Figure 4.12. SCB test results with vein ($0.5\times K_{Ic}^{rock}$ and $1\times E^{*rock}$) of approach angles from 20° to 90°. Red and blue boxes indicate fracture diversion and fracture crossing, respectively.

For the first set of examples (Figure 4.12), the vein was set to have the same stiffness ($1\times E^{*rock}$) as the rock but with lower parallel bond strengths ($0.5\times K_{\mathrm{Ic}}{}^{rock}$). The fracture toughness of the vein is half of the rock fracture toughness representing a weak discontinuity. The critical energy release rate of the vein can be expressed as

$$G_c{}^{vein} = \frac{\left(K_{\mathrm{Ic}}{}^{vein}\right)^2}{E^{*vein}} = \frac{\left(0.5\times K_{\mathrm{Ic}}{}^{rock}\right)^2}{1\times E^{*rock}} = 0.25\frac{\left(K_{\mathrm{Ic}}{}^{rock}\right)^2}{E^{*rock}} = 0.25\times G_c{}^{rock} \tag{4.4}$$

which is equal to the critical value predicted for the calcite vein in the experiment.

Parallel bond breakages are marked with green for tensile failure and magenta for shear mode failures. Scattered parallel bond breakages indicate microcracks and cluster of breakages that are continuous is interpreted as the propagating induced fracture. Figure 4.12 illustrates the SCB test results with the vein at various approach angles, showing that the fracture diversion to crossing transition occurs between $65°$ and $70°$. The diversion did not occur dramatically at a typical angle but the fracture travel distance within the vein before kinking back into the host rock gradually increased as the approach angle decreased, consistent with observations from other numerical (Zhang et al., 2014) and experimental studies (Wang et al., 2013). Dahi-Taleghani and Olson (2014) discussed that the point of fracture kink back can be predicted by evaluating $\left(G_{\max}/G_c{}^{rock}\right)$ to $\left(G_c{}^{vein}/G_c\right)$ ratio numerically, where $G_{\max}$ is the maximum energy release rate in θ direction and G_c is energy release rate in the direction of the natural fracture. Regardless of the interaction results of the fracture crossing versus diversion, the failure mode of the

induced fracture mostly indicated tensile mode (green marks) both in the vein and rock matrix rather than shear breakages (magenta marks) for all cases.

The numerical results show that the fracture did not divert into the fracture starting from the approach angle of $90°$, as was predicted by the energy release rate criterion when the G_c^{vein} is equal to $0.25 \times G_c^{rock}$ in Section 3.4. This discrepancy may arise from the fact that, in PFC3D, there were no internal flaws or weak planes in the vein that could be utilized to divert the fracture. Despite the mismatching quantitative values, fracture diversion was likely to occur more in the lower approach angles than the in higher angles following the trend of the experimental fracture interaction response.

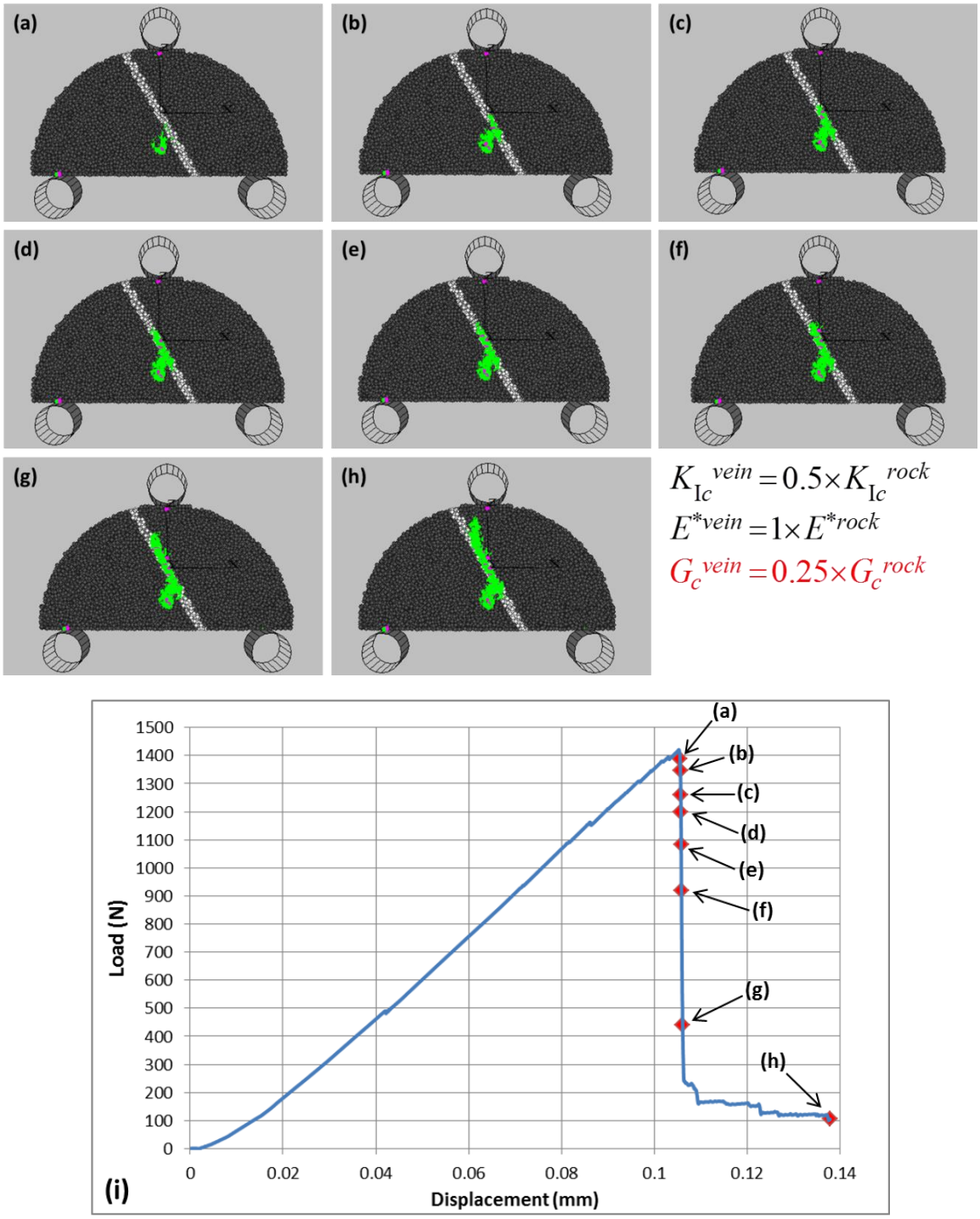

Figure 4.13. Induced fracture propagation in PFC3D specimens with a vein ($0.5 \times K_{Ic}^{rock}$ and $1 \times E^{*rock}$) at an approach angle of 30°. Figures (a) to (h) correspond to the points marked in the (i) load–displacement curve measured from the loading roller.

Figure 4.13 illustrates the fracture propagation process in the SCB test with the corresponding load-displacement curve for the SCB specimen with a vein at an approach angle of 30° (from Figure 4.12). At the peak load, tensile cracks from the notch tip were observed (Figure 4.13a) and the fracture started to propagate. A few microcracks were generated in the vein before the induced fracture, initiating from the notch tip, encountered the vein (Figure 4.13b). When the opening mode fracture approached the vein, it utilized the induced microcracks and diverted into the vein (Figure 4.13c). The interaction process occurred within 300 N of the load drop right after the peak load (from Figure 4.13a to Figure 4.13d). After the interaction, the induced fracture propagated within the vein while the load dropped continuously (from Figure 4.13e to Figure 4.13g). Finally, the induced fracture kinked back into the shale matrix (Figure 4.13h) due to the compressive stress concentration at the edge of the SCB sample. Overall, the failure behavior of the sample was very brittle as the load dropped abruptly and the interaction between the opening mode fracture and the vein occurred instantaneously after the peak load.

4.7 INFLUENCE OF VEIN STIFFNESS ON FRACTURE PATH

One important thing in the energy release rate criterion is that the consideration of the vein stiffness in estimating the critical energy release rate (see Equation (4.4)). Such inclusions are generally neglected in other fracture interaction analyses (Blanton, 1986; Warpinski and Teufel, 1987; Renshaw and Pollard, 1995; Gu and Weng, 2010). The second set of samples include veins of parallel bond strength the same as that of rock

($1.0\times K_{Ic}^{rock}$) but ten times the stiffness ($10\times E^{*rock}$) so as to determine if the vein stiffness controls the vein to act as a plane of weakness in the fracture-interaction process. As in the previous case, the approach angle is varied by $5°$. This example's vein critical energy release rate (G_c^{vein}), calculated from Equation (4.4), is $0.1\times G_c^{rock}$.

The PFC3D results (Figure 4.14) show similar responses to the first set of samples with the same stiffness as the rock and a lower parallel bond strength ($1\times E^{*rock}$ and $0.5\times K_{Ic}^{rock}$). The induced fracture diverted into the vein from an approach angle of $65°$ and lower. The exceptions were samples with a vein at 20° and 40° where the induced fractures first diverted into the vein but kinked back into the rock matrix before propagating to the end of the vein. The difference for samples with veins of higher stiffness was that the propagating fracture left more vein-parallel damage even when the induced fracture crossed the vein. The vein-parallel damage extended to both wings of the vein when fracture diversion occurred, whereas the previous case (Figure 4.12) generally utilized only one wing—the one with the lower approach angle between the two—for the propagation path.

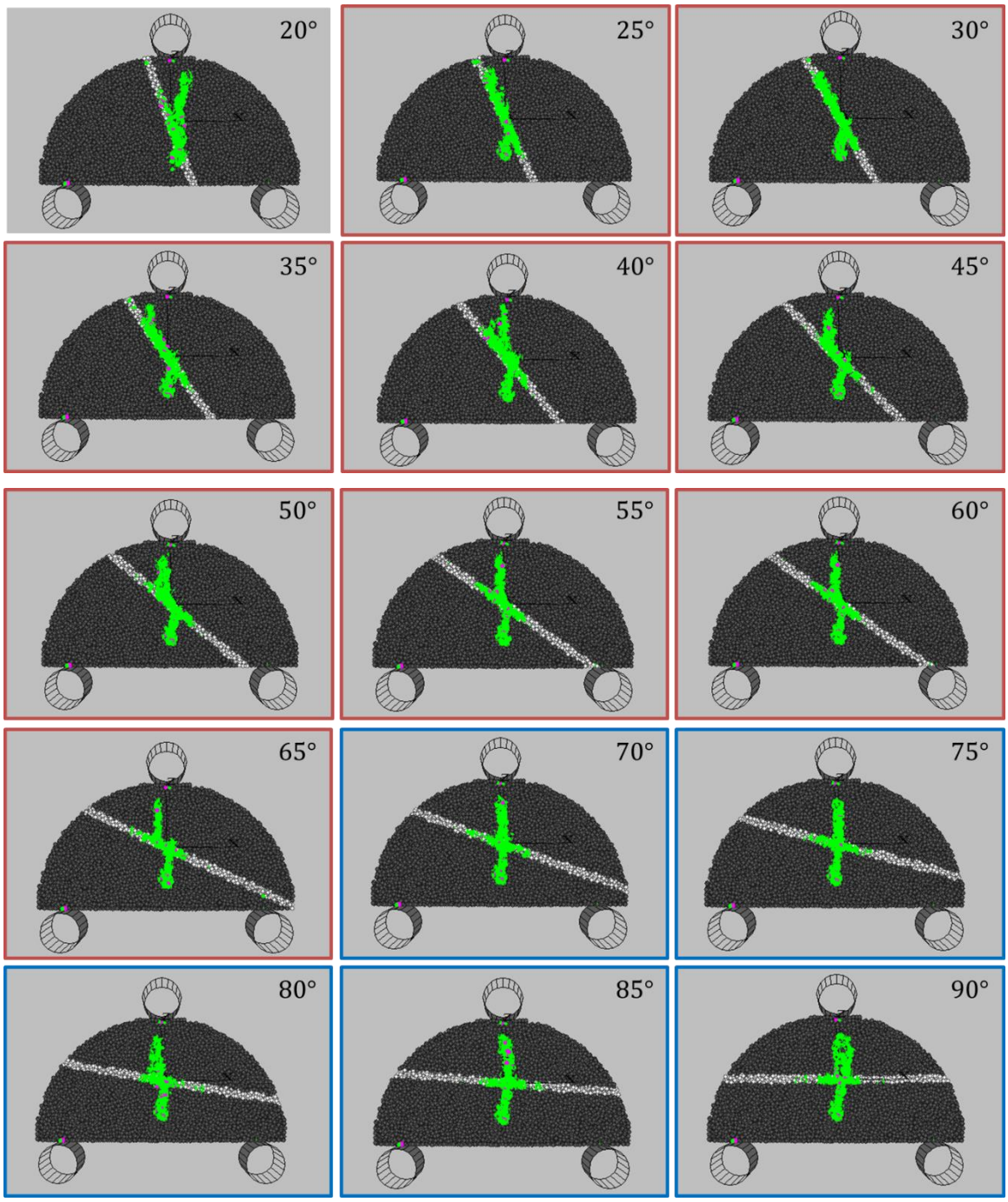

Figure 4.14. SCB test results with veins ($1.0\times K_{Ic}^{rock}$ and $10\times E^{*rock}$) at approach angles from 20° to 90°. Red and blue boxes indicate diversion and crossing, respectively.

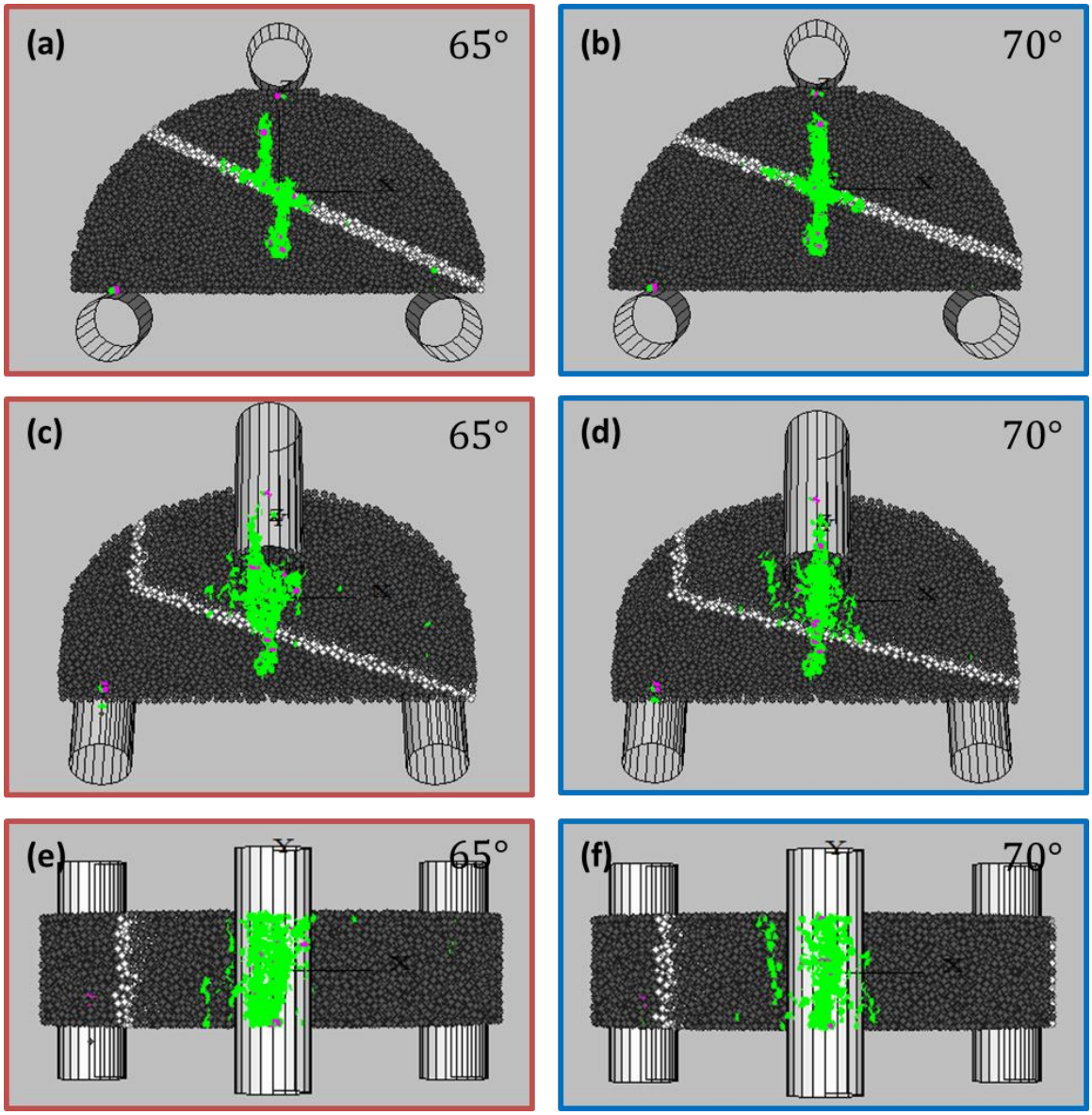

Figure 4.15. SCB test results with veins ($1.0\times K_{Ic}^{rock}$ and $10\times E^{*rock}$) of approach angles of 65° and 70° from three view angles: (a) and (b) are 0° or front view, (c) and (d) are 45°-inclined, (e) and (f) are 90° or top view. Red and blue boxes indicate fracture diversion and crossing, respectively.

In 3D analysis, defining fracture interaction results between crossing and diversion requires various view angles of the assembly in order to track the main induced fracture path. Microcracks in the PFC3D samples confuse the matter of determining fracture

geometry from only the front view of the assembly. Figure 4.15 shows three views of the sample at approach angles of $65°$ and $70°$: the front view, the $45°$-inclined view, and the top view. These view angles provide the distinction between microcracks and the propagating induced fracture. Combining all three views, the sample with the vein at an approach angle of $65°$ clearly shows that the fracture diverted into the vein and kinked back into the host rock after a short travel distance inside the vein, whereas the induced fracture in the $70°$ case crossed the vein without diversion. The parallel bond breakages in the vein were not connected and scattered to the left and right of the main fracture path.

Next, we focus on the sample of vein at an approach angle of $30°$. Compared to the fracture propagation process for the first case in Figure 4.13 (a sample with vein of $1\times E^{*rock}$ and $0.5\times K_{Ic}{}^{rock}$), more microcracks were generated before the induced fracture encountered the vein (see Figure 4.16b). Another difference is that the load dropped down to 100 N immediately after the peak load without any additional loading (Figure 4.16i) which was required for the first case where the induced fracture kinked back into the rock matrix.

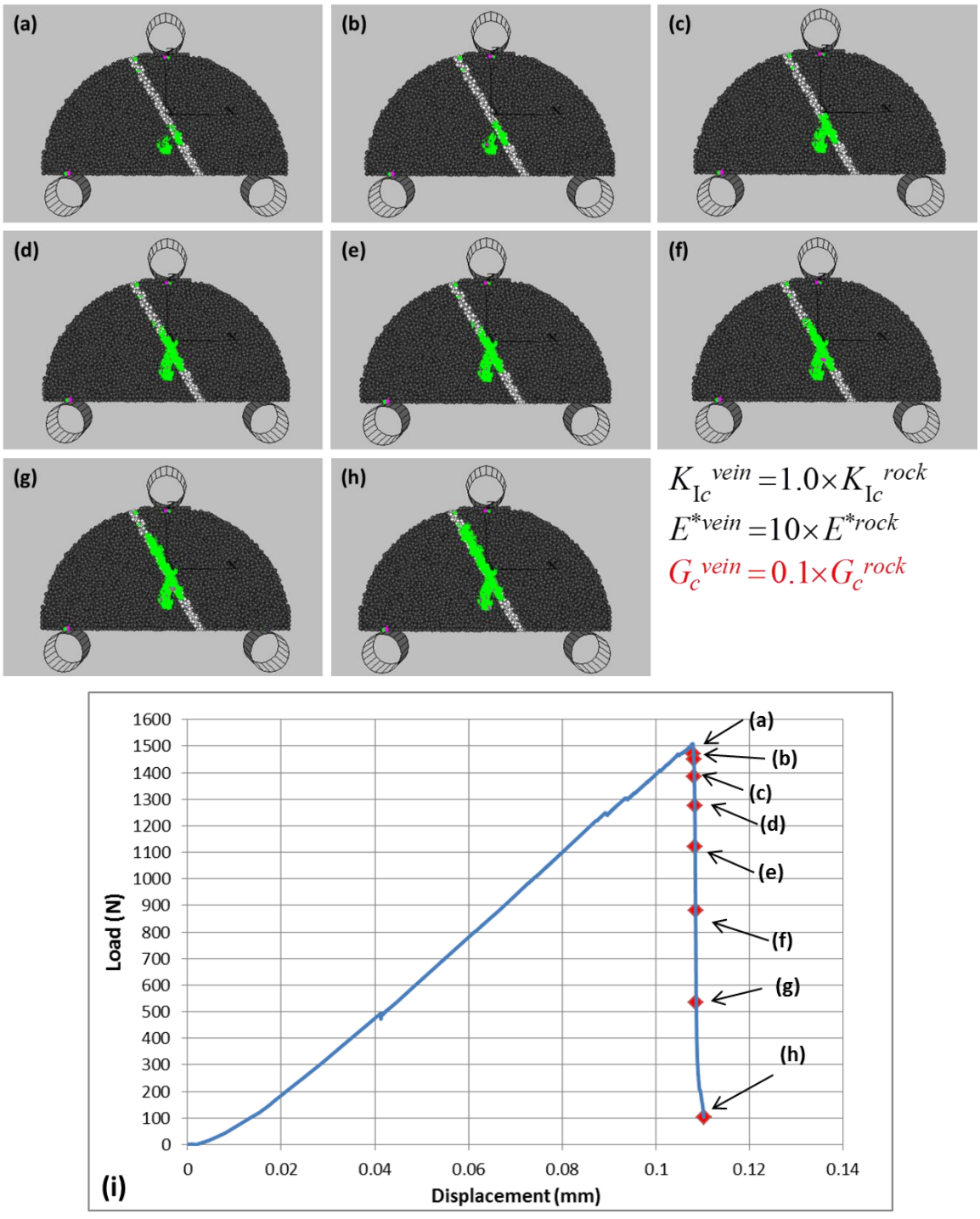

Figure 4.16. Induced fracture propagation in PFC3D specimens with a vein ($1.0 \times K_{Ic}^{rock}$ and $10 \times E^{*rock}$) at an approach angle of 30°. Figures (a) to (h) correspond to the points marked in the (i) load–displacement curve measured from the loading roller.

In order to examine the stiffness impact specifically, the study performed SCB tests on samples with veins at 60° with three different E^{*vein} ($1\times E^{*rock}$, $5\times E^{*rock}$, $10\times E^{*rock}$) and a constant parallel bond strength ($0.5\times K_{Ic}{}^{rock}$). The induced fracture in Figure 4.17a and Figure 4.17b both diverted into the vein but the fracture propagated through the vein with a longer distance for the vein with a higher stiffness. This is because higher E^{*vein} generates higher stress in the vein than in the shale causing the vein to act more like a weaker plane. Furthermore, the case of $10\times E^{*rock}$ (Figure 4.17c) failed through the vein even before the fracture reached the vein. This is similar to the failure of weak or initially damaged vein samples in the laboratory experiments.

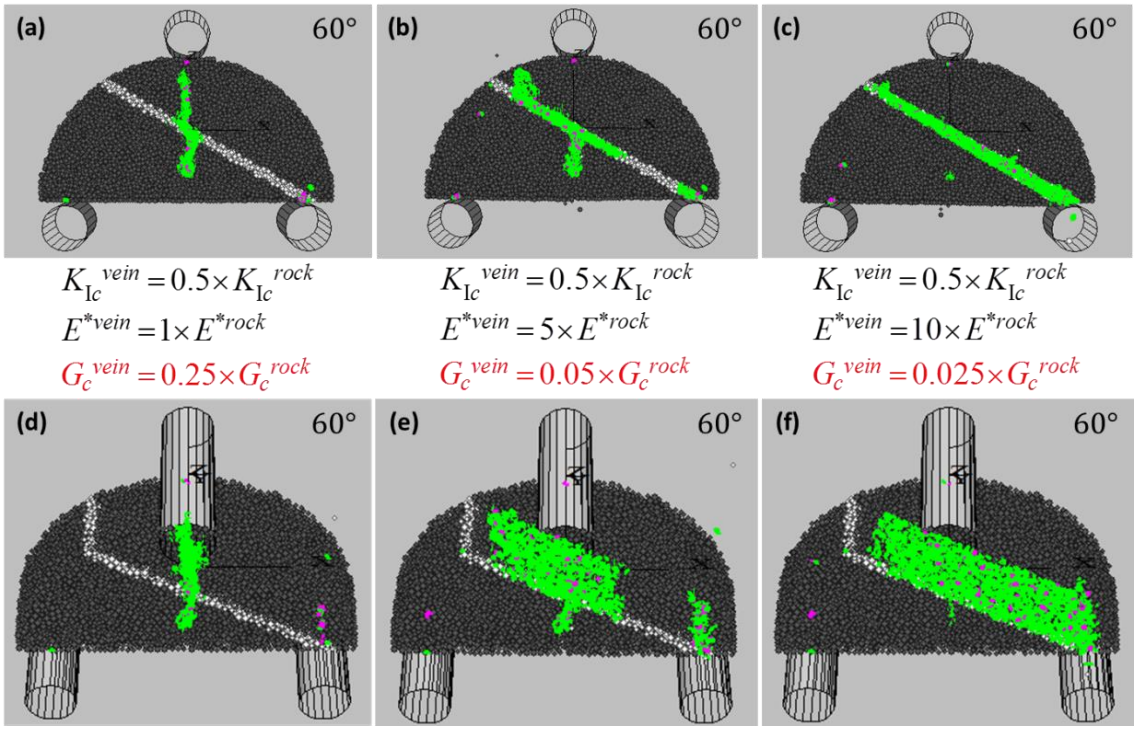

Figure 4.17. SCB results of veins at 60° with three stiffnesses: stiffness of (a) $1\times E^{*rock}$, (b) $5\times E^{*rock}$, and (c) $10\times E^{*rock}$. (d), (e), (f) are the 45°-inclined view of (a), (b), (c), respectively. The fracture toughness of the vein is kept constant with 0.5 ratio to the rock fracture toughness ($0.5\times K_{Ic}{}^{rock}$) for all three cases.

4.8 INFLUENCE OF VEIN STRENGTH ON FRACTURE PATH

To evaluate the vein fracture toughness impact on the fracture interaction feature, the vein parallel bond strength is varied while keeping all other properties constant ($\theta_o = 60°$, $E^{*vein} = 5 \times E^{*rock}$). By lowering the vein fracture toughness to a 1.0, 0.7, and 0.5 ratio to the shale fracture toughness, the opening mode fracture tended to divert and follow the vein for a longer distance generating a longer step over (Figure 4.18). As the parallel bond strength increased, the tendency of fracture interaction was toward crossing (Figure 4.18c). Overall, the weaker veins had greater impact on the fracture propagation trajectory.

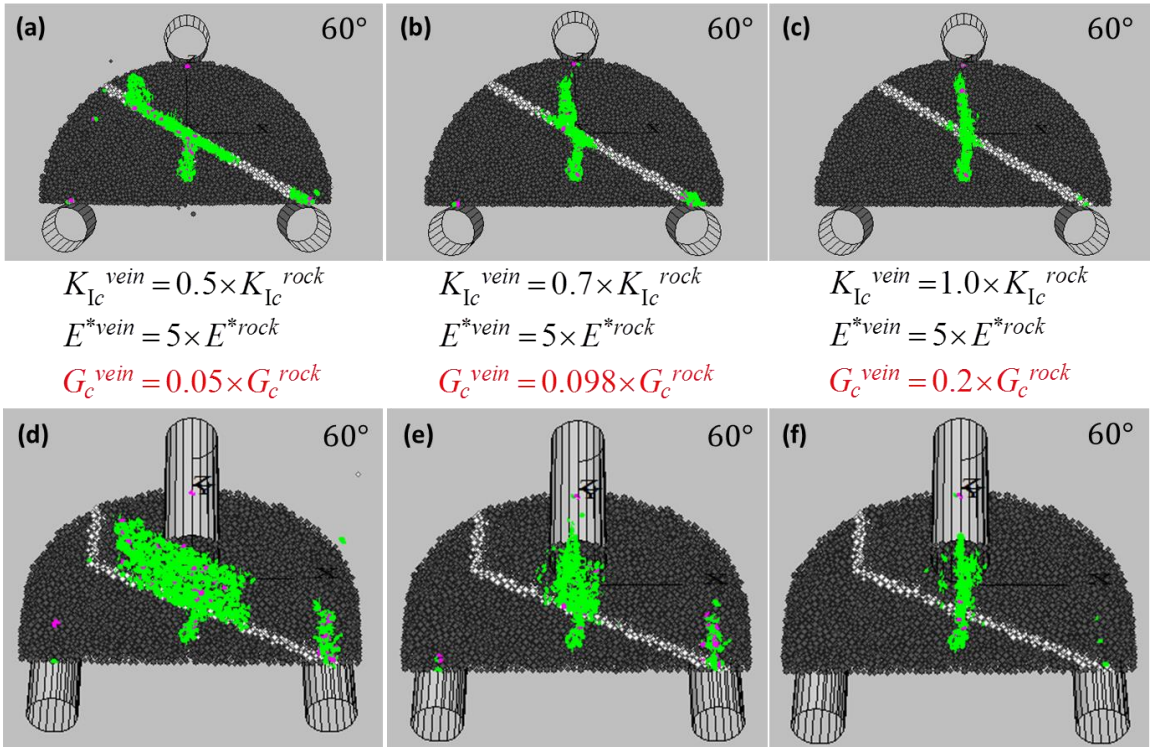

Figure 4.18. SCB results of veins at 60° with three parallel bond strengths: fracture toughness of (a) $0.5 \times K_{Ic}^{rock}$, (b) $0.7 \times K_{Ic}^{rock}$, (c) $1.0 \times K_{Ic}^{rock}$. (d), (e), (f) are the 45°-inclined view of (a), (b), (c), respectively. For all samples, the vein stiffness is 5 times greater than the rock matrix ($5 \times E^{*rock}$).

4.9 INFLUENCE OF VEIN THICKNESS ON FRACTURE PATH

The impact of vein thickness on the fracture interaction is assessed numerically to understand the experimental results in Section 3.8. That is, whether the microstructure in the vein is significant or the thickness itself also contributes to the fracture interaction. In general, as the relative stiffness of the vein to the rock increases, stress concentration develops in the vein which can lead to the failure of the weak plane as observed in Figure 4.16. It is important to examine if the increment of the vein aperture strengthens this effect, which can eventually influence the fracture interaction behavior. Therefore, the SCB test was used to examine specimens with three different vein thicknesses (3.2 mm, 2.5 mm, and 1.9 mm). The first set of samples contained veins with a stiffness of $5\times E^{*rock}$ and strength of $0.5\times K_{\mathrm{Ic}}{}^{rock}$ at an approach angle of $90°$ (Figure 4.19).

The SCB results from PFC3D show that the thickest vein sample (Figure 4.19c – 3.2 mm) diverted into the vein and propagated almost to the end of the sample and kinked back into the rock matrix due to the compressive stress concentration generated by the three-point bending load. However, the induced fracture of two other samples with thinner veins (Figure 4.19a – 2.5 mm and Figure 4.19b – 1.9 mm) diverted into the vein but kinked back into the rock matrix closer to the point of the initial deflection without promoting the total breakage of the vein. This feature is similar to the vein-parallel damages observed in the thin Section photomicrographs in Figure 3.11b or Figure 3.12c.

Despite the same G_c^{vein} for all four samples, the fracture traveld in the vein for a longer distance as the aperture became larger.

$K_{Ic}^{vein} = 0.5 \times K_{Ic}^{rock}$

$E^{*vein} = 5 \times E^{*rock}$

$G_c^{vein} = 0.05 \times G_c^{rock}$

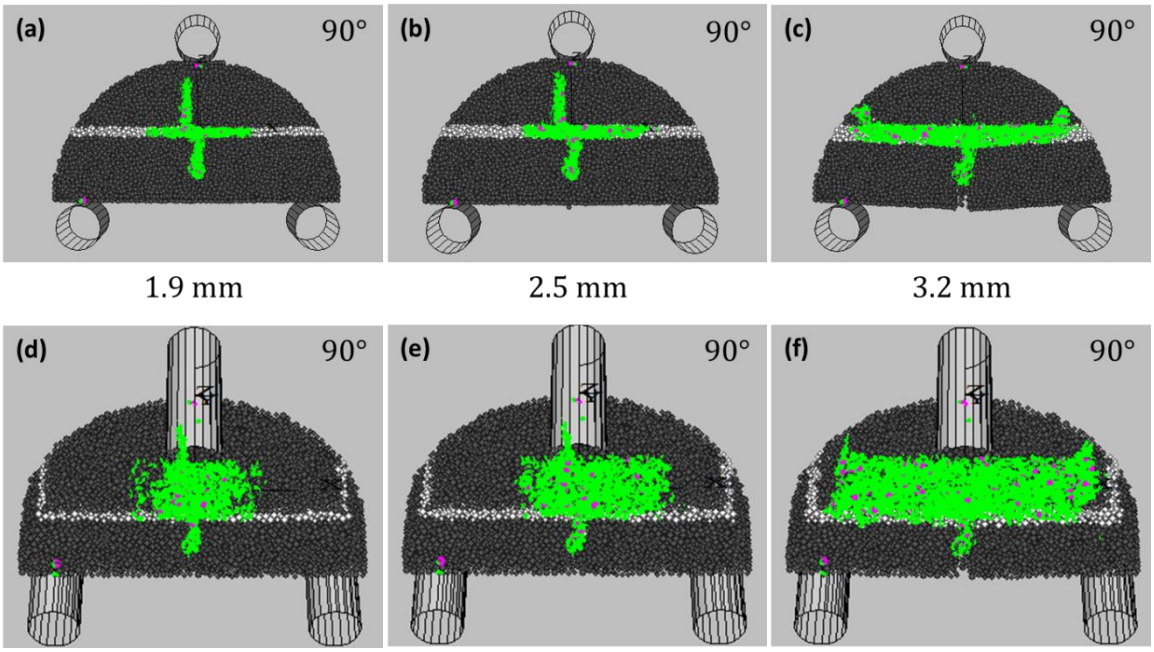

Figure 4.19. SCB results of veins at 90° with three thicknesses: (a) 1.9 mm, (b) 2.5 mm, (c) 3.2 mm. For all samples, the vein stiffness is 5 times greater than the rock matrix ($5 \times E^{*rock}$) and the fracture toughness is 0.5 ratio ($0.5 \times K_{Ic}^{rock}$) to the rock matrix. (d), (e), (f) are the 45°-inclined view of (a), (b), (c), respectively.

The second case (Figure 4.20) was to set the stiffness of the vein equal to the rock matrix ($1 \times E^{*rock}$) with a lower parallel bond strength. This allows us to understand if the stiffness of the vein dominantly controls the vein thickness impact on the fracture interaction process or if the strength of the vein also contributes to fracture diversion. The study selected a vein parallel bond strength of 0.3 ratio to the rock matrix ($0.3 \times K_{Ic}^{rock}$). This was because all the induced fractures in the SCB samples with vein strengths greater

than the 0.3 ratio to the rock matrix crossed the vein despite the variation of the vein thickness.

$K_{Ic}^{vein} = 0.3 \times K_{Ic}^{rock}$

$E^{*vein} = 1 \times E^{*rock}$

$G_c^{vein} = 0.09 \times G_c^{rock}$

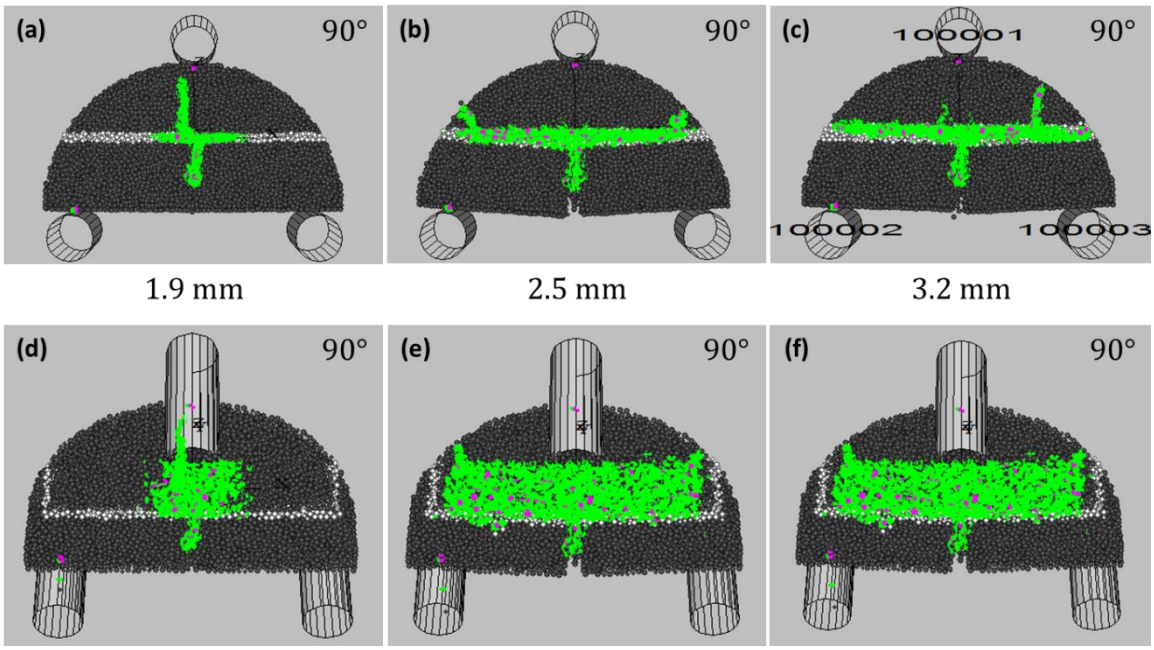

Figure 4.20. SCB results of veins at 90° with three thicknesses: (a) 1.9 mm, (b) 2.5 mm, (c) 3.2 mm. For all samples, the vein stiffness is same with the rock matrix ($1 \times E^{*rock}$) and the fracture toughness is 0.3 ratio ($0.3 \times K_{Ic}^{rock}$) to the rock matrix. (d), (e), (f) are the 45°-inclined view of (a), (b), (c), respectively.

Figure 4.20 shows results analogous to those of the high-stiffness veins in Figure 4.19, indicating that thicker veins generated longer fracture step overs even for weaker veins with same stiffness as the rock matrix. In fact, for the same vein aperture of 2.5 mm, the second case (Figure 4.20b), with a critical energy release rate of $0.09 \times G_c^{rock}$ produced a longer step over compared to the first case (Figure 4.19b – $0.05 \times G_c^{rock}$), which was the sample with a higher vein stiffness ($5 \times E^{*rock}$). Although the numerical

results were insufficient to show the influence of the vein aperture on the fracture crossing-versus-diversion results, the thicker veins produced a greater fracture propagation distance in the vein before kinking back into the rock matrix than that of the thinner veins showing a weaker vein response on the fracture interaction.

4.10 Influence of Vein Location

One question that may arise from the SCB test is that: Could the distance between the notch tip and the vein (l) in the SCB specimen have an impact on the fracture interaction result? All the veins in the previous SCB tests were located so as to pass through the middle of the sample, which is one and half times the notch length ($1.5a$) above the notch tip. Closer ($1a$) and further ($2a$) locations of veins are set to evaluate the impact of the vein location on the fracture interaction results.

Figure 4.21 shows that the propagating fracture slightly curved into the vein when the vein was closer, rather than exhibiting a straight propagation such as the behavior in the example with veins further away from the notch tip. The fracture kinked back into the host rock with a shorter propagation distance inside the vein after the diversion as the vein location moved further away from the notch tip (Figure 4.21) due to the SCB specimen geometry and the stress concentration at the edge of the specimen. The samples with thicker and stiffer veins showed more damage in the vein when the vein was closer to the notch tip (Figure 4.22). However, for both examples, the vein location had no

significant impact on the fracture interaction result between the fracture crossing and the diversion.

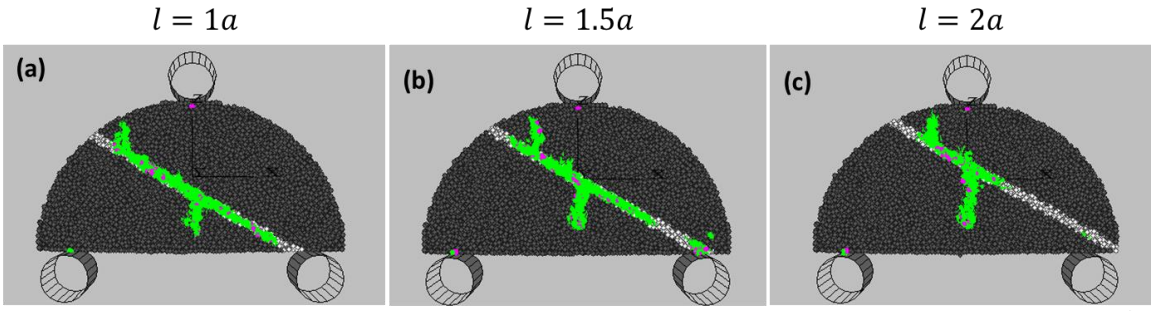

Figure 4.21. SCB test results with three different vein locations. : (a) $1a$, (b) $1.5a$, and (c) $2a$ above the notch tip. The vein approach angle, thickness, stiffness, parallel bond strength are kept constant with 60°, 1.9 mm, $1 \times E^{*rock}$ and $0.3 \times K_{Ic}^{rock}$, respectively.

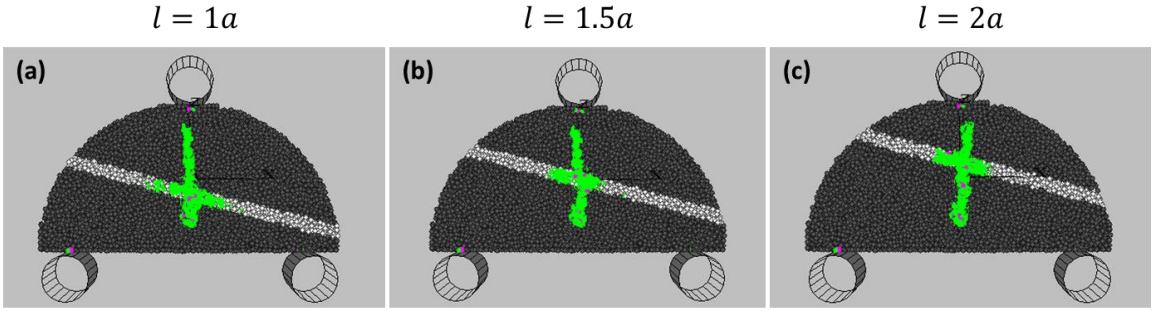

Figure 4.22. SCB test results with three different vein locations. : (a) $1a$, (b) $1.5a$, and (c) $2a$ above the notch tip. The vein approach angle, thickness, stiffness, parallel bond strength are kept constant with 75°, 2.5 mm, $10 \times E^{*rock}$, and $1.0 \times K_{Ic}^{rock}$, respectively.

4.11 DISCUSSION

Since all the numerical tests were based on the same densely packed particle assemblage, it is possible that the fracture interaction results depend on the particle distribution within the assemblage. To address this concern, a sample assembly of 56-mm (2.2-inch) diameter (d) was modeled with a different particle distribution (Figure 4.23b and Figure 4.24b) to compare the fracture interaction results with the original sample (Figure 4.23a and Figure 4.24a). The first example is the vein with stiffness of $1\times E^{*rock}$ and fracture toughness of $0.5\times K_{\mathrm{Ic}}{}^{rock}$, and the second example is the vein with stiffness of $10\times E^{*rock}$ and fracture toughness of $1.0\times K_{\mathrm{Ic}}{}^{rock}$. All other vein properties were kept the same for both cases of 58.4-mm (2.3-inch) and 56-mm (2.2-inch) diameter SCB specimens.

Figure 4.23 and Figure 4.24 illustrate that the interaction results did not change with the particle distribution in the sample assembly. Microcracks in the 56-mm (2.2-inch) diameter samples indicated more shear failure compared to the 58.4-mm (2.3-inch) diameter samples but the location where the fracture kinked back into the host rock seems to be similar for two different cases, thereby confirming the reproducibility of the PFC3D tests with different particle distribution.

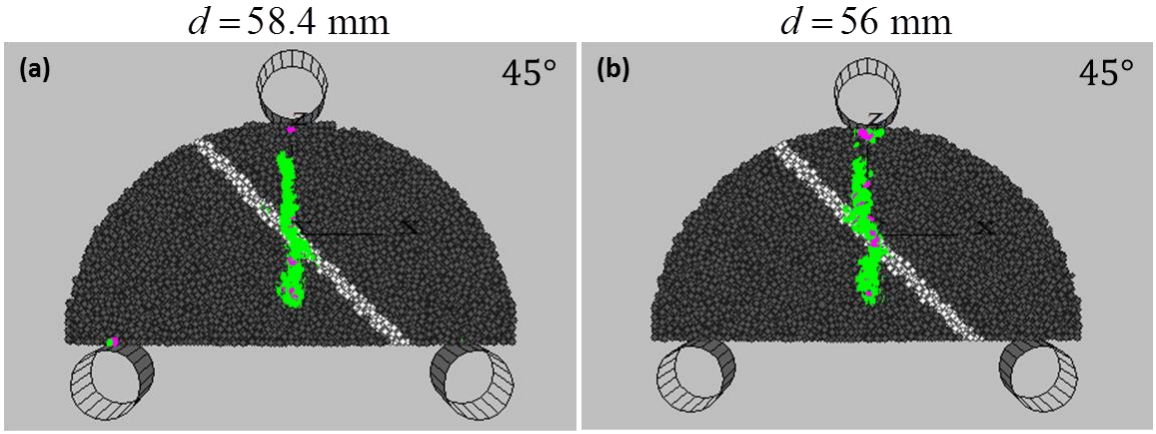

$K_{Ic}^{vein} = 0.5 \times K_{Ic}^{rock}$

$E^{*vein} = 1 \times E^{*rock}$

$G_c^{vein} = 0.25 \times G_c^{rock}$

Figure 4.23. PFC3D results of the SCB test with (a) 58.4-mm (2.3-inch) and (b) 56-mm (2.2-inch) diamter samples with veins of same properties ($1 \times E^{*rock}$ and $0.5 \times K_{Ic}^{rock}$) at 45°.

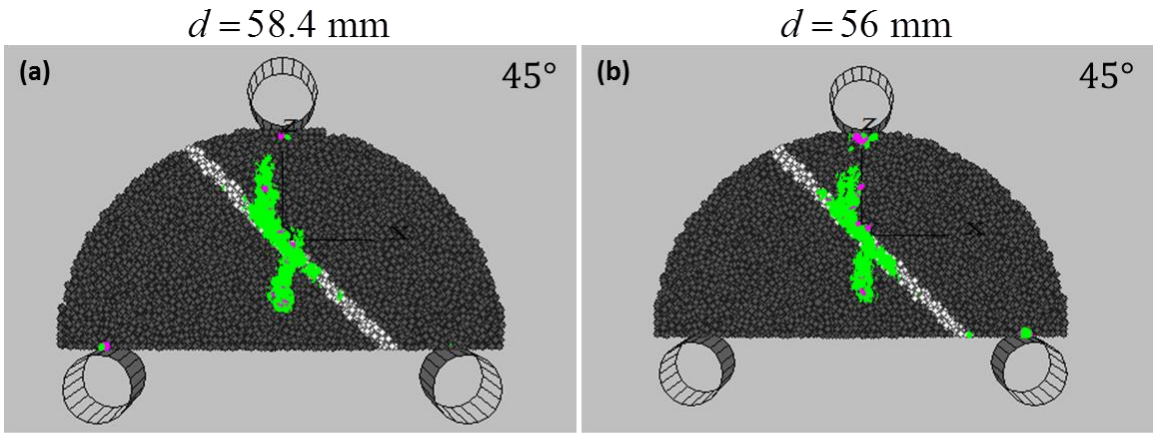

$K_{Ic}^{vein} = 1.0 \times K_{Ic}^{rock}$

$E^{*vein} = 10 \times E^{*rock}$

$G_c^{vein} = 0.1 \times G_c^{rock}$

Figure 4.24. PFC3D results of the SCB test with (a) 58.4-mm (2.3-inch) and (b) 56-mm (2.2-inch) diamter samples with veins of same properties ($10 \times E^{*rock}$ and $1.0 \times K_{Ic}^{rock}$) at 45°.

The effect of particle size to sample size ratio was examined using SCB sample diameters of 38.1 mm (1.5 inch), 76.2 mm (3.0 inch), and 101.6 mm (4 inch), while keeping particle size distribution and thickness of the specimen consistent with the standard case of the 58.4-mm (2.3-inch) sample. Total numbers of particles and parallel bonds are listed in Table 4.4 for each size. For all cases, veins were 1.9-mm thick at an approach angle of $45°$ with properties of $1\times E^{*rock}$ and $0.5\times K_{\mathrm{Ic}}{}^{rock}$.

Table 4.4. Number of particles and parallel bonds for various SCB sample sizes

Diameter of the sample	Number of particles	Number of parallel bonds
38.1 mm (1.5 inch)	7,635	20,706
58.4 mm (2.3 inch)	19,697	54,544
76.2 mm (3 inch)	30,404	84,319
101.6 mm (4 inch)	54,051	151,402

When the diameter of the sample was larger than 58.4 mm, all SCB tests generated fracture diversion with a short fracture travel distance inside the vein (Figure 4.25). Despite the difference in some failure modes of microcracks and the total length of the induced fracture with increasing sample size, the fracture patterns were analogous for all three cases (58.4 mm; Figure 4.25b, 76.2 mm; Figure 4.25c, 101.6 mm; Figure 4.25d). However, the smallest sample (38.1 mm; Figure 4.25a) broke along the vein before the fracture propagated from the notch tip, showing a different response compared to other larger samples. These numerical results indicate that the SCB sample needs to be greater than 38.1 mm and closer to 56 mm (Figure 4.23b) in diameter for a representative result with the current particle size distribution. Thus, it confirms that the SCB tests with

samples of 58.4-mm diameter in this study are reasonable to evaluate fracture diversion results.

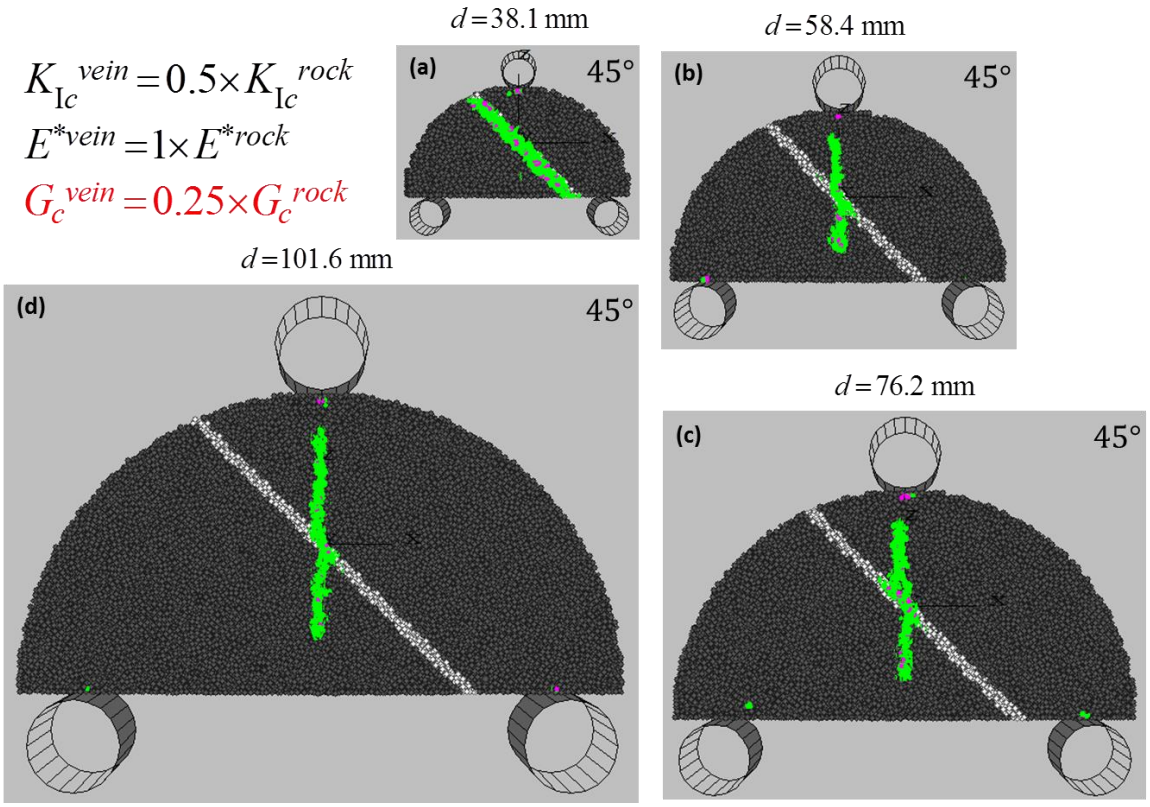

Figure 4.25. PFC3D results of the SCB test with (a) 38.1-mm (1.5-inch), (b) 58.4-mm (2.3-inch), (c) 76.2-mm (3-inch) and (d) 101.6-mm (4-inch) diamter samples with veins of same properties ($1 \times E^{*rock}$ and $0.5 \times K_{Ic}^{rock}$) at $45°$.

4.12 CONCLUSIONS

In this chapter, PFC3D was utilized to numerically model fracture interaction experiments. The interaction behavior between opening mode fractures and veins from the experimental results of Marcellus shale with calcite veins were reproduced numerically. PFC3D was used to perform further sensitivity analysis of the approach

angle, strength, stiffness, thickness, location of the vein on the interaction with induced fracture.

Generally, the trend of the fracture propagation path using PFC3D followed the results of Marcellus shale experiments, the analytical prediction of the energy release rate criterion (Dahi-Taleghani and Olson, 2009), and other numerical results (Virgo et al., 2013). Fracture crossing was likely to occur for veins with greater approach angles and strength, with all other vein properties being kept constant. These parameters not only controlled the fracture diversion-versus-crossing result but also governed the the fracture travel distance in the vein. In addition, the PFC3D results validated that the stiffness of the discontinuity is a very important factor in determining fracture interaction results. This confirmed that the critical energy release rate is an appropriate parameter for expressing the strength of the vein rather than just the fracture toughness or frictional properties of the discontinuity.

The veins of various apertures in Marcellus shale contained different microstructures which could have influenced the SCB test results. PFC3D was utilized to understand and focus on the impact of the vein aperture on the interaction with the induced fracture. Numerical results implied that the thicker veins extended the fracture propagation distance in the vein showing greater impact on the fracture propagation path. This agrees with the SCB results on hydrostone with inclusions (Wang et al., 2013).

One of the advantages of PFC3D is that it provides information on the interaction process by tracking parallel bond breakages with a corresponding load-displacement curve. The fracture interaction mostly occurred right after the peak load within 300 N of

load drop. Microcracks were generated inside the vein before the induced fracture reached the vein and as the vein stiffness increased the total number of microcracks increased. These microcracks were utilized when fracture diversion occurred while some induced fractures crossed the vein, avoiding the significant damage in the vein, especially for veins of higher stiffness. The damage in the vein will increase greatly if the weak microstructures observed in the thin section photomicrographs were embedded in the PFC3D model. Also, the failure mode of the parallel bonds showed that the tensile failure dominated in the vein rather than the shear failure when the induced fracture approached and propagated through the vein.

CHAPTER 5: CONCLUSIONS AND RECOMMENDATIONS

5.1 CONCLUSIONS

This study investigated mixed-mode fracture interaction effects that could influence hydraulic fracture and/or natural fracture propagation in geologic media. The study primarily focused on determining the consequences of the intersection of a mixed-mode I–II fracture with a preexisting cemented fracture, experimentally and numerically showing the conditions under which the fracture would cross or divert into the preexisting discontinuity. In addition, I developed a modified mixed-mode fracture propagation criterion, providing a better description of the role of remote compressive stresses on propagation path. Hydraulic fracturing is the primary application of this work, but it is applicable to any mixed-mode propagation problem as well.

The standard mixed-mode fracture propagation models, based on near-tip stress approximations, have limitation on applications of fractures under far-field stresses. Most studies in engineering mechanics focused on extending or modifying the standard models to solve mixed-mode fracture propagation under tensile loading, which is the typical service loading in things like airplanes, bridges, and cars. However, for geomechanics and geologic applications, the ambient stress is compressive, and internal fluid pressure or frictional stress can play an important role in the near-tip stress field and the propagation path. Chapter 2 introduced the modified maximum principal tangential stress criterion (MMTPS-criterion) to deal with the effect of the remote and internal crack stresses on the fracture propagation trajectory. The MMTPS-criterion predicts that the

fracture growth occurs in finite length increments (r_c) from the fracture tip, defined by the size of process zone, in the direction where the maximum principal tangential stress exceeds the tensile strength of the material.

Published analysis of the MMTPS-criterion shows that it agrees with the previous experimental results on cracks under both tensile and compressive external loadings (Pook, 1971; Williams and Ewing, 1972; Tirosh and Catz, 1981). I extended the existing literature on mixed-mode fracture propagation with uniaxial compressive tests on hydrostone samples, focusing on the impact of the fracture half-length (a) on the r_c value of open fractures under compression. The experimental results indicated that the fracture length should satisfy the SSY conditions in order to utilize the r_c calculated from the simplified maximum principal stress model of Schmidt (1980). An interesting aspect of the problem was accounting for whether the initial crack was open or closed. In the cases of initially open cracks, compressive loading was interpreted to generate negative K_{I} values, whose inclusion in the propagation criterion improved path prediction considerably. On the other hand, K_{I} was set zero for initially closed fracture under compression, and the friction coefficient became important in the evaluation of the fracture propagation path. The predictions of the MMTPS-criterion agreed with the limited experimental results of frictional cracks under compression (Bobet, 2000; Park and Bobet, 2010) and generally showed a lower fracture propagation angle, a less deviation from the initial crack plane, with the increase in the friction coefficient.

To fill the present knowledge gap in predicting natural and hydraulic fracture interactions and to help optimize completion strategies, Chapter 3 examined the interaction of an opening mode fracture and preexisting discontinuities by the Semi-Circular Bend (SCB) test with naturally fractured Marcellus shale samples. The SCB test was attractive for this work because of its benefit in simple set up and minimizing the amount of core samples needed. The SCB test results showed that a lower approach angle contributed more greatly for the fracture to divert into the vein, consistent with other hydraulic fracturing block experiments with frictional and bonded interfaces (Blanton, 1982; Warpinski and Teufel, 1987; Gu et al., 2011). The energy release rate criterion from Dahi-Taleghani and Olson (2009) was employed to quantify the strength of the calcite-filled veins in the Marcellus samples based on the SCB test results. This indirect method of measuring the vein strength in an intact sample is a significant contribution in providing input to completion best practices since there is no other way to evaluate the strength directly.

Microstructural analysis on the SCB specimens with calcite-filled veins revealed that fracture diversion occurred in the middle of the vein but not at the shale–calcite interface for all cases examined. The microstructures in the veins, such as the cleavage planes and the fluid-inclusion planes from crack-seal crystal growth mechanisms, exerted control on the fracture diversion. In this set of calcite-filled veins from Marcellus shale cores, thicker veins were more likely to divert the induced fracture than thinner veins, probably as a result of the existence of more weak planes.

Tracking parallel bond breakages by Particle Flow Code in 3-Dimensions (PFC3D), which is a numerical modeling software based on the Discrete Element Method (DEM), in Chapter 4 provided a better understanding of the fracture interaction process. Numerical SCB test results qualitatively matched with the fracture diversion results of the physical experiments as the fracture diverted more into the veins for veins of lower approach angles. Also, the fracture diversion was likely to occur for the samples of veins with higher stiffness or lower strength which corresponds to a lower critical energy release rate. PFC3D results proved that the critical strength of the vein should be defined by both the stiffness and strength of the vein. For samples with thicker veins, a longer fracture travel distance was generated inside the vein before kinking back to the host rock, which agrees with the physical experimental results, showing that the thickness of a weak plane also contributes to fracture diversion.

Microcracks were observed inside the vein before the induced fracture intersected it and microcrack-related damage increased as the stiffness of the vein increased. When the opening mode fracture diverted into the vein, it utilized the microcracks to propagate along the vein but some induced fractures, especially for samples with high stiffnesses and approach angles, crossed the vein regardless the locations of microcrack damage in the vein. All of the induced fractures in PFC3D, including both fractures that crossed and diverted, propagated continuously without jumping across the vein and initiating on the other side of the rock matrix. The failure mode of the parallel bonds in the vein during the fracture interaction process was mostly tensile rather than shear failure which is consistent with the experimental results.

5.2 RECOMMENDATIONS

There are many interesting studies that can extend the work in this dissertation. These studies include (1) applications in structural geology to estimate the trajectory of natural fractures, such as splay fractures from faults, and (2) in petroleum industry to model complex hydraulic fracture network under subsurface conditions in order to optimize production and recovery.

As discussed in this study, for closed cracks under compressive remote stresses in the subsurface, the friction coefficient of the interface is an important parameter governing the kink angles of the tensile wing fractures. Some experimental studies (Bobet and Einstein, 1998; Bobet, 2000; Park and Bobet, 2010) have been performed on closed fractures under compressive loadings but the results are limited to truly validate the impact of the friction coefficicent on the analytical prediction of the MMTPS-criterion. Furthermore laboratory experiments on frictional interfaces with various fracture inclination angles and friction coefficients under compressive loadings are necessary to expand the applicability of the MMTPS-criterion. In addition, studies have examined the variation of the friction coefficient along the fracture plane in natural fractures, such as joints and faults, due to lithology, temperature, presence of fluids and etc. (Scholz, 1990; Cooke, 1997). Thus, for practical applications, the mode II stress intensity factor requires advanced interpretation and modification from the simplified estimation, based on Coulomb's law of friction, in this study.

To predict the interaction between hydraulic fractures and veins in subsurface conditions, the directional SIFs (Nuismer, 1975) utilized in the crack propagation criterion proposed by Dahi-Taleghani and Olson (2009) require modification to include the remote and internal crack stresses. The directional SIFs for branch cracks are expressed by Nuismer (1975) as

$$\begin{aligned} \overline{K_{\mathrm{I}}} &= \lim_{r \to r_c} \sqrt{2\pi r}\, \sigma_{\theta\theta}\big|_{\theta=\theta_o} \\ \overline{K_{\mathrm{II}}} &= \lim_{r \to r_c} \sqrt{2\pi r}\, \sigma_{r\theta}\big|_{\theta=\theta_o} \end{aligned} . \tag{5.1}$$

and the Nuismer's directional SIFs (Equation (2.5)) are derived based on the singular terms of the near-tip stress equations. These directional SIFs can be modified by utilizing the near-tip stress components in Equation (2.19). However, since the method by Nuismer (1975) is limited to problems of $K_I \geq 0$, a new boundary value problem must be solved to account for problems of fractures with $K_I < 0$. With an appropriate method and the quantified strength of the natural fracture, the interaction of hydraulic fractures and natural fractures under remote differential compression stress can be determined analytically.

There are many potential opportunities to extend the application of the SCB test to simulate fracture interaction under subsurface conditions, such as the effect of the confining stress, crack-parallel differential stress, and fracture propagation rate.

1. Fractures under confining stress propagate stably compared to the unstable propagation of fractures under tensile loading. Some studies have performed confined SCB tests (Seto et al., 2001; Kuruppu et al., 2010)

which could be considered in further applications to generate opening mode fractures propagating under confining stress and to evaluate the impact of the fracture growth behavior on fracture interaction results, fracture crossing-versus-diversion.

2. Many studies have shown that the interaction between hydraulic fractures and preexisting discontinuities is highly dependent on the remote differential stress (Renshaw and Pollard, 1995; Gu and Weng, 2010). In the SCB test, Ayatollahi and Aliha (2007) discussed that the crack-parallel stress can be controlled by changing the notch length (a) and the length from the notch to the supporting rollers (s). By changing a and s for SCB specimens with the same natural fracture at the same approach angle, the SCB test results will be available to assess the impact of the crack-parallel compressive stress on the interaction between the opening mode fracture and the plane of weakness.
3. Subcritical crack growth is an important mechanism for natural fracture development (Segall, 1984; Olson, 1993; Holder et al., 2001) which might generate different fracture crossing-versus-diversion results compared to the critical growth of hydraulic fractures. The impact of the crack propagation rate can be considered with the chevron-notched SCB test (Kurrupu and Chong, 2012) as an additional to the original SCB test (flat notch) in order to allow the crack to propagate subcritically before it reaches the peak load. With a high-speed camera, the location of the fracture tip can be observed

and correlated with the load–displacement curve. The estimation of the induced fracture velocity at any specific point is possible by reading and measuring the distance traveled within a certain time (through captured images).

4. This study only focuses on the SCB test results of dry Marcellus shale samples with calcite-filled veins which were taken from different depths of the same well. In the subsurface, the formation is saturated with fluid and has a pore pressure which is different from the dry cores that were tested in the laboratory. Some studies demonstrate that the mechanical properties of rock change due to desiccation after retrieval. Shale can strengthen with loss of pore water (Josh et al., 2012), and the elastic properties of shale can change with water content variation (Ghorbani et al., 2009). Although the estimate of K_{Ic} for the calcite-filled vein can be influenced by fluid saturation, the new method introduced in this study, utilizing the combination of the SCB test and the energy release rater criterion, is still valid for preserved samples since the critical energy release rate of a vein is calculated by the relative strength of the rock matrix and the vein. More SCB tests on samples of both dry and preserved will allow us to evaluate the impact of the fluid type and saturation on the relative strength (critical energy release rate) between the rock matrix and the vein.

5. In addition, SCB tests with veins of different mineral types from various shale plays will allow us to compile a guideline for the strength of veins in each formation.

Two drawbacks of the SCB test with regard to the application of its results to hydraulic fracturing are the fact that it is unconfined and there is no fluid loading. Kresse et al. (2013) discussed that the increase in the viscosity of the fracturing fluid resulted in more fracture crossing which indicates the impact of the fluid properties. Numerical modeling can overcome the limitation of the laboratory SCB tests of simulating pressurized fractures in reservoir conditions. The PFC3D results in this study only concentrate on analyzing the experimental SCB tests, however, they can expand to fluid-driven fractures under confining stress with predefined microscopic properties of the Marcellus shale and the calcite-filled vein. Further applications of PFC3D could possibly include the impact of the flow rate and the fracturing fluid viscosity on the interaction between hydraulic fractures and preexisting discontinuities.

References

Abou-Sayed, A.S., Brechtel, C.E., Clifton, R.J., 1978, Insitu stress determination by hydrofracturing: A fracture mechanics approach, Journal of Geophysical Research, 83, pp. 2851-2862

Aliha, M.R.M, Ayatollahi, M.R., Smith, D.J., Pavier, M.J., 2010, Geometry and size effects on fracture trajectory in a limestone rock under mixed mode loading, Engineering Fracture Mechanics, 77, pp. 2200-2212

Aliha, M.R.M, Ayatollahi, M.R., 2011, Mixed mode I/II brittle fracture evaluation of marble using SCB specimen, Procedia Engineering, 10, pp. 311-318

Anderson, G.D., 1981, Effects of friction on hydraulic fracture growth near unbonded interfaces in rocks, SPE 8347

Atkinson, B.K., 1987, Introduction to fracture mechanics, in B.K. Atkinson ed. Fracture mechanics of rock, London, England, Academic press, pp.1-26

Ayatollahi, M.R., Aliha, M.R.M, 2007, Wide range data for crack tip parameters in two disc-type specimens under mixed mode loading, Computational Materials Science, 38, pp. 660-670

Bahorich, B.L., 2012, Examining the effect of cemented natural fractures on hydraulic fracture propagation in hydrostone block experiments, Thesis, The University of Texas at Austin, Austin, Texas, USA

Bahorich, B.L., Olson, J. E., Holder, J., 2012, Examining the effect of cemented natural fractures on hydraulic fracture propagation in hydrostone block experiments, In SPE Hydraulic Fracturing Technology Conference, The Woodlands, Texas, USA

Barton, C.A., Zoback, M.D., 2002, Wellbore imaging technologies appliedto reservoir geomechanics and environmental engineering, in M. Lovell and N. Parkinson eds. Geological applications of well logs, AAPG Methods inExploration, (13), pp. 229-239

Basham, K.D., 1989, Nonlinear fracture mechanics using semi-circular specimens and tension softening Behavior, PhD Dissertation, The University of Wyoming, Laramie, Wyoming, USA

Beckwith, R., 2010, Hydraulic fracturing: the fuss, the facts, and the future, Journal of Petroleum Technology,62(12), pp. 34-40

Beugelsdijk, L.J.L., de Pater, C.J., Sato, K., 2000, Experimental hydraulic fracture propagation in a multi-fractured medium, SPE 59419

Bieniawski, Z.T., 1967, Mechanism of brittle fracture of rock: Part I - theory of the fracture process, International Journal of Rock Mechanics and Mining Sciences, 4, pp. 395-406

Blair, S.C., Thorpe, R.K., Heuze, F.E., Shaffer, R.J., 1989, Laboratory observations of the effect of geological discontinuities on hydrofracture propagation, ARMA 89-0443 presented at The 30th U.S. Symposium on Rock Mechanics(USRMS), Morgantown, WV, USA, June 19-22

Blanton, T.L., 1982, Anexperimental study of interaction between hydraulically induced and pre-existing fractures, In SPE Unconventional Gas Recovery Symposium., Pittsburgh, PA, USA

Blanton, T.L., 1986, Propagation of hydraulically and dynamically Induced Fractures in Naturally Fractured Reservoirs, SPE 15261

Bobet, A., 1997, Fracture coalescence in rock materials: Experimental observations and numerical predictions, PhD Dissertation, MassachusettsInstitute ofTechnology, Cambridge, Massachusetts, USA

Bobet, A., Einstein, H.H., 1998, Fracture coalescence in rock-type materials under uniaxial and biaxial compression, International Journal of Rock Mechanics and Mining Sciences, 35 (7), pp. 863-888

Bobet, A., 2000, The initiation of secondary cracks in compression, Engineering Fracture Mechanics, 66, pp. 187-219

Bombolakis, E.G., 1963, Photoelastic stress analysis ofcrack propagation within a compressive stressfield, PhD Dissertation, MassachusettsInstitute ofTechnology, Cambridge, Massachusetts, USA

Brace, W.F., Bombolakis, E.G., 1963, A note on brittle crack growth in compression, Journal of Geophysical Research, 68 (12)

Bruner, W.M., 1984, Crack growth during unroofing of crustal rocks: Effects on thermoelastic behavior and near-surface stresses, Journal of GeophysicalResearch, 89, pp. 4167-4184

Byerlee, J., 1978, Friction of rocks, Pure and Applied Geophysics, 116 (4-5), pp. 615-626

Cahoy, D.R., Gehman, J., Lei, Z., 2012, Fracking patents:The emergence of patents as information-containment tools in shale drilling, Michigan Telecommunications and Technology Law Review, 19 (2)

Camacho, B.I., 2001, Mechanical properties of granular material as measured from velocity of shear waves, Report, The University of Texas at Austin, Austin, Texas, USA

Caputo, R., 2010, Why joints are more abundant than faults: A conceptual model to estimate their ratio in layered carbonate rocks, Journal of Structural Geology, 32, pp. 1257-1270

Carmichael, R.S., 1989, Practical handbook of physical properties of rock and minerals, CRC Press, Boca Raton, FL

Chaker, C., Barquins, M., 1996, Sliding effect on branch crack, Physics and Chemistry of the Earth, 21 (4), pp. 319-323

Chang, K.J., Wu, H.C., 1980, Angled elliptic notch problem under biaxial loading, Journal of Applied Mechanics, 47, pp. 57-63

Chang, K.J., 1982, A further examination on the application of the strain energy density theory to the angled crack problem, Journal of Applied Mechanics, 49, pp. 377-382

Chao, Y.J., Zhang, X.H., 1997, Constraint effect in brittle fracture, in R.S. Piascik, J.C. Newman, D.E. Dowling eds. Fatigue and Fracture Mechanics, ASTM STP 1296, pp. 41-60

Charlez, P.A., 1997, Rock mechanics: Petroleum applications, Paris: Editions Technip., 2, pp. 239

Chen, C.S., Wawrzynek, P.A., Ingraffea, A.R., 1999, Crack growth simulation and residual strength prediction in airplane fuselages, NASA/CR-1999-209115, Langley Research Center, Hampton, VA

Cho, N., Martin, C.D., Sego, D.C., 2007, A clumped particle model for rock, International Journal of Rock Mechanics and Mining Sciences, 44, pp. 997-1010

Chong, K.P., Kuruppu, M.D., 1984, New specimen for fracture toughness determination for rock and other materials, International Journal of Fracture, 26(2), R59-R62

Chong, K.P., Kuruppu, M.D., Kuszmaul, J. S., 1987, Fracture toughness determination of layered materials, Engineering Fracture Mechanics, 28(1), pp. 43-54

Chuprakov, D., Melchaeva, O., Prioul, R., 2013, Injection-sensitive mechanics of hydraulic fracture interaction with discontinuities, ARMA 13-252

Chuprakov, D., Melchaeva, O., Prioul, R., 2014, Injection-sensitive mechanics of hydraulic fracture interaction with discontinuities, Rock Mechanics and Rock Engineering, 47, pp. 1625-1640

Cipolla, C.L., Warpinski, N.R., Mayerhofer, M. J., 2008, Hydraulic fracture complexity: diagnosis, remediation, and exploitation, SPE 115771, presented at the SPE Asia Pacific Oil & Gas Conference and Exhibition held in Perth, Australia, October 20-22

Claesson, J., Bohloli, B., 2002, Brazilian test: stress field and tensile strength of anisotropic rocks using an analytical solution, International Journal of Rock Mechanics and Mining Sciences, 39, pp. 991-1004

Cooke, M.L., 1997, Fracture localization along faults with spatially varying friction, Journal of Geophysical Research, 102 (B10), pp. 22,425-22,434

Cotterell, B., 1966, Notes on the paths and stability of cracks, International Journal of Fracture Mechanics., 2, pp. 526-533

Cotterell, B., 1972, Brittle fracture in compression, International Journal of Fracture Mechanics., 8 (2), pp. 195-208

Cotterell, B., Rice, J.R., 1980, Slightly curved or kinked cracks, International Journal of Fracture, 16 (2), pp.155-169

Cruikshank, K.M., Zhao, G., Johnson, A.M., 1991, Analysis of minor fractures associated with joints and faulted joints, Journal of Structural Geology, 13 (8), pp. 865-886

Cundall, P.A., 1971, Acomputer model for simulating progressive large scale movements in blocky rock systems, Proceeding of 1st Symposium of theInternational Society of Rock Mechanics, Nancy, France, 1

Cundall, P.A., Strack, O.D.L., 1979, A Discrete Numerical Model for Granular Assemblies, Géotechnique, 29 (1), pp. 47-65

Dahi-Taleghani, A., Olson, J.E., 2009, Numerical modeling of multi-stranded hydraulic fracture propagation: accounting for the interaction between induced and natural fractures, SPE Journal, 16(03), pp. 575-581

Dahi-Taleghani, A., 2009, Analysis of hydraulic fracture propagation in fracturedreservoirs: An improved model for the interaction betweeninduced and natural fractures, PhD Dissertation, The University of Texas at Austin, Austin, Texas, USA

Delaney, P.T., Pollard, D.D., Ziony, J.I., McKee, E.H., 1986, Field relations between dikes and joints: Emplacement processes and paleostress analysis, Journal of Geophysical Research, 91 (B5), pp. 4920-4938

de Pater, C.J., Beugelsdijk, L.J.L., 2005, Experiments and numerical simulation of hydraulic fracturing in naturally fractured rock, ARMA/USRMS 05-780

Ding, X., Zhang, L., Zhu, H., Zhang, Q., 2014, Effect of model scale and particle size distribution on PFC3D, Rock Mechanics and Rock Engineering, 47 (6), pp. 2139-2156

Eftis, J., Subramonian, N., 1978, The inclined crack under biaxial load, Engineering Fracture Mechanics, 10, pp. 43-67

Engelder, T., Geiser, P., 1980, On the use of regional joint sets as trajectories of paleostress fields during the development of the Appalachian Plateau, New York, Journal of Geophysical Research, 85 (B11), pp. 6319-6341

Engelder, T., 1987, Joints and shear fractures in rock, in B.K. Atkinson ed. Fracture mechanics of rock, London, England, Academic press, pp.27-69

Erdogan, F., Tuncel, O., Paris, P, 1962, An experimental investigation of the crack tip stress intensity factors in plates under cylindrical bending, Journal of Basic Engineering, 84, pp. 542-546

Erdogan, F., Sih, G.C., 1963, On the crack extension in plates under plane loading and transverse shear, Trans. ASME, Journal of Basic Engineering, 85 (D), pp. 519-525

Finch, E., Hardy, S., Gawthorpe, R., 2003, Discrete element modelling of contractional fault-propagation folding above rigid basement fault blocks, Journal of Structural Geology, 25, pp. 515-528

Finnie, I., Saith, A., 1973, A note on the angled crack problem and the directional stability of cracks, International Journal of Fracture, 9, pp. 484-486

Fisher, K., Warpinski,N., 2012, Hydraulic-fracture-height growth: Real data, SPE Production & Operations, 27 (1), pp. 8-1

Fisher, M.K., Heinze, J.R., Harris, C.D., McDavidson, B.M., Wright, C.A., Dunn, K.P., 2004, Optimizing horizontal completion techniques in the Barnett Shale using Microseismic fracture mapping, SPE 90051, presented at the SPE Annual Technical Conference and Exhibition, Houston, TX, September 26-29

Fisher, M.K., Wright,C.A., Davidson,B.M., Goodwin,A.K., Fielder,E.O., Buckler,W.S., Steinsberger, N.P., 2002, Integrating fracture mapping technologies to optimize stimulations in the Barnett Shale, SPE Production & Facilities, 20 (02), pp. 85-93

Fisher, M.K.,Wright, C.A., Davidson,B.M., Goodwin,A.K., Fielder,E.O., Buckler,W.S., Steinsberger,N.P., 2005, Integrating fracture-mapping technologies to improve stimulations in the Barnett Shale, SPE Production and Facilities, pp. 85-93.

Gale, J.F.W., 2002, Specifying lengths of horizontal wells in fractured reservoirs, SPE 78600, pp. 266-272

Gale, J.F.W.,Reed, R.M., Holder, J., 2007, Natural fractures in the Barnett shale and their importance for hydraulic fracture treatments, AAPG Bulletin, 91(4), pp. 603-622

Gale, J.F.W., Laubach, S.E., Olson, J.E., Eichhubl, P., Fall, A., 2014, Natural fractures in shale: A review and new observations, AAPG Bulletin, 98 (11), pp.2165-2216

Gallegos, T.J., Varela, B.A., 2015, Trends in hydraulic fracturing distributions and treatment fluids, additives, proppants, and water volumes applied to wells drilled in the United States from 1947 through 2010—Data analysis and comparison to the literature, U.S. Geological Survey Scientific Investigations Report 2014–5131

Gargouri, M., 2012, Multicomponent 3D seismic interpretation of the Marcellus shale Bradford county, Pennsylvania, Thesis, University of Houston,Houston, Texas, USA

Ghazvinian, A., Sarfarazi, V., Schubert, W., Blumel, M., 2012, A study the failure mechanism of planar non-persistent open joints using PFC2D, Rock Mechanics and Rock Engineering, 45, pp. 677-693

Ghorbani, A., Zamora, M., Cosenza, P., 2009, Effects of desiccation on the elastic wave velocities of clay-rocks, International Journal of Rock Mechanics and Mining Sciences, 46, pp. 1267-1272

Griffith, A.A., 1920, The phenomena of rupture and flow in solids, Philosophical Transactions of the Royal Society of London, 221 (A), pp. 163-198

Griggs, D., Handin, J., 1960, Observations on fracture and a hypothesis of earthquakes, Chapter 13., Geological Society of America Memoirs, 79, pp. 347-364

Gu, H., Weng, X., 2010, Criterion for fractures crossing frictional interfaces at non-orthogonal angles, In 44th U.S. Rock Mechanics Symposium and 5th U.S.-Canada Rock Mechanics Symposium, ARMA 10-198, Salt Lake City, Utah.

Gu, H., Weng,X., Lund,J., Mack,M., Granguly,U., Suarez-Rivera, R., 2011, Hydraulic Fracture Crossing Natural Fracture at Non-orthogonal angles, A Criterion, Its Validation and Applications, In SPE Hydraulic Fracturing Technology Conference, The Woodlands, Texas, USA

Gumbsch, P., 1995, An atomistic study of brittle fracture: Toward explicit failure criteria from atomistic modeling, Journal of Materials Research, 10 (11), pp. 2897-2907

Hainey, B.W., Keck,R.G., Smith,M.B., Lynch,K.W., Barth,J.W., 1999, On-site fracturing disposal of oilfield-waste solids in Wilmington field, California, SPE Production& Facilities, 14, pp. 88-93

Hardy, S., Finch, E., 2006, Discrete element modelling of the influence of cover strength on basement-involved fault-propagation folding, Tectonophysics, 415, pp. 225-238

Hardy, S., Finch, E., 2007, Mechanical stratigraphy and the transition from trishear to kink-band fault-propagation fold forms above blind basement thrust faults: A discrete-element study, Marine and Petroleum Geolgy, 24 pp. 75-90

Hazzard, J.F., Young, R.P., Maxwell, S.C., 2000, Micromechanical modeling of cracking and failure in brittle rocks, Journal of Geophysical Research, 105 (B7), pp. 16683-16697

Hoagland R.G., Hahn, G.T., Rosenfield, A.R., 1973, Influence of microstructure on fracture propagation in rock, Rock Mechanics, 5, pp. 77-106

Hoek, E., Bieniawski, Z.T., 1965, Brittle rock fracture propagation in rock under compression, International Journal of Fracture Mechanics, 1(3), pp. 137-155

Holder, J., Olson, J.E., Philip, Z., 2001, Experimental determination of subcritical crack growth parameters in sedimentary rock, Geophysical Research Letters, 28 (4), pp. 599-602

Huang, J., Chen, G., Zhao, Y., Wang, R., 1990, An experimental study of the strain field development prior to failure of a marble plate under compression, Tectonophysics, 175, pp. 269-284

Hussain, M.A., Pu, S.L., Underwood, J., 1974, Strain energy release rate for a crack under combined mode I and mode II fracture analysis, ASTM STP 560, American Society for Testing and Materials, Philadelphia, pp. 2–28

Ichikawa, M., Tanaka, S., 1982, A critical analysis of the relationship between the energy release rate and the stress intensity factors for non-coplanar crack extension, International Journal of Fracture, 18 (1), pp. 19-28

Ingraffea, A.R., Heuze, F.E., 1980, Finite element models for rock fracture mechanics, International Journal for Numerical and Analytical Methods in Geomechanics, 4, pp. 25-43

Ingraffea, A.R., Wawrzynek, P.A., 2003, Finite element methods for linear elastic fracture mechanics, in I. Milne, R.O. Ritchie, B.L. Karihaloo ed. Comprehensive structural integrity, Elsevier, 3, pp. 1-88

Irwin, G.R., 1957, Analysis of stresses and strains near the end of a crack traversing a plate, Journal of Applied Mechanics, 24, pp. 361-364

Irwin, G.R., 1958, Fracture, in S. Flugge ed. Encyclopedia of Physics, VI, New York, Springer-Verlag, pp. 551-590

International Society of Rock Mechanics (ISRM), 1978, Suggested methods for determining tensile strength ofrock materials, International Journal of Rock Mechanics and Mining Science & Geomechanics Abstracts, 15(3), pp. 99-103

Itasca Consulting Group, Inc., 2008, Particle Flow Code in 3 Dimensions (PFC3D) Manual, Version 4.0

Izadi, G., Junca, J., Cade, C., Rowan, T., 2014, Multidisciplinary study of hydraulic fracturing in the Marcellus shale, ARMA 14-6975

Jaeger, J.C., Cook, N.G.W., 1979, Fundamentals of rock mechanics, London, Chapman and Hall

Jeffrey, R.G., Zhang, X., Thiercelin, M., 2009, Hydraulic fracture offsetting in naturally fractured reservoirs: Quantifyung a long-recognized process, SPE 119351

Josh, M., Esteban, L., Delle Piane, C., Sarout, J., Dewhurst, D.N., Clennell, M.B., 2012, Laboratory characterisation of shale properties, Journal of Petroleum Science and Engineering, 88-89, pp. 107-124

Khan, S.M.A., Khraisheh, M.K., 2000, Analysis of mixed mode crack initiation angles under various loading conditions, Engineering Fracture Mechanics, 67, pp. 397-419

King, G.E., 2010, Thirty years of Gas hale fracturing: what have we learned?, SPE 133456, presented at the SPE Annual Technical Conference and Exhibition held in Florence, Italy, September 19-22

King, G.E., 2012, Hydraulic Fracturing 101: What every representative, environmentalist, regulator, reporter, investor, university researcher, neighbor and engineer should know about estimating frac risk and improving frac performance in unconventional gas and oil wells, SPE 1525969

Kipp, M.E., Sih, G.C., 1975, The strain energy density failure criterion applied to notched elastic solids, International Journal of Solids and Structures, 11, pp. 153-173

Kong, X.M., Schluter, N., Dahl, W., 1995, Effect of triaxial stress on mixed-mode fracture, Engineering Fracture Mechanics, 52 (2), pp. 379-388

Kosai, M., Kobayashi, A.S., Ramulu, M., 1992, Tear straps in airplane fuselage, in S.N. Harris, C.E.A. Hoggard, N. Miller, S.G. Sampath eds. Durability of Metal Aircraft Structures, Atlanta Technology Publications, pp. 443-457

Kresse, O., Weng, X., Chuprakov, D., Prioul, R., Cohen, C., 2013, Effect of flow rate and viscosity on complex fracture development in ufm model, International Conference for Effective and Sustainable Hydraulic Fracturing, Brisbane, Austrailia, May 20-22

Kuruppu, M., Obara, Y., Kataoka, M., 2010, Determination of fracture toughness of anisotropic rocks under water vapour pressure by semicircular bend test, in E. Topal and M. Kuruppued. Mine Planning & Equipment Selection, December 2010, pp. 599-610

Kurrupu, M. D., Chong, K. P., 2012, Fracture toughness testing of brittle materials using semi-circular bend (SCB) specimen, Engineering Fracture Mechanics, 91, pp. 133-150

Lajtai, E.Z., 1970, A theoretical and experimental evaluation of the Griffith theory of brittle fracture, Tectonophysics, 11, pp. 129-153

Lajtai, E.Z., and Lajtai, V.N., 1974,The evolution of brittle fracture inrocks, Journal of the Geological Society, London, 130(1), pp. 1-18.

Laubach, S.E., 2003, Practical approaches to identifying sealed and open fractures, AAPG Bulletin, 87 (4), pp. 561-579

Lawn, B. R., Wilshaw, T. R., 1975, Fracture of brittle solids, Cambridge University Press, Cambridge

Lee, J.S., Kemeny, J., Ko, T.Y., 2006, Modified PTS test and clump modeling on mixed mode crack growth in granite, ARMA/USRMS 06-937

Lee, H.P., Olson, J.E., Holder, H., Gale, J.F.W., Myers, R.D., 2015, The interaction of propagating opening mode fractures with preexisting discontinuities in shale, Journal of Geophysical Research: Solid Earth, 120 (1), pp. 169-181

Li, V.C. and Rice, J.R., 1983, Preseismic rupture progression and great earthquake instabilities at plate boundaries, Journal of Geophysical Research, 88, pp. 4231-4246

Li, X., Liu, G, Lee, K.Y., 2009, Effects of T-stresses on fracture initiation for a closed crack in compression with frictional crack faces, International Journal of Fracture, 160, pp. 19-30

Li, X., Lee, K.Y., Liu, G, 2012, Kink angle and fracture load for an angled crack subjected to far-field compressive loading, Engineering Fracture Mechanics, 82, pp. 172-184

Lim, I.L., Johnson,I.W., Choi,S.K., Boland, J.N., 1994, Fracture testing of a soft rock with semi-circular specimens under three-point bending–Part 1:Mode I, International Journal of Rock Mechanics and Mining Sciences & Geomechanics Abstracts, 31 (3), pp. 185-197

Lim, I.L., Johnson,I.W., Choi, S.K., 1993, Stress intensity factors for semi-circular specimens under three-point bending, Engineering Fracture Mechanics, 44 (3), pp. 363-382

Maiti, S.K., Smith, R.A., 1983, Comparison of the criteria for mixed mode brittle fracture based on the preinstability stress-strain field– Part I: Slit and elliptical cracks under uniaxial tensile loading, International Journal of Fracture, 23, pp. 281-295

Maiti, S.K., Smith, R.A., 1984, Comparison of the criteria for mixed mode brittle fracture based on the preinstability stress-strain field– Part II: Pure shear and uniaxial compressive loading, International Journal of Fracture, 24, pp. 5-22

Maji, A.K., Tasdemir, M.A., Shah, S.P., 1991, Mixed mode crack propagation in quasi-brittle materials, Engineering Fracture Mechanics, 38 (2/3), pp. 129-145

Marrett, R., 1996, Aggregate properties of fracture populations, Journal of Structural Geology, 18 (2/3), pp. 169-178

Marrett, R., Ortega, O.J., Kelsey, C.M., 1999, Extent of power-law scaling for natural fractures in rock, Geology, 27 (9), pp. 799-802

Martel, S.J., Pollard, D.D., Segall, P., 1988, Development of simple strike-slip fault zones, Mount Abbot quadrangle, Sierra Nevada, California, Geological Society of America Bulletin, 100, pp. 1451-1465

Martel, S.J., 1997, Effects of cohesive zones on small faults and implications for secondary fracturing and fault trace geometry, Journal of Structural Geology, 19 (6), pp.835-847

Martin, A., Economides, M., 2010, Best practices for candidate selection, design and evaluation of hydraulic fracture treatments, SPE 135669, paper presented at the SPE Production and Operations Conference and Exhibition, Tunis, Tunisia

Maxwell, S.C., Urbancic,T.I.,Steinsberger,N., Zinno, R., 2002, Microseismic imaging of hydraulic fracture complexity in the Barnett shale, SPE 77440, In SPE Annual Technical Conference and Exhibition, San Antonio, Texas, USA

McClure, M.W., 2012, Modeling and characterization of hydraulic stimulation and induced seismicity in geothermal and shale gas reservoirs, PhD Dissertation, Stanford University, Stanford, California, USA

Montgomery, C.T., Smith, M.B., 2010, Hydraulic fracturing: History of an enduring technology, Journal of Petroleum Technology

Narayanasamy, R., 2002, The effect of cementation on granular materials, Thesis, The University of Texas at Austin, Austin, Texas, USA

Nazir, R., Momeni, E., Armaghani, D.J., Amin, M.F.M., 2013, Correlation between unconfined compressive strength and indirect tensile strength of limestone rock samples, Electronic Journal of Geotechnical Engineering, 18, pp. 1737-1746

Nelson, R.A., 1968, Modeling a jointed rock mass, Thesis, MassachusettsInstitute ofTechnology, Cambridge, Massachusetts, USA

Nemat-Nasser, S., Horii, H., 1982, Compression-Induced nonplanar crack extension with application to splitting, exfoliation, and rockburst, Journal of Geophysical Research, 87 (B8), pp. 6805-6821

Nuismer, R.J., 1975, An energy release rate criterion for mixed mode fracture, International Journal of Fracture, 11(2), pp. 245-250

Ode, H., 1957, Mechanical analysis of the dike pattern of the Spanish Peaks area, Colorado, Geological Society of America Bulletin, 68, pp. 567-576

Olson, J.E., Pollard, D.D., 1988, Inferring stress states from detailed joint geometry, ARMA 88-0159

Olson, J.E., Pollard, D.D., 1989, Inferring paleostresses from natural fracture patterns: A new method, Geology, 17 (4), pp. 345-348

Olson, J.E., Pollard, D.D., 1991, The initiation and growth of en echelon veins, Jounrnal of Structural Geology, 13 (4), pp. 595-608

Olson, J.E., 1993, Joint pattern development: Effects of subcritical crack growth and mechanical crack interaction, Journal of Geophysical Research, 98 (B7), pp. 12251-12265

Olson, J.E., Laubach, S.E., Lander, R.H., 2009, Natural fracture characterization in tight gas sandstones: Integrating mechanics and diagenesis, AAPG Bulletin, 93 (11), pp. 1535-1549

Olson, J.E., Bahorich, B., Holder, J., 2012, Examining hydraulic fracture - natural fracture interaction in hydrostone block experiments, SPE 152618

Olson, J.E., 1991, Fracture mechanics analysis of joints and veins, PhD Dissertation, Stanford University, Stanford, California, USA

Palaniswamy, K., Knauss, W.G., 1972, Propagation of a crack under general, in-plane tension, International Journal of Fracture Mechanics, 8, pp. 114-117

Papadopoulos, G.A., Poniridis, P.I, 1989, Crack initiation under biaxial loading with higher-order approximation, Engineering Fracture Mechanics, 32 (3), pp.351-360

Park, C.H., Bobet, A., 2010, Crack initiation, propagation and coalescence from frictional flaws in uniaxial compression, Engineering Fracture Mechanics, 77, pp. 2727-2748

Park, N., Holder, J., Olson, J.E., 2004, Discrete Element Modeling of Fracture Toughness Tests in Weakly Cemented Sandstone, ARMA/NARMS 04-553

Park, J., Song, J., 2009, Numerical simulation of a direct shear test on a rock joint using a bonded-particle model, International Journal of Rock Mechanics and Mining Sciences, 46, pp. 1315-1328

Park, N., 2006, Discrete Element Modeling of Rock Fracture Behavior: Fracture Toughness and Time-Dependent, PhD Dissertation, The University of Texas at Austin, Austin, Texas, USA

Petit, J., Barquins, M., 1988, Can natural faults propagate under mode II conditions?, Tectonics, 7 (6), pp. 1243-1256

Pettit, R.G., 2000, Crack turning in integrally stiffened aircraft structures, PhD Dissertation, Cornell Univeristy, Ithaca, NY, USA

Pollard, D.D., Aydin, A., 1984, Propagation and linkage of oceanic ridge segments, Journal of Geophysical Research, 89 (B12), pp. 10017-10028

Pollard, D.D., Aydin, A., 1988, Progress in Understanding Jointing over the PastCentury, Geological Society of America Bulletin, 100, pp. 1181-1204

Pollard, D.D., Segall, P, 1987, Theoretical displacements and stresses near fractures in rock: With applications to faults, joints, veins, dikes, and solution surfaces, in B.K. Atkinson ed. Fracture mechanics of rock, London, England, Academic press, pp. 277-349

Pook, L.P., 1971, The effect of crack angle on fracture toughness, Engineering Fracture Mechanics, 3, pp. 205-218

Potluri, N., Zhu, D., Hill, A.D., 2005, Effect of natural fractures on hydraulic fracture propagation, SPE 94568

Potyondy, D.O., Cundall, P.A., Lee, C.A., 1996, Modelling rock using bonded assemblies of circular particles, In M. Aubertin, F. Hassani, H. Mitri ed. Rock Mechanics, Balkema, Rotterdam, pp. 1937-1944

Potyondy, D.O., Cundall, P.A., 2004A bonded-particle model for rock, International Journal of Rock Mechanics and Mining Sciences, 41, pp. 1329-1364

Price, N.J., 1966, Fault and joint development in brittle and semi-brittle rock, Pergamon press, pp. 1-176

Ramsay, J.G., 1980, The crack-seal mechanism of rock deformation, Nature, 284 (5752), pp. 135-139

Renard, F., Bernard, D., Desrues, J., Ougier-Simonin, A., 2009, 3D imaging of fracture propagation using synchrotron X-ray microtomography, Earth and Planetary Science Letters, 289, pp. 285-291

Renshaw, C.E., Pollard, D.D., 1994, Are large differential stresses required for straight fracture propagation paths?, Journal of Structural Geology, 16 (6), pp. 817-822

Renshaw, C.E., Pollard, D.D., 1995, An experimentally verified criterion for propagation across unbounded frictional interfaces in brittle, linear elastic materials, International Journal of Rock Mechanics and Mining Sciences & Geomechanics Abstracts, 32 (3), pp. 237-249

Reyes, O.M., Einstein, H.H., 1991, Failure mechanisms of fractured rock – a fracture coalescence model, In: Proceedings 7th International Congress of Rock Mechanics, 1, pp. 333-340.

Reyes, O.M., 1991, Experimental study and analytical modelling of compressive fractures in brittle materials, PhD Dissertation, MassachusettsInstitute ofTechnology, Cambridge, Massachusetts, USA

Rice, J.R., Rudnicki, J.W., 1979, Earthquake precursory effects due to pore fluid stabilization of a weakening fault zone, Journal of Geophysical Research, 84, pp. 2177-2193

Rudnicki, J.W., 1980, Fracture Mechanics Applied to the Earth's Crust, Annual Review ofEarth and Planetary Sciences, 8, pp. 489-525

Sadd, M.H., 2009, Elasticity: Theory, Applications, and Numerics, Academic Press

Sasaki, S., 1998, Characteristics of microseismic events induced during hydraulicfracturing experiments at the Hijiori hot dry rock geothermal energy site, Yamagata,Japan, Tectonophysics, 289, pp. 171-188

Schmidt, R.A., Huddle, C.W., 1977, Effect of confining pressure on fracture toughness of Indiana limestone, International Journal of Rock Mechanics and Mining Sciences & Geomechanics Abstracts, 14, pp. 289-293

Schmidt, R.A., 1980, A microcrack model and its significance to hydraulic fracturing and fracture toughness testing, Proceeding of 21st U.S. Symposium on Rock Mechanics, pp. 581-590

Scholz, C.H., 1990, The mechanics of earthquakes and faulting, Cambridge University Press, New York

Schöpfer, M.P.J., Abe, S., Childs, C., Walsh, J.J., 2009, The impact of porosity and crack density on the elasticity, strength and friction of cohesive granular materials: Insights from DEM modelling, International Journal of Rock Mechanics and Mining Sciences, 46, pp. 250-261

Secor, D.T., 1965, Role of fluid pressure in jointing, American Journal of Science, 263, pp. 633-646

Segall, P., Pollard, D.D., 1983, Nucleation and growth of strike slip faults in granite, Journal of Geophysical Research, 88 (B1), pp. 555-568

Segall, P., 1984, Formation and growth of extensional fracture sets, Geological Society of America Bulletin, 95 (4), 454-462

Seto, M., Kuruppu, M.D., Funatsu, T., 2001, Fracture toughness testing of rock at elevated temperatures and pressures, ARMA 01-0745

Shen, B., Stephansson, O., Einstein, H.H., Ghahreman, B., 1995, Coalescence of fractures under shear stresses in experiments, Journal of Geophysical Research, 100 (B4), pp. 5975-5990

Shen, B., Stephansson, O., Rinne, M., 2014, Modelling rock fracturing processes: A fracture mechanics approach using FRACOD, Springer

Sih, G.C., Paris, P.C., Erdogan, F., 1962, Crack tip stress intensity factors for plane extension and plate bending problems, Journal of Applied Mechanics, 29, Trans. ASME, 84 (E), pp. 306-312

Sih, G.C., Kipp, M.E., 1974, Discussion on "Fracture under complex stress – The angled crack problem" by J.G. Williams and P.D. Ewing, International Journal of Fracture, 10 (2), pp. 261-265

Sih, G.C., 1973, Energy-density concept in fracture mechanics, Engineering Fracture Mechanics, 5, pp. 1037-1040

Smith, D.J., Ayatollahi, M.R., Pavier, M.J., 2001, The role of T-stress in brittle fracture for linear elastic materials under mixed-mode loading, Fatigue and Fracture of Engineering Materials and Structures, 24, pp. 137-150

Smith, D.J., Ayatollahi, M.R., Pavier, M.J., 2006,On the consequences of T-stress in elastic brittle fracture, Proceedings of the Royal Society A, 462, pp. 2415-2437

Smrecak, T. A., 2011, Why the geology matters, Paleontological Research Institution Marcellus Shale, 2

Spence, G.H., Finch, E., 2014, Influences of nodular chert rhythmites on natural fracture networks in carbonates: An outcrop and two-dimensional discrete element modelling study, Geological Society, London, Special Publications

Streit, R., Finnie, I., 1980, An experimental investigation of crack-path direction stability, Experimental Mechanics, 20, pp. 17-23

Suarez-Rivera, R., Connor, B., Kieschnick, J., Green, S., 2006, Hydraulic fracturing experiments help understanding fracture branching on tight gas shales, ARMA/USRMS 06-1130

Suarez-Rivera, R., Burghardt, J., Stanchits, S., Edelman, E., Surdi, A., 2013, Understanding the effect of rock fabric on fracture complexity for improving completion design and well performance, IPTC 17018

Theocaris, P.S., Andrianopoulos, N.P., 1982, A modified strain energy density criterion applied to crack propagation, Journal of Applied Mechanics, 49, pp. 81-86

Thallak, S., Rothenburg, L., Dusseault, M., 1991, Simulation of multiple hydraulic fractures in a discrete element system, ARMA 91-271, The 32nd U.S. Symposium on Rock Mechanics (USRMS), Norman, Oklahoma, July10-12

Theocaris, P.S., Papadopoulos, G., 1982, The distribution of the elastic strain-energy density at the crack tip for fracture modes I and II, International Journal of Fracture, 18 (2)

Theocaris, P.S., Sakellariou, M., 1990, Cracks and slits in compression and shear - an experimentla study, Acta Mechanica, 85, pp. 55-70

Thiercelin, M., Roegiers, J.C., 1986, Toughness determination with the modified ring test, in Proceeding of 27th U.S. Symposium on Rock Mechanics: Key to Energy Production, edited by H.L. Hartmann, SME, Littleton, Colorado, pp. 615-622

Thomas, A. L., Pollard, D. D., 1993, The geometry of echelon fractures in rock: Implications from laboratory and numerical experiments, Journal of Structural Geology, 15, pp. 323-334

Tirosh, J., Catz, E., 1981, Mixed-mode fracture angle and fracture locus of materials subjected to compressive loading, Engineering Fracture Mechanics, 14, pp. 27-38

Ueda, Y., Ikeda, K., Yao, T., Aoki, M., Yoshie, T., Shirakura, T., 1977, Brittle fracture initiation characteristics under bi-axial loading, Fracture 1977, 2, pp.173-182

U. S. Department of Energy (DOE), 2013, How is shale gas produced: Questions and answers

U. S. Energy Information Administration (EIA), 2011, Review of emerging resources: U.S. shale gas and shale oil plays

U. S. Energy Information Administration (EIA), 2014, Annual energy outlook 2014 with projections to 2040

U. S. Energy Information Administration (EIA), 2015, Annual energy outlook 2015 with projections to 2040

Valko, P., Economides, M.J., 1995, Hydraulic Fracture Mechanics, Wiley

Vallejo, L.E., 1987, The brittle and ductile behavior of a material containing a crack under mixed-mode loading, 28th US Symposium on Rock Mechanics, Tucson, June 19 - July 1, pp. 383-390

Virgo, S., Abe, S., Urai, J.L., 2013, Extension fracture propagation in rocks with veins: Insight into the crack-seal process using Discrete Element Method modeling, Journal of Geophysical Research: Solid Earth, 118 (10), pp. 5236-5251

Virgo, S., Abe, S., Urai, J.L., 2014, The evolution of crack seal vein and fracture networks in an evolving stress field: Insights from Discrete Element Models of fracture sealing, Journal of Geophysical Research: Solid Earth, 119 (12), pp. 8708-8727

Vutukuri, V. S., Lama,R. D.,Saluja.,S. S., 1974, Handbook on mechanical properties of rocks: Testing techniques and results, Trans Tech Publications

Wang, T.C., 1977, Fracture criterion for combined mode cracks, in D.M. Taplin ed. Fracture 1977, 4, pp. 135-154

Wang, M., 1985, A modified S theory, Engineering Fracture Mechanics, 22 (4), pp. 579-584

Wang, W., Olson, J.E., Prodanovic, M., 2013, Natural and hydraulic fracture interaction study based on semi-circular bending experiments, SPE 168714/URTeC 1576910

Warpinski, N.R., Lorenz, J.C., Branagan, P.T., Myal, F.R., Gall, B.L., 1993, Examination of a cored hydraulic fracture in a deep gas well, paper presenting at SPE conference, DOE; USDOE, Dallas, TX, USA

Warpinski, N.R., Teufel, L.F., 1987, Influence of geological discontinuities on hydraulic fracture propagation, Journal of Petroleum Technology, 39 (02), pp. 209-220

Warpinski, N.R., 1991, Hydraulic fracturing in tight, fissured media, Journal ofPetroleum Technology, pp. 146-209

Waters, G., Heinze, J., Jackson, R., Ketter, A., Daniels, J., Bentley, D., 2006, Use of horizontal well image tools to optimize Barnett shale reservoir exploitation, SPE 103202

Waters, G., Dean, B., Downie, R., 2009, Simultaneous hydraulic fracturing of adjacent horizontal wells in the Woodford shale, SPE 119635

Whittaker, B.N., Singh, R.N., Sun, G., 1992, Rock fracture mechanics: Principles, design and applications, Amsterdam, Elsevier

Wiley, C., Barree, B., Eberhard, M., 2004, Improved horizontal well stimulations in the Bakken formation, Williston Basin, Montana, SPE 90697

Willemse, E.J.M., Pollard, D.D., 1998, On the orientation and patterns of wing cracks and solution surfaces at the tips of a sliding flaw or fault, Journal of Geophysical Research, 103 (B2), pp. 2427-2438

Williams, M.L., 1957, On the stress distribution at the base of a stationary crack, Journal of Applied Mechanics, 24, pp. 109-114

Williams, J.G., Ewing, P.D., 1972, Fracture under complex stress – The angled crack problem, International Journal of Fracture Mechanics, 8, pp. 441-446

Wong, J.N.Y., Einstein, H.H., 2006, Fracturing Behavior of Prismatic Specimens Containing Single Flaws, ARMA/USRMS 06-899

Woo, C.W., Ling, L.H., 1984, On angled crack initiation under biaxial loading, Journal of Strain Analysis, 19(1), pp. 51-59.

Wu, H.C., Chang, K.J., 1978, Angled elliptic notch problem in compression and tension, Journal of Applied Mechanics, 45, pp. 258-262

Wu, X., Li, X., 1989, Analysis and modification of fracture criteria for mixed-mode crack, Engineering Fracture Mechanics, 34 (1), pp. 55-64

Wu, K., Olson, J.E., 2014, Simultaneous multifracture treatments: Fully coupled fluid flow and fracture mechanics for horizontal wells, SPE 167626

Wu, K., 2014, Numerical modeling of complex hydraulic fracture development inunconventional reservoirs, PhD Dissertation, The University of Texas at Austin, Austin, Texas, USA

Yeh, H., Kim, C.H., 1994, Mixed mode crack propagation studied by the Yeh-Stratton criterion, Engineering Fracture Mechanics, 48 (4), pp. 595-607

Young, R.P., Pettitt, W.S., 2000, Investigating the stability of engineered structures using acoustic validation of numerical models, Trends in Rock Mechanics,ASCE Geotechnical Special Publication No. 102, pp. 1-15

Zhang, X., Wong, L.N.Y., 2013, Loading rate effects on cracking behavior of flaw-contained specimens under uniaxial compression, International Journal of Fracture, 180 (1), pp. 93-110

Zhang, F., Nagel, N., Sheibani, F., 2014, Evaluation of hydraulic fractures crossing natural fractures at high angles using a hybrid discrete-continuum model, ARMA 14-7540

Zhou, J., Chen, M., Jin, Y., Zhang, G., 2008, Analysis of fracture propagation behavior and fracture geometry using a tri-axial fracturing system in naturally fractured reservoirs, International Journal of Rock Mechanics and Mining Sciences, 45 (7), pp. 1143-1152

Zietlow, W.K., Labuz, J.F., 1998, Measurement of the intrinsic process zone in rock using acoustic emission, International Journal of Rock Mechanics and Mining Sciences, 35 (3), pp. 291-299